PNNL-12208
UC-2000

Pacific Northwest
National Laboratory
Operated by Battelle for the
U.S. Department of Energy

Science to Support DOE Site Cleanup: The Pacific Northwest National Laboratory Environmental Management Science Program Awards

Fiscal Year 1999 Mid-Year Progress Report

May 1999

Prepared for the U.S. Department of Energy
under Contract DE-AC06-76RLO 1830

DISCLAIMER

PACIFIC NORTHWEST NATIONAL LABORATORY
operated by
BATTELLE
for the
UNITED STATES DEPARTMENT OF ENERGY
under Contract DE-AC06-76RLO 1830

Printed in the United States of America

Available to DOE and DOE contractors from the Office of Scientific and Technical Information, P.O. Box 62, Oak Ridge, TN 37831; prices available from (615) 576-8401.

Available to the public from the National Technical Information Service, U.S. Department of Commerce, 5285 Port Royal Rd., Springfield, VA 22161


This document was printed on recycled paper.

PNNL-12208
UC-2000

Science to Support DOE Site Cleanup: The Pacific Northwest National Laboratory Environmental Management Science Program Awards

Fiscal Year 1999 Mid-Year Progress Report

May 1999

Prepared for
the U.S. Department of Energy
under Contract DE-AC06-76RLO 1830

Pacific Northwest National Laboratory
Richland, Washington 99352

Summary

Pacific Northwest National Laboratory
June 1, 1999

Pacific Northwest National Laboratory was awarded ten (10) Environmental Management Science Program (EMSP) research grants in fiscal year 1996, six (6) in fiscal year 1997, and eight (8) in fiscal year 1998.[a] This section summarizes how each grant addresses significant U.S. Department of Energy (DOE) cleanup issues, including those at the Hanford Site. The technical progress made to date in each of these research projects is addressed in more detail in the individual progress reports contained in this document.

This research is focused primarily in five areas: Tank Waste Remediation, Decontamination and Decommissioning, Spent Nuclear Fuel and Nuclear Materials, Soil and Groundwater Cleanup, and Health Effects.

Tank Waste Remediation

More than 300 underground storage tanks containing about 350,000 cubic meters (92 million gallons) of mixed chemical and radioactive waste are located at the Hanford Site (Washington), Oak Ridge Reservation (Tennessee), Savannah River Site (South Carolina), Idaho National Engineering and Environmental Laboratory (Idaho), and West Valley Site (New York). The liquids, sludges, saltcake, and calcined solids (at Idaho) in these tanks contain about 70% (720 million curies) of the man-made radioactivity existing in the DOE complex. Remediation of this tank waste is one of the most technically complex, scientifically challenging, and potentially expensive problems facing DOE.

Hanford has 60% of the waste volume and 30% of the radioactivity for all DOE high-level waste tanks. At Hanford there are 177 underground storage tanks containing 210,000 cubic meters (54 million gallons) of high-level waste. The current baseline approach to remediating this tank waste is to retrieve the waste and then separate the solids from the liquid. Once cesium, strontium, and other radionuclides are removed from the liquid, it will become a relatively low-activity stream that can be immobilized as low-level radioactive and chemical waste. The solid, high-activity stream will be pretreated to reduce its volume (mainly through the removal of nonradioactive inorganic components such as chromium, phosphorous, and aluminum) and then immobilized as high-level radioactive waste.

Safe Storage

Even safe storage of the waste in the tanks gives rise to technical issues. Chemical reactions in the tanks, including reactions caused by radiation and the slow corrosion of the steel tank walls, produce gases in the waste such as hydrogen, nitrogen, nitrous oxide, ammonia, and methane. Many of these gases are flammable, toxic, or both. In addition to generating gases, the reactions degrade organic compounds in the waste, change organic fuel and oxidant concentrations, and alter the surface chemistry of insoluble colloids, influencing sedimentation and gas/solid interactions. The EMSP projects "**Interfacial**

(a) PNNL researchers are the lead principal investigators in these 24 projects. PNNL also collaborates with researchers at other institutions on 28 other EMSP projects. This document, however, does not include the annual reports for those collaborations, which are submitted through the lead institutions.

Radiolysis Effects in Tank Waste Speciation" (page 1.1) and **"Mechanisms and Kinetics of Organic Aging in High-Level Nuclear Wastes"** (page 1.11) are focused on understanding the radiolytic processes in these mixed-phase systems. The goals are to determine and understand the radiation-induced physical and chemical changes in the wastes and the rates at which they occur.

Most of the tanks have a layer of solids that can trap bubbles of generated gas. If too many bubbles become lodged in the solids layer it becomes buoyant, and the entire layer or pieces of it may rise to the surface and suddenly release the trapped gas. Other processes that disturb the waste may also release gas. Very large releases have the potential to create a flammable atmosphere in the headspace of a tank that, if ignited, could rupture the tank or filters in the ventilation system that control radionuclides. Determining the amount of retained gas in the tanks is therefore a critical component of evaluating the safety hazard of the tanks.

Periodic, direct measurements of the gas volume in each tank would be very expensive and, in some cases, impossible. However, previous work has established that the waste level responds to barometric pressure changes, leading to a method for estimating the volume of retained gas. Interactions between the gas bubbles and the rheologically complex waste are poorly understood, though, causing inaccuracies in this method. The objective of the EMSP project **"Mechanics of Bubbles in Sludges and Slurries"** (page 1.23) is to gain a fundamental understanding of these interactions and improve the accuracy of gas volume estimates.

Characterization

Characterizing the complex and heterogeneous wastes is difficult and expensive. Yet, an adequate characterization is vital to making decisions about storage and each treatment step. At Hanford, waste delivered to the privatization contractor must be demonstrated to be within certain specifications on composition, solids content, etc. Likewise, payments made to the contractor will be based on the waste content of the immobilized product.

Laser mass spectrometry techniques have, in principle, the capability to provide rapid, accurate characterization of complex materials at the pico- or even femtomolar sensitivity level — a capability which would dramatically reduce the sample quantities required for accurate characterization of waste material and which would also make possible on-line monitoring of waste streams. This, in turn, would reduce exposure to laboratory workers and make it substantially easier and cheaper to measure waste composition. However, analytical techniques now available do not yet provide this capability. An EMSP project, **"Mass Spectrometric Fingerprinting of Tank Waste Using Tunable, Ultrafast Infrared Lasers"** (page 1.35), is developing protocols for the quantitative analysis of tank waste materials based on the use of tunable infrared ultrashort-pulse lasers.

Retrieval and Waste Transfer

The wastes are complex and highly alkaline mixtures of many species, with sodium, nitrate, and hydroxide being predominant. Some of the most interesting thermodynamics in the waste involve aluminum phases, which can precipitate or dissolve during waste processing depending on the waste's pH and the concentrations of certain ions. Changes in pH or waste composition during waste retrieval, transfer, and processing must be done thoughtfully to prevent unwanted precipitation or scale formation. Of all constituents of tank waste, aluminum species have the greatest potential for clogging pipes and transfer lines, fouling highly radioactive components such as ion exchangers, and shutting down processing operations. The primary focus of **"Dissolution, Precipitation, and Deposition of**

Aluminum-Containing Phases in Tank Wastes" (page 1.39) is to understand the major factors controlling precipitation, scale formation, and cementation of existing insoluble particles by aluminum-containing phases so that fouling and clogging can be avoided.

The presence of submicron, colloidal particles in the waste complicates nearly every aspect of waste processing. They make the separation of solid and liquid waste streams difficult by forming colloidal suspensions, which may take months to settle, if at all. These suspensions can also form sediments or gels, clogging pipes and interrupting waste transfer operations.

Colloidal particles can also contaminate the liquid waste, complicating downstream processing. Radionuclides can adsorb to the particles' surfaces and radioactively contaminate the low-level liquid waste stream, forcing it to be treated as high-activity waste, thereby increasing treatment costs. In other cases, the presence of colloidal particles interferes with separations processes by plugging ion exchange columns, causing schedule delays and increased costs.

The EMSP project **"Colloidal Agglomerates in Tank Sludge: Impact on Waste Processing"** (page 1.49) is conducting experiments to understand and identify the chemical conditions that control the formation and agglomeration of colloidal particles. In this way, the effect that agglomerate structures have on the rheology and sedimentation properties of the waste can be quantified, and methods for manipulating agglomerate structures to optimize tank waste transfer and processing conditions can be developed. It is important to note that the new knowledge and data generated by this project will also be of benefit to the cleanup of K-Basin liquids at Hanford and the tank wastes at the Oak Ridge Reservation and the Savannah River Site.

Pretreatment

Several EMSP projects are investigating innovative approaches in the area of separation processes. Radionuclides must be removed to prepare the liquid waste stream for immobilization as low-level waste, while nonradioactive species must be extracted from the high-activity waste stream to minimize its volume. Both aspects present a series of technical challenges.

Current strategies for reducing the volume of the solid, high-activity waste stream involve developing methods to selectively dissolve and remove nonradioactive elements such as aluminum, phosphorus, and chromium while retaining the radioactive elements in the sludges. The EMSP project **"Speciation, Dissolution, and Redox Reactions of Chromium Relevant to Pretreatment and Separation of High-Level Tank Wastes"** (page 1.61) looks specifically at chromium, which is not effectively removed by current sludge washing techniques and is difficult to incorporate into glass. The project seeks to understand the speciation, dissolution, and redox reactions of chromium under conditions relevant to high-level waste, i.e., multicomponent, highly nonideal electrolyte systems. The project will provide critical data to support the development of pretreatment processes for the removal of chromium and thereby help to achieve major cost savings in high-level waste disposal.

Turning to the low-level waste stream, the removal of cesium appears to be straightforward, with ion-exchange technologies capable of meeting the performance criteria. In conventional ion-exchange processes, the cesium-bearing liquid passes through a reactor packed with an organic resin or other ion-exchange material. The cesium binds to the resin but not permanently. Once the resin has reached its cesium capacity, the cesium is flushed from the resin with acid and reused. However, this creates a second liquid waste stream that must be processed further (e.g., by incorporating into borosilicate glass) for long-term storage or disposal.

The EMSP project "**New Silicotitanate Waste Forms: Development and Characterization**" (page 1.69) is investigating a new strategy for disposing of crystalline silicotitanate (CST) ion exchangers by in situ heat treatment with minimal or no additives to produce an alternative waste form. The CST is the most promising commercially available candidate for removal of cesium and strontium from tank wastes; however, it has been identified as a risk to vitrification due to its high level of TiO_2. This EMSP project is characterizing the phase relationships, structures, and thermodynamic and kinetic stabilities of CST waste forms and establishing a sound technical basis for understanding key waste form properties, such as melting temperatures and aqueous durability, based on an in-depth understanding of waste form structures and thermochemistry. This approach could significantly reduce the volume and costs associated with waste disposal, minimize the risk of environmental contamination during processing, eliminate problems associated with radiolytic hydrogen generation during short-term storage, and provide DOE with technical alternatives for waste disposal.

In some tanks, there may be a need to remove the lanthanides and actinides (because of their long half-lives of 10^2–10^6 years) and/or strontium, which has been complexed by organic chelating agents present in the waste. Partitioning during the separation processes is complicated by the presence of organic chelating agents, which bind up both radionuclides and nonradioactive metals. During pretreatment, the radionuclides must be displaced from the chelating agents by manipulating the hydroxide concentration or the concentration of other metals. To minimize the high-level waste volume, however, this displacement must be selective. Designing a selective separation process for the highly complex waste without resorting to an ad hoc approach requires a fundamental understanding of what controls the conformation of the chelating agents and their interactions with metals and other ions. "**Development of Fundamental Data on Chemical Speciation for Strontium and Americium in High-Level Waste: Predictive Modeling of Phase Partitioning During Tank Processing**" (page 1.81) addresses the problem of trivalent actinide (americium/cesium) and strontium speciation and solubility in tank liquids. The resulting data will be used to develop thermodynamic models to predict changes in chemical speciation and solubility as a result of changes in tank processing conditions. In this way, existing processes can be optimized and new processes can be developed.

Self-assembled monolayers on mesoporous supports (SAMMS) is one such example of a new separation medium that could be applied to tank waste processing. A PNNL-developed technology, SAMMS sequesters heavy metals within small pores coated with a single molecular layer of ligands. The EMSP project "**Actinide-Specific Interfacial Chemistry of Monolayer Coated Mesoporous Ceramics**" (page 1.89) is developing a SAMMS material to selectively bind actinides. These studies are aimed at understanding and optimizing the chemistry of the ligand monolayer and its interactions with the target actinide species.

The EMSP project "**Architectural Design Criteria for *f*-Block Metal Sequestering Agents**" (page 1.99) uses computational and experimental methods to optimize ligand architecture for sequestering *f*-block metals, including many actinides and lanthanides. By developing an accurate set of criteria for ligand architecture design, ligand structures can be targeted for synthesis, dramatically reducing the time and cost associated with metal-specific ligand development. This provides cleanup projects with more cost-effective and efficient separations agents that can reduce schedules and save money, especially the costs associated with the regeneration of separations materials and/or the disposal of spent separations materials.

Another approach to removing complexed strontium is to first destroy the organic complexants. The EMSP project "**Ionizing Radiation-Induced Catalysis on Metal Oxide Particles**" (page 1.117) is developing a novel approach for organic destruction using the redox chemistry resulting from the

radiation already present in the tanks. This approach has the advantages of being nonthermal and emission-free. Moreover, it is applicable to any organic-containing waste stream, and it can also make use of the currently unused cesium and strontium capsules at Hanford as radiation sources.

Two EMSP projects are exploring novel approaches for technetium removal. Technetium has a moderately long half-life and, if left in the immobilized low-activity waste, would soon become the dominant source of radioactivity. Removing technetium would therefore make the low-level waste form more benign. Technetium is also a relatively volatile material that is difficult to incorporate into glass under the high temperatures used in standard vitrification. However, technetium removal is complicated by its speciation in tank waste, which is thought to be pertechnetate anion, TcO_4^-. While traditional ion exchange processes are quite effective on cations such as cesium and strontium, they are much less effective on anions. The EMSP project **"Electroactive Materials for Anion Separation – Technetium from Nitrate"** (page 1.123) is investigating how to use electroactive materials to sorb technetium without also extracting nitrate anions, which are present in very high concentration. This new process expels (elutes) the technetium electrochemically rather than using a chemical eluant, reducing the amount of chemicals added and thereby minimizing waste. The research focuses on manipulating specific properties of redox polymers to control their reversibility, selectivity, stability, intercalation/de-intercalation rates, and capacity.

Another EMSP project, led by Penn State in collaboration with PNNL, takes a different approach. The investigators of **"Removal of Technetium, Carbon Tetrachloride, and Metals from DOE Properties"** (page 1.133) have prepared a new class of powerful reducing agents called Ferragels, which consist of finely divided zero-valent metals on high surface area supports. Because the rate of the surface oxidation-reduction reaction depends on available surface area, Ferragels are more effective than unsupported metals. The benefit of this approach is that the loaded Ferragels employing inorganic support materials could be vitrified with significantly low technetium volatility into a separate waste form. PNNL has demonstrated that Ferragels can reduce and extract pertechnetate from simulated low-level waste streams. The work at PNNL is focused on improving the compatibility of the Ferragel supports with highly alkaline tank waste.

Immobilization

Once the high-activity stream has been reduced in volume, the remaining waste, with its concentrated radionuclides, will be immobilized. The approach DOE has chosen for most of its sites is to vitrify the waste, that is, to incorporate it into glass. With DOE support, large electrically heated melters have been developed for waste processing. However, a number of scientific issues remain that could affect melter operation and the amount of waste that can be incorporated into the glass without reducing its durability. The EMSP project **"Modeling of Spinel Settling in Waste Glass Melter"** (page 1.137) studies the formation and settling of spinel, the most common crystalline phase that precipitates in molten high-level waste glass. Spinel is a product of an interaction between Cr_2O_3, Fe_2O_3, NiO, FeO, and other oxides that are components of virtually all high-level waste streams at Hanford and Savannah River. Spinel formation in a high-level waste melter limits the waste fraction in glass because accumulation of spinel interferes with melter operation and shortens its lifetime. Understanding and preventing spinel formation will therefore enable higher waste loading, reducing the costs of high-level waste disposal potentially by billions of dollars.

Storage and Disposal

Once immobilized, the low-activity waste will be disposed on site, while the high-activity waste is to be disposed at the federal geologic repository. However, interactions between alkali ions (such as sodium) and radionuclides in the immobilized waste that could affect their release rate are not well understood. The impact of internal radiation on the long-term performance of these immobilized forms is also unclear. And, given the time frames involved (ca. 10,000 years) the data will not be gathered from simple experimentation. The EMSP project "**Ion Exchange Processes and Mechanisms in Glasses**" (page 1.151) investigates ion exchange reactions and kinetics within the glass and relates those kinetics to glass structural properties. The EMSP project "**Radiation Effects in Nuclear Waste Materials**" (page 1.161) is focused on developing a fundamental understanding of radiation effects in glass and ceramic waste forms. The understanding and associated data from both of these projects will improve models assessing the long-term performance of these waste forms. It is also important to note that these studies will benefit the assessment of waste forms proposed for the immobilization and disposal of plutonium residues and scrap and excess weapons plutonium.

Decontamination and Decommissioning

DOE built thousands of facilities to generate and process nuclear weapons material. Part of the cleanup agenda involves closing the buildings themselves (e.g., nuclear reactors, chemical processing facilities, and reactor fuel pools) after characterizing, dismantling, and cleaning out facilities within them (e.g., glove boxes and hot cells). Radioactive contamination must often be cleaned from surfaces in these facilities to close ("decommission") them. Contamination may be physically removed by wiping, scraping, or scabbling, or it may be washed off using special cleaning agents. Virtually every DOE site has facilities awaiting or undergoing decontamination and decommissioning, and the major sites may have hundreds.

Two PNNL EMSP projects are focused on understanding and improving the methods used for cleaning surfaces. "**Microbially Promoted Solubilization of Steel Corrosion Products and Fate of Associated Actinides**" (page 2.1) probes some of the fundamental scientific issues regarding a microbial process with potential for decontaminating corroding metal surfaces. Certain iron-reducing bacteria can dissolve the rust and oxide layers on steel and thereby release radionuclide contaminants attached to those surfaces. The actinides are sorbed by cell surfaces or precipitated within biofilms that can be removed and recovered by an enzymatic digestion of the microbes. This environmentally benign, enzymatic process avoids the use of hazardous or toxic chemicals and minimizes the volume and toxicity of secondary wastes. Similarly, "**Contaminant-Organic Complexes, Their Structure and Energetics in Surface Decontaminant Processes**" (page 2.9) investigates the use of powerful, microbially produced chelates (called siderophores) as decontamination and sequestering agents. Studies of these compounds demonstrate that their binding affinity for iron and actinides with a (IV) valence state are as much as 20 orders of magnitude higher than other chelating agents (i.e., EDTA).

Spent Nuclear Fuel and Nuclear Materials

Another legacy of nuclear weapon production is spent nuclear fuel, plutonium residues, and scrap and excess weapons plutonium. DOE has 2500 metric tons of spent nuclear fuel (SNF) in water storage across the complex. For example, the Hanford Site K-Basins hold 2100 metric tons of spent fuel, much of it severely corroded. Similar situations exist elsewhere in the DOE complex, especially at Savannah River and Idaho National Engineering and Environmental Laboratory. DOE plans to remove much of

this fuel and seal it in canisters for "dry" interim storage for up to 75 years awaiting permanent disposition. However, chemically bound water will remain in cracks and remain bound to surfaces even following proposed drying steps, leading to possible long-term corrosion of the containers and/or fuel rods themselves, radiolytic generation of H_2 and O_2 gas, which could lead to deflagration or detonation, and reactions of pyrophoric uranium hydrides. No thoroughly tested model is currently available to predict fuel behavior during pre-processing, processing, or storage. The EMSP project **"Radiolytic and Thermal Process Relevant to Dry Storage of Spent Nuclear Fuels"** (page 3.1) is therefore studying the radiolytic reactions, "drying" processes, and corrosion behavior of actual SNF materials and pure and mixed-phase samples. These studies will determine what is omitted from current models: radiolysis of water adsorbed on or in hydrates or hydroxides, thermodynamics of interfacial phases, and kinetics of drying.

Dried and packaged SNF will ultimately be shipped to the federal geologic repository for final disposal, while transuranic materials such as plutonium and uranium will be treated (if necessary), packaged, and shipped to the Waste Isolation Pilot Plant near Carlsbad, New Mexico. The EMSP project **"Distribution and Solubility of Radionuclides and Neutron Absorbers in Waste Forms for Disposition of Plutonium Ash and Scraps, Excess Plutonium, and Miscellaneous Spent Nuclear Fuels"** (page 3.7) is working to understand the distributions, solubilities, and releases of radionuclides and neutron absorbers in these materials after disposition. The results will provide the underpinning knowledge for developing, evaluating, selecting, and matching waste forms for safe disposal and for developing models of their long-term performance.

Soil and Groundwater Cleanup[(a)]

Contaminant plumes, contaminated soils, and landfills account for some 4,800 waste sites on DOE property in 31 states (DOE 1995). Approximately 35 million cubic meters of soil are contaminated with low-level and mixed low-level waste (ORNL 1994). Another 1.2 million cubic meters of soil is contaminated with transuranic and mixed transuranic waste. Landfills of buried waste are estimated to contain 3 million cubic meters of low-level waste. This includes 105,000 cubic meters of retrievably stored transuranic waste. Several hundred square miles of groundwater are contaminated with a variety of radionuclides and hazardous chemicals in concentrations above drinking water standards and DOE's concentration guidelines.

Nearly 150 square miles of groundwater contamination underlies Hanford. The radioactive and hazardous wastes are dispersed through large volumes of soil and groundwater, making potential treatment by conventional soil excavation and groundwater cleanup technologies ineffective and costly. In addition, some 650,000 metric tons of solid waste is buried at Hanford.

The current baseline approach for treating contaminated groundwaters is to pump out the groundwater, treat it ex situ, and return it to the subsurface ("pump and treat"). For contaminated soils, the plan is simple: dig it up and dispose of it in a controlled disposal unit. At Hanford, that unit is the Environmental Restoration Disposal Facility (ERDF).

(a) The FY 1999 EMSP call for proposals specifically requested research proposals in the area of subsurface contamination and vadose zone issues. PNNL submitted 39 proposals to this call (17 in which PNNL was the lead organization and 22 led by collaborators). At the time this report was printed, these projects had not yet been awarded.

ERDF, centrally located on the 200 Area plateau, is receiving contaminated soils and solid waste from the 100 Area. Two cells are now operating with a capacity of approximately 1.2 million cubic yards each. The potential exists for eight new cells depending upon future needs. These cells, classified as RCRA (Resource Conservation and Recovery Act) landfills, have a design life of approximately 20–30 years, which may be extended through the use of caps and/or engineered barriers.

While ex situ options may be available and effective over the short term, they are more expensive, labor intensive, and have a greater potential for worker and environmental risk than in situ methods. Consequently, there are many drivers for the development of in situ treatment, monitoring, and characterization solutions.

One class of in situ treatment approaches holding great promise uses biological organisms to effect the cleanup (bioremediation). The EMSP project "**Dynamics of Coupled Contaminant and Microbial Transport in Heterogeneous Porous Media**" (page 4.1) is providing fundamental data on the attachment/detachment dynamics of anaerobic bacteria in porous media under growth and growth-limiting conditions. The dynamics of attachment/detachment vary with individual bacterial species and are especially important when a contaminant is collectively degraded by bacterial consortia. This understanding of coupled contaminant and bacterial transport in actual subsurface media is critical to the design, evaluation, and success of any bioremediation or biobarrier strategy.

Another critical factor controlling the success of bioremediation efforts is the response of the subsurface microbial community and individual bacteria to the stresses encountered at contaminated sites. These stresses include low nutrient concentrations, low oxygen concentrations, and the presence of pollutants. Defining bacterial responses to these stresses presents an opportunity for improving bioremediation strategies, both with indigenous populations and genetically engineered microbes, and will reduce the cost and time required to achieve cleanup goals.

The EMSP project "**Genetic Analysis of Stress Responses in Soil Bacteria for Enhanced Bioremediation of Mixed Contaminants**" (page 4.13) is focused on identifying the stress-inducible genes from soil bacteria with unique degradative capabilities. Investigators will then demonstrate how the manipulation and expression of these genes will allow the degradation of trichloroethylene under low-nutrient conditions.

Non-biologically controlled processes can also contribute to the in situ treatment of subsurface contaminants. For example, many of the inorganic and organic contaminants present in the soils and groundwater at Hanford and other DOE sites can be altered, immobilized, or destroyed by reduction and oxidation reactions occurring at mineral surfaces. The EMSP project "**Molecular-Level Processes Governing the Interaction of Contaminants with Iron and Manganese Oxides**" (page 4.21) is a combined experimental and theoretical study. Researchers will develop a detailed understanding of specific mineral surface (iron and manganese oxides) and contaminant (chromate and chlorinated solvents) reactivities that will substantially improve models of contaminant fate and transport in geologic systems. This work will also help technology developers optimize the manipulation of geochemical reduction and oxidation processes for improved subsurface treatment.

Finally, the rate of migration of radioactive cesium and other contaminants in the subsurface from tank leakage or waste cribs has received considerable attention at Hanford lately. Although it is strongly sorbed by the micaceous fraction of the soil, cesium appears to be moving faster towards the groundwater and, ultimately, the Columbia River than previously thought possible. Two EMSP projects are focused on understanding contaminant fate and transport. The EMSP project "**Mineral Surface Processes Responsible for the Decreased Retardation (or Enhanced Mobilization) of ^{137}Cs from High-Level**

Waste Tank Discharges" (page 4.37) is investigating the geochemistry of cesium ion adsorption under conditions appropriate to high-level waste tank releases. High sodium concentrations in tank waste are thought to suppress all but the most selective cesium sorption sites on the frayed edges of micaceous particles. The hydroxide and aluminate compounds in high-level waste may alter these sites chemically, leading to faster transport through the soil.

Previous attempts to predict vadose zone transport have neglected driving forces and mechanisms of nonuniform contaminant migration, which result in erratic flow patterns and cause contaminants to bypass much of the unsaturated soil matrix. The primary objective of "**Rapid Migration of Radionuclides Leaked from High-Level Waste Tanks: A Study of Salinity Gradients, Wetted Path Geometry, and Water Vapor Transport**" (page 4.47) is to investigate the causes and extent of nonuniform flow in the vadose zone and its effects on the migration of contaminants leaked from single-shell tanks. These driving forces include the effect of elevated surface tension of highly saline fluids on wetting front instability, finger formation, and contaminant mobility and osmotically driven vapor flux. The project will incorporate its findings into an existing DOE-developed numerical simulator to improve predictions of contaminant migration.

Health Effects

Future land uses, regulatory requirements, stakeholder and tribal concerns, and the potential health impacts from hazardous waste and radionuclide contamination will dictate the acceptable treatment approaches and cleanup levels at Hanford and other DOE sites. Trichloroethylene (TCE), a chlorinated solvent, is one of the most common chlorinated organic contaminants at DOE sites (including Hanford, though carbon tetrachloride is a more widespread problem there). Cleanup costs for chlorinated solvents are driven most frequently by TCE because it is both widespread and is generally present at the highest concentrations on DOE sites. The EMSP project "**Mechanisms Involved in Trichloroethylene-Induced Liver Cancer: Importance to Environmental Cleanup**" (page 5.1) is developing critical data for updating the human health and safety risk-based cleanup standards for TCE that were developed 20 years ago. These data could potentially allow changes in risk-based standards for TCE that could reduce complex-wide cleanup costs by several billions of dollars while still protecting humans and the environment.

References

DOE. 1995. *Estimating the Cold War Mortgage: The 1995 Baseline Environmental Management Report.* DOE/EM-0232, U.S. Department of Energy, Washington, D.C.

ORNL. 1994. *Integrated Data Base Report-1993: U.S. Spent Nuclear Fuel and Radioactive Waste Inventories, Projections, and Characteristics.* DOE/RW-0006 Rev. 10, Oak Ridge National Laboratory, Oak Ridge, Tennessee.

For more information contact:

Dr. Rod K. Quinn
Manager, Environmental Science and Technology
Pacific Northwest National Laboratory
(509) 375-6625
rod.quinn@pnl.gov

Dr. Loni M. Peurrung
Environmental Science and Technology
Pacific Northwest National Laboratory
(509) 373-0201
loni.peurrung@pnl.gov

or

Mr. Roy E. Gephart
Program Manager
Environmental and Health Sciences Division
Pacific Northwest National Laboratory
(509) 375-6754
roy.gephart@pnl.gov

Contents

1.0 Tank Waste Remediation

2.0 Decommissioning and Decontamination

Tank Waste Remediation

Interfacial Radiolysis Effects in Tank Waste Speciation

(First Year of Funding: 1996)

Principal Investigator

T. M. Orlando
Pacific Northwest National Laboratory
P.O. Box 999, MSIN K8-88
Richland, WA 99352
(509) 376-9420 (phone)
(509) 376-6066 (fax)
thomas.orlando@pnl.gov

Co-Principal Investigators

D. Meisel
Notre Dame Radiation Laboratory
University of Notre Dame
Notre Dame, IN 46556-0579
(219) 631-5457 (phone)
(630) 631-3646 (fax)
dani@nd.edu

D. M. Camaioni
Pacific Northwest National Laboratory
P.O. Box 999, MSIN K2-44
Richland, WA 99352
(509) 375-2739 (phone)
(509) 375-2186 (fax)
donald.camaioni@pnl.gov

Contributors and Collaborators

K. Knutsen (Assoc. Western Universities Postdoctoral Fellow)
N. Petrik (Assoc. Western Universities Visiting Research Scientist)
A. R. Cook (Argonne National Laboratory Assistant Scientist)
N. Dimitrievic (Argonne National Laboratory Visiting Scientist)
T. Schatz (Argonne National Laboratory Postdoctoral Fellow)
N. Zevos (State University of New York, Potsdam Visiting Professor)
Amit K. Sharma (Pacific Northwest National Laboratory)

Research Objective

The purpose of this program is to deliver pertinent, fundamental information that can be used to make technically defensible decisions on safety issues and processing strategies for mixed chemical and radioactive waste cleanup at U.S. Department of Energy (DOE) sites. We intend to establish an understanding of radiolysis in mixed-phase systems typical of heterogeneous, radioactive, and chemical wastes. This is an important scientific concern with respect to understanding tank waste chemistry issues; until now, it has received relatively little attention. The importance of understanding solid-state radiolysis, secondary electron interactions, charge-transfer dynamics, and the general effect of heterogeneous solids (interface and particulate surface chemistry) on tank waste radiation processes will be demonstrated. In particular, we will investigate 1) the role of solid-state and interfacial radiolysis in the generation of gases, 2) the mechanisms of organic compound degradation, 3) scientific issues underlying safe interim storage, and 4) the effects of colloid surface-chemical properties on waste chemistry.

Research Statement

The radioactive and chemical wastes present in DOE underground storage tanks contain complex mixtures of sludges, salts, and supernatant liquids. These mixtures, which comprise a wide variety of oxide materials, aqueous solvents, and organic components, are constantly bombarded with energetic particles produced through the decay of radioactive ^{137}Cs and ^{90}Sr. A vital need exists to understand radiolysis of organic and inorganic species present in mixed waste tanks because these processes

- produce mixtures of toxic, flammable, and potentially explosive gases (i.e., H_2, N_2O, and volatile organics)
- degrade organics, possibly to gas-generating organic fragments, even as the degradation reduces the hazards associated with nitrate-organic mixtures
- alter the surface chemistry of insoluble colloids in tank sludge, influencing sedimentation and the gas/solid interactions that may lead to gas entrapment phenomena.

Unfortunately, the mixed chemical and radiolytic nature of the problem greatly complicates the interactions, and the information available on radiolytic processes in multiphase heterogeneous systems is insufficient to develop accurate safety margins or radiolysis models that adequately describe DOE tank waste chemistry to support technically sound decision making.

Research Progress

Progress is reported in three areas: 1) electron-beam interactions with $NaNO_3$ crystals, 2) radiation effects in aqueous suspensions of oxide particles, and 3) reactions of organic complexants with NO_2 in water. The first two areas involve controlled radiolysis studies using pulsed, low- (5–150 eV) and high- (3 MeV) energy electron beams at Pacific Northwest National Laboratory (PNNL) and at the Radiation Laboratory of the University of Notre Dame, respectively. The low-energy electron irradiation studies suggest that O_2 and NO are the dominant oxidizing species generated by radiolysis of the solid $NaNO_3$ components in tank wastes at the Hanford Site. These oxidants contribute to the degradation of organic waste constituents but also help initiate the generation of flammable gas. NO_2 is the dominant oxidant in the solution phase, and studies have been carried out on elucidating the

kinetics and products of NO_2 reactions with organics. The research disclosed in this report is the result of collaborations between the listed investigators, who closely coordinate their efforts on this project, another EMSP project located at the University of Notre Dame ("NO_x System in Nuclear Waste," PI: D. Meisel), and a project in the Tank Waste Safety Program at the Hanford Site ("Waste Aging Studies Project," PI: D. M. Camaioni).

Electron Beam Interactions with $NaNO_3$ Solids and Methanol Overlayers

The aim of some of the work in FY 1999 was to study electron-induced degradation of $NaNO_3$ crystals as a function of substrate temperature and to probe radiation-induced processes at the $NaNO_3$/methanol interface.

Production of NO and O_2 from Low-Energy Electron Impact on Solution-Grown $NaNO_3$ Single Crystals at Low Temperature

$NaNO_3$ crystals were irradiated with a continuous 100 eV electron beam, and damage was analyzed for substrate temperatures from 100–450K. NO and O_2, the two primary molecular products produced during electron-beam irradiation of $NaNO_3$, were detected via quadrupole mass spectrometry. The formation of NO and O_2 is consistent with previous work using pulsed electron and photon irradiation of $NaNO_3$ single crystals (Knutsen and Orlando 1996, 1997, 1998). In the case of solid-state radiolysis, the NO_2 yield is very low in comparison to O_2 and NO. The temperature dependence of the NO and O_2 steady-state electron-stimulated desorption (ESD) rates is identical and can be approximated by the sum of two exponents. These exponents, 0.16 ± 0.03 and 0.010 ± 0.004 eV, correspond to activation energies for NO and O_2 desorption.

A significant fraction of the O_2 molecules produced by radiation remain trapped in the crystal matrix. Molecular oxygen is then released from the crystal during temperature programmed annealing. The temperature-programmed desorption (TPD) curve indicates at least two distinct mechanisms for O_2 production and desorption. The high-temperature peak at 340K is consistent with temperature decomposition of the peroxynitrite ion $ONOO^-$ in accordance with a well-known scheme of $NaNO_3$ bulk radiolysis/photolysis:

$$NO_3^- \rightarrow ONOO^- \quad (1)$$

$$ONOO^- \rightarrow NO_2^- + O \ (\sim 340K) \quad (2)$$

$$O + NO_3^- \rightarrow NO_2^- + O_2 \quad (3)$$

$$O + O \rightarrow O_2 \quad (4)$$

The sharp, low-temperature TPD peak at 240K likely corresponds to temperature decay of the caged complex $[NO_2^-, O]$. This releases an atomic oxygen species that reacts according to the schemes listed above.

The temperature dependence of the O_2 yields indicate that O_2 can be produced at tank waste chemistry temperatures; thus the production of oxidants such as O_2 and NO via solid-state radiolysis contributes to tank waste aging and the production of flammable gases.

Low-Energy Electron Impact on $NaNO_3$/Methanol Interface

Irradiation of complex tank wastes should generate new products as a result of reactions of organic radicals and molecules at the organic/$NaNO_3$ interface. The importance of these interfacial reaction pathways was investigated by controlled electron beam-induced radiolysis of $NaNO_3$ surfaces

containing multilayers of CH_3OH. Several monolayers (ML) of CH_3OH were adsorbed on the $NaNO_3$ surface at substrate temperatures of 114–120K. Irradiation of this interface with 100 eV electrons primarily produced NO and O_2 from the $NaNO_3$ surface and H_2, CO, CH_4, CO_2, and CH_2O (formaldehyde) from the methanol overlayer. The NO and O_2 yields from $NaNO_3$ did not depend on the CH_3OH coverage up to 7 mL. This may indicate that the O_2 arises mainly from subsurface processes. Post-irradiation TPD experiments revealed the formation of lower-volatility products such as water, dimethyl ether (CH_3OCH_3), ethanol (C_2H_5OH), ethylene glycol ($(CH_2OH)_2$), and methoxymethanol (CH_3OCH_2OH). All of these products were detected after low-energy electron irradiation of methanol overlayers on a metal surface (Harris et al. 1995). No significant amounts of R-NO compounds were produced under the 100 eV irradiation conditions. The results demonstrate that O and NO radicals produced at the $NaNO_3$ surface do not react significantly with methanol under these thin-film experimental conditions. We expect the major reactions to occur in deeper layers of the organic liquid phase (Camaioni et al. 1998).

Radiation Effects in Aqueous Suspensions of Particles

Pulse radiolysis studies indicate that absorption of the radiation in the solid particles may lead to the transfer of charge across the particle-liquid interface and initiate chemistry at the interface and in the surrounding solution (Schatz et al. 1998). Because the fraction of energy (ionizing radiation) absorbed by the particles increases with loading, this observation suggests that the absorption of radiation by the solid particles causes electrons to be ejected into the surrounding solution. Studies have been carried out on charge trapping at the interface and the fate of holes that are initially generated in the particle. Results indicate that electrons escape into solution, whereas the holes may remain in the material.

The nanoparticle radiolysis results have many practical implications. Most obviously, storage of nuclear material in an "inert" matrix of small particles (e.g., grout) may lead to adverse effects. If the particles are small, the enhanced absorption of energy in the matrix will lead to more pronounced aqueous radiation chemistry. For high-level radionuclides stored in suspensions in large tanks, the presence of the particles will promote generation of water radiolysis products (of particular concern is H_2) in the vicinity of the particles. This may increase the probability of retention of products near the particles, e.g., by gas-bubble attachment to the particle, and may lead to serious safety concerns. On the other hand, ionizing irradiation is often considered a viable advanced oxidation technique in various cleanup operations such as water decontamination or soil remediation. Such a radiocatalytic approach, analogous to the proliferating photocatalysis, will clearly be most efficient with small particles.

Reactions of Model Organic Complexants with NO_2 in Water

Radiolysis of homogeneous aqueous waste solutions generate primarily OH/O^- and NO_2. Because nitrite concentrations are high in aqueous wastes, a significant fraction of the O^- generated at the solution crystal interfaces will probably convert to NO_2. Therefore, reactions of NO_2 with organic species in solution are being studied. Though NO_2 is one of the dominant oxidizing radicals generated by radiation effects on nuclear waste, there is little knowledge of its reactions with organic compounds that were used in nuclear materials processing and stored in waste tanks. Waste aging studies have been performed at the Hanford Site to explain waste characterization data and predict effects of organic aging on the potential combustion hazards of organic-containing nitrate-rich wastes. These studies simulated waste aging by gamma-irradiating nonradioactive waste simulants. We have performed complementary experiments in this EMSP project to verify the role of NO_2 and to elucidate reaction kinetics and products for development of mechanistic kinetic models. The experiments contact aqueous alkaline solutions of organic species with N_2 containing 10–100 ppm NO_2. The NO_2 dissolves in the solutions and hydrolyzes competitively with reduction by organic solutes. Preliminary experiments have surveyed the reactions of nitrilotriacetate (NTA), iminodiacetate (IDA),

glycine, and formate. Products were analyzed using ^{1}H and ^{13}C nuclear magnetic resonance spectroscopies and ion chromatography. The results show that NTA degrades via stepwise dealkylation giving mainly formate, carbonate, and oxalate. Formate degrades to carbonate when reacted with NO_2 but at a slower rate. Relative reactivities from competition experiments show NTA>IDA> glycine> formate. Similar results have been obtained in Hanford Waste Aging Studies that irradiated simulated waste solutions containing these compounds. Therefore, the NO_2 contact experiments appear to corroborate our view that NO_2 is generated during radiolysis of waste simulants, and therefore actual wastes, and it is the species that oxidizes organic chemicals in the wastes.

We have developed methods for measuring rate constants for NO_2 oxidizing complexants relative to oxidizing formate ion. To convert relative rate constants to absolute rate constants, we determined the rate of formate oxidation relative to NO_2 hydrolysis:

$$2NO_2 + HCO_2^- + 2OH^- \rightarrow NO_2^- + CO_3^{2-} \quad (5)$$

$$2NO_2 + 2HO^- \rightarrow NO_2^- + NO_3^- + H_2O \quad (6)$$

The rates of production of carbonate and nitrate ions were measured at different hydroxide ion and NO_2 concentrations. The behavior showed that the rate laws for producing carbonate and nitrate ions were, respectively, first and second order in NO_2. Accordingly, the relative rate expression (Equation 7) is derived by squaring the rate law for carbonate production and dividing by the rate law for nitrate production:

$$\frac{k_5}{k_6^{\frac{1}{2}}} = \frac{\frac{\Delta[CO_3^{2-}]}{\Delta t}}{\sqrt{\frac{\Delta[NO_3^-]}{\Delta t}}} \frac{1}{[HCO_2^-]} \quad (7)$$

We obtained $k_5/k_6^{1/2} = (1.00\pm0.05)\times10^{-4}$ $(M^{-1}\ s^{-1})^{1/2}$ from two experiments that contacted 25 and 100 ppm NO_2 gas with 0.1 M sodium formate in 1 M NaOH over a period of two weeks. The rates were determined by sampling the reactions at 24–48-hour intervals and measuring nitrate and nitrite concentrations by using ion chromatography. The carbonate concentration was calculated from Equation 8, which derives from the stoichiometries of Reactions 5 and 6.

$$\frac{\Delta[CO_3^{2-}]}{\Delta t} = \frac{1}{2}\left(\frac{\Delta[NO_2^-]}{\Delta t} - \frac{\Delta[NO_3^-]}{\Delta t}\right) \quad (8)$$

The rate constant for hydrolysis of NO_2 in neutral water is $6\times10^7\ M^{-1}\ s^{-1}$ (Park and Lee 1988; Lee and Scharwtz 1981). The reaction occurs in two steps: reversible association of two molecules of NO_2 to make a molecule of N_2O_4 followed by reaction of N_2O_4 with water to nitrous and nitric acids.

$$2NO_2 \rightleftharpoons N_2O_4 \qquad k_9 = 5\times10^8\ M^{-1}\ s^{-1};\ k_{-9} = 6.7\times10^3\ s^{-1} \quad (9)$$

$$N_2O_4 + H_2O \rightarrow HNO_2 + HNO_3^- \qquad k_{10} = 1\times10^3\ s^{-1} \quad (10)$$

If hydrolysis of N_2O_4 (Reaction 10) is accelerated by HO^-, then Reaction 9 could become rate limiting such that the rate constant for Reaction 6 approaches that for Reaction 9. Therefore, we know that the rate constant for Reaction 5 may take values within the range $0.77 \le k_5 \le 2.2\ M^{-1}\ s^{-1}$. The absolute maximum may be set conservatively at $10\ M^{-1}\ s^{-1}$ allowing that the diffusion-limited

rate constants do not exceed 10^{10} $M^{-1}s^{-1}$. We will experiment at lower hydroxide concentrations to determine whether effects are consistent with our analysis.

Experiments with glycine were investigated to gain insight into the mechanism of oxidation of aminocarboxylates by NO_2. 1- and 2-^{13}C-labeled glycines were contacted and analyzed by ^{13}C NMR. The branching ratio is ~ 60/40 formate/oxalate. Thus, from competition experiments that determined yields of ^{12}C-formate ion from ^{12}C-glycine relative to ^{13}C-carbonate from ^{13}C-formate ion, we know the rate constant for glycine reacting with NO_2 to be ~10 $M^{-1}s^{-1}$.

Depending on conditions, other products-adducts are formed during oxidation of glycine. One of the major adducts was identified as hydroxyaspartate ion. How it is formed is as yet unknown; however, we observed that when 1 M NO_2^- is present, production of hydroxyaspartate ion and other adducts were substantially reduced—formate, oxalate, and carbonate ions amounted to ~90% of the products. Thus it seems that higher molecular weight products could form as a result of radiolysis, but the high concentrations of nitrite ion in the wastes probably suppresses their production.

Planned Activities

Though this EMSP program will conclude at the end of FY 1999, it has branched off into several new directions. Specifically, results obtained in this program led to the submission of a FY 1999 proposal entitled "Effects of Water Radiolysis in Water Cooled Nuclear Reactors" to the Nuclear Energy Research Initiative by Pimblott, LaVerne and Miesel (Univ. of Notre Dame) and Orlando (PNNL). Results were also incorporated into a recently funded EMSP program entitled "Mechanisms and Kinetics of Organic Aging in High-Level Wastes," PI: D. M. Camaioni (PNNL). This project will combine the kinetics of radiolytically induced organic reactions with the kinetics of thermally activated organic reactions to develop global models for organic degradation in nuclear wastes. Finally, a collaborative effort is just beginning to theoretically characterize organic intermediates generated in high-level wastes. This work will involve the PIs of this project and theorist colleagues at PNNL and NDRL. The effort, to be directed under the "Organic Aging" EMSP project, will foster understanding of organic aging and the development of mechanistic kinetic models by calculating thermochemical properties that are difficult to measure by experiment.

References

Camaioni DM, WD Samuels, JC Linehan, AK Sharma, AT Autrey, MA Lilga, MO Hogan, SA Clauss, KL Wahl, and JA Campbell. 1998. *Organic Tanks Safety Program Waste Aging Studies Final Report.* PNNL-11909, Rev. 1, Pacific Northwest National Laboratory, Richland, Washington.

Harris TD, DH Lee, MQ Blumberg, and CR Arumainayagam. 1995. "*J. Phys. Chem.* 99:9530.

Knutsen K and TM Orlando. 1996. "Low-energy (5- 80 eV) electron-stimulated desorption of H^+ (D^+), O^+, and NO^+ from solution grown $NaNO_3$ single crystals." *Surf. Sci.* 348:143.

Knutsen K and TM Orlando. 1997. "Photon-stimulated desorption of O(^{3}P) and NO($^2\Pi$) from $NaNO_3$ single crystals." *Phys. Rev. B.* 55:13246.

Knutsen K and TM Orlando. 1998. "Low-energy (5-100 eV) electron and ultraviolet (6.4 eV) photon-stimulated desorption of neutral fragments from $NaNO_3$ single crystals." *Appl. Surf. Sci.* 127–129:1.

Lee Y-N and SE Schwartz. 1981. "Reaction kinetics of nitrogen dioxide with liquid water at low partial pressure." *J. Phys. Chem.* 85:840-848.

Park J-Y and Y-N Lee. 1988. "Solubility and decomposition of kinetics of nitrous acid in aqueous solution." *J. Phys. Chem.* 92:6294-6302.

Schatz T, AR Cook, and D Meisel. 1998. "Charge transfer across the silica nanoparticle/water Interface." *J. Phys. Chem.* 102:7225-30.

Information Access

This project and the Notre Dame EMSP project, "The NO_x System in Nuclear Waste," are strongly coupled with the "Waste Aging Studies" project at the Hanford Site. The basic studies are performed at ND and PNNL, and the information is continuously shared with the Tank Waste Safety Program. Information from the projects is also shared directly with Westinghouse Savannah River staff. To further facilitate the exchange of information and the immediate incorporation of results into operations, we conduct at least semi-annual "coordination meetings" in which the Hanford Site operators (e.g., from DESH, Numatec, WSRC, etc.) participate both as contributors and as observers. In addition, we participate in national and international meetings of scientific societies such as the American Chemical Society, the Electrochemical Society, the American Physical Society, the American Nuclear Society, and the IEEE. We also publish essentially all of our work in the open literature. The following is a list of publications and conference presentations for the project.

Publications

Camaioni DM, N Zevos, AK Sharma, JC Linehan, and D Miesel. "Mechanisms and kinetics of the NO_2 with complexants in alkaline solutions. 1. Formate ion." *J. Am. Chem. Soc.* (in preparation).

Camaioni DM, N Zevos, AK Sharma, JC Linehan, and D Miesel. "Mechanisms and kinetics of the NO_2 with complexants in alkaline solutions. 2. Glycine." *J. Am. Chem. Soc. (*in preparation).

Dimitrijevic NM, A Henglein, and D Meisel. "Charge separation across the silica nanoparticle interface." *J. Phys. Chem.* (submitted for publication).

Johnson JA, ML Saboungi, P Thiyagarajan, R Csencsits, and D Meisel. 1999. "Selenium nano-particles: A small angle neutron scattering study." *J. Phys. Chem.* 103:59-63.

Knutsen K and TM Orlando. 1998. "Low-energy electron- and ultraviolet (6.4 eV) photon-stimulated desorption of neutral fragments from $NaNO_3$ single crystals." *Appl. Surf. Sci.* 127:1.

Makarova OV, AE Ostafin, H Miyoshi, JR Norris Jr, and D Meisel. "Adsorption and encapsulation of fluorescent probes in nanoparticles." *J. Phys. Chem.* (accepted for publication).

Meisel D. 1997. "Charge transfer in nanoparticles semiconductor nanoclusters - physical, chemical and catalytic aspects." *Studies in Surface Science and Catalysis*, PV Kamat and D Meisel, eds. Elsevier, Amsterdam, Vol. 103, pp. 79-97.

Meisel D, AR Cook, D Camaioni, and TM Orlando. 1997. "Chemistry, radiation, and interfaces in suspensions of nuclear waste simulants." *Photoelectrochemistry*, K Rajeshwar, LM Peter, A Fujishima, D Meissner, and M Tomkiewicz, eds. Electrochemical Society, Vol. 97-20:350-7.

Papparazzo E, R Ponniah, N Zema, M Piacentini, and TM Orlando. "Electronic structure of $NaNO_3$ single crystals: Band structure calculations and electron-energy-loss measurements." *Phys. Rev. B.* (in preparation).

Petrik NG, K Knutsen, D Camaioni, S Lea, E Papparazzo, and TM Orlando. "Electron-beam interactions with $NaNO_3$ single crystals." *J. Chem. Phys.* (submitted for publication).

Schatz T, AR Cook, and D Meisel. 1998. "Charge transfer across the silica nanoparticle/water interface." *J. Phys. Chem.* 102:7225-30.

Presentations

Camaioni DM, AK Sharma, JC Linehan, T Orlando, N Zevos, and D Meisel. August 22-26, 1999. "Radiolytic effects on organic chemicals in high level wastes." Symposium on First Accomplishments of the Environmental Management Science Program, Annual Meeting, American Chemical Society, New Orleans (invited talk).

Camaioni DM, N Zevos, AK Sharma, JC Linehan, and D Miesel. March 21-25, 1999. "Reactions of NO_2 with organic complexants in alkaline solutions." Symposium on Free Radicals in the Condensed Phase, Annual Meeting, American Chemical Society, Anaheim, California.

Meisel D. February 10, 1999. "Radiocatalysis: Fundamentals and applications." Northwestern University, Evanston, Illinois (invited seminar).

Meisel D. April 2, 1998. "Radiation and chemistry in the nuclear arena: Radicals, particles and interfaces." Seminar, Radiation Laboratory, University of Notre Dame, South Bend, Indiana.

Meisel D. April 19-22. 1998. "Radiation and chemistry in the management of nuclear wastes: Colloids, interfaces and radicals." Research Needs and Opportunities in Radiation Chemistry. DOE Workshop, Chesterton, Indiana (invited talk).

Meisel D. May 2-7, 1999. "Ionizing radiation induced charge carriers in colloidal nanoparticle surfaces," Symposium on Nanomaterials for Energy Conversion. 195th Meeting of the Electrochemistry Society, Seattle (invited talk).

Meisel D. July 16-24, 1999. "Radiation induced charge carriers in nanoparticles suspensions." Radiation Research Congress, Dublin, Ireland.

Meisel D. September 15, 1998. "Charge carriers across interfaces." School of Engineering, University of Notre Dame, South Bend, Indiana.

Meisel D, D Camaioni, and T Orlando. August 22-26, 1999. "Radiolytic effects in homogeneous and heterogeneous high level simulants." Symposium on First Accomplishments of the Environmental Management Science Program. Annual Meeting, American Chemical Society, New Orleans (invited talk).

Meisel D and T Schatz. November 14-18, 1999. "Gas generation in aqueous suspensions." Symposium on Gas Generation in Solid Phase Radioactive Materials. Annual Meeting, American Nuclear Society, Long Beach, California (invited talk).

Orlando TM. Jan. 15, 1998. "Quantum state-resolved desorption studies of wide band-gap materials." Rutgers, The State University of New Jersey, Piscatawuy, New Jersey (invited talk).

Orlando TM. June 8, 1998. "Quantum state-resolved desorption studies of wide band-gap materials." Nanophysics Laboratory, University of Birmingham, United Kingdom (invited talk).

Orlando TM, N Petrik, S Marshman, and DM Camaioni. November 14-18, 1999. "Nonthermal surface processes in the generation of gas in mixed wastes." Annual Meeting, American Nuclear Society, Long Beach, California (invited talk).

Petrik N, S Marshman, DM Camaioni, and TM Orlando. August 22-26, 1999. "Nonthermal surface and interface processes in the storage of spent nuclear fuel and mixed wastes." Annual Symposium on First Accomplishments of the Environmental Management Science Program. Annual Meeting, American Chemical Society, New Orleans.

Schatz T, AR Cook and D Meisel. Aug. 23-27, 1998. "Interfacial charge transfer in irradiated suspensions: implications to nuclear wastes." Symposium on Actinide Solution Chemistry. Annual Meeting, American Chemical Society, Boston (invited talk).

Schatz T, D Meisel, and A Cook. March 21-25, 1999. "Radicals from ionizing radiation in suspensions of nanoparticles." Symposium on Free Radicals in the Condensed Phase. Annual Meeting, American Chemical Society, Anaheim, California (invited talk).

Mechanisms and Kinetics of Organic Aging in High-Level Wastes

(First Year of Funding: 1998)

Principal Investigators

Dr. Donald M. Camaioni
Pacific Northwest National Laboratory
P.O. Box 999, MSIN K2-57
Richland, WA 99352
(509) 375-2739 (phone)
donald.camaioni@pnl.gov

Dr. S. Tom Autrey
Pacific Northwest National Laboratory
P.O. Box 999, MSIN K2-57
Richland, WA 99352
(509) 375-3792 (phone)
tom.autrey@pnl.gov

PNNL Contributor

Dr. John Linehan
Pacific Northwest National Laboratory
P.O. Box 999, MSIN K2-57
Richland, WA 99352
(509) 375-3983 (phone)
john.linehan@pnl.gov

Research Objective

The goal of this project is to develop a fundamental understanding of organic aging and to assemble a model that describes and predicts the thermal and radiolytic aging of organic compounds in high-level wastes (HLW). To reach this goal, we will measure kinetics and elucidate products and mechanisms of organic reactions occurring under conditions of waste storage, retrieval, and processing. Initial emphasis will be placed on studying thermal effects, because organic reaction mechanisms and effects of varying conditions are uncertain, and because we benefit from collaborations with earlier Environmental Management Science Program (EMSP) projects that have worked on radiation effects. Organic complexants are of greatest concern regarding both safety and pretreatment because they have been found to degrade to gases, combust in dry wastes, and interfere with radionuclide separations. Therefore, efforts will be focused on studying the reactions of these organic chemicals and associated degradation products.

In preliminary work, the authors have used mechanistic kinetic modeling techniques to successfully model the radiolytic degradation of formate to carbonate in HLW simulants. The research will continue development of the model using an iterative process that measures degradation products and kinetics of increasingly complex molecules while adapting the model to reproduce the results each step of the way. Several mechanistic probe experiments have been designed to learn the fundamental mechanisms that operate during thermal degradations so that thermal and radiolytic processes may be integrated within the model. Key kinetic data and thermodynamic properties relating to thermal reactivity will also be acquired so that rate-controlling and product-forming reactions can be predicted. Thermochemical properties of key intermediates will be experimentally and/or theoretically determined to facilitate mechanism verification, structure/reactivity correlation, and prediction of reaction rates.

We expect a comprehensive understanding of organic reactivity in HLW will accrue from the work. This understanding will be embodied in organic reaction models capable of predicting distributions of species, including gases, with respect to time, temperature, and radiation history. These models will assist waste management decisions by predicting impacts of organic chemicals on safe storage, waste retrieval, and pretreatment of HLW.

Problem Statement

Uranium and plutonium production at the Hanford and Savannah River Sites produced large quantities of radioactive byproducts and contaminated process chemicals that are stored in underground tanks awaiting treatment and disposal. Scientific information is needed to support decisions and issue resolutions for safe, effective, and efficient waste storage and processing activities, including development of the Hanford Phase II privatization request for proposals (Foreman 1998a, b). Tanks that contain organic process chemicals have many issues, including the following:

- If allowed to dry out, wastes can be at risk for fuel-nitrate deflagration accidents (Meacham et al. 1998).
- The generation of flammable gases by organic-containing wastes is a major safety concern. Radiolytic and thermochemical processes degrade ("age") organic solutes into smaller fragments of lower energy content, thereby reducing the hazard, while contributing to the generation of toxic, flammable and potentially explosive gases (i.e., volatile organic chemicals, NH_3, H_2, and N_2O) (Meisel et al. 1993; Ashby et al. 1994; Camaioni et al. 1998).

- Aging of organic chemicals also produces toxic volatile organic vapors. Release of these vapors by the wastes causes concern for the health and safety of personnel working about the waste tanks.

- Changing waste storage conditions may alter organic aging to increase gas and organic vapor production. However, changes that accelerate aging of organic complexants also decrease the potential for combustion reactions and facilitate separation of radionuclides.

- Organic complexants in wastes interfere with radionuclide separation and affect the subsurface transport characteristics of metal ions. Partitioning of radionuclides between the liquid and solid phases in the waste is hindered by organic complexants present in the wastes. The complexation of radionuclides must be controlled to separate the waste into high- and low-level fractions effectively. This may entail destroying the complexants or removing the dissolved radionuclides using advanced separation processes.

Organic reactions induced by heat and radiation need to be studied to assess hazards, better understand methods for organic destruction, and be able to predict rates of production of gases in the wastes. The studies should include organic chemicals that were added to tank wastes and their aging products as well as organic chemicals and materials that may be used in processing the wastes.

Research Progress

We have developed a broadly applicable approach to obtaining kinetic and thermochemical measurements of nitrite ester reactions, especially those derived from organic complexants (e.g., glycolic acid, hydroxyethylethylenediaminetriacetic acid [HETDA], citric acid). The approach takes advantage of the facile exchange reactions that occur between nitrite esters and alcohols. By measuring the effects of added substrate on reaction rates, we will extract absolute rate constants for generation and reaction of nitrite esters derived from complexants and their thermodynamic stabilities. In the sections that follow, we provide background to specific problems on which we are working and report progress to date.

Background

The major complexants used in Hanford nuclear materials processing were the sodium salts of N-(2-hydroxyethyl) ethylenediaminetetraacetic acid (HEDTA), glycolic acid, ethylenediaminetetraacetic acid (EDTA), and citric acid (Meacham et al. 1998). Of these, only HEDTA and glycolate ion are readily oxidized by thermally activated reactions to give flammable gases (Ashby et al. 1994). EDTA, which is structurally quite similar to HEDTA, is relatively unreactive (Delegard 1987; Ashby et al. 1994; Camaioni et al. 1998). Nitrite ion appears to supply the oxidizing equivalents for thermal oxidation. Aluminate ions, or other aluminum species, are catalysts, and hydroxide ion promotes the oxidation (Delagard 1980, 1987; Ashby et al. 1994).

Products from HEDTA include oxalate, formate, carbonate, ethylenediaminetriacetate, nitrogenous gases (N_2 and N_2O), and H_2 (Ashby et al. 1994; Barefield et al. 1996; Camaioni et al. 1998) Glycolate ion gives formate, oxalate, carbonate, and the gases as well (Ashby et al. 1994; Barefield et al. 1995). Mechanisms and rate controlling steps are poorly understood. Barefield et al. (1995, 1996) and Ashby et al. (1994) hypothesize that the reactions occur as depicted in Equations 1 and 2, where R = $(^-O_2CCH_2)_2NCH_2CH_2N(CO_2^-)CH_2$ and CO_2^-).

$$RCH_2OH + NO_2^- \rightleftharpoons RCH_2ONO + OH^- \quad (1)$$

$$RCH_2ONO \longrightarrow \text{Products} \quad (2)$$

Reaction 1 is endothermic, and activation barriers for the reverse, Reaction -1 (alkaline hydrolysis), are relatively large (Oae et al. 1978). Even in molar hydroxide solutions, hydrolyses of alkyl nitrites occur slowly. Thus Reaction 1 is very unfavorable in alkaline conditions such as those encountered in Hanford tank wastes. Accordingly, it has been suggested that $Al(OH_4)^-$ serves to catalyze Reaction 1 (see Figure 1) (Ashby et al. 1994; Barefield et al. 1996).

Alkyl nitrite esters may undergo internal redox reactions (Equation 3) to give NO^- and ketone/aldehyde products competitively with hydrolysis:

$$RCH_2ONO + OH^- \longrightarrow RCHO + NO^- + H_2O \qquad (3)$$

Reaction 3 was shown to occur quantitatively in basic anhydrous media by Friedman and Bayless (1969). They observed that 2-methylpentyl nitrite yielded N_2O and 2-methylpentanal when reacted with sodium *t*-amyloxide in *t*-amyl alcohol. This type of reaction has been proposed by Ashby et al. (1994) to explain the formation of oxalate during thermal decomposition of methyl nitrosyloxyacetate in aqueous hydroxide solutions. However, product studies by Oae et al. (1978) of reactions of benzyl nitrite and phenylethyl nitrite in 0.1 M HO^- showed quantitative conversion to hydrolysis products, benzyl alcohol, and phenylethyl alcohol (no benzaldehyde or phenethylaldehyde were observed). Thus, Reactions 1-3 are not understood well enough to predict the outcome for simple alkyl nitrites, let alone for more functionalized structures involving glycolate and HEDTA.

To test the hypothesis expressed in Figure 1 and obtain predictive reaction parameters, we are measuring the rates of alkaline hydrolysis of nitrosyloxyacetate ion (nitrite ester of glycolate ion) in the presence and absence of $NaAl(OH)_4$. In the sections that follow, we report on 1) the reactions of ethyl nitrite in alkaline solutions, 2) nitrosyl exchange reactions between simple alkyl nitrite esters and glycolate ion, and 3) kinetic measurements of the effect of glycolate ion on the hydrolysis of ethyl nitrite.

Hydrolysis and Internal Redox Reactions of Ethyl Nitrite

We opened our investigations by revisiting the reactions of alkyl nitrites in sodium hydroxide solution as a preliminary step toward studying nitrite esters of complexants. Figure 1 shows absorbance spectra recorded during and after decomposition of EtONO in sodium hydroxide solution and the expected products for Reactions 1 and 3.

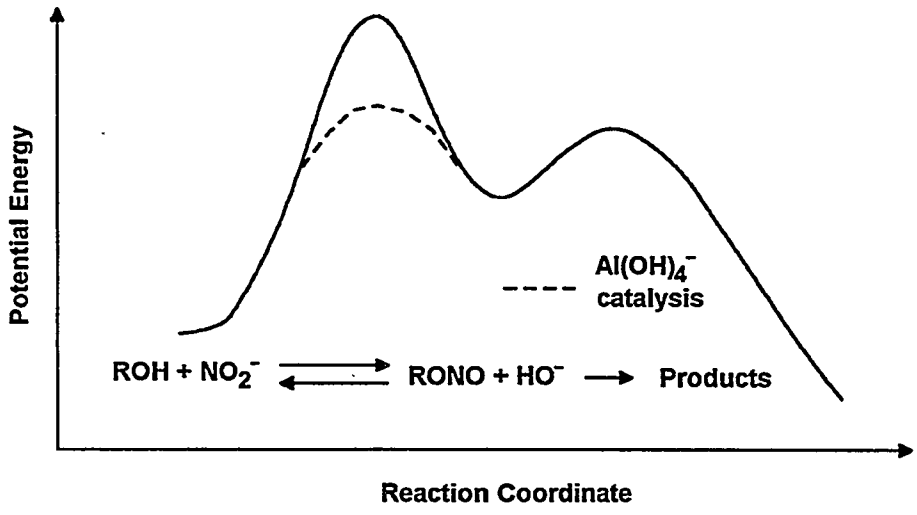

Figure 1. Potential Energy Diagram Showing How $Al(OH)_4^-$ May Catalyze Oxidation of Glycolate and HEDTA (Ashby et al. 1994)

At the end of the reaction, the nitrite ester absorbance bands have disappeared to be replaced by nitrite ion (355 nm) and aldehyde (275 nm) bands. Neither sodium nitrite (see Figure 2) nor ethanol exhibits a maximum at 275 nm. However, acetaldehyde (Figure 2) does absorb at this wavelength and, as discussed above, could be produced as shown in Reaction 3 (R = H). The spectra taken after alkaline hydrolysis provide evidence for a competition between Reactions -1 and 3 for EtONO at ambient temperatures.

This is an important finding; the observation of products from competing reactions justifies further work into acquiring rate constants for reactions such as Equation 3. These results will provide the necessary thermochemical kinetic data to develop a model for thermal degradation of organic complexants in HLW.

Nitrosyl Exchange Reactions

Doyle et al. (1983) measured the rates of hydrolysis of a series of alkyl nitrites and examined the nitrosyl exchange reactions with *t*-BuONO with a series of aliphatic alcohols, as in Equation 4.

$$\text{ROH} + t\text{-BuONO} \rightleftharpoons \text{RONO} + t\text{-BuOH} \qquad (4)$$

They found that equilibrium constants for reactions of primary alkanols with *t*-BuONO are uniformly near 10. The rate of exchange occurred within 1 minute at room temperature. For primary alcohols containing β electron withdrawing groups, e.g., 2-ethoxyethyl nitrite, *K* decreased to 5.8. Given these favorable equilibria, *t*-BuONO has been used to synthesize a variety of nitrite esters.

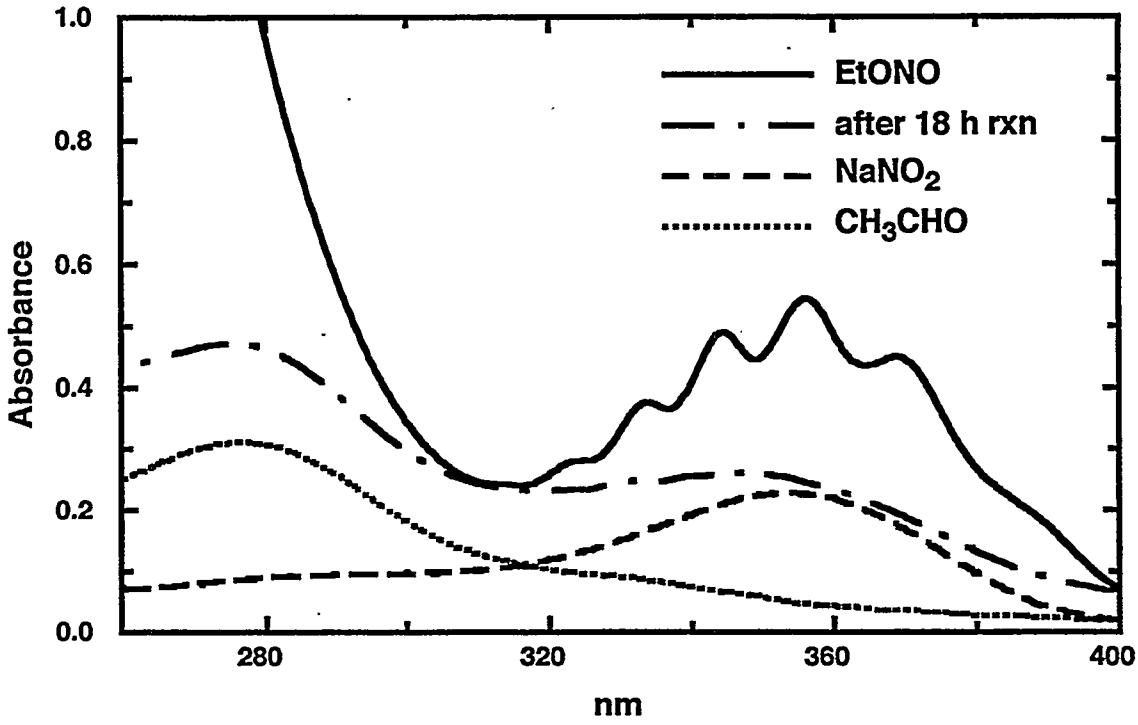

Figure 2. Absorbance Spectra of Ethyl Nitrite at Start (—) and Completion (—·—) of Alkaline Hydrolysis Reaction Compared with Spectra for $NaNO_2$ (- - -) and for Acetaldehyde (·····)

Exchange equilibrium constants (K_4) for glycolate ion, methyl glycolate, and ethanol reacting with *t*-BuONO were determined by ^{1}H-NMR spectroscopy. Measurements for EtOH and methyl glycolate were obtained in $CDCl_3$ solvent. The measurement for glycolate ion was made in DMSO-d_6 solvent. The protons attached to the carbon adjacent to the nitrosyl group are slightly broadened and shifted downfield from the protons attached to the carbon adjacent to the hydroxyl group by approximately δ 1 – 1.1 ppm. The fractions, [RONO]/[ROH] and [*t*-BuOH]/[*t*-BuONO], were determined from the normalized integrated areas of the ^{1}H-NMR resonances. The product of these equate to the equilibrium constant for exchange values, and K_5 for any alcohol with *t*-BuONO can be determined according to Equation 5:

$$K_4 = \frac{[t-\text{BuOH}][\text{RONO}]}{[t-\text{BuONO}][\text{ROH}]} \tag{5}$$

Using this method, we obtain $K_4 = 9.8$ for *t*-BuONO reacting with EtOH. The literature value is 10.6 (Doyle et al. 1983). For *t*-BuONO reacting with methyl glycolate in $CDCl_3$ and with sodium glycolate in DMSO-d_6, we obtain $K_4 = 0.15$. The equilibrium constant for exchange between EtONO and sodium glycolate is about 0.015. The observation that the equilibrium constant is much less than unity shows that nitrosyloxyacetate ion is much less stable than simple alkyl nitrite esters. Using Equation 6, we calculate that nitrosyloxyacetate is 2.5 kcal/mol less stable than ethyl nitrite:

$$\Delta G = -\text{RTln}(K_4) \tag{6}$$

The exchange equilibrium constant provides a direct measure of the relative stability of nitrite esters. In addition to the thermodynamic data obtainable by nuclear magnetic resonance (NMR) spectroscopy, kinetic analysis of the equilibrium mixtures will provide rate constants for base-induced decomposition of unstable, difficult-to-prepare nitrite esters.

Effect of Glycolate Ion on the Alkaline Hydrolysis of Ethyl Nitrite

There is no report in the literature for the synthesis and isolation of the nitrosyloxyacetate ion. Kornblum (1956) prepared ethyl nitrosyloxyacetate and found that hydrolysis to ethyl glycolate occurred within a few seconds at room temperature. We prepared nitrosyloxyacetate ion and nitrosyloxyacetic acid in situ by reacting sodium nitrite with glycolic acid in the presence of a drying agent in dimethyl sulfoxide (DMSO) and by reacting glycolic acid with *t*-BuONO in DMSO. Identifications were made by proton NMR, which showed the appearance of a new methylene resonance (δ ~5.1 ppm) downfield from the methylene resonance (δ ~4 ppm) of glycolate ion/glycolic acid. Nitrosyloxyacetate ion hydrolyzed within seconds on mixing with water, aqueous sodium carbonate, or 0.1 M NaOH. The absorbance spectra recorded after mixing showed only the characteristic nitrite ion band at 355 nm. Clearly, the nitrosyloxyacetate ion is less stable than alkyl nitrite esters and more reactive toward hydrolysis. Because the equilibrium constants for nitrosyl exchange and rate constants for hydrolysis of ethyl nitrite are readily measured, we take the approach of measuring the effect of glycolate ion on the hydrolysis kinetics of ethyl nitrite. Preliminary results already provide new thermochemical kinetic data and insight to the potential energy surface for formation and reaction of the nitrosyloxyacetate ion.

Figure 3 shows absorbance at 355 nm of aqueous alkaline EtONO solutions (2 M HO^-, room temperature, 33% DMSO) as a function of time in the presence and absence of glycolate. The absorbance decays by a first-order kinetic process giving satisfactory fits to Equation 7:

$$A_t = (A_o - A_\infty)e^{-k_{OH}[HO^-]t} + A_\infty \tag{7}$$

where A_∞ is the absorbance due to sodium nitrite at completion of hydrolysis.

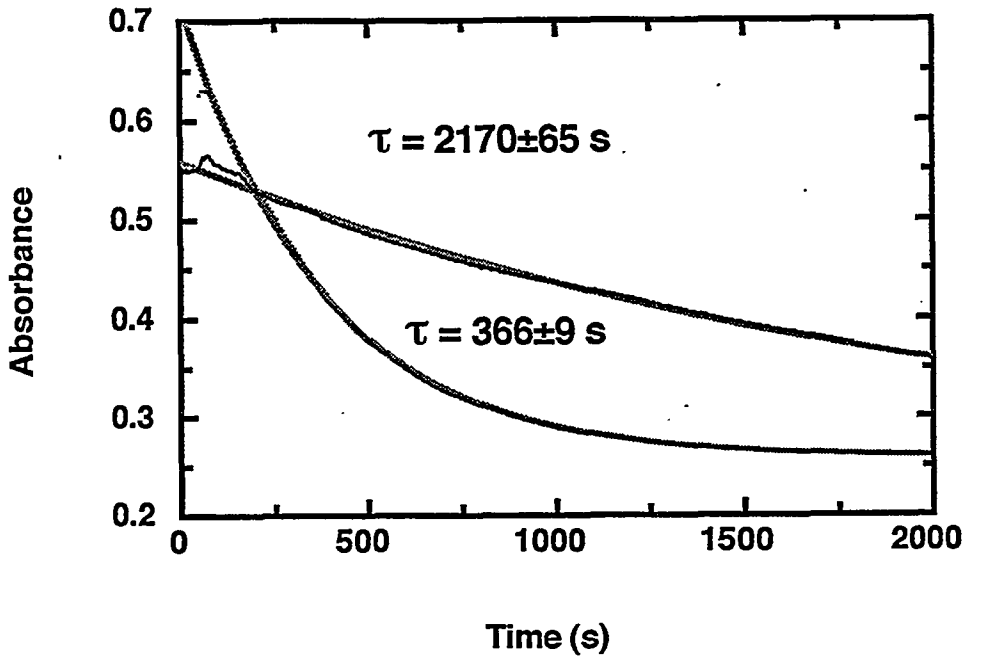

Figure 3. Lifetime of Ethyl Nitrite in 2 M NaOH is *Shorter* When Glycolate Ion is Present than When it is Absent: $\tau = 2170$ s, 0.01 M EtONO; $\tau = 366$ s with 0.009 M EtONO and 0.65 M Glycolate Ion. Solutions are 33 vol% DMSO/water with ~0.09 M EtOH at start. Absorbance measured at 355 nm.

When glycolate ion is present at 0.65 M, the lifetime of EtONO is much shorter, suggesting that a reaction system such as Scheme 1 is operating.

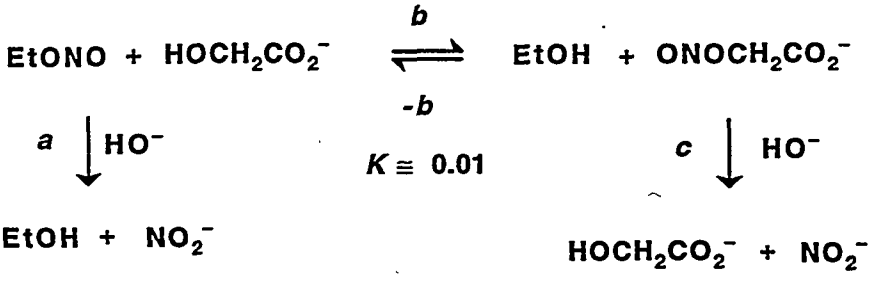

Scheme 1. Mechanism for Promotion Alkaline Hydrolysis of Ethyl Nitrite by Glycolate Ion: Steps *b* and *c* are Faster than Step *a*

Given that the reaction in the presence of glycolate follows first-order kinetics, nitrosyl transfer (step *b* in Scheme 1) must be rate-limiting under the reaction conditions. If step *c* were rate-limiting, then a more complex time-dependence would be observed. Analysis of the experimental data leads to rate constants, as shown in Table 1.

Table 1. Rate Constants and Estimated Free Energies for Reactions in Scheme 1

Rxn Step	k $M^{-1}\ s^{-1}$	$\Delta G^{\ddagger}$ kcal/mol	$\Delta G°$ kcal/mol
a	2.3×10^{-4}	23.9[a]	-17.4[b]
b[c]	3.49×10^{-3}	22.2	2.8
c[c]	≥0.2	≤19.8	-20.2

(a) Oae et al. 1978.
(b) Alred et al. 1982.
(c) Rate constants and free energies from this work.

The rate constant for nitrosyl transfer step *b* is more than 10 times larger than EtONO alkaline hydrolysis step *a*. The rate constant for alkaline hydrolysis of nitrosyloxyacetate ion is more than 1000 times larger than the rate constant for EtONO hydrolysis. These rate data have been converted to free energies of activation and are included in Table 1 with corresponding reaction free energies. Figure 4 depicts the potential energy diagram based on data given in Table 1. Consistent with the observed kinetic behavior, the transition state for nitrosyl transfer and nitrosyloxyacetate hydrolysis are lower in energy that the transition state for EtONO hydrolysis. Therefore, addition of glycolate ion accelerates hydrolysis of EtONO even though formation of nitrosyloxyacetate ion is endergonic by ca. 2.5 kcal/mol.

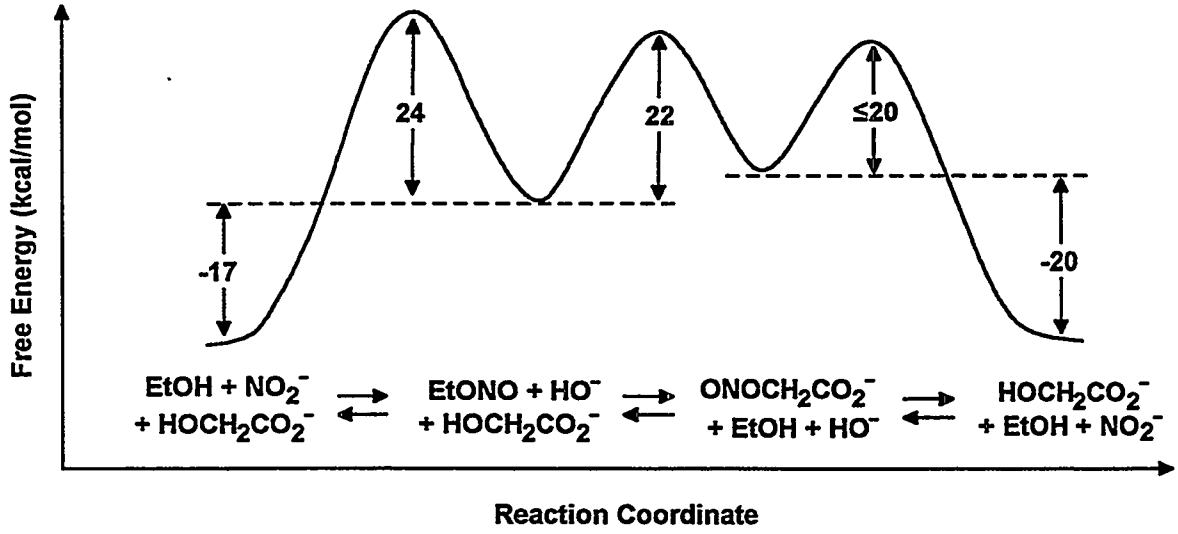

Figure 4. Free-Energy Diagram for Alkaline Hydrolysis of Ethyl Nitrite Promoted by Glycolate Ion. Barriers for reaction of EtONO going to the right are lower than the barrier for reaction with hydroxide ion such that glycolate ion promotes EtONO hydrolysis.

The rate constant we obtained for alkaline hydrolysis of EtONO at 25°C is ca. 2.5 times faster than that observed by Oae et al. (1978) for n-butyl nitrite at 35°C in 60% dioxane/water. The faster reaction may be due to the use of a different solvent system or possibly the participation of Reaction 3 at the higher hydroxide concentrations we used. The short lifetime (≤5 seconds) for nitrosyloxyacetate ion in alkaline solution is an interesting observation to consider. The result requires decomposition Reactions 8 and 9 to be comparably rapid if they are to compete according to the mechanism originally envisioned (Figure 1), in which nitrosation of glycolate ion is catalyzed by aluminate ion.

$$^{-}OC(O)CH_2ONO + HO^{-} \longrightarrow HC(O)CO_2^{-} + NO^{-} \quad (8)$$

$$^{-}OC(O)CH_2ONO \longrightarrow CO_2 + CH_2O + NO^{-} \quad (9)$$

The energy of the transition state leading to the formation of nitrosyloxyacetate from glycolate ion and sodium nitrite is an upper limit (see Figure 4). If the energy is much lower, then it may be feasible to generate the nitrosyloxyacetate without having to invoke aluminate catalysis, as proposed in Figure 1. Therefore, we must consider the possibility that aluminate ion catalyzes Reactions 8 and 9 instead of Reaction 1. We are in the process of determining whether aluminate may accelerate alkaline hydrolysis of EtONO and nitrosyloxyacetate ion. Preliminary results suggest aluminate has little effect on hydrolysis of EtONO.

Planned Activities

The research planned for the coming year will continue the current investigations into thermal oxidation mechanisms of glycolate ion. We will alter conditions in subsequent experiments to make step *c* in Scheme 1 rate-limiting so that accurate rate data for this reaction may be obtained. For example, lowering the hydroxide ion concentration, increasing the glycolate ion concentration, and/or lowering the ethanol concentration may cause step *c* to be rate-limiting. Kinetic measurements will be made at different temperatures to determine thermochemical kinetic parameters for nitrosyl transfer, nitrite ester hydrolysis, and elimination of NO^{-}. Also, we will perform measurements in the presence and absence of aluminate to determine catalytic effects. Investigation of the analogous system based on HEDTA will also begin.

This project builds on two earlier collaborative EMSP projects that focused primarily on radiolytic processes in tank wastes.[(a)] Because these projects will conclude in FY 1999, we will continue with those aspects of the projects that concern mechanisms and kinetics of organic aging by radiolytic processes. Specifically, we will continue experiments that measure the rates of NO_2 reacting with complexants in alkaline solutions. Prior work has examined the reactions of formate ion and glycine, and performed preliminary studies of iminodiacetate (IDA) and nitrilotriacetate (NTA) ions. We will carry the IDA and NTA work to completion and extend the NO_2 oxidation studies to HEDTA-related systems and to glycolate, acetate, and citrate ions. Concurrent with these activities, we will incorporate rate and mechanistic data into a predictive kinetic model.

Finally, a collaborative effort will theoretically characterize organic intermediates generated in HLW. This work will involve the Principal Investigators of this project and theorist colleagues at PNNL and Notre Dame Radiation Laboratory. The effort will foster understanding of organic aging and the development of mechanistic kinetic models by calculating thermochemical properties that are difficult to measure by experiment.

References

Ashby EC, A Annis, EK Barefield, D Boatright, F Doctorovich, CL Liotta, HM Neumann, A Konda, C-F Yao, K Zhang, and NG McDuffie. 1994. *Synthetic waste chemical mechanism studies.* WHC-EP-0823, Westinghouse Hanford Company, Richland, Washington.

(a) "The NO_x System in Nuclear Waste," principal investigators: D Meisel (Notre Dame Radiation Laboratory) and D Camaioni (PNNL); "Interfacial Radiolysis Effects in Tank Waste Speciation," principal investigators: T Orlando (PNNL), DD Meisel, and D Camaioni).

Barefield EK, D Boatright, A Deshpande, F Doctorovich, CL Liotta, HM Neumann, and S Seymore. 1995. *Mechanisms of Gas Generation from Simulated SY Tank Farm Wastes: FY 1994 Progress Report.* PNL-10822, Pacific Northwest Laboratory, Richland, Washington.

Barefield EK, D Boatright, A Deshpande, F Doctorovich, CL Liotta, HM Neumann, and S Seymore. 1996. *Mechanisms of Gas Generation from Simulated SY Tank Farm Wastes: FY 1995 Progress Report.* PNNL-11247, Pacific Northwest National Laboratory, Richland, Washington.

Camaioni DM, WD Samuels, JC Linehan, AK Sharma, ST Autrey, MA Lilga, MO Hogan, SA Clauss, KL Wahl, and JA Campbell. 1998. *Organic Tanks Safety Program Waste Aging Studies Final Report.* PNNL-11909, Pacific Northwest National Laboratory, Richland, Washington.

Challis BC and DEG Shuker. 1979. "Rapid nitrosation of amines in aqueous alkaline solutions by β–substitute alkly nitrites." *JCS Chem Comm.* 315-316.

Delegard C. 1980. *Laboratory Studies of Complexed Waste Slurry Volumes Volume Growth in Tank 241-SY-101.* RHO-LD-124, Rockwell Hanford Operations, Richland, Washington.

Delegard HC. 1987. *Identities of HEDTA and Glycolate Degradation Products in Simulated Hanford High-Level Waste.* RHO-RE-ST-55P, Rockwell Hanford Operations, Richland, Washington.

Doyle MP, JW Terpstra, RA Pickering, and DM LePoire. 1983. "Hydrolysis, nitrosyl exchange, and synthesis of alkyl nitrites." *J. Org Chem.* 48:3379-3382.

Foreman S. 1998a. "Effect of organic constituents on waste processing." RL-WT050-S, U.S Department of Energy Environmental Management Needs Management System, http://em-Needs.em.doe.gov/Home/Entry.asp.

Foreman S. 1998b. "Flammable gas generation, retention, and release in HLW Tanks." RL-WT042-S, U.S Department of Energy, Environmental Management, Needs Management System, http://em-Needs.em.doe.gov/Home/Entry.asp.

Friedman L and JH Bayless. 1969. "Aprotic diazotization of aliphatic amines. Hydrocarbon products and reaction parameters." *J. Am. Chem. Soc.* 91:1790-1794.

Kornblum N and JH Eicher. 1956. "A new reaction of α-nitroesters." *J. Am. Chem. Soc.* 78:1494-1497.

Meacham JE, AB Webb, NW Kirch, JA Lechelt, DA Reynolds, GS Barney, DM Camaioni, F Gao, RT Hallen, and PG Heasler. 1998. *Organic complexant topical report.* HNF-SD-WM-CN-058 Rev. 2, DE&S Hanford, Richland, Washington.

Oae S, N Asai, and K Fujimori. 1978. "Alkaline hydrolysis of alkyl nitrites and related carboxylic esters." *JCS Perkin II*, pp. 571-577.

Presentations

Autrey ST. April 30, 1999. "Nitrosyl transfer reactions are not catalyzed by $Al(OH)_4$." Notre Dame Radiation Laboratory and Pacific Northwest National Laboratory EEMSP Coordination Meeting and Technical exchange.

Camaioni DM. Oct. 29, 1998. "Mechanisms and kinetics of the degradation of organic complexants in nuclear waste." Chemistry Seminar, Notre Dame Radiation Laboratory, Notre Dame, Indiana.

Camaioni DM. Nov. 17, 1998. "Mechanisms and kinetics of organic aging in high level wastes." EMSP/Tanks Focus Area Workshop, Richland, Washington.

August 22-26, 1999. "Thermochemical kinetic analysis of thermal pathways for oxidation of organic complexants in high level wastes." *First Accomplishments of the Environmental Management Science Program.* Annual Meeting, Am. Chem. Soc., New Orleans.

Mechanics of Bubbles in Sludges and Slurries

(First Year of Funding: 1997)

Principal Investigators

Dr. Phillip A. Gauglitz (Lead PI)
Pacific Northwest National Laboratory
P.O. Box 999, MSIN K6-28
Richland, WA 99352
(509) 372-1210 (phone)
(509) 372-1861 (fax)
phillip.gauglitz@pnl.gov

Professor Morton M. Denn, LBNL
Professor Susan J. Muller, LBNL
Chemical Engineering Department
University of California
Berkeley, CA 94720-1462
(510)-642-0176 (phone)
(510)-642-4778 (fax)
denn@cchem.berkeley.edu

Professor William R. Rossen
Petroleum and Geosystems Engineering Department
The University of Texas at Austin
Austin, TX 78712-1061
(512) 471-3246 (phone)
(512) 471-9605 (fax)
william_rossen@pe.utexas.edu

Dr. Guillermo Terrones
Pacific Northwest National Laboratory
P.O. Box 999, MSIN K7-15
Richland, WA 99352
(509) 375-2183 (phone)
(509) 375-3641 (fax)
g_terrones@pnl.gov

Research Objective

This project is focusing on key issues associated with the flammable gas safety hazard and its role in safe storage and future waste operations such as salt-well pumping, waste transfers, and sluicing and retrieval of tank waste. The purpose of this project is to develop a basic understanding of how single bubbles (of flammable gases) behave in representative waste simulants and then develop a framework for predicting macroscopic full-tank behavior from the underlying single-bubble behavior.

The specific objectives of this research are as follows:

1. quantitatively describe the interaction of bubbles with waste materials (both sludges and slurries) to understand the physical mechanisms by which barometric pressure changes give rise to a hysteresis between level and pressure

2. develop improved methods for estimating retained gas by properly accounting for the interactions of bubbles with the waste

3. determine how to estimate waste physical properties from the observed hysteresis and the limitations of these estimates

4. determine how barometric pressure fluctuations induce slow upward migration and release of gas bubbles.

Problem Statement

Previous studies have established that the waste level of Hanford tanks responds to barometric pressure changes, the compressibility of retained bubbles accounts for the level changes, and the volume of retained gas can be determined from the measured waste level and barometric pressure changes. However, interactions between the gas bubbles and rheologically complex waste cause inaccurate retained gas estimates and are not well understood. Because the retained gas is typically a flammable mixture of hydrogen, ammonia, and nitrous oxide, accurate determination of the retained gas volume is a critical component for establishing the safety hazard of the tanks. Accurate estimates of retained gas from level/pressure data are highly desirable because direct in situ measurements are very expensive in an individual tank and impossible in many single-shell tanks. The elucidation of the bubble waste interactions will have a direct influence on improving the accuracy of gas volume estimates, provide for more accurate models for estimating waste properties from level/pressure data, and should quantify the effect of barometric pressure fluctuations on the slow rise and release of bubbles. The results of this research will support critical operations at the Hanford Site associated with the flammable gas safety hazard and future waste operations such as salt-well pumping, waste transfers, and sluicing/retrieval.

Research Progress

This research program, which began in FY 1998, is separated into four related activities on bubble behavior, as shown schematically in Figure 1. Modeling studies on continuum materials (sludges) are being conducted from both the solid mechanics and fluid mechanics viewpoints. The solid mechanics

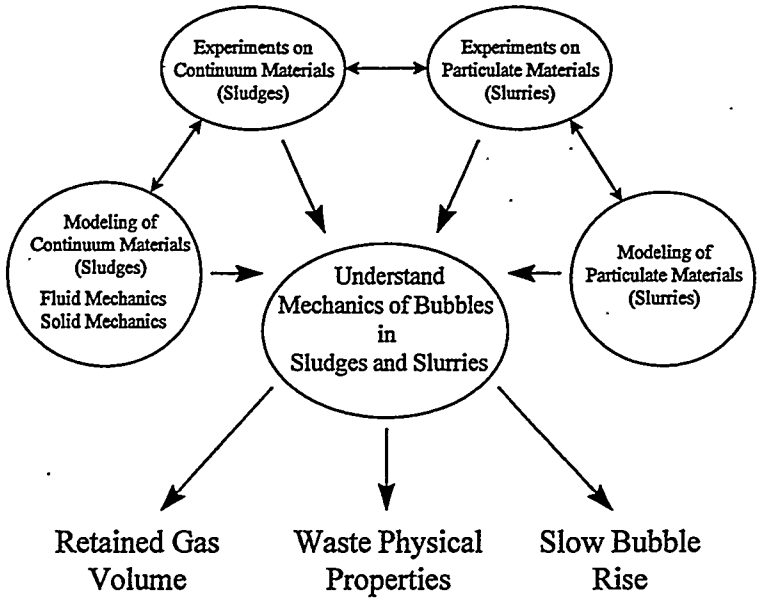

Figure 1. Interrelationship of the Individual Research Problems with the Overall Program Objectives

models are being developed by Terrones at Pacific Northwest National Laboratory (PNNL) and the fluid mechanics solution approach is being developed by Denn and Muller at the University of California at Berkeley. The modeling studies of bubble behavior in particulate materials (slurries) are being conducted by Rossen at the University of Texas at Austin. Finally, experimental studies on both sludges and slurries are being conducted by Gauglitz at PNNL. Bubbles retained in sludges and slurries have significantly different behavior, thus it is appropriate to approach modeling these materials from different viewpoints, though the experimental studies are more closely related. Progress has been made in each of these activities and is summarized in the following sections.

Experimental Studies on Single and Multiple Bubbles

The objective of this research activity is to quantify the effects of small pressure changes on bubble volumes in waste simulants. These experiments investigate both individual bubbles in a small apparatus and multiple bubbles in a larger apparatus. In this section, we describe the apparatus and simulants that we have investigated and some results that highlight the significant new findings.

The test stand for examining single bubbles and multiple bubbles is depicted in Figure 2. For the single-bubble experiments, centrifuge tubes act as the vessel for the experiment and we use a centrifuge to remove extraneous bubbles from the simulant before testing. In the multi-bubble case, bubbly simulant is loaded into larger tanks. In both cases, a supernatant fluid of known density is used to fill the apparatus to the desired level where we can most accurately measure level changes. The apparatus is attached to a pressure regulation system to induce changes in bubble volume and hence level. In general, step changes or sinusoidal cycles of pressure are made and the level changes are tracked. For single bubbles, cameras are used to image bubble shape and changes and the meniscus in a capillary tube that stands over the vessel. The capillary magnifies level changes in the vessel itself. The position of the meniscus is determined with image analysis software (LabVIEW) to obtain the level as a function of pressure

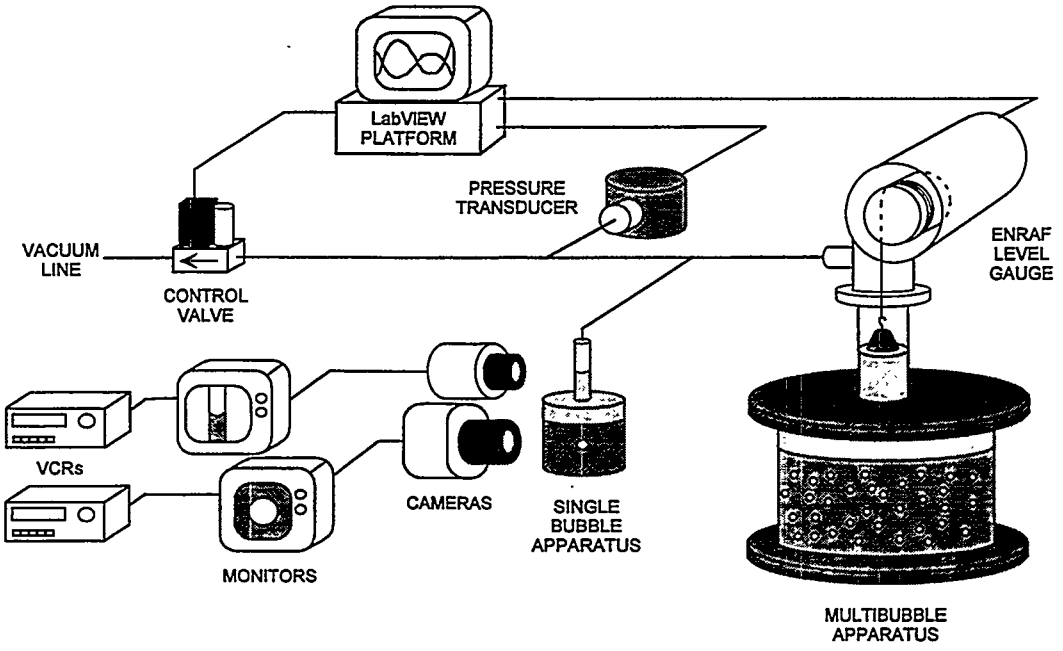

Figure 2. Apparatus for Measuring dl/dp on Single and Multiple Bubbles

automatically. For multiple-bubble experiments, an Enraf (854 ATG) gauge is used to obtain the level. This gauge is identical to the level gauge used in the Hanford tanks. All measurements of pressure and level are automatically recorded using LabVIEW software.

Experiments thus far have been challenging. Data on single bubbles is difficult to obtain because the simulant must be transparent, yet still have properties (shear strength and Young's modulus) that are close to tank waste. A variety of particulate-liquid systems have been employed. There are two systems that show promise, but each has limitations. The first system is carboxyl polymethylene (Carbopol)–water, which is a polymer solution rather than two-phase, and the second is a silica-oil system. The Carbopol solutions are crystal clear and have the desired yielding behavior (50 to 2000 Pa strength), but the Young's modulus is low, which results in accentuated elastic behavior. The oil-silica system has all the desirable properties, but air is quite soluble in the mineral oil that is needed to obtain a clear dispersion. This results in bubble volume changes from gas within the bubble dissolving, and this complicates data analysis. More detail on these phenomena will be discussed below. Data have been collected on both systems, and the search continues for a water-silica system (low gas solubility) that will have good yielding properties and a high Young's modulus.

Figure 3 shows the response of a water-based simulant and an oil-based simulant to a step change increase in pressure. Notice that the level in the water-based system steps down and remains constant while the level in the oil-based system steps down and slowly creeps lower. When the pressure is raised above the oil-based simulant, the pressure in the gas bubbles rise. Because the solubility of air is substantial in mineral oil, some of the gas within the bubble partitions into the liquid over time. In general, hydrogen has a low solubility in the actual tank waste, and partitioning of hydrogen across the surface of bubbles is not expected. However, many of the tanks have significant amounts of trapped ammonia gas, and ammonia is soluble in tank waste. Therefore, we believe the oil-based silica simulant are valuable for examining these phenomena further.

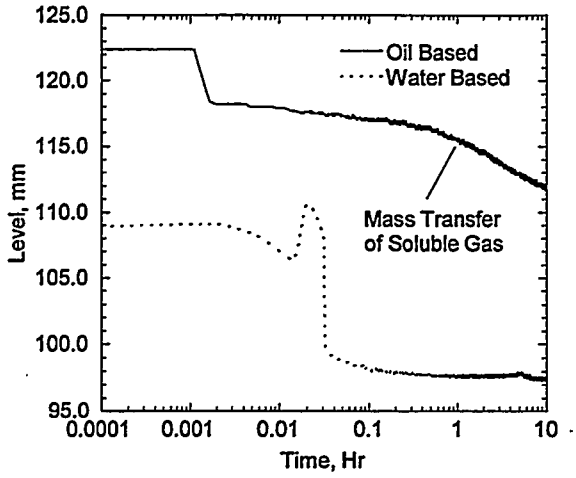

Figure 3. Step Changes in Pressure Show the Effects of Mass Transfer Across the Bubble Surface

Figure 4 shows normalized pressure and level (dL/dP) data from single- and multi-bubble experiments with the calculation for an ideal gas. Both data sets show hysteresis, but the corners of the hysteresis loop are rounded versus the square dL/dP profiles apparent in many actual tank data. The model developed under this program would predict that the reason for such smoothing is a lower Young's modulus of elasticity. The difference in the degree of hysteresis between the single- and multi-bubble data is unexpected. Both sets of data were taken on a simulant with a shear strength of ~1000 Pa (4% Carbopol–water). At this time we cannot explain the discrepancy, but possible factors include relaxation of residual stresses and to a lesser degree bubble-bubble interactions.

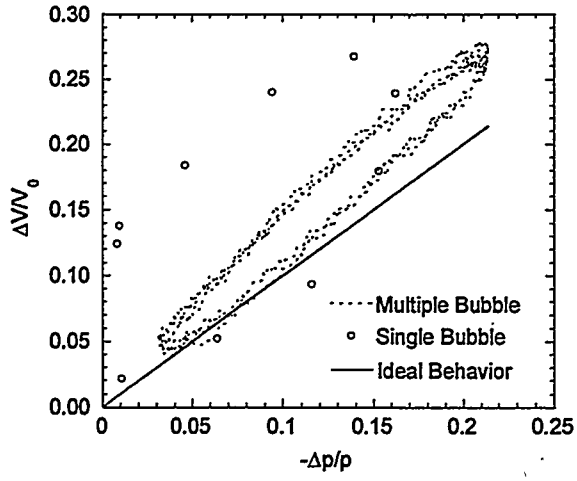

Figure 4. Pressure Cycles Representative of Natural Weather Events Show Hysteresis in Pressure and Level Measurements

Solid Mechanics Modeling

The objective of this research activity is to model the effect of small pressure changes on bubble volumes. In this section, we summarize progress on developing this model and comment on the significance of the new findings. During last year, a general procedure was developed to find the stress and strain fields produced by periodic pressure variations (of frequency ω) for an internally or externally pressurized single bubble embedded in an elastic-plastic medium. With this procedure, analytic expressions can be obtained for the bubble radii as a function of applied pressure. Driving pressure amplitudes, p_A, are chosen so that finite plastic deformations occur during the expansion or the compression of the bubble. This choice of pressure amplitude leads to the development of residual stresses after each

pressure sweep. These stresses are taken into account to determine the stress field at the subsequent sweep. In the present parametric study, the following initial conditions (at t = 0) were used

$$\varepsilon_r(r;0)=\varepsilon_\theta(r;0)=0, \qquad \sigma_r(r;0)=\sigma_\theta(r;0)=-p_o$$

where, ε_r and ε_θ are the radial and angular strains, σ_r and σ_θ are the radial and angular stresses, and ρ_o is the reference pressure. Boundary conditions for an infinite as well as a finite medium were used. Solutions of the elastic-plastic equations were found by using the boundary conditions (for t > 0) shown in Table 1. Numerous cases have been computed for a series of different sets of parameters, including experimental data. A parameter set includes the yield stress of the material, Poisson ration, Young's modulus of elasticity, pressure amplitude, initial bubble radius, outer boundary radius, solubility of the gas in the medium, and reference pressure.

Table 1. Boundary Conditions for Parametric Study

	Radial Stress at the Bubble Radius	Radial Stress at the Outermost Boundary
1	$\sigma_r(a(t))=-p_o-p_A\sin(\omega t)$	$\sigma_r(\infty)=-p_o$
2	$\sigma_r(a(t))=-p_o-p_A\sin(\omega t)$	$\sigma_r(b(t))=-p_o$
3	$\sigma_r(a(t))=-p_o\left(\frac{a_o}{a(t)}\right)^3$	$\sigma_r(\infty)=-p_o-p_A\sin(\omega t)$
4	$\sigma_r(a(t))=-p_o\left(\frac{a_o}{a(t)}\right)^3$	$\sigma_r(\infty)=-p_o-p_A\lvert\sin(\omega t)\rvert$
5	$\sigma_r(a(t))=-p_o\left(\frac{a_o}{a(t)}\right)^3$	$\sigma_r(b(t))=-p_o-p_A\sin(\omega t)$
6	$\sigma_r(a(t))=-p_o\frac{a_o^3+SRT\left(b_o^3-a_o^3\right)}{a(t)^3+SRT\left(b(t)^3-a(t)^3\right)}$	$\sigma_r(b(t))=-p_o-p_A\sin(\omega t)$

In Table 1, a(t) is the bubble radius as a function of time (a_0 at t = 0), and b(t) is the outer radius of the spherical medium (b_0 at t = 0). When the outer boundary is finite, the number of equations for the elastic and plastic deformations is twice that of infinite media. At each pressure sweep, the expressions for these deformations (elastic and plastic) are obtained analytically and solved numerically because they involve transcendental functions. Boundary conditions 1 and 2 correspond to an internally pressurized bubble in which the amount of gas inside the bubble would be continually changing to maintain a periodic pressure cycle. Although these conditions are not realistic in modeling bubbles inside sludge, they were used to generalize the solution of the elastic-plastic equations for an arbitrary number of pressure cycles (these conditions reduce the algebra considerably). Conditions 3 to 5 correspond to realistic boundary conditions because the internal bubble pressure is implicitly coupled to the bubble radius and the pressure fluctuations are externally applied to the medium. It was assumed the bubbles contain an ideal gas (R is the universal gas constant) and that the compression/expansion of the bubble is isothermal (at temperature T). Boundary condition 6 is a generalization of conditions 3 to 5 to include the effect of gas solubility in the elastic-plastic medium. Under the assumption of thermodynamic equilibrium, this condition is

derived by equating the number of moles of gas inside the bubble and in the medium at t = 0 to that at any other time. The product of the solubility coefficient S (in mol/bar/m3) and the bubble gas pressure gives C the gas concentration inside the bubble.

In the present study, the effects that the parameters have on bubble deformations have been studied. Interesting and new topologies for the bubble radius as a function of pressure have been observed for different combinations of parameters and boundary conditions. As an example, the effect of the solubility S on an expansion-compression sweep is shown in Figure 5. This parameter has a significant influence on the plastic deformations and thus the bubble radius.

The current model is significantly more rigorous than previous studies. This more careful analysis has resulted in two significant new results. First, the rounded corners of the pressure level hysteresis loops, as was mentioned in the experimental section above, results from elastic behavior and are directly associated with the Young's modulus of the simulant. Second, our estimate of material strength from level-pressure hysteresis is about 10-fold smaller than previous calculations that neglected residual stresses and did not have a rigorous inclusion of elastic and plastic regions.

Fluid Mechanics Modeling on Continuum Materials and Rheology of Simulated Waste Materials

The slurries in the Hanford storage tanks are complex fluids that exhibit a yield stress and most likely deform elastically below the yield stress. We are studying the behavior of bubbles in these slurries under the influence of gravity and changing barometric pressure through a computational and theoretical effort. Specifically, we are interested in how multiple bubbles suspended in a yield-stress fluid interact, coalesce, and move. The issues involved are intuitively clear: an expanding single bubble strains the surrounding fluid to a point where the yield stress is exceeded, the fluid structure within that yielded region collapses,

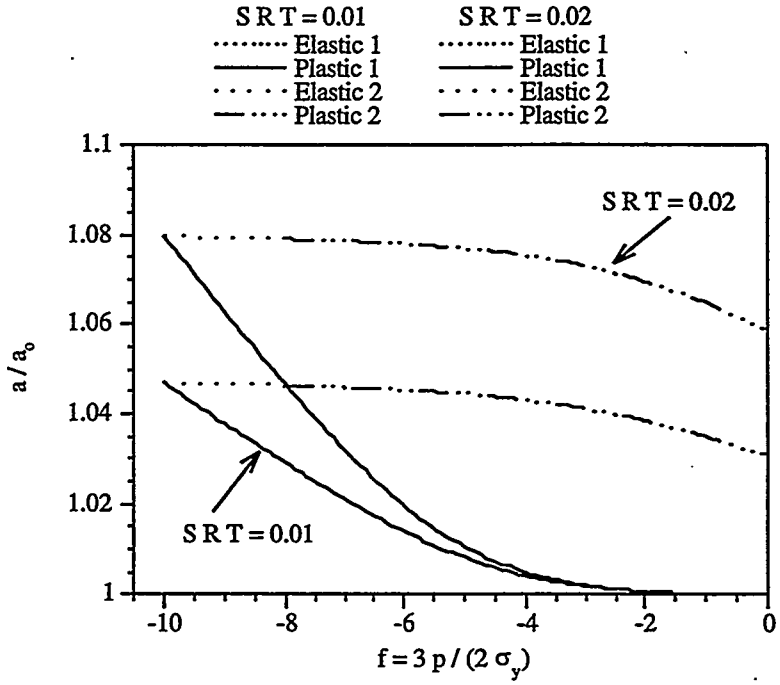

Figure 5. Effect of Solubility on Plastic Deformation (ρ_o = 1 atm, f_{max} = -10, σ_y = 500 Pa, E = 80 kPa, $b_0 = 10a_0$, S R T = 0.01)

the fluid around the bubble flows but remains surrounded by a region that continues to deform elastically. The yielded region will continue to grow in size as the bubble grows. In an array of bubbles, the yielded regions will interact. How this interaction occurs and what happens when the yielded regions intersect is the heart of the problem. When there is a fully connected yielded region, bubbles can move about, coalesce, and rise.

We chose to begin our study of the flow of fluids exhibiting a yield stress with squeeze flow, or flow between converging planes, which contains some of the same issues regarding singularities and unyielded regions as we expect to find with flow around submerged bubbles. Numerical studies using the commercial finite-element code POLYFLOW gave results consistent with those published by O'Donovan and Tanner (1984). We encountered numerical problems with the commercial code, however, when the simulation was extended to the unbounded flow around a rigid sphere. We then focused on the development of a specialized finite-element code to deal specifically with the Bingham plastic.

Bingham plastics pose an interesting computational problem because of a discontinuity in the stress-deformation rate constitutive relation at the yield stress. The conventional computational fluid mechanics approach is to introduce a smooth "regularized" constitutive relation which converges to the analytical Bingham material when a regularization parameter becomes infinite. This is the approach employed in POLYFLOW and in our own finite-element code. From the point of view of understanding the mechanics of the fluid around a submerged bubble, we are most interested in determining which regions are yielded (and thus act like viscous liquids) and which regions are unyielded (and thus act as solids). Our method of determining the numerical solution is to solve the regularized equations and to gradually increase the regularization parameter until convergence is attained in the flow field. The method has been validated in pipe flow and squeeze flow.

Flow around a rigid sphere captures many of the relevant features of flow past a bubble, without adding the complexity of the mobile interface; the flow requires approximation of an unbounded domain and the presence of a yielded region surrounding the sphere. Moreover, some prior numerical work exists for this problem (Beris et al. 1985, Blackery and Mitsoulis 1997). One of the issues of concern to us is the effect of a finite computational regime on the solution of the unbounded problem. In the work of Blackery and Mitsoulis (1997), for example, we see an effect of altering the radius of an enclosing cylinder (i.e., the extent of the computational boundary) even when the apparent yielded region does not reach this boundary. Physically, this cannot be correct, because the unyielded region should, in principle, act as a rigid solid and thus make the presence of the outer boundary irrelevant. We seek to determine why this discrepancy exists and whether the general method used by Blackery and Mitsoulis (1997) (which closely parallels our current method) is equivalent to the free boundary problem solved by Beris et al. (1985).

We are now applying our code to flow around a submerged rigid sphere. We are able to obtain solutions that show unyielded regions near the sphere surface and at a distance from the sphere, but the outer yield surface is sensitive to the choice of the regularization parameter, and it is not clear that it is converging. We have identified several possible sources of this problem, including the proper criterion to use for convergence and the relative tradeoff between convergence of the continuity (mass balance) and momentum (velocity and stress) equations. In addition, we are exploring issues associated with roundoff error and the possible need for selective mesh refinement.

Modeling of Bubbles in Particulate Materials (Slurries)

We are investigating the mechanics of bubble movement in representative particulate waste layer (slurry) in a Hanford tank using a one-dimensional biconical-pore network model. The goal of this work is to determine the effective compressibility of the gas in the slurry. With this information, one could

determine the volume of gas in the slurry from changes in waste level upon fluctuations in barometric pressure. The compressibility of the gas depends on its pressure, which is the sum of barometric pressure (known as a function of time), hydrostatic pressure from the liquid in the tank (also known), and capillary pressure in the porous medium formed by the slurry. Accordingly, determining gas compressibility requires determining the average capillary pressure of the population of bubbles responding to gas generation and changes in barometric pressure over time.

Three time scales are involved in the process of gas accumulation and response to barometric pressure. Over a period of months or years chemical reactions in the liquid create volatile components that diffuse to and accumulates in the bubbles. During this period, bubble mass and volume increase slowly at fixed liquid pressure. This process determines the initial states of bubbles when barometric pressure changes. On a shorter time scale of hours, bubble volume responds to changes in barometric pressure at fixed mass. It is on this time scale that effective compressibility is observed. On a still-shorter time scale, of seconds or less, interfaces advance or retreat impulsively, driven by capillary forces. These jumps occur at fixed barometric pressure and bubble mass. Impulsive jumps occur from pore throat to (near) pore throat for expanding bubbles, whether due to accumulation of mass over a period of months or to a short-term decreases in barometric pressure. In contract, interfaces jump from pore *body* to pore body during pressure increases.

These jumps are crucial to the effective compressibility of gas in the slurry for two reasons. First, because these jumps have occurred during the slow growth of bubbles over months, most bubbles are lodged at pore throats. In particular, for large bubbles occupying many pores, expanding bubbles jump from one pore throat nearly to the next pore throat. As a result, the population of bubbles present as barometric pressure changes is biased toward bubbles poised in pore throats, ready to jump again if pressure decreases. However, these same bubbles do *not* jump backwards if pressure increases, until their interfaces first retreat to pore bodies.

Second, the outward jumps of interfaces as pressure decreases implies 1) an infinite compressibility for individual bubbles at the moment of the jump and 2) a comparatively large effective compressibility for a population of bubbles that includes a few that do jump and many that do not. On the other hand, upon an increase in pressure, the effective compressibility is small until interfaces retreat to pore bodies. This implies a significantly higher effective compressibility for a population of bubbles upon a pressure decrease than upon a pressure increase.

Our model can fit tank data with level-pressure hysteresis from the Hanford Site such as shown in Figure 6 (Whitney et al. 1996). One might idealize the trend of these data as a linear increase in tank level during the initial decrease in pressure, no change at first in tank level upon an increase in pressure, and thereafter a linear drop in tank level, with the same slope as for the initial increase in tank level. Fitting these data requires that bubbles be long, occupying many pores. Unfortunately, it is impossible to determine capillary pressure directly from these data. That is, one can fit this trend with either narrow pores (high capillary pressure) or wider pores (lower capillary pressure) depending on pore geometry. One can also fit the data with pores modeled as smooth cylindrical tubes, if contact-angle hysteresis is introduced into the model. Further study is needed to resolve the apparent indeterminacy of capillary pressure to determine gas compressibility from tank data. Independent data on pore geometry and contact-angle hysteresis could resolve this problem. It is also possible that a more sophisticated analysis of tank-level data might identify subtle features that could be used to fit the capillary pressure unambiguously. This is indeed an objective for the coming year.

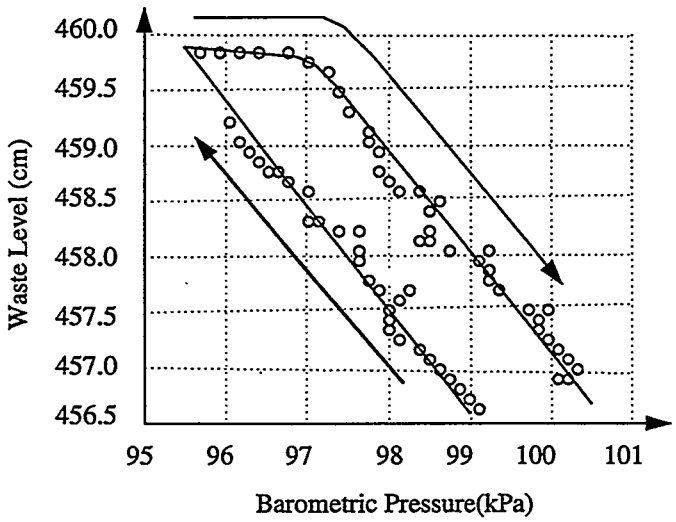

Figure 6. Variation of Tank Waste Level with Changes in Barometric Pressure (from Whitney et al. 1996)

Insights from other research on tank waste may provide the independent information on pore geometry needed to identify gas compressibility unambiguously. We will work with other groups involved in research on the slurry to provide this information. In addition, we will analyze the pressure-level data more completely, looking for features with which we can fit the capillary pressure with less ambiguity than the data in Figure 6.

Two important factors not accounted for here alter the initial distribution of bubbles that then respond to changes in barometric pressure. First, bubbles grow over a period of months or years, not at constant barometric pressure but with barometric pressure fluctuating over the period of bubble growth. This factor can be introduced into the model of bubble growth. Second, bubble growth depends on diffusion, which, in turn, depends on chemical potential and thereby on bubble pressure. Thus bubbles pushing into pore throats with relatively high capillary pressure grow more slowly than bubbles with interfaces farther from the throats. This would tend to bias the distribution of bubbles more toward more bubbles in pore throats and thereby toward higher effective compressibility for the population as a whole. We will also introduce insights from the study of growth of gas bubbles in oil reservoirs under primary production.

A three-dimensional (3D) pore network differs from the 1D biconical pore network assumed here, especially in the amount of liquid stored in the crevices and corners of pore bodies occupied by gas bubbles. This reservoir of liquid affects the jumps bubbles make and thus the effective compressibility of gas in the bubbles. We will test the sensitivity of the model to geometric factors to make it reflect 3D pore-network geometry more accurately.

Planned Activities

From an overall viewpoint we are midway through the second year of this project and are ready to shift to comparing experimental and modeling results from the initial focus of developing the computational frameworks and experimental apparatuses and methods. We are planning to complete the main

experimental studies of bubble expansion and compression toward the end of this year and the first part of the third year and will also be making detailed comparisons between experimental and modeling results during this period. Toward the end of this year, as planned, we also expect to start our experimental study on the mechanisms of slow bubble rise. This topic continues to be a crucial, but yet unexplained, issue in understanding gas migration in the actual waste tanks. We still expect that much of the third year will be devoted to reconciling the differences between theory and experiment, which will likely require additional experiments and numerical simulations.

References

Beris AN, JA Tsamopoulos, RC Armstrong, and RA Brown. 1985. "Creeping motion of a sphere through a Bingham plastic." *J. Fluid Mech.* 158:219-244.

Blackery J and E Mitsoulis. 1997. "Creeping motion of a sphere in tubes filled with a Bingham plastic material." *J. Non-Newtonian Fluid Mech.* 70:59-77.

O'Donovan EJ and RI Tanner. 1984. "Numerical study of the Bingham squeeze film problem." *J. Non-Newtonian Fluid Mech.* 15:75-83.

Whitney PD, PA Meyer, NE Wilkins, NE Miller, F Gao, and AG Wood. 1996. "Flammable gas data evaluation progress report." Pacific Northwest National Laboratory, Richland, Washington.

Publications

Denn MM and G Marrucci. "Squeeze flow between finite plates." *J. Non-Newtonian Fluid Mechanics* (submitted).

Kam SI and WR Rossen. "Anomalous capillary pressure, stress and stability of solids-coated bubbles." *J. Colloid Interface Sci.* (in press).

Kam SI. 1998. "Interactions between bubbles and solids: Three applications." Department of Petroleum and Geosystems Engineering, The University of Texas at Austin.

Presentations

Gauglitz PA, G Terrones, CL Aardahl, DP Mendoza, and LA Mahoney. 1999. "Mechanics of bubbles in sludges and slurries: Experimental studies and solid mechanics modeling results." Engineering Foundation Conference on Rheology in the Minerals Industry II, Oahu, Hawaii, March 14-19.

Gauglitz PA, G Terrones, DP Mendoza, CL Aardahl, MM Denn, SJ Muller, and WR Rossen. January 1999. "Mechanics of bubbles in sludges and slurries." Presented to Hanford Site Technology Coordinating Group - Tank Subgroup, Richland, Washington.

Gauglitz PA, G Terrones, DP Mendoza, MM Denn, SJ Muller, and WR Rossen. June 1998. "Mechanics of bubbles in sludges and slurries: Initial progress." Hanford Technical Exchange, Richland, Washington.

Web Site Address

http://www.doe.gov/html/em52/60451.html

Mass Spectrometric Fingerprinting of Tank Waste Using Tunable, Ultrafast Infrared Lasers

(First Year of Funding: 1998)

Principal Investigator

Professor Richard F. Haglund, Jr.
Department of Physics and Astronomy
Vanderbilt University
Nashville, Tennessee 37325
Phone: (615) 322-7964; Fax: (615) 343-7263
Email: haglunrf@ctrvax.vanderbilt.edu

Co-Principal Investigator

Dr. Wayne P. Hess
Pacific Northwest National Laboratory
P.O. Box 999, K8-88
Richland, Washington 99352
Phone: (509) 376-9907; Fax: (509) 376-6066
Email: wayne.hess@pnl.gov

Research Objective

We propose to develop protocols for quantitative analysis of tank waste materials based on the use of tunable infrared ultrashort-pulse lasers. Our goals are to 1) demonstrate atomic, molecular, and substrate characterization in model solids by laser desorption-ionization (LDI) and matrix-assisted (MA) LDI mass spectrometry; 2) develop the capability for generating quantitative analyses by measuring the total energy budget and identifying the principal reaction channels in LDI and MALDI-MS, and use this information to benchmark appropriate models for the procedures. Following the demonstration of these protocols in model materials, we will demonstrate their applicability to complex heterogeneous tank wastes from the Hanford Site. The research will be carried out by the team of Vanderbilt University and Pacific Northwest National Laboratory (PNNL) investigators who have already been collaborating for two years. The detailed tasks in the research plan presented here are based on preliminary studies, which show that subpicosecond infrared laser pulses can be wavelength-tuned to optimize desorption and ionization while minimizing fragmentation and the amount of material removed; MALDI of several small molecules appears to show fewer adducts and less matrix interference in the infrared than in the ultraviolet; the use of ultrafast tunable laser pulses in LDI and MALDI provides greater specificity and sensitivity than is available from nanosecond lasers.

This research program has the potential for significant impact within the framework of the Environmental Management Science Program. It provides important benefits in critical areas of detection of molecular species in a way that can provide information about reactivity and abundance at high sensitivity and a coordinated effort to study both model materials - which can lead to computational benchmarks of the analytical procedures - and realistic samples of tank waste. We plan a quantitative emphasis of extracting reaction rates, branching ratios, and absolute budgets for sample size and laser inputs required for successful analysis. Moreover, the protocols have significant promise for translation into field-deployable instrumentation and real-time waste-stream processing monitoring.

Problem Statement

The U.S. Department of Energy faces a major challenge in characterizing, managing, and eventually transforming or disposing of high-level radioactive wastes stored at its Hanford, Washington site. Atomic and molecular characterization of these wastes is critical to maintaining and assuring workers and the public about the safety and appropriateness of every step in environmental remediation, from hazard assessment to final disposal.

Laser mass spectrometry techniques have, in principle, the capability to provide rapid, accurate characterization of complex materials at the pico- or even femtomolar sensitivity level - a capability that would dramatically reduce the sample quantities required for accurate characterization of waste material and that would also make possible on-line monitoring of waste streams. This, in turn, would make it substantially easier and cheaper to avoid personnel safety hazards, flammable or explosive chemical reactions, and threats to tank integrity. However, analytical techniques now available do not yet provide quantitative information for this task.

Research Progress

Early efforts at PNNL were focused on hiring an exceptional postdoctoral research associate. Advertisements were run in Physics Today and Chemical and Engineering News in late September and several interviews were conducted between November 1998 and February 1999. Jun Kim, a graduate student in the Yale Chemistry Department, has accepted this position and will join our group at PNNL in July 1999. Laboratory research will begin in earnest earlier than Dr. Kim's arrival when Mike Papantonakis, a graduate student in Professor Richard Haglund's research group at Vanderbilt, arrives in June for a summer internship at PNNL. Mr. Papantonakis is already contributing to this EMSP project as part of his graduate training at Vanderbilt University. In the meantime, instrument preparation and detailed research planning will be completed.

Laboratory work to date has included modification and development of the major experimental research equipment. We have adapted a Bruker reflectron time-of-flight (RETOF) mass spectrometer for matrix-assisted laser-induced desorption ionization (MALDI) experiments. This work involves design of a cooled sample stage for liquid samples and a micro-titer device for multiple sample operation. The Bruker has excellent mass resolution; it is far superior to the limited resolution of the linear TOF used in preliminary studies.

A second mass spectrometer, based on RF trapping technology, is being modified for tank waste analysis. The modifications include adaptation of the RF trap for MALDI-based analysis and implementation of a patented new asymmetric trap design. This work is being performed by Dr. Michael Alexander of PNNL.

Planned Activities

The research plan proposed here is a collaborative effort involving scientific staff and graduate students at Vanderbilt University and PNNL. The major elements of the plan include the following:

- Materials characterization. Choose a set of model substrate or host materials, including $CaCO_3$, $NaNO_3$, $NaNO_2$ and sulfate, phosphate, metal-salt and oxide compounds.
- Measure neutral-to-ion ratios. Laser-induced desorption from insulators tends to produce an overwhelming fraction of neutral species.
- Measure ion yields. We will carry out measurements on model materials in various phases (solid, liquid, slurry, and colloidal) as a function of laser pulse duration (at 100 fs, 1-2 ps, and 5 ns) and laser wavelength (0.3-10 μm), as well as fluence and intensity.
- Correlate "fingerprints" from heterogeneous samples to energetics. We propose to do this using chemometric techniques, cross-checked against ab initio calculations of desorption and ionization rates to establish the limits of our quantitation.

The timeline for PNNL activities follows.

Table 1. Time Line for Operating Plan

Task	1998 - 1999		1999 - 2000		2000 - 2001	
Instrumentation development						
• Modify Bruker TOF		→				
• Test Bruker TOF		→				
Study neutral and ion desorption mechanisms						
• Constituents of model solids		→	→	→		
• Adsorbed organic impurities			→	→	→	
• Begin discussions about models					→	→
Issues in quantitative mass spectrometry						
• Sample morphology and preparation			→	→		
• Slurries, liquids and thin films			→	→	→	
Application to heterogeneous mixtures						
• Choose prototype materials		→				
• Start ion trap MALDI MS at PNNL			→	→	→	→
• Study effects of water, radiation			→	→	→	→
Computational studies of MALDI/LDI						
• Discussions of LDI in model materials			→			
• Model and compute selected test cases				→		
• Evaluate systematics of MS data sets				→	→	
• Consider possible chemometric studies						→

Publications and Presentations

"Mass Spectrometric Fingerprinting of Tank Waste Using Tunable Ultrafast Infrared Lasers." November 1998. EMSP Tank Focus Area Workshop, Richland, Washington.

Web Site Address: wayne.hess@pnl.gov

Dissolution, Precipitation, and Deposition of Aluminum-Containing Phases in Tank Wastes

(First Year of Funding: 1998)

Principal Investigator

Dr. Jun Liu
Pacific Northwest National Laboratory
P.O. Box 999, MISN K2-44
Richland, WA 99352
(509) 375-2616 (phone)
(509) 375-2186 (fax)
j_liu@pnl.gov

Co-Principal Investigator

Dr. David Hobbs
Savannah River Technology Center
Aiken, SC 29808
(803) 725-2838 (phone)
(803) 725-4704 (fax)
david.hobbs@srs.gov

PNNL Co-Investigator

Dr. LiQiong Wang
Pacific Northwest National Laboratory
P.O. Box 999, MISN K2-44
Richland, WA 99352
(509) 376-2685 (phone)
(509) 376-2303 (fax)

University Collaborator

Dr. Dan Dabbs and Professor Ilhan Aksay
Princeton University
Princeton Materials Institute
Princeton Center for Complex Materials
Bowen Hall, Rm. 231
70 Prospect Avenue
Princeton, NJ 08580-5211
(609) 258-1572 (phone)
(609) 258-6878 (fax)
ddabbs@princeton.edu

Research Objective

The goal of this work is to understand the kinetics of dissolution, precipitation, and scale formation involving aluminum-containing phases in alkaline salt solutions representative of tank wastes. This research will identify aluminum-containing phases that are likely to form or be present, and predict conditions under which such phases are likely to form or be present. Experiments will identify processing conditions that either promote or inhibit the heterogeneous or homogeneous nucleation and growth of aluminum-containing phases to form precipitates or scales. Test conditions will encompass conditions anticipated for waste storage, washing, leaching, concentration in evaporators, and contact with pipes, ion exchangers, and other processing media.

Problem Statement

Aluminum is one of the principal elements in alkaline nuclear wastes stored at DOE sites, including Hanford and Savannah River. Both the insoluble and soluble fractions pose serious challenges to waste processing. Aluminum removal during processing is desired because it is a major waste component that dictates the volume of waste glass produced via vitrification of both high- and low-level waste streams. It is critical to understand factors controlling the extent and rate of dissolution for aluminum-containing phases.

Soluble aluminates represent a major component of supernatant liquids in most tanks even prior to sludge dissolution. Aluminum concentrations in many solutions are near saturation levels. Changes in solution conditions can lead to supersaturation, promoting precipitation and scale formation. Aluminate precipitates are known to have clogged pipes in the tank farms at Hanford. Scale formation may have contributed to the clogging of cross-site transfer lines. At Savannah River, precipitation of alumino-silicates led to the clogging of evaporator gravity drain lines. Precipitation due to pH, temperature, or ionic strength gradients within ion exchange columns and filters could lead to fouling and clogging of units having high radioactive inventories.

While the solubility of aluminum oxides and hydroxides has been studied extensively, limited information is available regarding the behavior of solid phases or soluble aluminum species in highly basic salt solutions, especially in the presence of silicate or phosphate species. Almost nothing is known about the kinetics of nucleation and growth leading to precipitation and/or scale formation from supersaturated aluminate solutions.

Research Progress

Interaction with Savannah River Technology Center and Hanford to Address Specific Tank Waste Needs

After detailed discussion with Savannah River Technology Center (SRTC) staff, the following areas have been identified as significant tank waste problems at SRTC.

1. Effect of aging of aluminum-containing sludges: One of the main processes of the Extended Sludge Processing operation at the Savannah River Site (SRS) is aluminum leaching. Aluminum leaching is

accomplished by treating the sludge with hot caustic solution. Despite many theoretical models on aluminum speciation during leaching and washing, there are still many questions regarding the effects of other variables (such as temperature, chemical environment, and radiation) on the formation and transformation of aluminum-containing phases in high-level nuclear wastes. Much of the testing performed to determine parameters for aluminum leaching in sludges used freshly precipitated sludges. Aging of the sludge is known to convert aluminum phases. Thus, aluminum leaching characteristics of aged waste solutions may be vastly different than freshly prepared materials. Testing is needed to determine the important parameters and the rates of phase transformations.

2. Interaction with silicate: The introduction of elevated quantities of silicon in the 2H-evaporator system at SRS from the DWPF recycle stream resulted in the formation of aluminosilicate solids that plugged the evaporator gravity drain line. Several million dollars were spent on cleaning the line because this evaporator is critical to maintain adequate storage space for HLW at the SRS. Testing is needed to determine allowable solution-phase concentrations of aluminum and silicon so that aluminosilicate formation can be prevented.

At the Hanford Site, ESP models have been widely used to predict the mineral contents in the tank wastes. Experimental verification of the ESP models, especially in the high aluminum tank wastes, remain critical.

Main Solid Phases and Implication on Tank Waste Processing

TEM studies have been performed on many tank waste samples in the past several years (Lafemina 1995), and the main results are summarized below.

Although the tank composition and history are very complicated, the most abundant elements in many tanks include Fe, Al, P, Ca, Si, and Bi. Among these, aluminum is one of the most prevalent elements in tank wastes. Figure 1 shows a TEM image of the solid phases observed in C-112. The major component in C-112 is large gibbsite ($Al(OH)_3$) particles, ranging from micrometers to tens of micrometers in size. Other phases are also observed, including uranium phosphate, calcium phosphate, and boehmite. The boehmite (AlOOH) and calcium phosphate are in the nanometer size range and exist as agglomerates. Besides gibbsite, aluminum-containing phases also exist as boehmite, hydrated alumina, although in some tanks they also exist as sodium aluminate, aluminum phosphate, and aluminosilicate. Boehmite (Figure 2) is the main crystalline phase in many tanks from the redox process (S101, S111, S102, S107, S103, and S104). The boehmite exist as rectangular plate-like particles, with a thickness ranging from 1 to 10 nm, and a width ranging from 10 to a few hundred nanometers. The aluminum hydroxide and aluminosilicate usually are in the micrometer size range.

Another commonly encountered phase is iron oxyhydroxide (FeOOH). The FeOOH was usually formed as particles less than 10 nm in size and incorporated into hard agglomerates of spherical shapes about one micrometer in size (Figure 3). The crystallinity of the particles and the density of the agglomerates vary from tank to tank, most likely depending on the composition and history of the tank. When bismuth and silicon are also present, iron will mix with them to form iron bismuth silica agglomerates of similar size and shape, as shown in Figure 3. It is interesting that, in Figure 4, the agglomerate shows single crystalline diffraction pattern even though the primary particles can still be distinguished within the agglomerates, indicating the particles are sintered together. This is most likely due to the long heating history inside the tank. In other tanks, like B-111, T-111, and T-104, the primary particles in agglomerate of similar shape are much less crystalline.

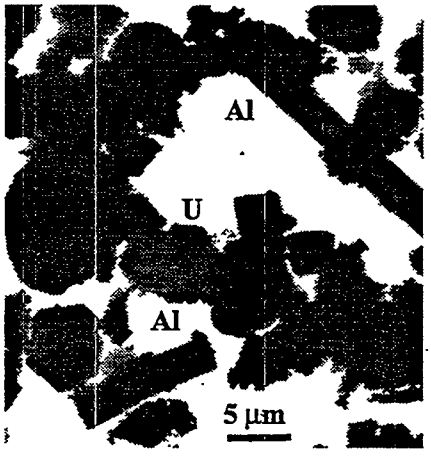

Figure 1. Gibbsite in C-112

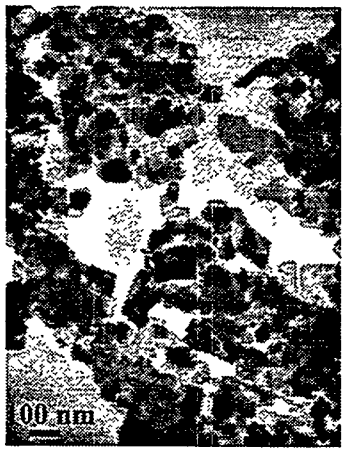

Figure 2. Boehmite in S-104

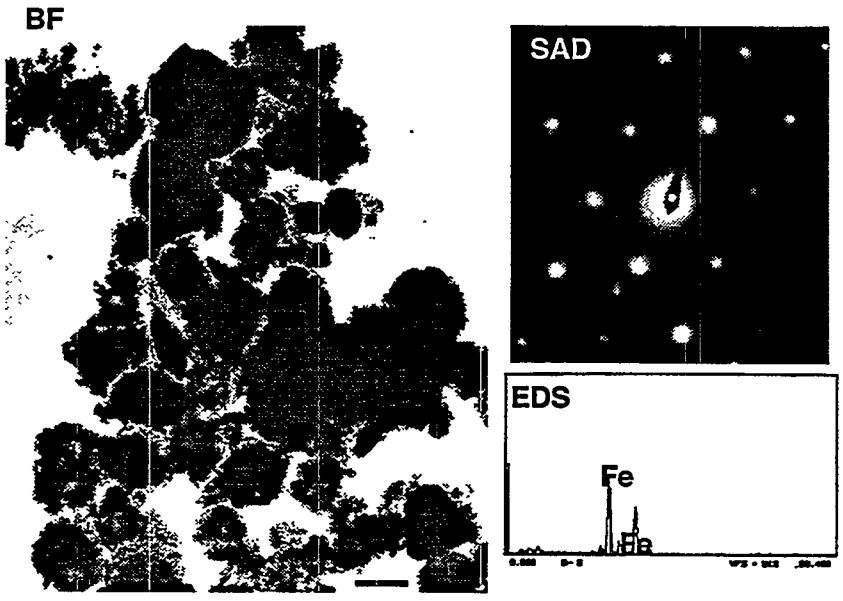

Figure 3. TEM Image of FeOOH Agglomerates in C-107 (bar 500 nm)

Although it is impossible to list all the minerals found even in one tank waste sample, different types of tank wastes have different degrees of complexity. S-101, S-102, S-103, S-104, S-107, S-111, SY-102, and SX-108 only have one mineral phase, boehmite, as the major constituent. B-111, T-111, and T-104 also have only one major morphology: spherical agglomerates of amorphous bismuth silicate ($Fe_2Bi(SiO_4)_2OH$), similar to the morphology in Figure 3. Many tank sludges, like C-106, C-107, C-112, and C-108, have two major solid phases, aluminum oxyhydroxide (gibbsite or boehmite) and iron oxyhydroxide (FeOOH). Even in more complicated tank sludges that contain many other phases, like BY-104, BY-108, BY-110, BX-112, and BX-110, gibbsite, boehmite, and iron oxyhydroxide are still the

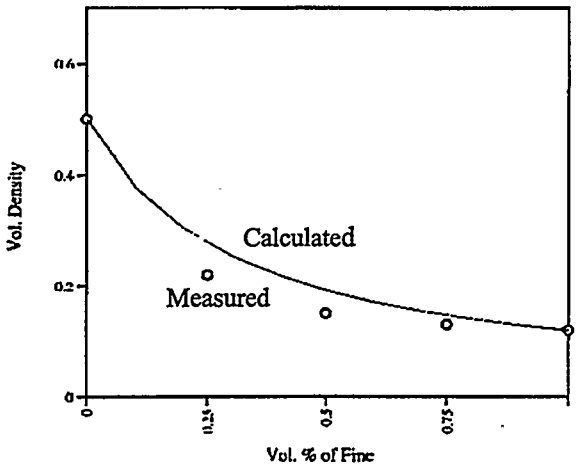

Figure 4. Sedimentation Density of Binary Aggregates (coarse particles and fine particles) as a Function of the Percentage of Fine Particles

majority phases. These observations give some useful lessons about the solid phases in tank waste sludges: 1) the major solid phases can be classified either as micrometer-sized colloidal particles, such as $Al(OH)_3$, or as agglomerates of nanometer-sized particles, such as AlOOH, FeOOH, or $(Fe_2Bi(SiO_4)_2OH)$; 2) although many phases are present in the tank, the different phases have not mixed with one another on a fine scale – it seems common for the fine particles to form aggregates of their own, rather than forming hetero-aggregates.

The TEM observations suggest that it is possible to use simple models to understand and predict the colloidal properties of the tank wastes: 1) under many conditions, the tank waste slurries can be simulated using one component system containing fine particles (boehmite, for example), or a two-component system consisting of fine particles and coarse particles; 2) because hetero-aggregation is not commonly observed, the model systems can be prepared by mixing different colloidal components.

We studied the sedimentation density of binary agglomerates of goethite (fine particles, primary particle sizes of less than 10 nm) and gibbsite (coarse particles, 1.3 μm). The sedimentation density is studied as a function of the relative volume fraction of the nanometer-sized particles, and the result is plotted in Figure 4. The sedimentation density decreases rapidly as the volume fraction of the fine particles increases. This behavior can be explained by a biphase mathematical model in which the two components are not intimately mixed; the fine particles form lower-density agglomerates by themselves, and the large particles form higher-density agglomerates by themselves. The sedimentation density of the fine particles is about 0.18 by volume, and the sedimentation density of the coarse particles is 0.5 by volume. The sedimentation density of the binary mixture can be calculated: $V = V_c V_f/[V_f(1-X)+V_c X]$, where V is the sedimentation density in the mixture, V_c the sedimentation density of coarse agglomerates, V_f that of the fine agglomerates, and X the weight fraction of the fine agglomerates. The expected density from this biphase model is plotted as the solid line. Over the whole range, the biphase model gives a good estimate for the sedimentation density compared with the experimental results. This biphase model is based on the TEM observation that the different phases do not mix intimately with one another. It does not make any assumptions about the agglomerate structure (size, density, fractal dimension, etc.) and provides a reasonable picture of the distribution of the two major phases in the tank waste. The only information needed is the maximum sedimentation density of the coarse and fine particles, which can be easily estimated.

Hydrothermal Treatment of Gibbsite

1. Gibbsite in caustic solution: (about 1.3 μm in diameter) Gibbsite was treated in caustic solutions containing high concentrations of sodium aluminate. After heating the solutions in sealed Teflon containers for up to 10 days at 80 and 100°C, TEM and XRD characterization indicated that there was no significant change in the crystalline phase and the particle morphology.

2. Hydrothermal treatment of gibbsite with silicate: 100 mL solution with 1 M sodium silicate solution (27%) and 2 M NaOH were heated to 100°C to dissolve the sodium silicate. The solution was then cooled to room temperature. Five grams of gibbsite were added to the above solution and stirred in a Teflon container for 30 minutes. These solutions were heated in the sealed Teflon containers for up to 10 days. After the hydrothermal treatment, the samples were centrifuged and washed several times until the pH value of the supernatant reached 6. The solid materials were dried and analyzed by TEM and XRD.

In the first two hours, at both 80 and 100°C, no significant reaction was observed. Between two hours and one day, many intermediate products were formed, including cristobalite, quartz, faujasite, and tridymite. After seven days, the principal reaction product is zeolite P2 (sodium-exchanged, artificial). Figure 5 shows the TEM micrographs of the reaction products, and Figure 6 shows the XRD results of the reaction products at different times.

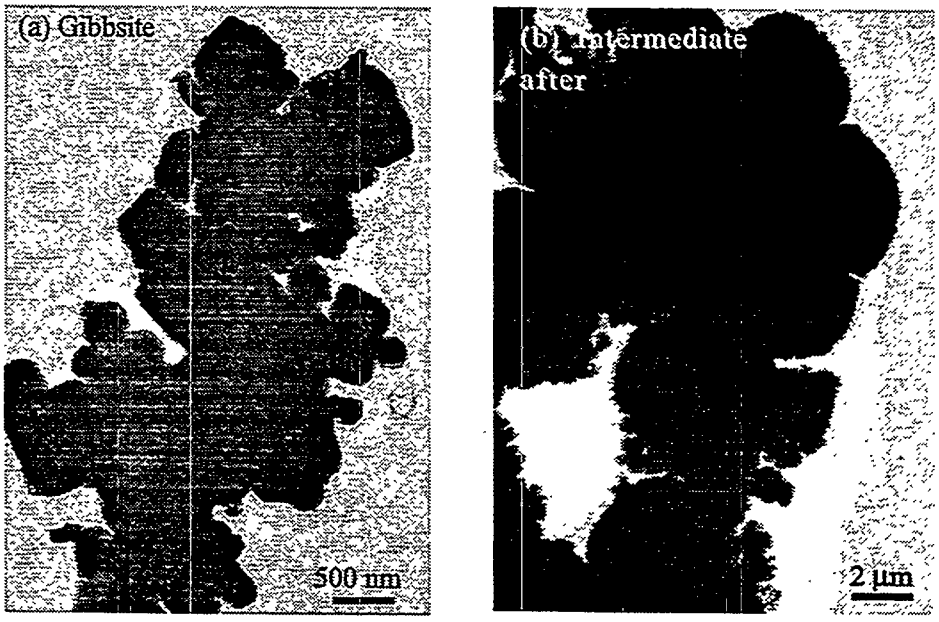

Figure 5. TEM images of Gibbsite and the Reaction Product at 100°C

These results suggest that the presence of silicate has a drastic effect on the activities of aluminum hydroxide. Although this phenomenon has been well documented, there is no detailed study of how gibbsite reacts with silicate in caustic solutions. These reactions will be the subject of future study.

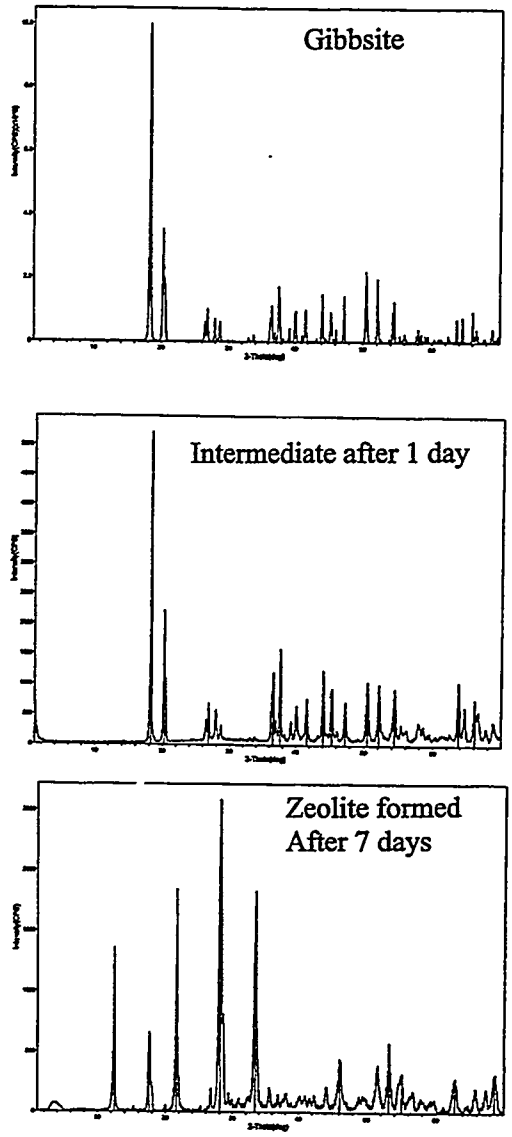

Figure 6. XRD of Gibbsite Reacted in a Caustic Solutions at 100°C

Control of Aluminum Solubility

The program goals of the Princeton University team are 1) to maintain and enhance the solubility of aluminum-containing species in high-pH aqueous solutions and 2) to stabilize suspensions of ultrafine aluminum-containing nuclei or submicron particles and thereby prevent deposition of insoluble materials in waste tanks and transfer lines. To these ends, three areas of study were emphasized: 1) the solubility of aluminum in high-pH solutions in the presence of organic molecules, 2) the kinetics of aluminum-containing phase precipitation, and 3) the composition and structure of aluminum-containing precipitates and soluble species. Additionally, the chemistry of hydration and the mechanisms of nucleation and growth of hydrated alumina solids will be studied to control the precipitation of aluminum-containing materials and thereby prevent unwanted precipitation.

In the initial stage we are screening simple organic molecules that might affect the solubility of aluminum-containing anions in solution through the complexation of the aluminum or aluminum oxyhydroxides (Figure 7). We have started with simple, water soluble carboxylic acids: hexanoic acid, butyric acid, and glutaric acid, examining and contrasting their behavior in alkaline solutions with respect to the presence of soluble aluminum-containing species. Solutions of the stable polycation $Al_{13}O_4(OH)_{24}(H_2O)_{12}^{7+}$ ("Al-13") were used as the test matrix. The Al-13 solutions were made by the following procedure:

1. 0.5 M solution of Al^{3+} prepared from dissolving either aluminum nitrate nonahydrate ($Al(NO_3)_3 \cdot 9H_2O$) or aluminum chloride ($AlCl_3$) in deionized water.

2. The Al^{3+} solution was refluxed at 60°C for two hours; after two hours, 0.2 M NaOH was slowly added to the solution by dropwise addition until the OH/Al ratio was 2.46.

3. The solution was refluxed at 60°C for two more hours following the addition of NaOH (aq), then set aside to cool.

Solutions made by this procedure remained stable for several weeks. Varying amounts of the simple carboxylic acids listed above were added to separate Al-13 solutions to achieve acid/aluminum ratios ranging from 1:4 up to 1:1. Across all acid/aluminum ratios, the glutaric acid (a bicarboxlyic acid) served to immediately precipitate the aluminum oxyhydroxide from solution when added. Butyric acid and hexanoic acid solutions remained clear. Once stabilized, the acid-containing solutions were then titrated with 0.2 M NaOH (aq) to raise the OH/Al ratio in solution. Butyric acid solutions precipitated as the OH/Al ratio approached 2.46; hexanoic acid solutions remained clear up to an OH/Al ratio of 2.46, at which point titration was stopped. The hexanoic acid solutions were stable (e.g., free of visible precipitate) for several weeks. Dynamic light scattering on the hexanoic acid solutions failed to detect any submicron particles in suspension.

These results indicate that short-chain carboxylic acids have a large effect on aluminum oxyhydroxides in solution. We hypothesize that the glutaric acid acts as a bridge molecule, bringing the aluminum oxyhydroxides near each other through the presence of acid groups at either end of the molecule, thereby facilitating precipitation. The difference in behavior between the butyric acid ($C_4H_8O_2$) and hexanoic acid ($C_6H_{12}O_2$) may be explained by the two-carbon difference between the molecular structures. If so, this indicates the sensitivity of the aluminum oxyhydroxide system to chain length, and provides a direction for additional studies. We plan to characterize the structure of the oxyhydroxide in solution with hexanoic acid by NMR to determine whether the hexanoic acid is indeed stabilizing the Al-13 structure or perhaps maintaining another molecular species in solution.

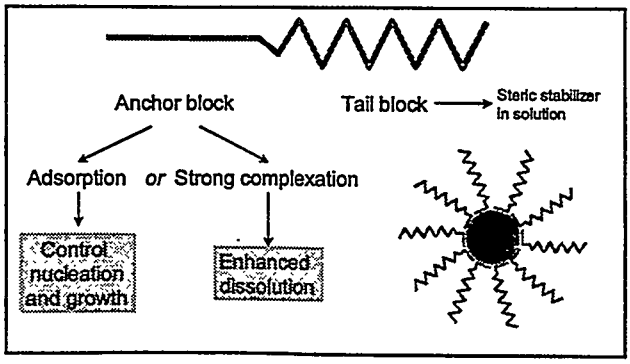

Figure 7. The Effect of Double-Hydrophilic Block Copolymers

Planned Activities

1. Map the solubility limit and the phase-stability limit of gibbsite in the presence of silicate by changing its composition and temperature. This study will provide information to SRTC.

2. Achieve phase transition of gibbsite during hydrothermal treatment.

3. Perform simulations studies to support the ESP modeling work at the Hanford Site, in collaboration with Dr. Albert Hu of Lockheed Martin Hanford Company.

4. Perform dissolution and phase transition of zeolites in caustic aluminate solutions.

5. Screen organic molecules as possible complexing agents. Bidentates and polyelectrolytes are two areas we plan to investigate, the latter involving the commercial polymers PMAA and PAA.

Reference

Lafemina JP. 1995. *Tank Waste Treatment Science Task Quarterly Report for April-June 1995.* PNL-10764, Pacific Northwest Laboratory, Richland, Washington.

Publication and Presentation

Liu J, GJ Lumetta, JW Virden, GL Graff, NG Colton, BC Bunker, and JL Krumhansl. 1999. "Characterization of Colloidal Phases in Tank Wastes." To be published in the *Proceedings of American Ceramic Society*, Indianapolis.

Colloidal Agglomerates in Tank Sludge: Impact on Waste Processing

(First Year of Funding: FY 1996)

Lead Principal Investigator

Dr. Joel M. Tingey
Pacific Northwest National Laboratory
P.O. Box 999, MSIN P7-25
Richland, WA 99352
(509) 376-2580 (phone)
(509) 372-3861 (fax)
joel.tingey@pnl.gov

Co-Investigators

Dr. J. A. Martin
Sandia National Laboratories
P.O. Box 5800
Albuquerque, NM 87185
(505) 844-9125 (phone)
(505) 844-4045 (fax)

Professor John D. Berg
University of Washington
Department of Chemical Engineering, BF-10
Seattle, WA 98195
(206) 543-2029 (phone)
(206) 543-3378 (fax)

Contributors

KD Keefer (PNNL)
AS Lea (PNNL)
DR Rector (PNNL)
JW Virden (PNNL)
S Stenkamp (Univerity of Washington)
KM Hill (SNL)
DA Adolf (SNL)

Research Objective

Insoluble colloidal sludges in hazardous waste streams such as tank wastes can pose serious problems for waste processing, interfering with retrieval, transport, separation, and solidification processes. Properties of sediment layers and sludge suspensions such as slurry viscosities, sedimentation rates, and final sediment densities can vary by orders of magnitude depending on the particle types present, the degree to which the particles agglomerate, and processing parameters such as shear rates, pH, salt content, and temperature. The objectives of this research are to

- understand the factors controlling the nature and extent of colloidal agglomeration under expected waste processing conditions
- determine how agglomeration phenomena influence physical properties relevant to waste processing including rheology, sedimentation, and filtration
- develop strategies for optimizing processing conditions via control of agglomeration phenomena.

Problem Statement

Complex radioactive mixtures of supernatant liquids (typically highly basic salt solutions), saltcake (consisting primarily of sodium nitrate and nitrite), and insoluble sludges consisting of submicron colloidal particles are stored at various locations on U.S. Department of Energy (DOE) sites. Over 100 million gallons of this radioactive waste is stored in underground tanks. The largest quantity and most complex mixtures of these radioactive wastes are located at the Hanford Site. Although the radioactivity is the primary concern in remediating these wastes, handling and processing the radioactive insoluble sludges provides a major technical challenge. Treatment and ultimate disposal of these wastes will require that these insoluble sludges be dispersed in aqueous solutions for retrieval and transport, separated from the liquid, and converted to a stable waste form. These tank wastes will be partitioned into high-level and low-level fractions because of the high cost of high-level waste vitrification and geologic disposal. The low-level fraction will be processed to remove ^{137}Cs (and possibly other radionuclides) and will then be immobilized in a glass matrix and disposed of by shallow burial on site. The high-level fraction will be immobilized in a borosilicate glass matrix, and the resulting glass canisters will be disposed of in a geologic repository. The maximum possible solids loading in each of the processing steps and the final waste forms are desired to minimize waste volumes.

The ability to maximize the solids loading and effectively process the wastes is dependent upon understanding and properly manipulating the colloidal behavior in these waste streams. Depending on processing conditions, these colloidal particles can form agglomerated networks having high viscosities that could clog transfer lines or produce high volumes of low-density sediments that interfere with solid-liquid separations such as settle-decant operations during sludge washing and leaching. Under different conditions, the particles can be dispersed to form very fine suspended particles that do not settle during settle-decant operations. These suspended particles may foul and contaminate downstream components such as ion exchangers or filtration systems. The formation and properties of viscous sludge layers also contribute significantly to the retention and periodic release of potentially flammable or explosive gas mixtures in some Hanford tanks. Colloidal agglomerates are also important to the processing and remediation of other waste streams, including the sludges present in fuel storage basins such as the K-Basins at Hanford.

Given the wide range of waste chemistries present at Hanford and other DOE sites, it is impractical to measure the properties of all possible sludge compositions under all potential processing conditions to design effective treatment procedures. Instead, a framework needs to be established to predict sludge property trends on a sound scientific basis. The underlying principles of colloid chemistry and physics provide such a framework, allowing us to predict and eventually control the physical properties of sludge suspensions and sediment layers in tank wastes and other waste processing streams.

Research Progress and Implications

This research project combines experimental and theoretical efforts to determine the impact of colloidal agglomeration on tank waste processing. Components of this research program include 1) understanding the nature of the primary particles and agglomerates that comprise tank sludge, 2) determining how particle and agglomerate distributions influence the physical properties of sludge, 3) understanding the critical interparticle interactions that control agglomerate distributions and slurry properties, and 4) developing chemical and physical methods to deliberately manipulate agglomerate structures during different waste processing steps. Work on the first two items was largely completed in FY 1997 and FY 1998. Work is in progress to understand how interparticle interactions influence agglomeration and sludge properties. A summary of the progress on items 1 and 2 is provided in this report, but the majority of the report will address items 3 and 4.

Particles and Agglomerates in Actual Tank Sludge

Work done prior to this year demonstrated that Hanford sludges consist largely of submicron ($<10^{-6}$ m) primary particles of hydrated oxides of Al, Fe, U, Zr, Mn, Cr, Ni, and Ti. Small particles of insoluble salts such as apatite $Ca_5(PO_4)_3OH$, uranium phosphate, aluminum phosphate, bismuth phosphate, and the zeolite cancrinite are also present. In existing tanks, and in most proposed tank processing schemes, the particles are in contact with highly basic (pH 10-14), high ionic strength (0.1-10 M) salt solutions (mainly $NaNO_3$ and NaOH). In such solutions, the electrical double layers associated with charged sites in particle surfaces collapse, and the electrostatic repulsions that can disperse particles of like charge disappear. Therefore, under most tank waste processing conditions, the particles comprising most sludges are predicted to be attracted to each other (van der Waals attraction dominates) resulting in extensive particle agglomeration. Most of the work performed in this project involves examining model suspensions containing mixtures of one or two of the major components found in actual wastes and studying how agglomeration influences physical properties such as viscosity and sedimentation. Experimental results on the simple systems are rationalized using theoretical models that describe particulate suspensions. Property models developed from theory and experiment on the simple suspensions are then applied to explain the limited results that have been obtained on actual tank wastes.

Rheological and physical data have been obtained on samples from 17 single-shell and 10 double-shell tanks. Many of these samples were processed to simulate the baseline processes proposed for ultimate disposal of these tank wastes. Physical properties and rheology have also been measured on these process samples. The results from these analyses have been compared with the results obtained on the simple systems used in this project. Large variability is observed in the properties of the waste in the tanks. This variability is also observed within an individual tank. In spite of this variability, the experimental results obtained for simple surrogate systems are comparable to actual tank waste samples under similar conditions.

The capabilities developed in this project have been used in obtaining more detailed physical properties on actual tank waste sludges and other radioactive waste samples such as K-Basin sludges. Extensive particle size distribution, sedimentation behavior, and particle density data have been obtained on samples from Hanford tanks 241-AW-101, 241-AN-107, and 241-AN-105 using the equipment and knowledge obtained in this project. Significant processing issues of the K-Basin sludges have been resolved based on data obtained and understood because of the research efforts associated with this project. Particle size distribution of samples obtained from the gunite tanks at ORNL is currently being considered at PNNL using these capabilities.

Agglomerate Structures: Impact on Sludge Properties

The properties of agglomerated sludges are dominated by the properties of the agglomerates, which are fractal objects whose mass scales as R^D, where R is the agglomerate size and D is the fractal dimension. For a diffusion-limited aggregate, D = 1.8; D = 3.0 for a dense three-dimensional object. Fractal agglomerates can have an enormous impact on slurry properties because they have lower densities and occupy much more space than dense particles at the same solids loading. The solids loading within an individual agglomerate, Φa, is given by the expression $\Phi a = (R/r)^{D-3}$, where r is the primary particle size. As shown in Figure 1, Φa can vary over three orders of magnitude depending on the ratio of the agglomerate size to the primary particle size and the fractal dimension. When agglomerates fill the solution and begin to contact each other (at a solids loading referred to as the percolation threshold or gel point ($\Phi g = 0.17\ \Phi a$), slurry viscosities can increase by orders of magnitude. Sediment densities are usually not much greater than Φg because sedimentation rates are slow to negligible above the gel point. Work on this project has shown that fairly accurate values for Φg can be calculated for both single component slurries and actual tank wastes if r, R, and D are determined experimentally.

For this program, primary particle size distributions have been determined using transmission electron microscopy, and agglomerate size distributions have been estimated using static light scattering on dilute suspensions. Direct measurements of the fractal dimension D have not been made, but based on literature studies on model systems, D = 2.2 has been used to model slurry properties (the theoretical value for a

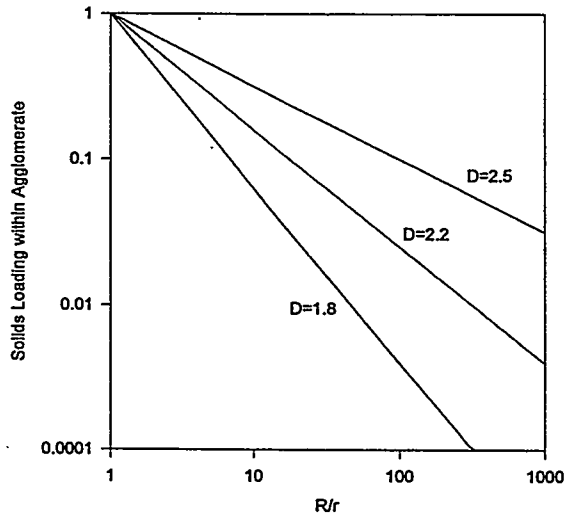

Figure 1. Solids Loading Within Fractal Agglomerates as a Function of R/r and D

rearranged reaction-limited aggregate). Using experimental r and R values and D = 2.2, sediment densities have been predicted to within about 20% for single component systems as well as actual sludges, solids loadings at which slurry viscosities will exceed the desired maximum of around 100 cP have been predicted to within about 30%, and sedimentation velocities in settle-decant operations have been predicted to within a factor of around 5. In terms of general trends, the least tractable slurries are those containing the smallest primary particles (10 nm particles are common in actual tank sludges), the largest agglomerate sizes, and the smallest fractal dimensions. Such slurries can have viscosities in excess of 10,000 cP at solids loadings as low as 1 vol%, which corresponds to the lowest sediment densities. At the other extreme, slurries containing primary particles larger than 10 μm can exhibit viscosities below 100 cP even at 30 vol% and pack to form dense sediments having solids loadings that exceed 35 vol%. Of the 20 or so distinct Hanford wastes examined to date, most exhibit gel points from 1-8 vol%. For the finest sludges, dilution factors as high as 20 may be required to keep from plugging pipes and transfer lines with viscous colloidal gels, generating millions of gallons of additional waste requiring treatment and ultimate disposal.

Interparticle Interactions: Impact on Sediment Densities

The focus of research during FY 1998 and FY 1999 has been on achieving an understanding of the relationships between interaction potentials and sediment densities in the high-salt, high-pH regime representative of most tank wastes. Work done prior to FY 1998 showed that changes in salt content representative of sludge washing and leaching operations can change sediment volumes by as much as a factor of two, having an enormous impact on processing tank utilization and separation efficiencies. Our practical goal is to be able to predict and control sediment densities in basic salt solutions. This regime is also of significant scientific interest because interaction potentials in such solutions cannot be described using classical electrical double-layer theory (the double layers collapse in high ionic strength solutions).

The macroscopic physical properties for a particular colloidal particle gel depend on both the gel microstructure and the interparticle forces. One example of a gel property is the compressive yield stress, $P_y(\phi)$, which is a measure of the force required to compact a gel network to a specified volume fraction, ϕ. The compressive yield stress controls both the final sediment height of a colloidal suspension and the rate at which the sediment compresses to reach that final height. A model has been developed to calculate the compressive yield stress as a function of gel microstructure and interparticle forces using the Brownian dynamics simulation method.

In this model, the initial particle network configuration was created using Brownian dynamics. A random distribution of noninteracting particles is formed using a series of Monte Carlo moves. Brownian motion then moves the individual particles or particle clusters until contact is made with another particle or cluster. The two are then combined to form a rigid cluster, which then has translational and rotational diffusion based on cluster size. This procedure continues until a continuous gel has been formed. The first series of three-dimensional colloidal gel models consisted of 10,000 particles and was created assuming diffusion limited aggregation. Gels were created for 2.0, 4.0, 6.0 and 8.0 vol%. A sample gel configuration is shown in Figure 2.

Once a gel configuration has been created, the rigid bonds are replaced with an interaction potential, which consists of both a repulsive core potential and a surface-bonding interaction. The core potential is based on the distance between particle centers. The surface-bonding interaction prevents a connecting particle from freely moving around the circumference of its partner, giving the gel its rigidity. The specified potential well depth determines the surface interaction strength. When the surface-point to surface-point distance exceeds a specified value, the connection is broken. If two particles move within the cutoff distance, a new connection is formed.

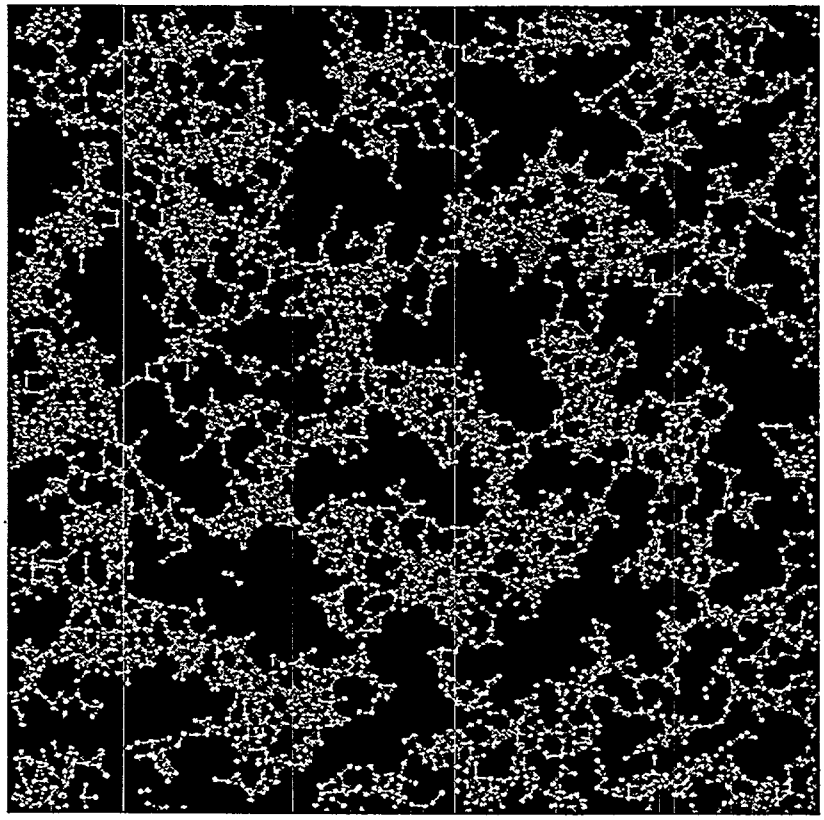

Figure 2. Initial Particle Gel Configuration from Brownian Dynamics Simulation

The compressive yield stress as a function of volume fraction is determined by performing a compression simulation on the gel structure and calculating the resulting stress tensor. The compression simulation is performed using a repeating sequence of two stages, a compression stage and an equilibrium stage. During the compression stage, the scaling factor is gradually reduced in a linear fashion. The rate of reduction depends on a variety of factors, including the potential well depth and temperature. During this stage, interparticle connections are broken and new ones are created as the gel network structure changes to accommodate the reduction in volume. After a period of time, the scaling factor is held constant and the system is allowed to reach equilibrium. The approach to equilibrium is monitored using the calculated values of the stress tensor. Once the system has reached equilibrium, quantities such as the stress tensor and the coordination number are calculated for that volume fraction. This procedure is repeated until the volume fraction reaches a specified value. The calculated stress is then plotted as a function of volume fraction. Preliminary results have been obtained for the initial volume fractions listed for a single form of the interparticle potential.

This simulation methodology provides a direct connection between the microscopic interparticle interaction potential, which is not directly measurable, and the macroscopic gel property compressive yield stress, which can be obtained from sedimentation experiments. By varying the interparticle potential and comparing the change in the compressive yield stress with experimental results, we may be able to infer the effect of changes in solution chemistry on the interparticle potential.

Sedimentation experiments were performed at varying solids loadings, pH, salt concentration, salt type, and applied pressure to determine the impact of chemical processing on the sediment densities that can be obtained during settle-decant processes. These results are also being compared with the models

being developed. Based on these results, it is possible to extract values for the gel point and the compressive yield stress of the sediment (which is a measure of how deformable and compressible the sediment is.) Once these parameters are known, sediment densities can be predicted for a wide range of processing geometries, including extrapolation from lab-scale tests to sedimentation in a one-million-gallon tank.

Sedimentation studies were conducted on 1.3 μm primary particles of gibbsite ($Al(OH)_3$) suspended in sodium nitrate solutions at different salt concentrations and pH values. At pH 4 and 0.01 M $NaNO_3$, the primary particles of gibbsite are dispersed. Because the particles are relatively large, they settle within a few days. The dispersed particles pack efficiently as they settle, yielding a sediment with a density of 50 vol% (the theoretical maximum solids loading for packed spheres is 63 vol%). Such a sediment would be ideal for maximizing the efficiency of solid-liquid separations. In contrast, the same gibbsite particles suspended in 0.1 M $NaNO_3$ at pH 4 yield a sediment density of only 4 vol% solids (consistent with 6-7 μm fractal agglomerates each containing around 30 primary particles). This means that the agglomerated sludge occupies over 10 times more space and contains 24 times the volume of non-removable interstitial liquids than the sediment formed from the dispersed sludge, having an adverse impact on the efficiency of solids-liquids separations. As salt concentrations are increased still farther, to 5 M, sediment densities increase to 5.1 vol%, suggesting that "short range" or "hydration" forces associated with adsorbed salt layers might be weakening the interactions between particles. High salt concentrations could also change sediment densities by changing agglomerate structures.

To investigate the role of adsorbed ions on interparticle interactions, systematic variations were made in the cations and anions present in dissolved salts to examine whether specific ions were more effective than others in weakening sediment structures. Gibbsite particles were suspended in aqueous solutions containing various salts ($NaNO_3$, NaCl, CsCl, LiCl, $Mg(NO_3)_2$, $CaCl_2$, and $BaCl_2$) as a function of pH (pH 4–14) and salt concentration (10^{-2} M–5 M) (Figure 3). All salts tested promote sediment compression at concentrations above 1 M. While anion (Cl^- for NO_3^-) and cation (Li^+ or Cs^+ for Na^+) substitutions have no apparent effect, salts of divalent cations (Mg^{2+}, Ca^{2+}, Ba^{2+}) all promote sediment compression. Most dramatic is the effect of $CaCl_2$, which yields sediments having solids loading of over 15 vol% (twice the particle density seen in $NaNO_3$ solutions). The effect is not merely an ionic strength effect, because $BaCl_2$:NaCl mixtures having the same ionic strength but different Ba:Na show greater compression as the Ba content is increased. The results suggest that heavily hydrated cations can act as "molecular ball bearings," allowing agglomerates to deform and compact. The results represent one example of how it may be possible to use chemical additives to control sludge behavior.

As is shown in Figure 4, pH has a significant impact on the sediment densities obtained during settle-decant operations. The lowest sediment density is observed near the isoelectric point of the particle with the sediment density increasing on either side of the isoelectric point. The isoelectric point of a particle is the pH value at which a reversal of the charge on the particle is observed electrophoretically. Zeta potential is the potential of the particle at the surface of shear and is related to the electrophoretic mobility of the particle; therefore, a measurement of the zeta potential of a slurry as a function of pH will provide insight into the impact of pH on the sediment densities that would be obtained during settle-decant operations.

Zeta potential measurement of colloidal dispersions at high salt concentrations is a new and unexplored scientific area with many reported departures from expected theory, including elimination of the isoelectric point and restabilization of colloidal particles with adsorbed surfactants.

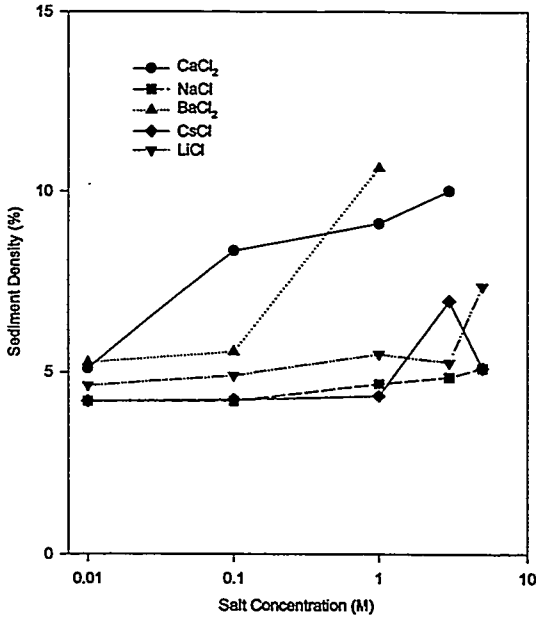

Figure 3. Impact of Salt Concentration and Type on Sediment Density

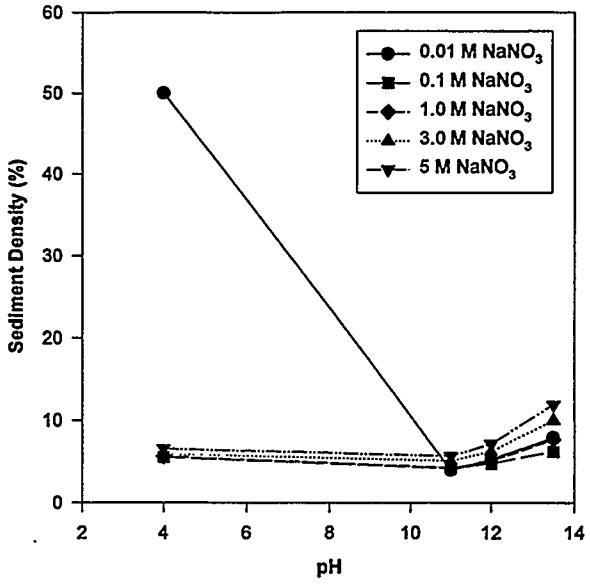

Figure 4. Impact of pH and Salt Content Salt on Sediment Density

Zeta potential is experimentally determined by measuring the motion of particles in solution under an applied electric field. Traditionally, these measurements are performed at low ionic concentrations due to experimental difficulties at high salt concentrations. The ZetaPals is designed to permit the measurement of zeta potential at high salt concentrations. These measurements are still problematic and require attention to establishing the proper experimental conditions (voltage, frequency, and sample count rate) and expertise combined with common sense in interpreting the results. The high conductivity of the concentrated salt solutions limit the voltage and current that can be applied to the solution while still imparting movement of the particles due to the applied electric field. If too high a voltage is applied, water is broken down to hydrogen and oxygen at the anode and cathode respectively. If too high a current is applied, the sample is heated and fluid-flow gradients are created that disturb the measurement of particle motion.

Over the last several months, the zeta potential of alumina (0.01 wt %) in water, $NaNO_3$, and LiCl has been measured. Zeta potential measurements of alumina in water as a function of pH compared well with values reported in the literature. Zeta potential measurements of alumina in $NaNO_3$, as a function of pH, at higher salt concentrations were then undertaken. Measurements were made at 0.1, 1.0, 2.0 and 3.0 M $NaNO_3$.

Results suggest that at the lower salt concentration (<2.0 M) double-layer theory is observed. This implies that the double layer has collapsed and that the system rapidly aggregates, forming a loose floc network of particles that exhibit a fast sedimentation time and a large sedimentation volume. Initial zeta potential measurements on alumina at 3.0 M $NaNO_3$ suggest that the particle dispersion is restabilized and that the isolelectic point (point of zero charge) is not present. The particles exhibit a positive zeta potential over the entire pH range investigated. This implies that the particles do not aggregate into a loose floc network and will exhibit a smaller sedimentation volume. This has been confirmed by previous sedimentation results.

The implication of this work is that the colloidal properties of tank waste under high salt conditions (greater than 2.0 M) may not behave as expected. If colloidal tank waste is in fact restabilized under high salt conditions, particle size may be smaller than expected, sedimentation time and volume may be different than expected, and filtration properties may be different.

Work performed on this project at the University of Washington is being directed at understanding how organic molecules called steric stabilizers function in the high salt regime of tank wastes. Once the factors controlling steric stabilization at high ionic strength are understood, it may be possible to manipulate sludge behavior with low concentrations of such organic additives. The polymers used as steric stabilizers were BAB block copolymers of polyethylene oxide B blocks and polypropylene oxide A blocks. The B blocks are the stabilizing moiety, and the A blocks anchor the polymer to the laytex surface. The core particle is a polystyrene latex with sulfate functional groups that allow the polymers to anchor to the core particle.

The impacts of polymer molecular weight, salt concentration, and salt type on steric stabilization were investigated. Increasing the molecular weight of the polymer causes an increase in steric stabilization. A small increase in molecular weight from an 11-monomer-length polymer to a 13-monomer-length polymer, showed dramatic increases in stabilization of the particle. This increase may be due to ion binding of the salt in the longer polymer that is not possible in the shorter polymer. Results obtained from the 13-monomer-length polymer indicate that order of stabilization in high ionic strength solutions is $BaCl_2 > NaNO_3$, LiCl, NaCl, KCl > KSCN, KNO_3. X-ray photoelectron spectroscopy (XPS) and RAMAN spectroscopy were performed on this same system in both KSCN and $BaCl_2$ to understand the processes that cause stabilization to occur in $BaCl_2$ and not in KSCN solutions. The results from these studies indicated that the Madelung shift (a constant representing the sum of the mutual potential coulombic attraction energy of all the ions in a lattice) correlates with the order in which the anions induce restabilization of these particles. It was also observed that $BaCl_2$ tends to weaken the ether oxygen bonds in the polyethylene oxide more than the KSCN, but the conformation of the polyethylene oxide is the same in both the KSCN and $BaCl_2$ solutions.

Planned Activities

Several key studies are in progress and will be completed before the end of FY 1999. These studies include a comparison of the actual waste rheology and sedimentation with the simple model systems, measurement of short-range forces, and modeling of agglomerate properties.

A report compiling the rheology data that has been collected on actual wastes and comparing these results with the data obtained by simple model systems will be prepared. This report will provide the basis for further improvements in rheological measurement of actual tank wastes.

Now that a simulation methodology has been established for predicting compressive yield stress based on gel structure and interparticle potentials, a parametric study will be performed to determine the effect of changes in the interparticle potential on the compressive yield stress behavior of a sediment. This information will be used to infer the effect of solution chemistry on the interparticle potential by comparing simulation results with experimentally determined compressive yield stress values.

Samples of the polystyrene latex particles with steric stabilizers attached have been submitted to NIST for surface force measurements. These measurements will be used to determine the magnitude of the short-range hydration forces in high ionic strength solutions. Samples have also been submitted for

nuclear magnetic resonance analysis to better understand ion binding in these model systems. Equilibrium dialysis, solvent extraction or specific ion electrode analysis will also be performed to quantitate the extent of ion binding.

Publication

Bunker BC, J Liu, DR Rector, GL Graff, PA Smith, PJ Bruinsma, L Song, XS Li, JD Virden, NG Colton, JR Philips, KD Keefer, and JM Tingey. 1999. "Fractal colloidal agglomerates in nuclear tank wastes: Impact on waste properties and processing" (submitted to *Radioactive Waste Management in Environmental Restoration*).

Presentations

Tingey JM, PR Bredt, and R Shekarriz. March 1999. "Rheology and settling behavior of Hanford tank wastes and the resulting process streams." Rheology in Mineral Industry II, Kahuku, Oahu, Hawaii.

Tingey JM, BC Bunker, GL Graff, KD Keefer, AS Lea, and DR Rector. November 1998. "Colloidal agglomerates in tank sludge and their impact on waste processing." Materials Research Society Fall Meeting, Boston.

Tingey JM, GL Graff, and DR Rector. March 1999. "Effect of colloidal aggregation on sedimentation and rheology in highly basic, high ionic strength salt solutions." Rheology in Mineral Industry II, Kahuku, Oahu, Hawaii.

Tingey JM, BC Bunker, GL Graff, KD Keefer, AS Lea, and DR Rector. November 1998. "Colloidal agglomerates in tank sludge and their impact on waste processing." Materials Research Society Fall Meeting, Boston.

Tingey JM, GL Graff, and DR Rector. March 1999. "Effect of colloidal aggregation on sedimentation and rheology in highly basic, high ionic strength salt solutions." Rheology in Mineral Industry II, Kahuku, Oahu, Hawaii.

Speciation, Dissolution, and Redox Reactions of Chromium Relevant to Pretreatment and Separation of High-Level Tank Wastes

(First Year of Funding: 1998)

Principal Investigators

Dhanpat Rai
Pacific Northwest National Laboratory
P.O. Box 999, MISN P7-50
Richland, WA 99352
(509) 373-5988 (phone)
(509) 372-1632 (fax)
dhan.rai@pnl.gov

Sue B. Clark
Washington State University
Department of Chemistry
Pullman, WA 99164
(509) 335-1411 (phone)
(509) 335-8867 (fax)
s_clark@mail.wsu.edu

Linfeng Rao
Lawrence Berkeley National Laboratory
MISN 70A-1150
One Cyclotron Road
Berkeley, CA 94720
(510) 486-5427 (phone)
(510) 486-5596 (fax)
lrao@lbl.gov

Nancy J. Hess
Pacific Northwest National Laboratory
P.O. Box 999, MISN P7-50
Richland, WA 99352
(509) 376-9808 (phone)
(509) 372-1632 (fax)
nancy.hess@pnl.gov

Contributors

Gregg J. Lumetta
Pacific Northwest National Laboratory
P.O. Box 999, MISN P7-25
Richland, WA 99352
(509) 376-6911 (phone)
(509) 372-3861 (fax)
nancy.hess@pnl.gov

Zhicheng Zhang (LBNL)

Research Objective

Pacific Northwest and Lawrence Berkeley National Laboratories, in collaboration with Washington State University, are developing fundamental data on the precipitation/dissolution reactions of Cr(III) compounds and the kinetics of oxidation of Cr(III) to Cr(VI) at room and elevated temperatures and under conditions relevant to high-level waste (HLW) processing. This integrated approach, which involves measuring solubility and oxidation rate constants and spectroscopic characterization of aqueous and solid species as a function of ionic strength, alkalinity, redox conditions, and temperature, will provide thermodynamic and kinetic data. These data are necessary to predict changes in chromium solubility and speciation in response to changes in pretreatment strategies or to develop cost-effective tank waste processing technologies that result from reducing the total amount of chromium in processed waste.

Problem Statement

Chromium, one of the problematic elements in tank sludges, is presently considered to be the most important constituent in defining the total volume of HLW glass to be produced from the Hanford tank wastes. This is because 1) it greatly complicates the vitrification process by forming separate phases in the molten glass, and 2) more importantly, current sludge washing processes are not effective in removing chromium. Inadequate removal of chromium from sludges could result in production of an unacceptably large volume of HLW glass.

The removal of chromium from tank sludges is complicated by factors including the complex chemistry of chromium, lack of fundamental data applicable to the HLW chemical systems (e.g., high heterogeneity, high ionic strength, high alkalinity, and the presence of inorganic and organic ligands), and the need to avoid processes that may adversely enhance the solubility of plutonium and other actinides. Significant gaps exist in the fundamental understanding of chromium chemistry in tank-like environments. Without such data/understanding, these strategies cannot be appropriately evaluated or optimized. The primary objective of the research being carried out under this project is to develop such information for HLW tank processing.

Research Progress

There are two ways of removing chromium from the wastes: solubilization of Cr (III) compounds, and the oxidation of Cr(III) to Cr(VI). Progress was made on both of these aspects. Specifically, studies were conducted 1) to develop appropriate analytical techniques for the analyses of oxidation states and concentrations of Cr in alkaline solutions, 2) measuring the solubilities of $Cr(OH)_3$(am) and Cr_2O_3 (c) in alkaline solutions, and 3) preliminary studies of the oxidation of Cr(III) to Cr(VI) by H_2O_2 in alkaline solutions.

Development of Analytical Techniques

A combination of inductively coupled plasma (ICP) or ICP-MS (mass spectrometry) and absorption spectrophotometry was found to be applicable to the analysis of chromium concentration and oxidation states. The absorption of Cr(VI) at 372 nm is appropriate for determining Cr(VI) in alkaline solutions with NaOH ranging from 0.01 to 8 M (lower detection limit ~1×10^{-5} M). This absorption band is also

useful for the determination of $[Cr]_{total}$ after the sample is treated with oxidants under alkaline conditions. ICP or ICP-MS analysis of $[Cr]_{total}$ was performed to double-check the results from absorption spectrophotometry.

X-ray absorption spectroscopy was evaluated for its use in determining oxidation states and the nature of the solid compounds. For the solubility results to be meaningful, it is important to be able to separate the solids from solutions. Solubility studies are needed and were conducted in NaOH solutions ranging in concentrations as high as 10 M. Although membrane filters with pore sizes as low as 0.0018 μm (e.g., Amicon Centriflo membrane cones) are available and have been extensively tested for their use in effectively separating chromium solids from solutions of relatively low alkalinity (Rai et al. 1987; Sass and Rai 1987), it is not known whether these filters can be used for separating solids from high alkalinity suspensions. Therefore, some limited studies were conducted to evaluate appropriate filters for use in the solubility studies involving high concentrations of NaOH.

Solubility of $Cr(OH)_3(am)$ in Concentrated NaOH Solutions

The $Cr(OH)_3(am)$ was prepared according to the method described by Rai et al. (1987) and was suspended in NaOH ranging in concentration from 0.01 to 10 M. Three different sets of experiments were conducted. It is expected that, in these relatively concentrated NaOH solutions, the $Cr(OH)_3(am)$ solids would precipitate and it should be possible to separate the solids from solutions by centrifugation. However, rather than relying only on centrifugation, we tested two different types of filters (0.2 μm nylon filters that are stable in high NaOH concentrations and syringe filters of 0.0018 μm pore size made of discs cut off from the Amicon Centriflo membrane cones). The observed chromium concentrations in solutions filtered through these two filters were similar (Figure 1), indicating that colloids of sizes >0.0018 μm do not exist in these suspensions, that either of these filters can be used to effectively separate solids from solutions, and that it should be possible to use these results in developing reliable thermodynamic data.

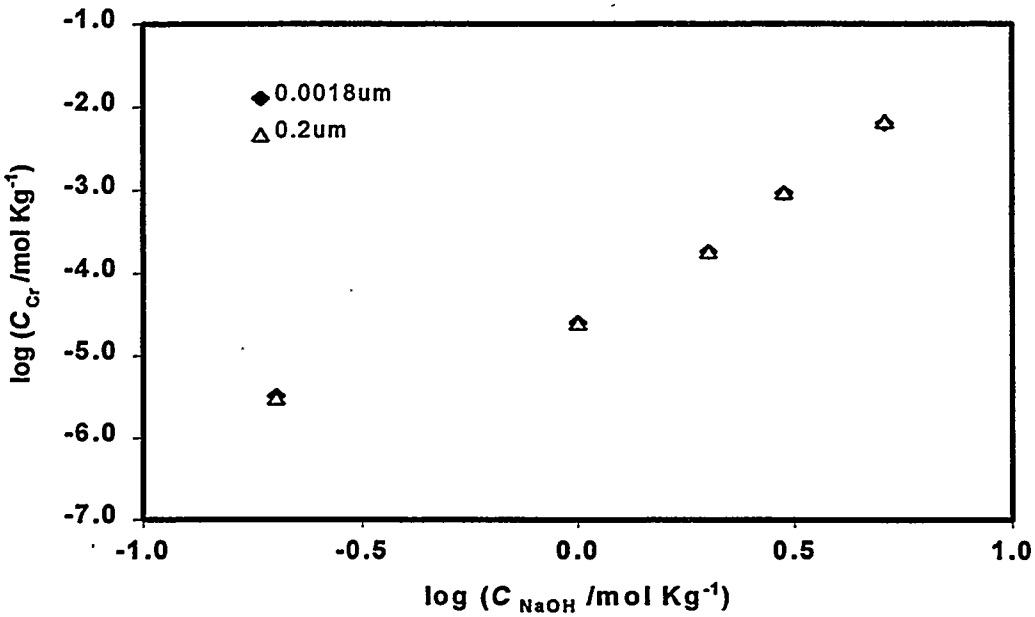

Figure 1. Comparison of Chromium Concentrations in 0.2 μm and 0.0018 μm Filtrates from $Cr(OH)_3(am)$ Suspensions in NaOH

The solubility of $Cr(OH)_3(am)$ increases dramatically with the increase in NaOH concentrations, especially between 1.0 and 10 M. The observed concentrations at different equilibration periods (16, 27, 45, and 73 days) and from different sets of samples are similar (Figure 2), indicating that the steady-state concentrations are reached rapidly and that the results are reproducible. These results, in conjunction with the data presented by Rai et al. (1987), show that the equilibrium in these systems is reached rapidly.

To develop reliable thermodynamic models based upon these data, it is important to ascertain the oxidation state of chromium in solution and solid phases and identify the aqueous and solid species. Oxidation states were determined by a combination of methods involving chromatographic and XAS techniques. X-ray diffraction (XRD) and x-ray absorption spectroscopy (XAS) were used to identify solid phases.

XRD analyses of the solid phases indicated that the solids are amorphous. Oxidation state analyses of most of the aqueous samples by chromatographic technique (Table 1) described by Olsen et al. (1994) and of limited samples by x-ray absorption near-edge structure (XANES) (Figure 3) showed that Cr(III) is the dominant oxidation state in the aqueous and solid phases. XAS experiments were conducted at Stanford Synchrotron Radiation Laboratory (beamline 4-1) to determine the local structure of trivalent chromium hydroxide solids and solutions. The sample descriptions are given in Table 2.

The extended x-ray absorption fine structure (EXAFS) was extracted by fitting a polynomial spline function through the post-edge region and normalizing the difference between this approximation to the solitary atom EXAFS and the actual data with the absorption decrease given by the McMaster tables. Fourier transforms were taken over photoelectron wave vector range from 2.7 to 12.8 $Å^{-1}$ for each sample. Nodes in EXAFS were selected as endpoints to the transform range and a two-sigma-wide Gaussian window was used to dampen the EXAFS oscillations at the transform range endpoints. The phase shift has not been removed from the Fourier transforms; as a result, the peaks in the transform moduli appear 0.2 to 0.5 Å shorter than the actual interatomic distance from the absorber to the shells of neighboring atoms.

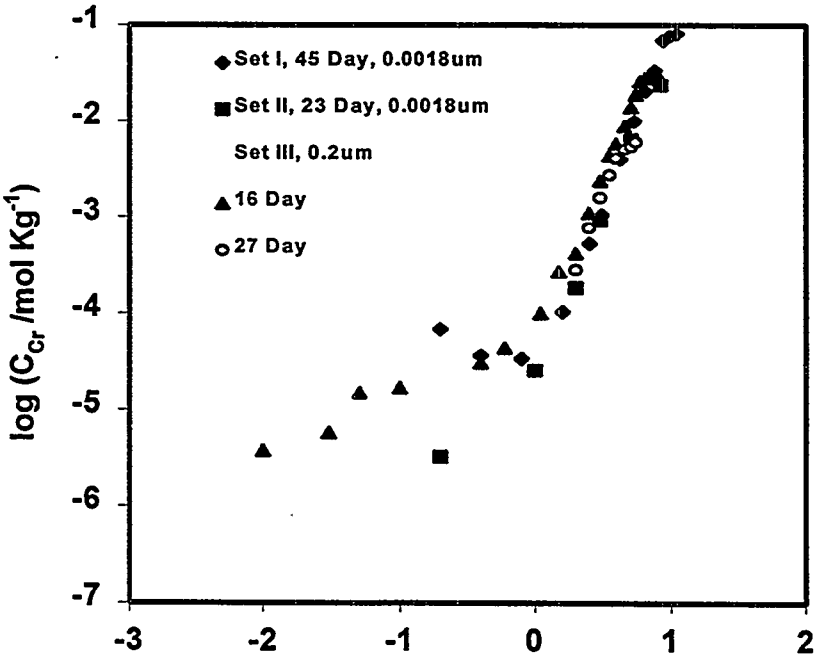

Figure 2. Chromium Concentrations in NaOH Solutions Contacting $Cr(OH)_3(am)$

Table 1. Chromium Oxidation State Analyses of 0-.0018 μm Filtrates from $Cr(OH)_3(am)$ Suspensions in NaOH

C NaOH/mol Kg^{-1}	% Cr(VI)
0.20	2
0.40	9
0.80	18
1.60	16
2.53	8
3.09	10
4.22	2
5.34	2
6.47	1
7.60	<1
8.72	<1
9.85	<1
10.97	<1

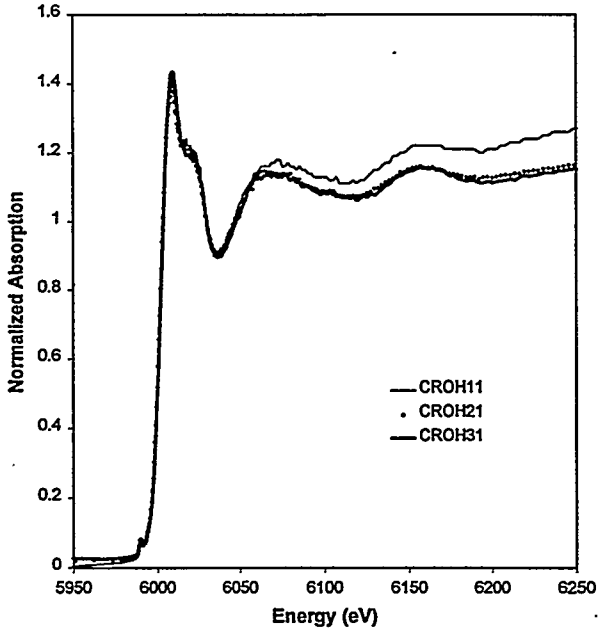

Figure 3. Chromium K-Edge XANES of Solid Phases in Equilibrium with 1.0 m, 2.0, and 3.0 m NaOH

The background-subtracted, normalized XANES spectra for all the chromium samples display a profile that is consistent with the Cr(III) oxidation state, as shown in Figure 3. The XANES profile of Cr(VI) oxidation state is characterized by a sharp pre-edge feature approximately 15 eV lower in energy than the main absorption edge. This pre-edge feature is not observed in any of the XANES profiles for the chromium samples, indicating that little, if any, Cr(VI) is present in these samples.

Table 2. Chromium Hydroxide Samples

Sample Name	Form	Description	Analysis
99CROH1-1	Solid	0.2 m NaOH	XANES/EXAFS
99CROH1-2	Solution	0.2 m NaOH	XANES
99CROH2-1	Solid	1.0 m NaOH	XANES/EXAFS
99CROH2-2	Solution	1.0 m NaOH	XANES
99CROH3-1	Solid	2.0 m NaOH	XANES/EXAFS
99CROH3-2	Solution	2.0 m NaOH	XANES
99CROH4-1	Solid	3.0 m NaOH	XANES/EXAFS
99CROH4-2	Solution	3.0 m NaOH	XANES
99CROH5-1	Solid	5.0 m NaOH	XANES/EXAFS
99CROH5-2	Solution	5.0 m NaOH	XANES/EXAFS
99CROH6-1	Solid	8.0 m NaOH	XANES/EXAFS
99CROH6-2	Solution	8.0 m NaOH	XANES/EXAFS

An attempt was made to collect EXAFS data on all the solid and solution samples; however, the concentration of chromium in some of the less basic solutions was too low for satisfactory EXAFS data. A full analysis of the EXAFS is in progress, but the initial analysis indicates that there is a change in the local structure of the solid phase in equilibrium with the 3.0 m and 5.0 m NaOH solutions. In addition, the chromium concentration is sufficiently high in the 5.0 and 8.0 m NaOH solutions to compare the local structure of the solution with the solid phase in equilibrium with these two samples, and they seem to be identical. The Fourier transforms of the solid phase in equilibrium with 1.0 m and 5.0 m NaOH are compared in Figure 4. There is a significant increase in the transform peak at 3.0 that may reflect a change in the structure of the solid phase.

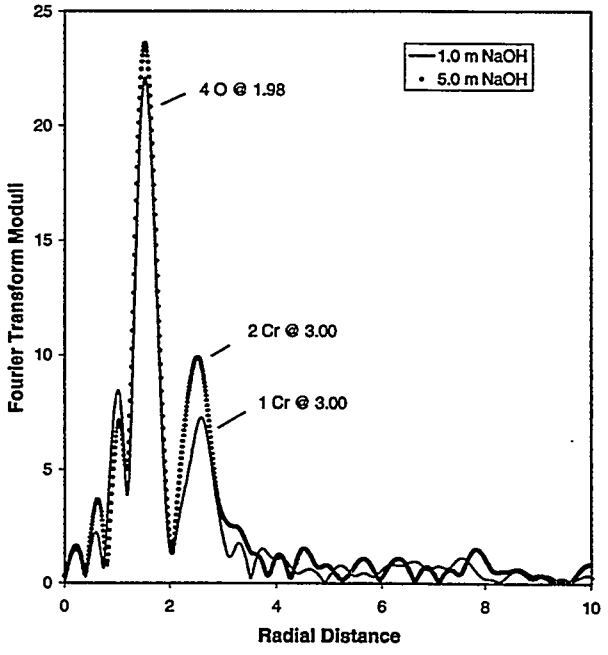

Figure 4. Fourier Transform of the Solid Phase in Equilibrium with 1.0 m and 5.0 m NaOH

Solubility of Cr_2O_3(c)

Studies on crystalline Cr_2O_3 solubility in concentrated NaOH solutions ranging in concentrations from 0.01 M to 8 M were initiated to check the effect of crystallinity of the initial solids on the solubility and the precipitation/dissolution kinetics of Cr_2O_3(c). The experimental procedures used for this study were identical to those used for $Cr(OH)_3$(am) with the exception that commercially purchased crystalline Cr_2O_3 was used as the initial solid. The samples have been shaken for 12 days and have not yet been analyzed. However, by observation it is obvious that the Cr concentrations in these solutions are much lower than those using $Cr(OH)_3$(am) as the starting material, suggesting that the solubility is strongly dependent on the crystallinity of the Cr compound and/or that the dissolution rate is much lower for crystalline Cr_2O_3.

The Effect of Hydrogen Peroxide on the Oxidation of Cr(III) to Cr(VI)

Only preliminary tests have been conducted so far. Several qualitative observations can be made:

- In alkaline solutions, upon addition of excess amounts of H_2O_2, the color of the Cr(III) solution changed completely from greenish blue to yellow in a few minutes, suggesting the aqueous homogeneous redox reaction between Cr(III) and peroxide is fairly rapid.

- In the presence of suspensions of $Cr(OH)_3$(am) in NaOH solutions, the $Cr(OH)_3$(am) solid gradually dissolved upon the addition of H_2O_2. When there was sufficient amount of H_2O_2, the color of the solution was found to change from greenish blue to yellow and the $Cr(OH)_3$(am) solid was eventually dissolved completely. This observation suggests that the oxidative dissolution of $Cr(OH)_3$(am) in the presence of peroxide is also fast: It takes about 10 minutes to complete the oxidative dissolution for the particular sample tested: about 230 mg $Cr(OH)_3$(am) solid in 1.5 M NaOH, H_2O_2 in excess with respect to chromium.

- For comparison, oxidative dissolution with a suspension of crystalline Cr_2O_3 in 1 M NaOH was also tested. No change in the color of the solution (very pale due to low concentration of chromium) was observed after addition of a large amount of H_2O_2. There was no identifiable change in the amount of Cr_2O_3 in the suspension, either.

Planned Activities

- Conduct studies to determine the effect of $NaNO_3$ (one of the important electrolytes present in tank wastes) on the solubility of $Cr(OH)_3$(am) in systems involving constant NaOH and variable concentrations of $NaNO_3$, and constant $NaNO_3$ and variable concentrations of NaOH.

- Develop thermodynamic model for the system Na^+-Cr^{3+}-OH^- - NO_3^- - H_2O to describe behavior of Cr(III) under conditions relevant to tank wastes.

- Continue the redox studies in homogeneous and heterogeneous systems with hydrogen peroxide, with the objective of obtaining quantitative kinetic data.

- Continue to follow the chromium concentrations in the suspensions of crystalline Cr_2O_3. Because it is difficult to design an "oversaturation" experiment for this solid, efforts will be made to raise the temperature of the $Cr(OH)_3(am)$ suspension (e.g., to 90°C) and monitor any possible changes in the solubility and in the crystallinity of the solid phase.

- Initiate studies to determine the oxidation kinetics of Cr(III) to Cr(VI) in the presence of several oxidants (e.g., O_2, peroxynitrite) and as a function of temperature so that effective oxidative dissolution treatments can be designed for tank sludge washing.

References

Rai D, BM Sass, and DA Moore. 1987. "Chromium (III) hydrolysis constants and solubility of chromium (III) hydroxide." *Inorganic Chemistry,* 26:345-349.

Sass BM, and D Rai. 1987. "Solubility of amorphous chromium (III) – iron(III) hydroxide solid solutions." *Inorganic Chemistry,* 26:2228-2232.

Olsen KB, J Wang, R Setiadji, and J Lu. 1994. "Field screening of chromium, cadmium, zinc, copper, and lead in sediments by stripping analysis." *Environmental Science and Technology,* 28:2074-2079.

Presentations

Rai D, L Rao, AR Felmy, and NJ Hess. August 16-22, 1999. "Measuring and modeling of the solubility of Cr(III) compounds in concentrated NaOH and $NaOH/NaNO_3$ solutions: Applications to pretreatment of high-level waste sludges." To be presented at the 1999 Fall National ACS Meeting, New Orleans.

New Silicotitanate Waste Forms: Development and Characterization

(First Year of Funding: 1997)

Principal Investigator

Dr. Mari Lou Balmer
Pacific Northwest National Laboratory
P.O. Box 999, MSIN K8-93
Battelle Blvd., Richland, WA 99352
(509) 376-2006 (phone)
lou.balmer@pnl.gov

Co-Investigators

Dr. Tina Nenoff
Sandia National Laboratories
P.O. Box 5800
Albuquerque, NM 87185-0709
(505) 844-0340 (phone)
tmnenof@sandia.gov

Prof. Alexandra Navrotsky
Department of Chemical Engineering and Material Science
University of California-Davis, Davis, CA 95616
(916) 752-3292 (phone)
anavrotsky@ucdavis.edu

Dr. Yali Su
Pacific Northwest National Laboratory
P.O. Box 999, MSIN K8-93
Battelle Blvd., Richland, WA 99352
(509) 376-5290 (phone)
ya.su@pnl.gov

Contributors and Collaborators

Bob Roth (NIST)
Hongwu Xu (UC Davis)
May Nyman (SNL)
Eric Bitten (PNNL)
Dave McCready (PNNL)
Bruce Bunker (SNL)

Research Objective

The objective of this program is to identify new waste forms and disposal strategies specific to crystalline silicotitanate (CST) secondary waste that is generated from cesium and strontium ion exchange processes. In particular, in situ heat treatment of CSTs to produce an alternative waste form is being examined. Waste forms that are developed in this work will offer an alternative to current disposal plans, which call for recombining the separated cesium, strontium-loaded CST into the high-activity waste (HAW) streams, then dissolving it in borosilicate glass. The goals of the program are to reduce the costs associated with CST waste disposal, minimize the risk of contamination to the environment during CST processing, and provide DOE with technical alternatives for CST disposal. Because there is uncertainty in repository availability and in waste acceptance criteria, it is likely that cesium and strontium-loaded ion exchangers will require short-term storage at Hanford or that new scenarios for long-term storage or disposal of nuclides with relatively short half-lives (such as ^{137}Cs and ^{90}Sr) will arise. Research activities in this program will generate information on the durabilities and stabilities of thermally consolidated CSTs so that the potential of these options as viable storage or disposal scenarios can be evaluated. The technical objectives of the proposed work are to fully characterize the phase relationships, structures, and thermodynamic and kinetic stabilities of crystalline silicotitanate waste forms and to establish a sound technical basis for understanding key waste form properties, such as melting temperatures and aqueous durability, based on an in-depth understanding of waste form structures and thermochemistry.

Research Statement

Plans are in place to retrieve, separate, and immobilize radioactive waste contained in 177 underground storage tanks at the Hanford Site. Likewise, nuclear wastes at other DOE sites across the country must be immobilized in a stable waste form for storage in underground repositories. A viable waste form must be chemically durable under environmental storage conditions (aqueous environments are of primary concern) and thermally stable under repository conditions over a geologic time scale. In addition, an adequate waste form should be capable of incorporating specific waste feeds to form a stable glass or ceramic material with a minimum of waste dilution (to minimize waste volumes) and be easy to process under remote handling conditions. Relatively low processing temperatures are desirable, as are simple heat-treatment cycles.

Borosilicate glass has been chosen as the baseline host for immobilization of HAW present at the Hanford Site. However, CST, the most promising candidate for removal of cesium and strontium from tank wastes, has been identified as a risk to the borosilicate vitrification process. TiO_2 in the CST promotes crystallization and immiscible phase separation, and affects the redox state and solubility of uranium in glass (Ewest et al. 1987; Galakhov et al. 1988; Bickford et al. 1990; Plodinec 1980). Because of this, a TiO_2 limit of 1 wt% is set for borosilicate waste glass at the Savannah River Defense Waste Processing Facility (DWPF) (Plodinec 1980). If these high levels of waste dilution are required to stabilize CST waste, the volume of expensive high-activity borosilicate waste glass produced for subsequent storage will be substantially increased. Dissolution of the CST in borosilicate glass (as opposed to direct thermal conversion) necessitates removal and transfer of the CST from the column, mixing with glass frit, and melting. Each of these steps significantly increases the risk of contamination to workers and/or the environment. The volume of HAW can be minimized and the process can be simplified by converting the separated, compositionally homogenous loaded exchanger into an alternate waste form rather than recombining it with the HAW for dissolution in glass.

Cesium-loaded silicotitanate ion exchangers contain the basic ingredients that can form a ceramic or glass at high temperature. The premise of this work is that for CST ion exchange waste, waste forms can be tailored to specific waste feeds rather than attempting to tailor waste feeds for accommodation by a single waste form. Direct in situ, thermal conversion of the CST will consolidate and immobilize the loaded ion exchange particulate, minimize handling risks, and remove water and hydroxyl groups thus eliminating radiolytic hydrogen generation during storage.

The research strategy for developing an alternate waste form for CSTs is based on an understanding of ceramic and glass structures and phase stabilities. The key components of the research include

- determining stable and metastable phases that form from heat treatment of the CST and development of phase diagrams for the component systems
- characterizing the structures of ceramic and glass waste form candidates
- developing structure-property relationships that will provide predictive capabilities regarding key performance parameters, including aqueous leach resistance, melt temperatures, melt viscosities, and ease of crystallization for select waste forms
- determining the enthalpies and free energies of formation of key compounds by high-temperature oxide melt solution calorimetry.

Research Progress

Work during the first year of the program showed that thermally converted CSTs have very high aqueous durablity (Su et al. 1998). These thermally converted waste forms are several orders of magnitude more durable than borosilicate glass. For example, standard engineering assessment (EA) borosilicate glass shows a seven-day leached concentration of alkali of 13.3 g/L (there is no cesium in this standard, only sodium) (Ferrara et al. 1997). In comparison, IE-911 heat-treated to 900°C has a seven-day cesium concentration of 0.008 g/L, or in the worst case for the 700°C heat-treatment, the seven-day cesium concentration is 0.175 g/L. Heat treatments of 900 and 500°C yielded the most durable ceramics; however, all residual water and hydroxy groups are not removed until 800°C. Therefore, 900°C is the optimum heat treatment because the possibility of hydrogen formation from radiolytic decay of physisorbed or chemisorbed water is eliminated.

This early, positive result fulfilled the milestone of defining the chemical durability of thermally converted waste forms. This year we have focused on defining the phase selection, especially the cesium-containing phases and thermodynamic stabilities of compounds related to the ion-exchanged CST and the thermally converted oxides.

Phase Selection of Thermally Converted CST

Phase stability and crystal chemistry studies for compositions related to the exchanger are vital to predicting long- and short-term performance of waste forms. In the first year of the program, several phases in the heat-treated waste form were identified; however, the cesium-containing phases were not obvious from x-ray diffraction (XRD) and nuclear magnetic resonance (NMR) studies. This year, transmission electron microscopy (TEM) and further XRD studies were performed. Figure 1 shows a micrograph of a thin section of 12 wt% cesium-exchanged IE-911 heat treated to 900°C. Energy dispersive spectroscopy on individual grains revealed that several oxide phases with unique compositions exist in the sample.

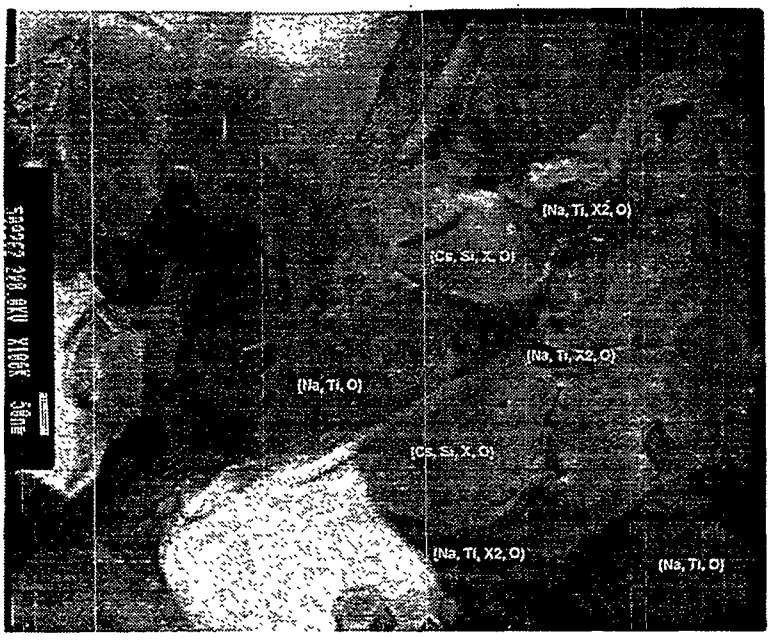

Figure 1. TEM Micrograph of a Thin Section of IE-911 that Was Treated in NaOH, Exchanged with 12 wt% Cesium, then Heat-Treated to 900°C. Energy dispersive spectroscopy of individual grains revealed the approximate compositions of the phases in this proposed waste form.

Among these were Cs, X1, Si oxide, Na, Ti oxide, Na, Ti, X2 oxide, and very minor Na, Cs, Ti, Si, X1 oxide, where X1 and X2 are proprietary components of the ion exchanger. Of these four phases, positive identification by XRD had already been achieved for the sodium titanate phase, $Na_2Ti_6O_{13}$. This structure is a layered structure. While there are known isomorphs for potassium and rubidium substitutions on this structure, cesium substitution had not been documented. The structure of the pure cesium analog, $Cs_2\ Ti_6O_{13}$, has a different structure than the sodium, potassium, or rubidium forms. To determine whether small amounts of cesium could reside in the $Na_2\ Ti_6O_{13}$ structure, a solid substitution series of $(Na, Cs)_2\ Ti_6O_{13}$ was synthesized and the lattice parameters were measured by XRD. This study surprisingly revealed that there is no measurable substitution of cesium for sodium on the $Na_2\ Ti_6O_{13}$ lattice, eliminating the possibility that small amounts of cesium could reside in this phase in heat-treated IE-911.

TEM revealed that the majority of the cesium is contained in a Cs, X1, Si oxide. This phase could not be synthesized by solid-state reaction; however, it was successfully synthesized using sol gel and hydrothermal reactions. The stoichiometry of the phase is $Cs_2X1Si_3O_9$. While a similar phase is reported in the literature, the crystal structure of this compound is unknown and the powder XRD data are incomplete. We attempted to grow single crystals of this compound; however, due to the refractory nature of the proprietary component, no suitable crystals have been synthesized to date. A search of the powder diffraction database revealed a compound that is a structural isomorph to $Cs_2X1Si_3O_9$. From this it was determined that the new cesium compound is hexagonal with a lattice parameter of a=7.23 Å and c=10.271 Å (space group P63/m). Efforts are under way to refine the structure to obtain the exact atomic positions. The simulated crystal structure based on the atomic positions of the isomorph and the lattice parameters of $Cs_2X1Si_3O_9$ is shown in Figure 2. It consists of silica tetrahedra and X1 octahedra that form three-membered and six-membered rings. The largest free aperture of the rings is approximately 2.2x2.6 Å, which is smaller than a cesium atom (~3.5Å). Therefore, the cesium in this phase will be immobile. Removal of cesium from the structure will

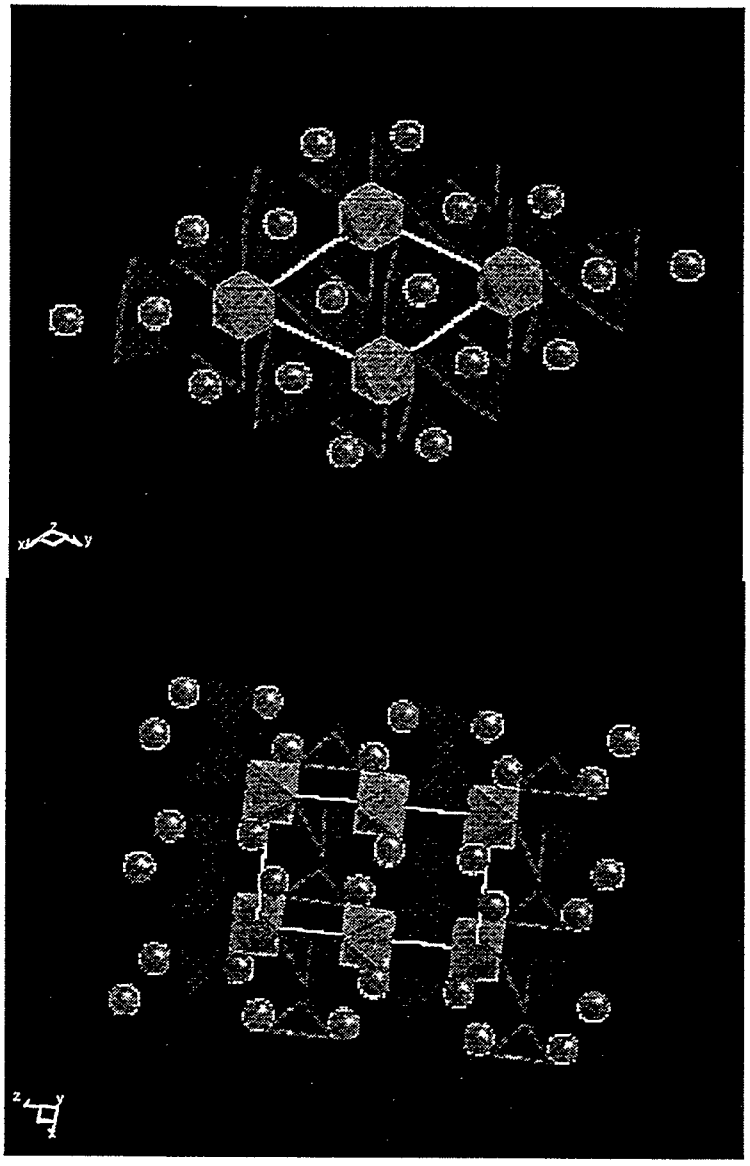

Figure 2. View of $Cs_2X1Si_3O_9$ Structure Down the [001] and [010] Directions. This is the major cesium-containing phase in thermally converted (900°C) IE-911.

require the cleavage of the strong, covalent Si-O and X1-O bonds. This structural feature in part explains the high resistance to leaching of cesium in thermally converted IE-911 that is exposed to aqueous solutions.

A second new phase discovered in TEM (Na, Ti, X2, oxide) has a structure similar to $NaX2O_3$. To determine the extent of titanium substitution in the mixed phase, a series of compounds with up to 20% titanium substituted for X2 were synthesized using a sol gel technique. A systematic shift of the lattice parameter as a function of titanium substitution could clearly be observed. Comparison of the heat-treated IE-911 with the synthesized compounds revealed that the phase in IE-911 has 15% titanium substitution on the lattice. The structure of the new compound is related to a perovskite; however the distribution of the cations in the structure is unknown.

With the discovery of the two new oxide phases in heat-treated CST, the phase identification is nearly complete. Figure 3 shows the XRD pattern of cesium-exchanged heat-treated IE-911 compared with a simulated x-ray pattern, which is a combination of the patterns of the three phases identified in this program, $Na_2Ti_6O_{13}$, $Cs_2X1Si_3O_9$, and $Na(Ti, X2)O_3$. It can be seen that all of the major peaks have been identified. Several very small peaks that appear in the thermally converted IE-911 pattern are not present in the simulated pattern. The intensity of these peaks decreases significantly with longer heat treatment at 900°C or with heat treatment to 1000°C, indicating that this phase is metastable. Some of these minor peaks may also correspond to the minor Cs, Na, Si, Ti, X1 oxide identified with TEM. Work will continue to determine the structure of this minor phase.

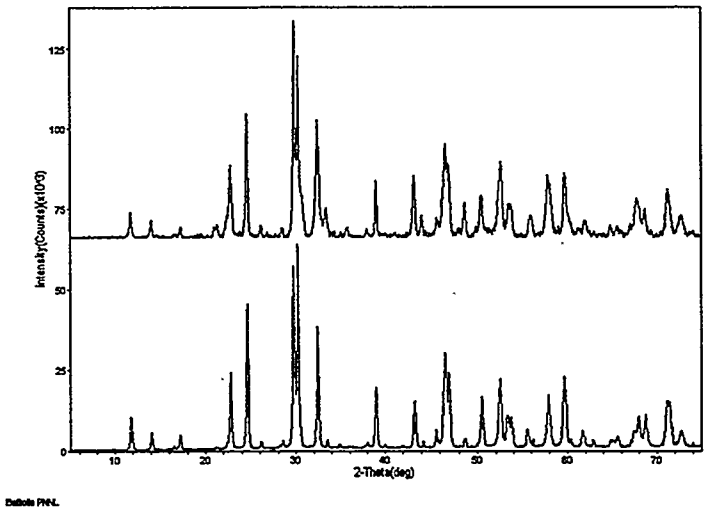

Figure 3. Comparison of the Experimental XRD Pattern of Mixed-Phase Cesium-Exchanged IE-911 Heat-Treated to 900°C (upper pattern) with a Simulated Pattern that Is a Compilation of the X-Ray Patterns from Synthesized Compounds $Na_2Ti_6O_{13}$, $Cs_2X1Si_3O_9$, and $Na(Ti, X2)O_3$ (lower pattern). The excellent match between the two patterns suggests that these compounds represent the major phases in the waste form.

Hydrothermal Synthesis of Metastable Phases

Cs_2O-TiO_2-SiO_2 Phases

Researchers at Sandia National Laboratory are studying the metastable phase development in the component systems that represent the cesium-loaded ion exchanger. This work complements the stable phase development studies at PNNL and allows for a complete understanding of the phase development from the metastable ion exchanger to the stable ceramic waste form. Hydrothermal Cs_2O-TiO_2-SiO_2 ternary phase searches have produced two novel phases, which we have designated SNL-A and SNL-B. The stability regions of these phases as a function of Cs_2O:TiO_2:SiO_2 precursor ratio (and pH) are plotted on the ternary diagram in Figure 4 for five days at 170°C (left) and 120°C (right). These experiments show a distinct relationship between SNL-B and SNL-A. At 170°C, SNL-B is formed in a mixture with SNL-A. With increased time at temperature, only SNL-A is formed. For example, at 120°C for 5–20 days, only SNL-B is formed, while at 120°C for 28 days, only SNL-A is formed. Also shown on the ternary plot is the stability region for TiO_2 and pharmacosiderite (a known microporous Cs_2O-TiO_2-SiO_2 ion exchanger).

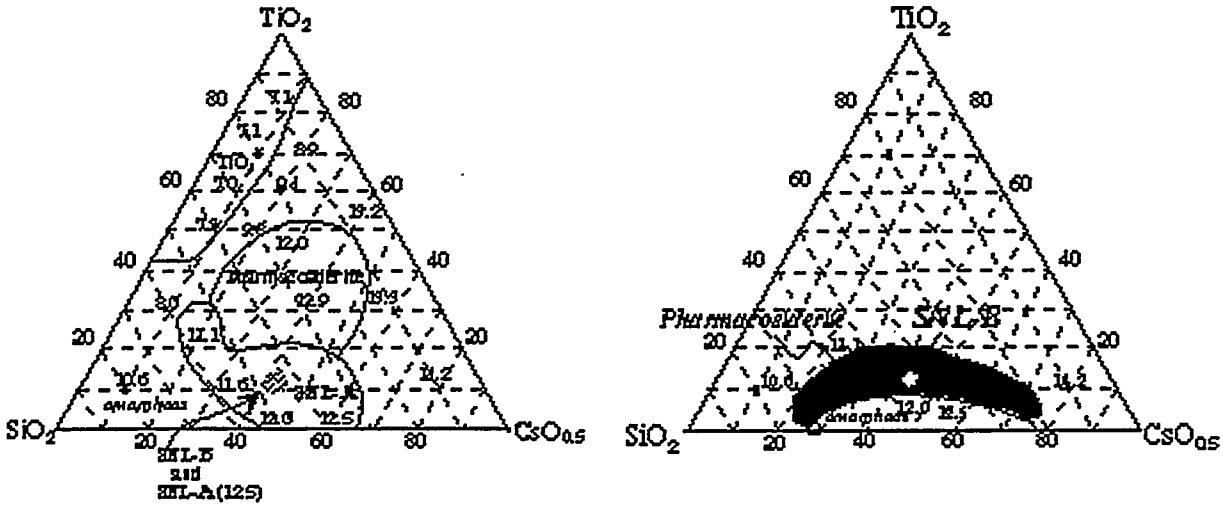

Figure 4. Stability of Hydrothermally Synthesized Cs_2O-TiO_2-SiO_2 Ternary Phases at 170°C (left) and 120°C (right)

SNL-B is a microporous ion exchanger with a chemical formula $CsTiSi_4O_{10.5}{\cdot}xH_2O$ and SNL-A is a condensed phase with a formula $Cs_2TiSi_4O_{11}$. Solid state ^{133}Cs and ^{29}Si MAS-NMR (magic angle spinning nuclear magnetic resonance) and CP (cross polarization) MAS NMR of SNL-A and SNL-B reveal that both phases are structurally complex with multiple silicon and cesium coordination sites. The chemical shifts of these sites are compiled in Table 1. All silicon atoms in both phases are in tetrahedral coordination sites (the "x" of Q^x gives the number of silicon atoms in the second coordination sphere and 4-x is the number of titanium atoms in the second coordination sphere). The CP-MAS NMR experiments show there is internal water in SNL-B and none in SNL-A.

Table 1. MAS-NMR Characterization of SNL-A and SNL-B

Experiment	Chemical Shifts (ppm)	Comments
SNL-A		
^{29}Si MAS NMR	-88 (Q^1) -96, -97 (Q^2) -100, -102 (Q^3) -107, -110 (Q^4)	Chemical shifts typical of silicotitanates
^{29}Si CP-MAS NMR	None	Indicative of no hydrogen associated with silicon in the crystal lattice (no OH^- or H_2O)
^{133}Cs MAS NMR	+65, +86	
SNL-B		
^{29}Si MAS NMR	-87 (Q^0) -97 (Q^1 - Q^2) -103, -105 (Q^4)	Chemical shifts typical of silicotitanates
^{29}Si CP-MAS NMR	-97 (Q^3)	The silicon associated with this chemical shift is near H_2O
^{133}Cs MAS NMR	+8, +23, +57	

This is confirmed by thermogravimetry experiments. The structural complexity of SNL-A, which is suggested by the multiple NMR chemical shifts (7 for silicon, 2 for cesium), is also seen by TEM analysis. These preliminary structural analyses reveal that SNL-A has a unit cell of low symmetry (either monoclinic or triclinic).

In situ TEM-monitored electron irradiation studies of SNL-A and SNL-B were also carried out (in collaboration with Dr. Rod Ewing at the University of Michigan) to determine the stability of these new phases in radioactive environments. The irradiation-induced transformation of microporous crystalline SNL-B to amorphous material is observed by fading Bragg-diffraction spots in the electron diffraction pattern. The irradiation dose needed for amorphization of SNL-B is inversely dependent on temperature. This corresponds to heat accelerated cesium and/or water loss, and finally a thermally induced phase change at 500°C (which is also observed by differential thermal analysis). This amorphization behavior is typical of other zeolite materials studied by Dr. Ewing. The condensed phase SNL-A, on the other hand, is very irradiation-resistant. It does not undergo any irradiation damage with very high dose rates. Ongoing and future work in characterization of SNL-A and SNL-B includes crystal growth experiments for structural characterization of these novel phases.

New Sr-Selective Microporous Ion Exchanger

In the course of Na_2O-TiO_2 hydrothermal phase searches, researchers at SNL discovered a class of Na_2O-TiO_2-X (X = transition metals) novel ion exchanger phases. One phase of this class, designated SNL-C, demonstrates extreme selectivity for divalent cations, especially strontium. The selectivity for strontium is demonstrated in a plot of K_d (mL/g) vs. concentration of a competitive cation (Na) in solution (Figure 5).

Table 2 gives distribution coefficients of a variety of RCRA metals, monovalent alkali metal, and divalent alkaline earth metals for SNL-C. This data shows the selectivity of SNL-C for divalent cations. Heating strontium-loaded SNL-C results in alteration to a perovskite, a very durable phase that has waste form applications. Structural characterization of SNL-C is under way.

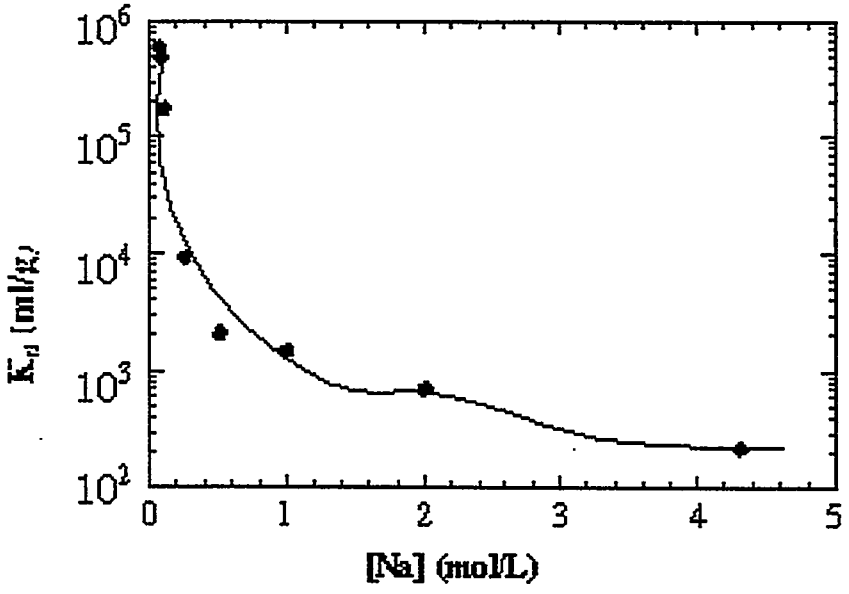

Figure 5. Selectivity of Strontium (50 ppm) as a Function of $NaNO_3$ Concentration in Solution

Table 2. Distribution Coefficients for Metals on SNL-C

Cation	Radius in pm (6-coordinate)	K_d (ml/g)[a]
La^{3+}	117	>199,800[b]
Sr^{2+}	132	>99,800[c]
Pb^{2+}	133	>99,800[c]
Ba^{2+}	149	>499,800[d]
Zn^{2+}	88	>99,800[c]
Cd^{2+}	109	>99,800[c]
Ni^{2+}	83	6,467
Cr^{2+}	94	3,371
Co^{2+}	89	1,208
Li^{+}	90	276
Mg^{2+}	86	467
Cd^{2+}	109	>99,800[c]
Cs^{+}	181	13
K^{+}	152	22

(a) Calculated for detection limit of metal.
(b) 0.05 ppm.
(c) 0.1 ppm.
(d) 0.02 ppm.

Energetics of Crystalline Cs_2O-Na_2O-SiO_2-TiO_2-H_2O Phases

Using hydrothermal methods, two series of microporous silicotitanates were synthesized at SNL: 1) $(Na_{1-x}Cs_x)_3Ti_4Si_2O_{13}(OH)\cdot xH_2O$ (x = 4-5) phases with a cubic structure of $P\bar{4}3m$ (analogues of the mineral pharmacosiderite), and 2) $(Na_xCs_{1-x})_3Ti_4Si_3O_{13}(OH)\cdot xH_2O$ (x = 4-5) phases with a tetragonal structure of $P4_2/mcm$. The enthalpies of drop solution in molten $2PbO\cdot B_2O_3$ at 974K were measured at UC Davis by high-temperature reaction calorimetry, and the enthalpies of formation have been determined from constituent oxides using appropriate thermochemical cycles. The enthalpies of formation for the cubic phases become more exothermic as Cs/(Na+Cs) increases (Figure 6a), whereas those for the tetragonal phases become less exothermic (Figure 6b). Therefore, the cesium uptake in the cubic phases is thermodynamically driven, while that in the tetragonal phases is kinetically driven. In addition, the cubic phases appear to be more stable than the corresponding tetragonal phases with the same Cs/Na ratio. We attribute these disparities in the energetic behavior for the two series to their differences in both local bonding configuration and degree of hydration.

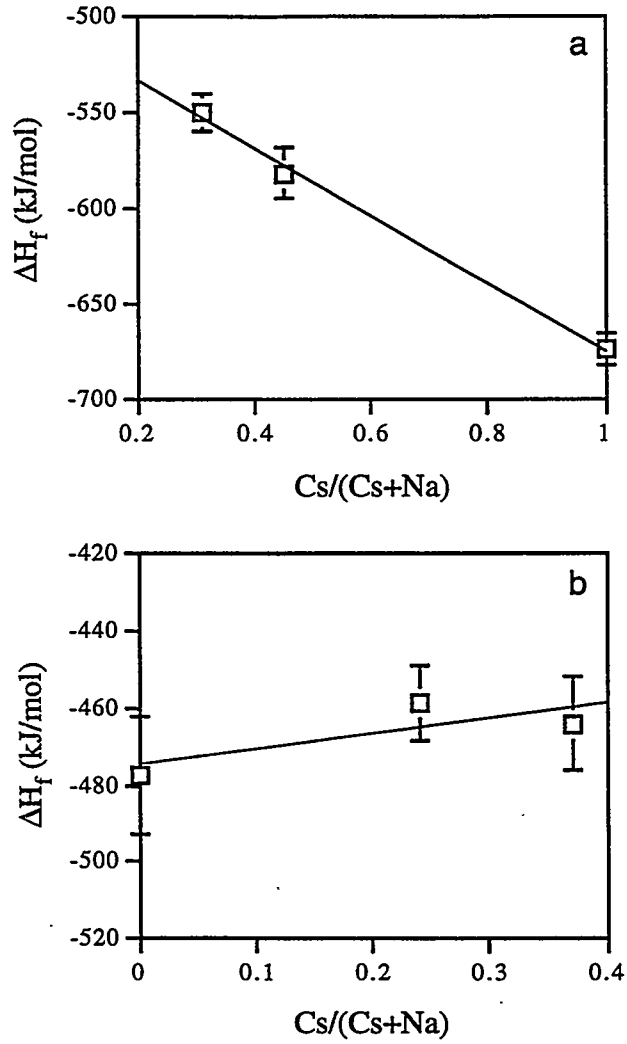

Figure 6. Enthalpies of Formation from Oxides of (a) the Cubic Phases and (b) the Tetragonal Phases as a Function of Composition

Summary

In summary, in the second year of the program, efforts focused on determining the stable and metastable phase development in a heat-treated, cesium-exchanged crystalline silicotitanate ion exchanger (IE-911). Transmission electron microscopy, XRD, and synthesis studies have revealed that the major phases in the ion exchanger are $Na_2Ti_6O_{13}$, $Cs_2X1Si_3O_9$, and $Na(Ti, X2)O_3$. The network structure of the cesium-containing phases precludes facile migration of the cesium ion, resulting in extremely high aqueous durability. Metastable phase-development studies have revealed three new phases. One of these shows extremely good selectivity for divalent ions even in high concentrations of sodium. In addition, the thermodynamic stabilities of metastable and stable compounds have been determined by solution drop calorimetry. This combined information on phase selection as a function of composition, chemical durablity, and thermodynamic stability can be used to determine processing windows and to predict long- and short-term stability of thermally converted CST ion exchangers.

Planned Activities

Future work will concentrate on determining the structures and refining the atomic positions of the two new compounds found in the heat-treated waste form and of the new compounds synthesized hydrothermally. The heat of formation of these compounds and related compounds in the representative ternary and quaternary systems will be measured. In addition, the radiation stability of thermally converted waste forms as well as of the single-phase cesium-containing constituent of the waste form ($Cs_2X1Si_3O_9$) will be measured.

References

Bickford DF, A Applewhite-Ramsey, CM Jantzen, and KG Brown. 1990. "Control of radioactive waste glass melters: I, Preliminary general limits at Savannah River." *J. Am. Cer. Soc.* 73 [10] 2896-2902.

Ewest E and H Wiese. 1987. "High level liquid waste vitrification with the Pamela Plant in Belgium." IAEA-CN-48/177, pp. 269-280, Vienna, Austria.

Ferrara DM, MK Andrews, JR Harbour, TL Fellinger, DT Herman, KM Marshall, and PJ Workman. Sept. 30, 1997. *Vitrification of ion exchange material.* WSRC-TR-97-00320, Westinghouse Savannah River Corporation, Aikin, South Carolina.

Galakhov FY, VT Vavilonova, VI Aver'yanov, and TV Slyshkina. 1988. "An experimental determination of the region of liquid-liquid phase separation in the Li_2O-Al_2O_3-TiO_2-SiO_2 system." Translated from *Fiz. khim. Stekla* 14(1):38-46.

Plodinec MJ. 1980. "Development of glass compositions for immobilization of Savannah River Plant waste." In *Scientific Bases for Nuclear Waste Management*, CJM Northrup Jr, ed. Vol. 2, pp. 223-229.

Su Y, ML Balmer, L Wang, B Bunker, M Nyman, TM Nenoff, and A Navrotsky. 1998. "Evaluation of themally converted silicotitanate waste forms II." *Proc. Mat. Res. Soc. Fall Meeting.*

Publications

Nyman M, TM Nenoff, ML Balmer, Y Su, A Navrotsky, H Xu, BX Gu, LM Wang, and RC Ewing. 1999. "Synthesis and characterization of Cs2TiSi4O11: A novel durable phase with potential waste form applications." *Chemistry of Materials* (in press).

Nyman M, TM Nenoff, ML Balmer, Y Su, A Navrotsky, H Xu, BX Gu, LM Wang, and RC Ewing. 1999. "Synthesis and characterization of a new microporous Cs-Ti-Si-O-H2O ion exchanger." *Chemistry of Materials* (in press).

Nyman MD, TM Nenoff, Y Su, ML Balmer, A Navrotsky, and H Xu. 1998. "CSTs: Stability and use as alternative waste forms." *Proc. Mat. Res. Soc. Fall Meeting.*

Su Y, ML Balmer, L Wang, B Bunker, TM Nenoff, M Nyman, and A Navrotsky. 1998. "Evaluation of thermally converted silicotitanate waste forms II." *Proc. Mat. Res. Soc.*

Presentations

Balmer ML, Y Su, E Bitten, H Xu, A Navrotsky, T Nenoff, and M Nyman. April 25-28, 1999. "Ceramic wasteforms from Cs-loaded crystalline silicotitanates." 101th Annual Meeting of the American Ceramic Society, Indianapolis.

Nyman MD and TM Nenoff. June 1999. "Selective inorganic crystalline ion exchange materials for cesium and strontium." United Engineering Foundation and AIChE.

Nyman MD, TM Nenoff, ML Balmer, Y Su, A Navrotsky, and H Xu. 1998. "CSTs: Stability and use as alternative waste forms." Mat. Res. Soc. Fall Meeting.

Nyman MD, TM Nenoff, ML Balmer, Y Su, A Navrotsky, and H Xu. 1999. "Hydrothermal synthesis of Cs-Ti-Si-O phases as alternative waste forms for Cs-loaded CST ion exchangers." 1999 Spring ACS meeting, Anaheim, California.

Su Y, ML Balmer, L Wang, B Bunker, M Nyman, TM Nenoff, and A Navrotsky. 1998. "Evaluation of thermally converted silicotitanate waste forms II." Mat. Res. Soc. Fall Meeting.

Xu H, A Navrotsky, TM Nenoff, MD Nyman, ML Balmer, and Y Su. April 25-28, 1999. "Thermochemistry of crystalline silicotitanate phases in the Cs_2O-Na_2O-SiO_2-TiO_2-H_2O system." 101th Annual Meeting of the Amer. Ceramic Soc., Indianapolis.

Development of Fundamental Data on Chemical Speciation and Solubility for Strontium and Americium in High-Level Waste: Predictive Modeling of Phase Partitioning During Tank Processing

(First Year of Funding: 1996)

Principal Investigators

Dr. Andrew R. Felmy
Pacific Northwest National Laboratory
P.O. Box 999, MSIN K9-77
Richland, WA 99352
(509) 376-4079 (phone)
(509) 376-3650 (fax)
ar.felmy@pnl.gov

Dr. Gregory Choppin
The Florida State University
Department of Chemistry, B-164
Tallahassee, FL 32606-3006
(904) 644-3875 (phone)
(904) 644-8281 (fax)
Choppin@chem.fsu.edu

Dr. David A. Dixon
Pacific Northwest National Laboratory
P.O. Box 999, MSIN K1-83
Richland, WA 99352
(509) 372-4999 (phone)
(509) 375-6631 (fax)
da.dixon@pnl.gov

Dr. James A. Campbell
Pacific Northwest National Laboratory
P.O. Box 999, MSIN P8-08
Richland, WA 99352
(509) 376-0899 (phone)
(509) 376-2329 (fax)
ja.campbell@pnl.gov

Research Objective

In this research program, Pacific Northwest National Laboratory (PNNL) and Florida State University (FSU) are investigating the speciation of strontium and americium/curium in the presence of selected organic chelating agents (ethylenediaminetetraacetic acid (EDTA), N-(2-hydroxyethyl) 'ethylenediaminetriacetic acid (HEDTA), nitrilotriacetic acid (NTA), and iminodiacetic acid (IDA)) over ranges of hydroxide, carbonate, ionic strength, and competing metal ion concentrations present in high-level waste tanks. The project is composed of integrated research tasks that approach the problem of chemical speciation using macroscopic thermodynamic measurements of metal-ligand competition reactions, molecular modeling studies to identify structures or complexes of unusual stability, and mass spectometry measurements of complex charge/mass ratio that can be applied to mixed metal-chelate systems. This fundamental information is then used to develop thermodynamic models, which allow the prediction of changes in chemical speciation and solubility that can occur in response to changes in tank processing conditions. In this way, we can develop new approaches that address fundamental problems in aqueous speciation and at the same time provide useful and practical information needed for tank processing.

Problem Statement

Current strategies for reducing the total volume of radioactive tank waste requiring disposal at Hanford and other DOE sites call for the development of methods to selectively dissolve and remove nonradioactive elements such as aluminum, phosphorus, and chromium while retaining or precipitating the radioactive elements, including strontium and the actinide elements, in the tank sludges. This partitioning between solids and precipitates is fundamentally dependent upon the chemical speciation of the elements present in the tank processing solutions. Of particular importance is separation of the radioactive and hazardous actinide elements and fission products from the sludges and supernatants, particularly from supernatants containing high concentrations of strong chelating agents, which can act to solubilize the actinides and fission products as well as interfere with subsequent metal ion extraction processes. Specifically, the fundamental understanding of chemical speciation reactions gained from these studies is needed to propose methodologies for removal of strontium and americium/curium from organic chelates present in high-level tank waste, via competition, displacement or other reactions, without the need for the development of costly and potentially hazardous organic destruction technologies.

Research Progress and Implications

The following section gives a brief description of the progress to date of the PNNL studies. The research at FSU, which is currently focused on the speciation of curium and americium under similar hydroxide and carbonate conditions, will be reported by Professor Choppin in a separate report. This section summarizes the research progress in three main areas: strontium speciation, trivalent actinide speciation, and supporting studies. The supporting studies are focused on solution calorimetry, isopiestic measurements, and applications of capillary electrophoresis-mass spectrometry.

Studies on Strontium Speciation

To unravel the speciation reactions of strontium in complex tank waste requires studies of speciation reactions in the presence and absence of chelators. Specifically, speciation reactions in four chemical systems—Na-Sr-OH-H_2O, Na-Sr-CO_3-H_2O, Na- Ca-OH-H_2O, Na-Ca-CO_3-H_2O, and the mixed system Na-Sr-Ca-OH-CO_3-H_2O with and without added chelators—were studied. The systems including californium as well as strontium were studied to begin to address the issue of metal ion competition and displacement of strontium from the chelates. Californium was chosen for these initial studies because it is present in large amounts in tanks waste; Ca^{2+} has approximately two orders of magnitude higher affinity for the organic chelators than Sr^{2+}.

These studies were largely completed in FY 1998, and the results have been published in the open literature and presented at national society meetings and conferences (Felmy and Mason 1998; Felmy et al. 1998; Felmy et al. 1997a,b,c). These studies resulted in the identification of the species present in these solutions and the development of the necessary thermodynamic data to predict the species' concentrations. The implications of these findings are described below.

Implications of Strontium Studies

The results for strontium have some interesting implications as regards processing basic/ carbonate solutions such as those in high-level tank waste. First, given the expected range in chelate concentrations present in tank waste and the fact that carbonate is present in significant concentration in all tanks, it is likely that the chemical speciation of strontium will be almost certainly unaffected by the presence of IDA and probably also unaffected by the NTA as well. Only HEDTA and EDTA appear to be present at high enough concentrations and to form strong enough complexes to significantly impact the speciation of strontium in tank waste. Such results are important in limiting the number of chemical species that need to be considered in chemical modeling of tank processing strategies. In addition, competition with other metal ions present in such solutions, in this case californium, can effectively displace strontium from the strong chelating agents HEDTA and EDTA, depending upon the concentration of strontium and the competing metal ions. This result indicates that metal ion displacement represents an acceptable alternative to costly and hazardous organic destruction technologies in reducing the impacts of organic chelates in tank processing, especially given the fact that the chelators represent only a small fraction of the total organic carbon in tank waste.

Trivalent Actinide Studies

Considerable progress has also been made in the study of the effects of hydrolysis on the displacement of trivalent actinides and actinide analogs from the organic chelates: EDTA, HEDTA, NTA, and IDA. Studies on the solubility of europium (a trivalent actinide analog) compounds [i.e., $Eu(OH)_3(c)$] have been completed as a function of base concentration in the presence of four organic chelates: EDTA, HEDTA, NTA, and IDA. $Eu(OH)_3(c)$ was chosen for study because of its very low solubility under high base concentration. These studies have shown that high base concentration can displace Eu(III) from all of the organic chelates studied. The effective NaOH concentration for the displacement reaction is dependent on the nature of the specific chelate studied and the chelate concentration.

As an example, the solubility data for $Eu(OH)_3(c)$ in the presence of different concentrations of EDTA (Figure 1) show that at NaOH concentrations >3 M all of the Eu(III) is removed from EDTA solutions (e.g., [EDTA] ≤0.01 M). At higher base concentration, the solubility of $Eu(OH)_3(c)$ increases, but this is as a result of the formation of soluble hydrolysis species (e.g., $Eu(OH)_4^-$, ...), not metal-chelate complexes. Similar results have been found for the other chelates (see Figures 2 and 3 for HEDTA and NTA, respectively). These data are also being used to develop accurate

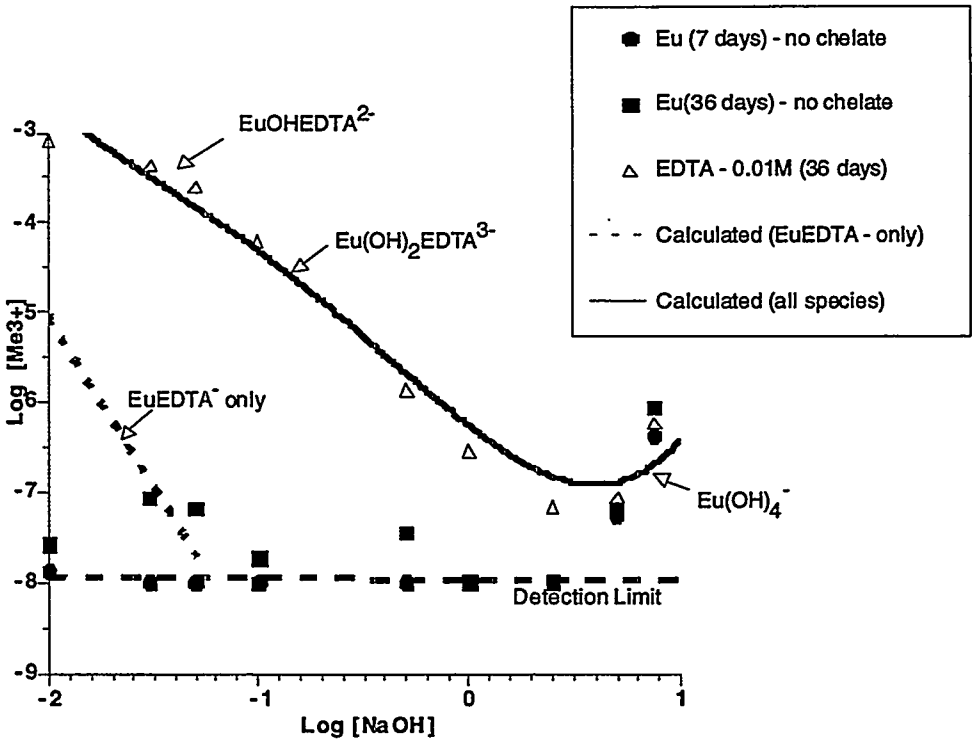

Figure 1. Solubility of $Eu(OH)_3(c)$ in NaOH in the Presence and Absence of Added EDTA

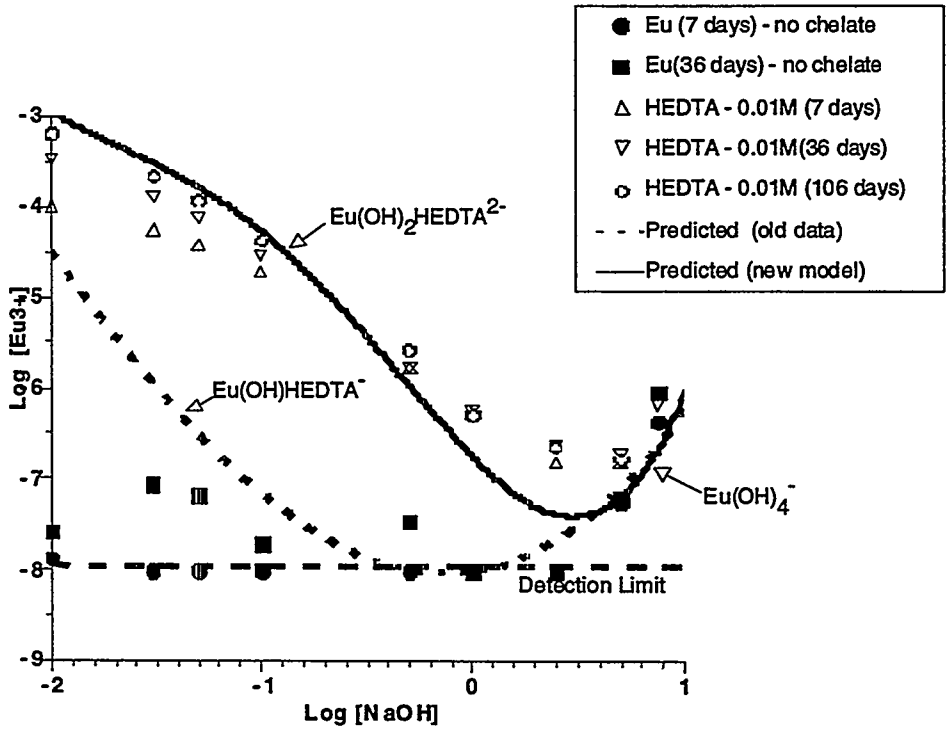

Figure 2. Solubility of $Eu(OH)_3(c)$ in NaOH in the Presence and Absence of Added HEDTA

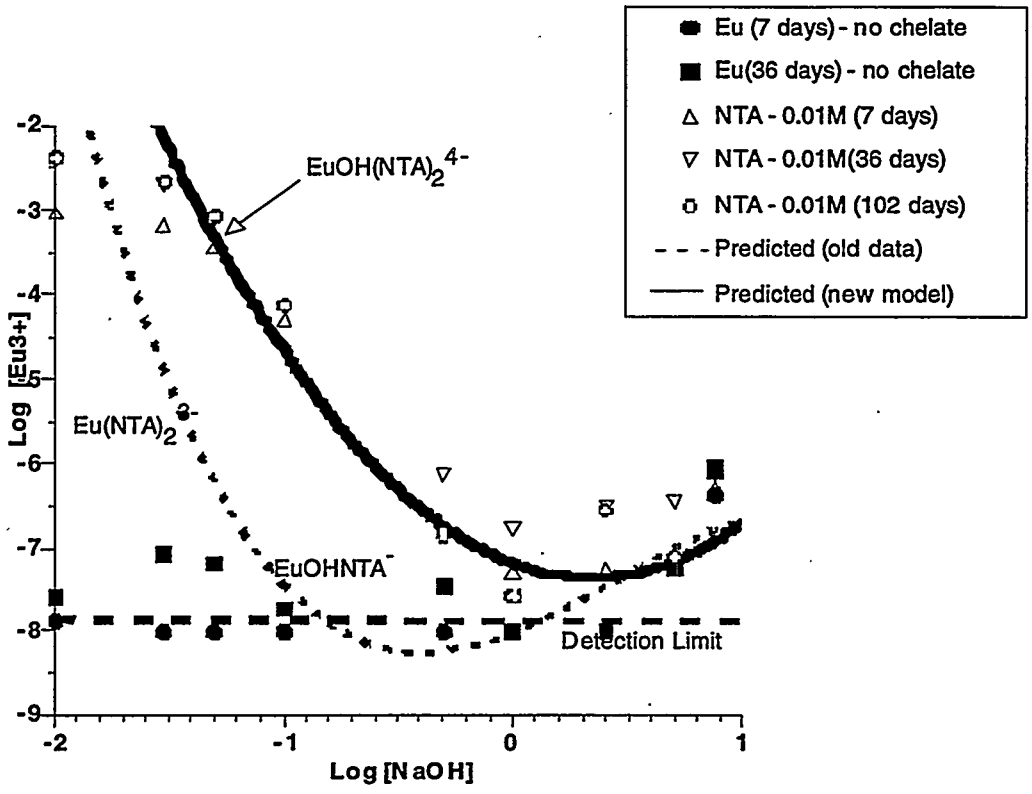

Figure 3. Solubility of $Eu(OH)_3(c)$ in NaOH in the Presence and Absence of Added NTA

thermodynamic models for trivalent actinide species under high base conditions. Such data are important because current thermodynamic models to predict actinide speciation and solubility in these chemical systems underpredict the solubilities by two to four orders of magnitude. As an example of this effect, the model calculations using literature data for the only aqueous complex previously proposed, i.e., $EuEDTA^-$, are several orders of magnitude lower than the experimental results. By using a combination of thermodynamic measurements, molecular modeling simulations, and measurements of fluorescence life times, it is apparent that this discrepancy is the result of the neglect of mixed metal-hydroxide-chelate complexes that form in these highly basic solutions. Using all of these combined data, we have developed a chemical equilibrium model that accurately represents all of the experimental measurements in this chemical system (see Figures 1–3). The calculated stability constants also correlate well with the gas phase binding energies developed from the molecular simulations. These results have been presented at society meetings (Felmy et al. 1999; Felmy and Mason 1998) and in the manuscripts that are in preparation or have been submitted (Felmy et al. 1999; Felmy and Rai 1999).

These models are currently being used by the Hanford private contractor, British Nuclear Fuels, Ltd., in the development of processing strategies for selected tank wastes.

Supporting Studies

In addition to the extensive experimental and computational modeling studies performed under the strontium and trivalent actinide studies outlined above, significant progress has also been made in the areas of solution-phase calorimetry, mass spectrometry, and isopiestic measurements. All three of these areas of study directly enhance our studies of solution-phase speciation.

Solution Phase Calorimetry

Calorimetric measurements are used both to extend the temperature range of validity of our thermodynamic models and to provide useful information on solution-phase reaction kinetics. Studies of reaction kinetics are possible because the heat of reaction is a sensitive parameter that can be directly studied as a function of time. This information is not only useful for developing temperature-dependent thermodynamics models for the organic chelate reactions but also provides useful kinetic information on the exchange of potentially kinetically inhibited species.

Enthalpy of dilution measurements have been conducted on Na_4EDTA-NaOH-H_2O mixtures to allow the activity coefficient expressions to be extrapolated over the range of temperatures (25–100°C) needed to develop tank waste processing strategies.

Isopiestic Measurements

Isopiestic studies of electrolyte solutions is a well-established technique for obtaining direct information on the activity of water, which, in turn, through the use of the Gibbs-Duhem relation yields direct information of the solution-phase activity coefficients of the species involved. The method is particularly useful at high electrolyte concentrations such as those relevant to this research. Therefore, as part of this study, extensive isopiestic measurements have been made of osmotic coefficients in the mixed NaOH-Na_4EDTA systems. These data are being used to develop better thermodynamic models (i.e., Pitzer ion-interaction coefficients) for Na^+-$EDTA^{4-}$ and OH^--$EDTA^{4-}$ interactions.

The results of the calorimetric and isopiestic measurements have also been presented and published in a number of sources (Oakes et al. 1999; Sterner et al. 1998, 1997a,b; Oakes and Felmy 1998, 1997).

Mass Spectrometry

As part of this study, solution speciation reactions are also planned using capillary electrophoresis-mass spectrometry (CE-MS). CE-MS offers the potential of determining the mass/charge ratio of complexes that may be present in mixed metal-chelate systems where unraveling complex spectral signatures will be difficult or impossible. Our initial results with CE-MS have proven to be effective in identifying metal-EDTA complexes in negative ion mode from mixed electrolyte solutions. This represents the first known combination of CE separation with mass spectrometry detection of metal-organic complexes under negative ion conditions that we are aware of. These results have been presented (Peterson et al. 1998).

Planned Activities

Studies at PNNL have been largely completed and published on the competitive effects of hydrolysis and carbonate complexation of strontium with the organic chelates at 25°C. This effort has resulted in several journal articles and scientific presentations (see below). Studies have also been largely completed with trivalent actinide analogs [using $Eu(OH)_3(c)$] in the presence of high base concentration. Manuscripts have either been submitted or are in preparation. Significant progress has also been made in the areas of solution calorimetry, mass spectrometry, and isopiestic studies. Plans for FY 1999 call for completing and publishing the results to date.

Support for studies in outer years will be required to 1) extend the trivalent actinide model to higher temperatures (>25°C), 2) unravel the speciation of tetravalent actinides (especially Pu(IV)),

and 3) include other important competing metal ions, such as nickel, manganese, and lead in the thermodynamic models. Such research is needed, important, and is being used at the Hanford Site.

Publications and Presentations

Felmy AR, DA Dixon, and MJ Mason. 1999. "The aqueous complexation of Eu(III) with organic chelating agents at high base concentration: Correlation of thermodynamic and molecular models." *J. Solution Chem.* (in preparation).

Felmy AR and D Rai. 1999. "Application of Pitzer's equations for modeling the aqueous thermodynamics of actinide species: A review." Invited paper for the special memorial edition of the *Journal of Solution Chemistry* in honor of Professor Kenneth Pitzer (in press).

Felmy AR and MJ Mason. 1998. "The displacement of strontium from organic chelates by hydroxide, carbonate, and calcium in concentrated electrolytes." *J. Solution Chemistry*, 27(5)435-454.

Felmy AR, DA Dixon, JR Rustad, MJ Mason, and LM Onishi. 1998. "The hydrolysis and carbonate complexation of strontium and calcium in aqueous electrolytes: Use of molecular modeling calculations in the development of aqueous thermodynamic models." *J. Chem. Thermodynamics* 30, 1103-1120.

Oakes CS, SM Sterner, and AR Felmy. 1999. "Thermodynamic properties of aqueous calcium nitrate [$Ca(NO_3)_2$] to 373K including new enthalpy of dilution data." *J. Chem. Thermodynamics* (in press).

Sterner SM, AR Felmy, CS Oakes, and KS Pitzer. 1998. "Correlation of thermodynamic data for aqueous electrolyte solutions to very high ionic strength using INSIGHT: Vapor saturated water activity in the system $CaCl_2$-H_2O to 250°C and solid saturation." *International Journal of Thermophysics*, 19(3)761-770.

Abstracts and Presentations

Felmy AR, DA Dixon, and MJ Mason. March 21-25, 1999. "Aqueous complexation of Eu(III) with organic chelating agents at high base concentration: Molecular and thermodynamic modeling results." 217th ACS National Meeting, Anaheim California.

Felmy AR and MJ Mason. August 9-14, 1998. "The aqueous complexation of Eu(III) with organic chelating agents at high base and high ionic strengths: Metal-chelate displacement induced by hydrolysis and precipitation reactions." 53rd Calorimetry Conference, Midland, Michigan.

Felmy AR, GR Choppin, DA Dixon, and JA Campbell. July 27-30, 1998. "Chemical speciation of strontium, americium, and curium in high-level waste: Predictive modeling of phase partitioning during tank processing." Two presentations and one poster. Presentations to the Hanford Tanks Site Technology Coordination Group (STCG) on November 10, 1998, and to PNNL staff on January 21, 1998. Poster presentation at the EMSP Principal Investigators Workshop, Chicago.

Felmy AR, DA Dixon, JA Campbell, and MJ Mason. September 7-11, 1997a. "The effects of OH, CO_3, and Ca on the displacement of strontium from organic chelates: Implications for waste processing." 214th ACS National Meeting, Las Vegas.

Felmy AR, DA Dixon, and MJ Mason. August 3-8, 1997b. "The complexation of alkaline earth cations by organic chelates at high ionic strength: Competitive effects of hydrolysis and carbonate complextion." 52nd Calorimetry Conference, Asilomar, California.

Felmy AR, DA Dixon, JR Rustad, MJ Mason, and LM Onishi. August 3-8, 1997c. "The use of molecular modeling calculations to improve the development of thermodynamic models: Hydrolysis, carbonate, and EDTA complexation of alkaline earth cations." 52nd Calorimetry Conference, Asilomar, California.

Oakes CS and AR Felmy. August 9-14, 1998. "Thermodynamics of [Na_4EDTA+NaOH]{aq}, including new isopiestic and enthalpy of dilution measurements." 53rd Calorimetry Conference, Midland, Michigan.

Oakes CS and AR Felmy. August 3-8, 1997. "Thermodynamics of [Na_4EDTA+NaOH]{aq}, including new isopiestic measurements, to 373K, 0.1MPa, and stoichiometric ionic strengths of 18·9mol·kg^{-1}." 52nd Calorimetry Conference, Asilomar, California.

Petersen CE, JA Campbell, AR Felmy, KL Wahl, and JW Finch. May 31-June 4, 1998. "Analysis of metal-organic complexes using CE/MS." 46th American Society of Mass Spectrometry Meeting, Orlando, Florida.

Sterner SM, AR Felmy, and KS Pitzer. June 22-27, 1997a. "Correlation of thermodynamic data for aqueous electrolyte solutions to very high ionic strength using INSIGHT: Vapor saturated water activity in the system $CaCl_2$-H_2O to 250°C and solid saturation." Thirteenth Symposium on Thermophysical Properties, Boulder, Colorado.

Sterner SM, AR Felmy, CS Oakes, JM Simonson, and K Pitzer. August 3-8, 1997b. "Thermodynamics of aqueous $CaCl_2$ to 250°C, 400 bars and solid saturation." 52nd Calorimetry Conference, Asilomar, California.

Actinide-Specific Interfacial Chemistry of Monolayer Coated Mesoporous Ceramics

(First Year of Funding: FY 1999)

Principal Investigator

Dr. Glen E. Fryxell
Pacific Northwest National Laboratory
P.O. Box 999, MSIN K2-44
Richland, WA 99352
(509) 375-3856 (phone)
(509) 375-2186 (fax)
ge_fryxell@pnl.gov

Co-Principal Investigator

Dr. Thomas S. Zemanian
Pacific Northwest National Laboratory
P.O. Box 999, MSIN P7-07
Richland, WA 99352
(509) 373-0344 (phone)
(509) 376-3002 (fax)
ts_zemanian@pnl.gov

PNNL Contributors

Dr. James A Franz
Dr. Yuehe Lin
Dr. Jerome C. Birnbaum
Dr. Meiling Gong
Mr. Kentin Alford (AWU Masters student)

External Collaborators

Professor K. N. Raymond
Department of Chemistry
University of California at Berkeley
Berkeley, CA 94720-1760
(510) 642-7219 (phone)
(510) 486-6145 (fax)
Raymond@socrates.berkeley.edu

Dr. Ken Kemner
Argonne National Laboratory
Argonne, IL 60439
(630) 252-1163 (phone)
Ken_Kemner@Qmgate.anl.gov

Research Objective

The objective of this program is to design, synthesize, and evaluate high-efficiency, high-capacity sorbent materials capable of selectively sequestering actinides from complex aqueous mixtures. One of the central goals of this project is to understand the fundamental interfacial science required to develop novel mesoporous materials coated with organized monolayers of rationally designed ligands, custom-tailored for binding specific actinide cations. This capability addresses waste management by separation of actinides, a central concern of high-level waste (HLW) management at several DOE sites.

PNNL has developed self-assembled monolayers on mesoporous supports (SAMMS) as a superior method of mercury and heavy metal sequestration. SAMMS has proven to be orders of magnitude faster and more effective than existing mercury-scavenging methods. This project builds on the SAMMS concept and extends the interfacial chemistry of monolayer-coated mesoporous materials to study the requirements of selective binding of actinides. The need exists in the management of DOE's HLW to be able to selectively and completely remove the actinides so that HLW volume can be minimized and the nonradioactive components can be segregated and disposed of as low-level waste (LLW). In addition, the short-term risk assessment for tank closure requires a complete and accurate accounting of actinide speciation. These needs dictate the development of selective and efficient separation of actinides from complex waste streams so as to minimize HLW volume, reduce waste management costs, and enhance long-term stability of the HLW form.

Research Statement

A large fraction of the DOE tank waste is made up of saltcake and liquid wastes containing nitrates and hydroxides as well as an assortment of actinides. If the radionuclides can be removed, this material can be segregated and disposed of as LLW, significantly reducing remediation costs. Selective separation of the actinide fraction thus forms a critical need for this waste management strategy.

There is also a need to determine actinide speciation within the tanks. This can be done either via direct separation or by concentration of low-level actinides and subsequent separation. Isolation of individual actinides such as americium is a key parameter in the risk assessment necessary for tank closure. There are currently no methods available to distinguish or separate americium from plutonium at extremely low concentrations. This is essential information for the short-term risk assessment for HLW tank closure.

The SAMMS concept allows for significant freedom in the design and synthesis of tailored materials for actinide separation. The mesoporous ceramic synthesis is quite general and can be used to prepare a variety of high surface area ceramic oxide supports that are stable in different environments (acidic, corrosive, oxidizing, etc.). The high surface area of the mesoporous support (ca. 1000 m^2/g) coupled with the high population density of binding groups creates a high loading capacity in the final SAMMS material. The ability to install various different monolayers, along with the ability to manipulate those monolayers post-installation, allows for the creation of a virtually endless list of chemical interfaces within the mesoporous matrix.

Research Progress

$SCCO_2$ Synthesis of SAMMS

The use of supercritical carbon dioxide ($SCCO_2$) as the reaction medium for the deposition of self-assembled monolayers in mesoporous ceramics mobil catalytic material #41 (MCM-41) has been found to provide significantly enhanced hydration and silanation kinetics, unprecedented degrees of surface coverage, and the lowest monolayer defect density reported to date. $SCCO_2$ provides a very fast, effective, and efficient method for derivatizing a range of porous materials and fine powders.

It is well beyond the scope of this report to fully describe criticality and its consequences. However, a brief description of the phenomenon as it pertains to the functionalization of surfaces in small pores may prove useful. Densities similar to that of liquid phases are achievable with a supercritical fluid, given high enough pressures. This allows the fluid to "shield" solute molecules from each other approximately as well as a liquid solvent. However, the elevated temperature prevents the molecules of the supercritical fluid from interacting attractively enough to form long-lived structures, resulting in diffusivities and viscosities similar to those of a gas. The combination of these properties makes supercritical fluids very useful solvents. In particular, supercritical fluids permeate and penetrate small orifices readily.

The kinetics of traditional solution-phase synthesis of SAMMS are restricted by the mass transport of the silane to the inner pore surfaces. This mass transport term is affected by the interfacial wettability of the solvent/silica system, solvent bilayer shear forces, and bulk solvent viscosity. Use of a supercritical fluid as the reaction medium takes advantage of the liquid-like solvating properties and gas-like physical properties of supercritical fluids. Carbon dioxide is an attractive solvent because it is environmentally benign, non-toxic, non-flammable, and inexpensive; the mild critical point conditions for CO_2 (T_c = 31.1°C, P_c = 73.8 bar) are easily attained and are unlikely to cause degradation of either the mesoporous starting material or the SAMMS product. In addition, performing the silanation in $SCCO_2$ also enhances delivery of the silane to the internal pore surface by direct pressure pumping.

In a hypothetical associative reaction between reagents A and B, increasing pressure can increase reaction rate (an excellent, detailed treatment of this subject is provided by Savage et al. [1995]). Both the transition state and the product will have a smaller molar volume than the starting materials. Therefore, both $\Delta v‡$ and $\Delta v°$ will be negative. Thus, increasing pressure will stabilize the transition state relative to the starting materials, thereby lowering the activation energy of the process and increasing the reaction rate, and any equilibrium will be shifted toward the product.

Thus, exploitation of $SCCO_2$ as the reaction medium for the synthesis of SAMMS can accelerate monolayer formation both by speeding up delivery of the silanes to the reaction site and by reducing the activation barrier to monolayer formation. The optimized synthetic protocol that we have developed to deposit mercaptopropyl(trimethoxy)silane (MPTMS) monolayers within the pores of MCM-41 involves a one-hour hydration step followed by a six-hour silanation step in refluxing toluene (Feng et al. 1997; Liu et al. 1998). At this stage, the silane coverage is limited to approximately 3.6 to 4.0 silane molecules/nm^2 (this population density is not enhanced by either extending the reaction time or increasing silane concentration). Following the silanation with a two- to three-hour azeotropic distillation helps

to fill in the defects and increases this surface population to 5.0 to 5.2 silanes/nm^2. This population density is representative of typical silane-based monolayers. In summary, the overall procedure takes about 10 hours of laboratory preparation time and 3 to 10 days of drying time.

Carrying out a similar MPTMS deposition, using $SCCO_2$ (7500 psi and 150°C) as the reaction medium increased reaction rate considerably. After only five minutes, it was found that this method had deposited a monolayer composed of 6.4 silanes/nm^2, or approximately 20% higher than our best efforts in liquid-phase solvents (population determined gravimetrically and by ^{29}Si NMR). To our knowledge, this is the highest documented population density ever reported for a silane-based monolayer.

TEM and BET surface area analyses confirmed that the ordered mesostructure is retained in the monolayer-coated product. The solid-state ^{29}Si nuclear magnetic resonance (NMR) spectrum of this five-minute sample is shown in Figure 1. The silane demographics of this sample are similar to those found in monolayers prepared under atmospheric pressure and routine solution-phase conditions (8% isolated siloxane, 47% terminal siloxane, and 45% internal siloxane). Maintaining the sample at elevated temperature and pressure resulted in a slow but steady evolution of the silane demographics, with a gradual decrease in the population of the terminal silane with a concomitant increase in the population of the internal silane over 24 hours and complete disappearance of the isolated silane (see Figure 3). Thermal curing of siloxane monolayers is known (Tripp and Hair 1991; Angst and Simmons 1991; Carson and Granick 1990). However, to our knowledge this is the highest degree of silane monolayer crosslinking documented by ^{29}Si NMR. Both the unprecedented surface population and the high degree of crosslinking are directly attributable to the use of $SCCO_2$ as the reaction medium.

Not only is the monolayer deposition step considerably accelerated relative to standard solution methods, but the final drying phase has been completely eliminated by the use of $SCCO_2$ as the reaction medium. The SAMMS product emerges from the reaction chamber dry and ready to use, constituting considerable time savings.

Design and Synthesis of New Classes of SAMMS

Instead of trying to create monolayers with a homogeneous dispersion of different silanes, we have chosen to design ligand synergy into our fundamental strategy by combining a protic ligand with a synergistic ligand, creating a cross-over, chelating ligand. We have employed three different synthetic pathways, exemplifying the versatility of our convergent SAMMS synthesis.

The first of these strategies is incorporation of the desired ligand via an amide linkage to commercially available aminopropylsiloxane (APS). This is accomplished by activating the carboxylate with carbonyl diimidazole (attempts to effect this amidation via the corresponding esters all failed). This reaction was followed immediately by deposition in freshly prepared MCM-41. This protocol resulted in the deposition of 1.1 silanes/nm^2, which is the expected level of coverage for a silane of this bulk. A similar strategy is currently being used to make the *p*-NO_2 analog.

A chelating carboxylic acid function was incorporated by treating isocyanate-SAMMS with a buffered solution of glycine. This approach tethers the acid via a urea linkage. In this fashion, we obtained less than expected surface coverage, presumably due to the steric congestion at the monolayer interface (Fryxell et al. 1996). This problem can be avoided by preforming the silane. This strategy has also been used with other amines (e.g., aminomethylpyridine, aminobenzothiazole).

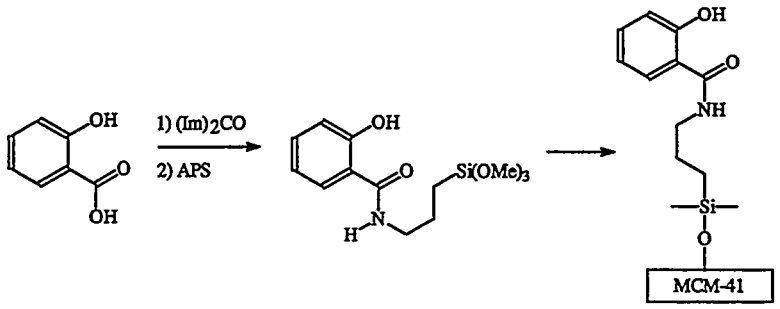

Figure 1.

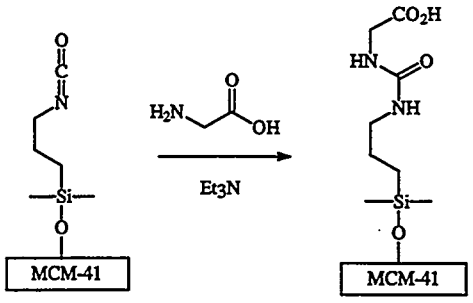

Figure 2.

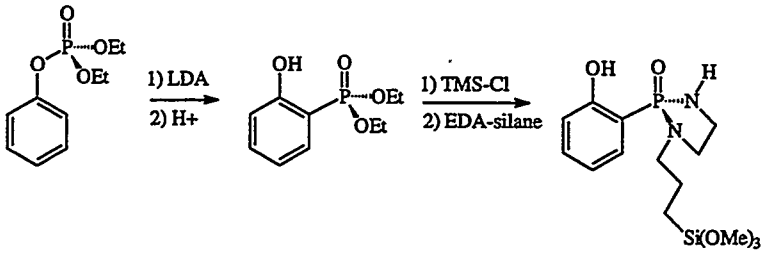

Figure 3.

Preparation of the o-hydroxyphosphonamide (HOPhos) ligand is outlined, as shown below. To date, the adjacent acidic phenolic proton has been problematic in the desired amidation process, but we have side-stepped that issue via protection of that functionality as the TMS ether.

Lanthanide Testing

Initial testing used lanthanides to mimic actinides to perform preliminary screening more cost-effectively by avoiding radioactive materials. Testing with actinides will begin when we have successfully refined our interface sufficiently to ensure effective scavenging in the desired pH window. To establish a baseline, tests were run using thiol SAMMS to bind the representative lanthanides chosen (lanthanum was chosen as a light lanthanide, neodymium was chosen as a representative lanthanide, and europium was chosen as an americium(III) mimic).

Two things are apparent from these data. First, the numbers are similar to those obtained in our preliminary tests using thiol SAMMS with plutonium(IV) and americium(III) (Feng et al. 1999), offering support for the decision to start with lanthanide models.

Thiol-SAMMS Binding of Representative Lanthanides

Metal	pH = 6.5	pH = 4.5	pH = 0.5
Lanthanum	4900	1440	41
Neodymium	2670	400	16
Europium	2070	810	8

0.1 M $NaNO_3$, 2 ppm solution of the lanthanide as the nitrate
0.100g SAMMS, 10 mL solution

Secondly, the distribution coefficients fall off with increasing acidity due to protonation of the ligand and release of the metal cation (this is related to the isoelectric point of the ligand). In fact, it is rather surprising that these metals are bound at all at a pH of 0.5.

Sal-SAMMS Binding of Representative Lanthanides

Metal	pH = 6.5	pH = 4.5	pH = 2.5	pH = 0.5
Lanthanum	7870	17	<1	<1
Neodymium	>100,000	18	<1	<1
Europium	>100,000	20	3	6

0.1 M $NaNO_3$, 2 ppm solution of the lanthanide as the nitrate
0.100g SAMMS, 10 mL solution

The sharp demarcation observed in the distribution coefficients determined for the Sal-SAMMS is a direct reflection of the isoelectric point of this ligand. While this is highly encouraging and stands as a validation of our design strategy, we need to create binding capability in a pH window between 2 and 4 because that is the range in which most actinide chemistry is performed (due to solubility and speciation). Thus, we need to lower the isoelectric point of the ligand from 4.5 to 5.0 to 3 or below.

One method of achieving this reduction is to employ the carboxylic acid functionality in conjunction with a suitable electron-withdrawing group (such as an amide or phosphine oxide). A quick test of this concept was explored by looking at the binding affinity of a glycine substituted urea. As the distribution coefficients below show, this material was surprisingly ineffective at scavenging lanthanides. (It should be noted that the surface coverage of this material was less than ideal. This will cause the saturation loading to be lowered but should not significantly affect the Kd value at sub-saturation loadings).

Gly-SAMMS Binding of Representative Lanthanides

Metal	pH = 6.5	pH = 4.5	pH = 2.5	pH = 0.5
Lanthanum	112	5	<1	<1
Neodymium	146	25	9	8
Europium	230	14	<1	36

0.1 M $NaNO_3$, 2 ppm solution of the lanthanide as the nitrate
0.100g SAMMS, 10 mL solution

Summary

Novel synthetic methods employing $SCCO_2$ have dramatically increased both the quality and production rate of SAMMS. This powerful synthetic strategy has been found to provide significantly enhanced hydration and silanation kinetics, unprecedented degrees of surface coverage, and the lowest monolayer defect density reported to date. New ligands have demonstrated a high affinity for the lanthanide mimics that we have tested so far. However, this affinity doesn't quite coincide with the pH window that we have targeted. Experiments are under way to alleviate this by incorporating ligands of appropriate acidity.

Planned Activities

We will be incorporating additional synergistic chelating ligands (e.g., the HOPO series, malonamide, phthalamide, and ortho-(phosphine oxide) acids) into the SAMMS interface. The focus will be on increasing the acidity of the protic portion of ligand so as to keep the isoelectric point below 4. We will also explore the amenability of each of these ligands to deposition from $SCCO_2$ so that we may exploit the desirable attributes that we have discovered inherent in this approach. In addition, we will acquire additional characterization of these lanthanide adducts by extended x-ray absorption fine structure to gain a better understanding of the stereochemistry and stoichiometry of the complexes. Evaluation with actinides (specifically thorium and uranium) will begin later this summer, and we will move on to testing with plutonium and americium this fall.

References

Angst DL and GW Simmons. 1991. *Langmuir* 7:2236.

Carson GA and S Granick. 1990. *J. Mater. Res.* 5:1745.

Feng X, GE Fryxell, LQ Wang, AY Kim, J Liu, and K Kemner. 1997. *Science* 276:923-926.

Feng X, L Rao, TR Mohs, J Xu, Y Xia, GE Fryxell, J Liu, and KN Raymond. 1999. *Ceramic Transactions* (in press).

Fryxell GE, PC Rieke, LL Woods, MH Engelhard, RE Williford, GL Graff, AA Campbell, RJ Wiacek, L Lee, and A Halverson. 1996. *Langmuir* 12:5064-5075.

Liu J, X Feng, GE Fryxell, LQ Wang, AY Kim, and M Gong. 1998. *Adv. Mat.* 10:161-165.

Savage PE, S Gopalan, TI Mizan, CJ Martino, and EE Brock. 1995. *AIChE Journal* 41:1723-1778.

Tripp CP, and ML Hair. 1991. *Langmuir* 8:1120.

Publications

Feng X, L Rao, TR Mohs, J Xu, Y Xia, GE Fryxell, J Liu, and KN Raymond. 1999. "Self-assembled monolayers on mesoporous silica, a super sponge for actinides." *Ceramic Transactions* (accepted, in press).

Fryxell GE and J Liu. 1999. "Designing surface chemistry in mesoporous silica." *Adsorption at Silica Surfaces*, E Papirer, ed., Marcel Dekker (in press).

Fryxell GE, J Liu, TA Hauser, Z Nie, KF Ferris, SV Mattigod, M Gong, and RT Hallen. 1999. "Design and synthesis of selective mesoporous anion traps." *Chemistry of Materials* (in press).

Fryxell GE, TS Zemanian, J Liu, JA Franz, and Z Nie. 1999. "Supercritical fluids in the synthesis of derivatized nanostructured materials." *Chemistry of Materials* (submitted).

Fryxell GE, J Liu, SV Mattigod, LQ Wang, M Gong, TA Hauser, Y. Lin, KF Ferris, and X Feng. "Environmental applications of interfacially modified mesoporous ceramics." To be published in the *Proceedings of the 101st National Meetings of the American Ceramic Society.*

Presentations

Fryxell GE, J Liu, M Gong, SV Mattigod, Y Lin, J Birnbaum, KA Alford, and X Feng. April 1999. "Design and synthesis of mesoporous lanthanide sorbent materials." To be presented at the 101st National Meeting of the American Ceramic Society (invited presentation).

Fryxell GE, J Liu, SV Mattigod, LQ Wang, M Gong, TA Hauser, Y. Lin, KF Ferris, and X Feng. April 1999. "Environmental applications of interfacially modified mesoporous ceramics." To be presented at the 101st National Meetings of the American Ceramic Society (invited presentation).

Fryxell GE, J Liu, TS Zemanian, TA Hauser, JA Franz, K Alford, and LQ Wang. June 1999. "Self-assembled monolayers on mesoporous supports: Synthesis of nanoscale hybrid materials and their applications." To be presented at the Northwestern Regional Meeting of the American Ceramic Society in Portland, Oregon.

Fryxell GE, TA Hauser, J Liu, Z Nie, RT Hallen, M Qian, and KF Ferris. June 1999. "High efficiency environmental sorbent materials: Self-assembled monolayers on mesoporous supports (SAMMS) for metal removal from aqueous systems." To be presented at the Northwestern Regional Meeting of the American Ceramic Society in Portland, Oregon.

Fryxell GE, TS Zemanian, Y Lin, J Liu, JC Birnbaum, TA Hauser, and K Alford. August 1999. "Environmental applications of self-assembled monolayers on mesoporous supports (SAMMS). To be presented at the National Meeting of the American Ceramic Society in New Orleans (invited presentation).

Patent Application

Fryxell GE, TS Zemanian, and J Liu. "Self-Assembled Monolayer and Method of Making." E-1693, filed March 1999.

Press Highlights

Popular Science (March 1999), p. 34, "Metal eaters."

Tri-City Herald (April 11, 1999), p. D1. "PNNL focuses on healthy environment."

Architectural Design Criteria for f-Block Metal Sequestering Agents

(First Year of Funding: 1996)

Principal Investigator

Dr. Benjamin P. Hay
Pacific Northwest National Laboratory
P.O. Box 999
Richland, WA 99352
(509) 372-6239 (phone)
ben.hay@pnl.gov

External Collaborators

Professor D. Max Roundhill
Department of Chemistry
Texas Tech University
Lubbock, TX 79409-1061
(806) 742-3067 (phone)
uldmr@ttacs.ttu.edu

Professor Robin D. Rogers
Department of Chemistry
The University of Alabama
Tuscaloosa, AL 35487-0336
(205) 348-4323 (phone)
rdrogers@ua1vm.ua.edu

Professor Robert T. Paine
Department of Chemistry
University of New Mexico
Albuquerque, NM 87131
(505) 277-1661 (phone).
rtpaine@unm.edu

Professor Kenneth N. Raymond
Department of Chemistry
University of California at Berkeley
Berkeley, CA 94720
(510) 642-7219 (phone)
raymond@garnet.berkeley.edu

Professor James E. Hutchison
Department of Chemistry
University of Oregon
Eugene, OR 97403
(541) 346-4228 (phone)
hutch@oregon.uoregon.edu

PNNL Contributors

Dr. David A. Dixon
Dr. Gregg J. Lumetta
Dr. Brian M. Rapko

LBNL Contributor

Dr. Linfeng Rao

Associated Western Universities Contributors

Dr. Omoshile Clement (Post Doctoral Research Associate)
Dr. Bruce K. McNamara (Post Doctoral Research Associate)
Dr. Giovanni Sandrone (Post Doctoral Research Associate)
Dr. Pier L. Zanonato (Visiting Scientist, University of Padova, Italy)
Dr. Robert D. Gilbertson (Post Doctoral Research Associate)
Dr. Rubicelia Vargas (Post Doctoral Research Associate)
Dr. Jorge Garza (Visiting Scientist, Metropolitan Autonomous University – Iztapalapa)

Research Objective

The objective of this project is to provide the means to optimize ligand architecture for f-block metal recognition. Our strategy builds on an innovative and successful molecular modeling approach in developing polyether ligand design criteria for the alkali and alkaline earth cations. The hypothesis underlying this proposal is that differences in metal ion binding with multidentate ligands bearing the same number and type of donor groups are primarily attributable to intramolecular steric factors. We propose quantifying these steric factors through the application of molecular mechanics models.

The proposed research involves close integration of theoretical and experimental chemistry. The experimental work entails synthesizing novel ligands and experimentally determining structures and binding constants for metal ion complexation by series of ligands in which architecture is systematically varied. The theoretical work entails using electronic structure calculations to parameterize a molecular mechanics force field for a range of metal ions and ligand types. The resulting molecular mechanics force field will be used to predict low energy structures for unidentate, bidentate, and multidentate ligands and their metal complexes through conformational searches. Results will be analyzed to assess the relative importance of several steric factors including optimal M-L length, optimal geometry at the metal center, optimal geometry at the donor atoms (complementarity), and conformation prior to binding (preorganization). An accurate set of criteria for the design of ligand architecture will be obtained from these results. These criteria will enable researchers to target ligand structures for synthesis and thereby dramatically reduce the time and cost associated with metal-specific ligand development.

Problem Statement

Critical tasks in the cleanup of U.S. Department of Energy (DOE) sites include processing radioactive wastes for disposal in long-term storage, remediation/restoration of environmental sites resulting from radioactive contamination, and decontamination/decommissioning of nuclear facilities. Because the radioactive components, most of which are metals, are typically present in very low concentrations, it is desirable to remove them from the bulk of the contaminated source (process waste stream, groundwater, soil) and concentrate them to minimize the volume of radioactive material destined for permanent subsurface disposal and thus minimize disposal costs. One group of radionuclides, the actinides, which are pervasive throughout the DOE complex, is of special concern. In particular, thorium, uranium, neptunium, plutonium, americium, and curium with half-lives ranging from 10^2 to 10^6 years can all be found in various DOE wastes, contaminated soils and groundwaters, and contaminated facilities. Lanthanide elements are also of concern because they form an important group of fission products that can persist in radioactive wastes for decades (e.g., ^{152,154,155}Eu).

Organic ligands with a high degree of metal ion specificity are essential components for developing separations processes for metal ions. Over the past 50 years, much research has focused on the discovery of selective ligands for f-block metal separations; both neutral and ionic ligands have been examined. Despite past success in the discovery of ligands that exhibit some degree of specificity for the f-block metal ions, the ability to further control binding affinity and selectivity remains a significant challenge to the synthetic chemist. The approach for developing these ligands has involved lengthy and costly experimental programs of organic synthesis and testing, which, in the absence of reliable methods for screening compounds before synthesis, requires an extensive research effort. Criteria for accurately selecting target ligands would result in much more effective use of resources.

Research Progress

This project combines a theoretical and experimental approach to developing ligand design criteria for selective complexation of f-block metal ions. These criteria will address how to best connect donor functionality to achieve metal ion recognition in multidentate ligands. For the f-block metal ions, donor groups of interest include amides, phosphine oxides, pyridine N-oxides, and catechols. Scoping studies were performed on these ligands during the first year of the project, FY 1997. A decision was made to focus solely on amides. Ligands containing the amide functional group are currently used in DIAMEX (an actinide separation process used for treatment of commercial reprocessing wastes) and TRUEX (actinide separation process under testing for use in tank waste cleanup at Idaho National Engineering and Environmental Laboratory).

The DIAMEX process uses a diamide ligand as the actinide extractant. Diamides such as malonamide and succinamide contain two oxygen donor groups and can form bidentate complexes. A bidentate ligand is the simplest case in which the issue of binding site organization arises. There are three structural variables that can affect binding site organization in a diamide: the length of the bridge between the two amides, the degree of bridge alkylation, and the steric bulk of the alkyl groups attached to the nitrogen. Understanding the effect of these structural variables on metal ion complexation provides criteria for optimizing the performance of multidentate amide ligands. In FY 1999 our research continues to focus on the synthesis and characterization of diamides and their complexes, the development and application of methods to measure ligand binding affinities for f-block metals, and the application of molecular models to these ligands and their metal complexes. The goal is to generate structure-function data and to correlate these data using molecular models. In a parallel effort, Professor D. Max Roundhill is preparing a series of calixarene amides and studying their behavior as metal ion extractants. We plan to use a molecular mechanics model to examine the metal binding site organization in these complex polyamides.

Synthesis and Characterization

We have prepared the diamides **1–14** in multigram quantities (see Figure 1). Compounds **5**, **7**, **8**, **12**, **13**, and **14** are previously unreported. All have been characterized by ^{1}H and ^{13}C NMR spectroscopy, IR spectroscopy, and GC-MS. These diamides represent the three types of structural variation. The bridge length is varied in **1** and **2**, and in **3** and **4**. The degree of bridge alkylation is varied in **1**, **5**, and **6**, in **3**, **7** and **8**, in **9** and **10**, in **11** and **12**, and in **4** and **13**. The steric bulk of the alkyl groups attached to the nitrogen is varied in **1**, **3**, **9**, **11**, and **14**, in **5**, **7**, and **12**, and in **6** and **8**.

The coordination chemistry of diamides with lanthanides has been explored with emphasis on the parent compounds **1** and **2** (presentation 7, 12, 20, and 23; publication 16, 25, 26, and 27). Solid state structural information was obtained by single-crystal x-ray diffraction at the University of Alabama in the laboratory of Professor R.D. Rogers and thermogravimetric analysis (TGA). The question of whether or not the solid state structures are maintained in solution was addressed through the use of infrared (IR) spectroscopy. The crystal structures determined in this work are shown in Figure 2. We have determined the first crystal structures for **1** with lanthanide nitrates. The La and Nd complexes are isostructural and have the same butterfly arrangement of the two malonamide chelates that has been observed with other malonamide derivatives. However, the Gd complex exhibits a different and previously unreported structural isomer.

TGA analysis reveals that the reaction of lanthanide nitrates with **1** yields 2:1 ligand:metal species for all the lanthanides examined (La, Nd, Gd, and Yb). The structures for La, Nd, and Gd have been determined by single crystal x-ray diffraction and were found to be monomeric with two bidentate chelating diamides, consistent with previous literature reports. Titrations of lanthanide

Varied Bridge Length

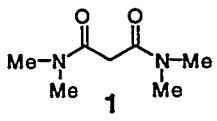

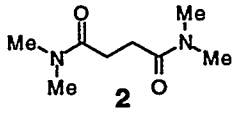

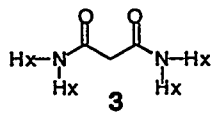

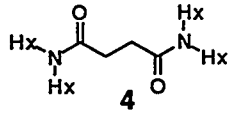

Varied Bridge Alkylation

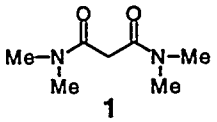

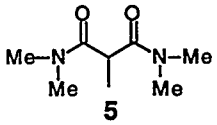

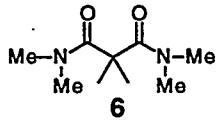

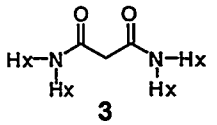

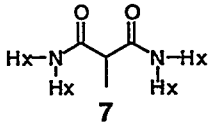

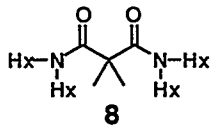

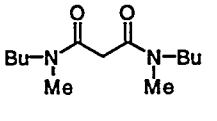

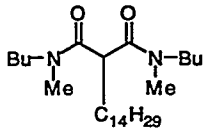

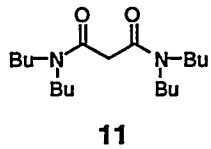

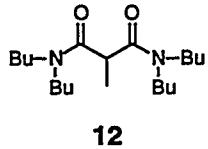

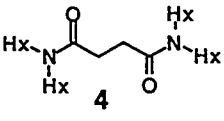

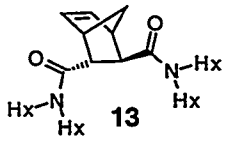

Varied N-Alkylation

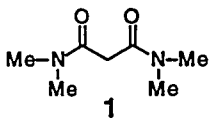

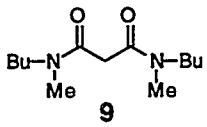

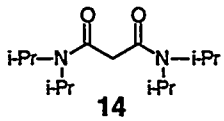

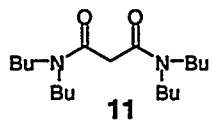

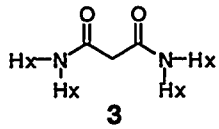

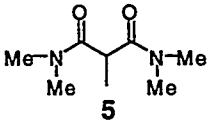

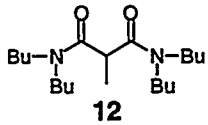

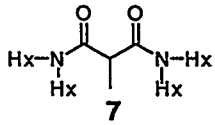

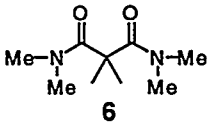

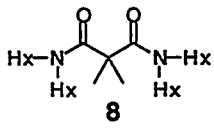

Figure 1. Diamide Derivatives Prepared for this Study

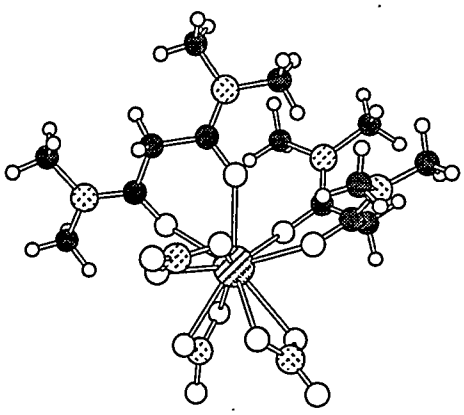

$[M(\mathbf{1})_2(NO_3)_3]$
(M = Gd)

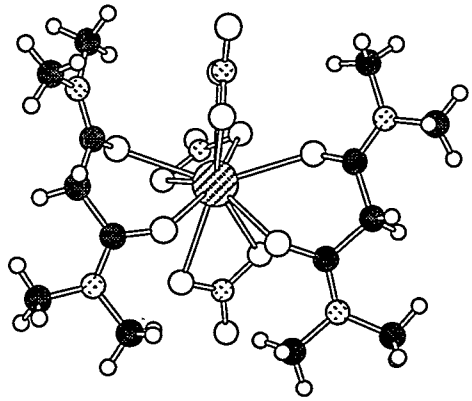

$[M(\mathbf{1})_2(NO_3)_3]$
(M = La, Nd)

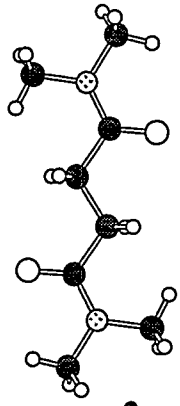

2

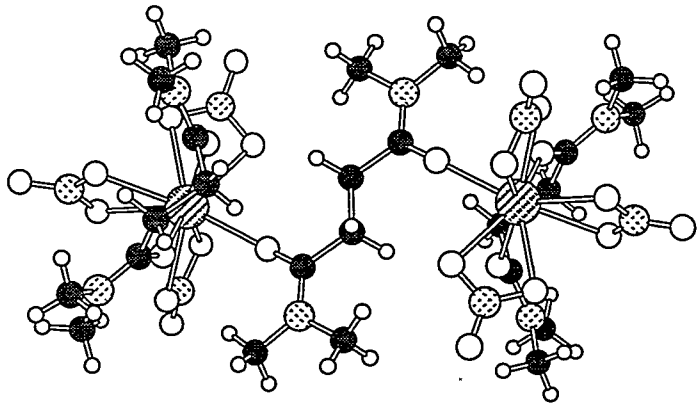

$[M_2(\mathbf{2})_3(NO_3)_6]$
(M = Ce, Pr, Nd, Gd, Yb)

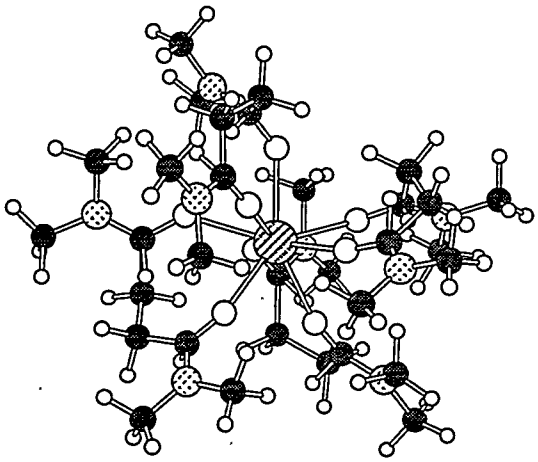

$[M(\mathbf{2})_4]^{3+}(X)_3$ (M = La, Nd, Eu, Lu)
(X = ClO_4^-, $CF_3SO_3^-$)

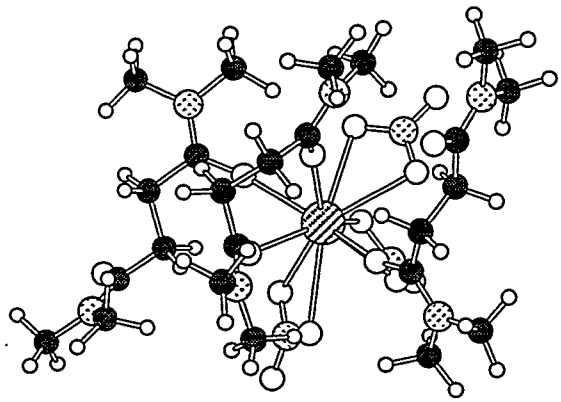

$[M(\mathbf{2})_2(NO_3)_3]_n$
(M = La, Ce)

Figure 2. X-Ray Crystal Structures for **2** and Metal Complexes of **1** and **2**

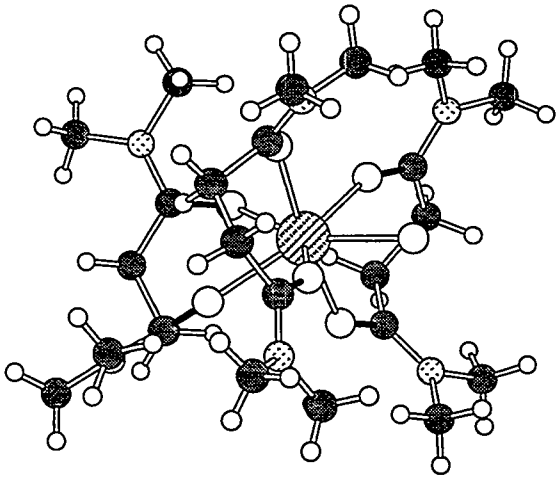

$[M(\mathbf{2})_3(H_2O)]^{3+}(ClO_4)^-_3$ (M = Yb)

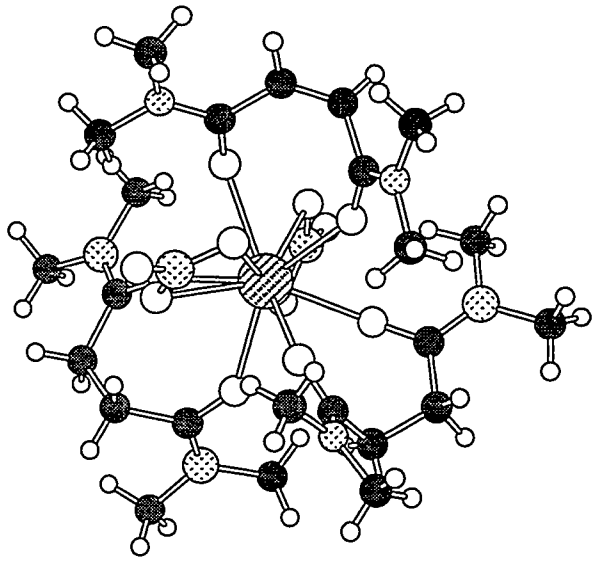

$[M(\mathbf{2})_3(NO_3)_2]^{2+}[M(NO_3)_6]^{2-}$ (M = Th)

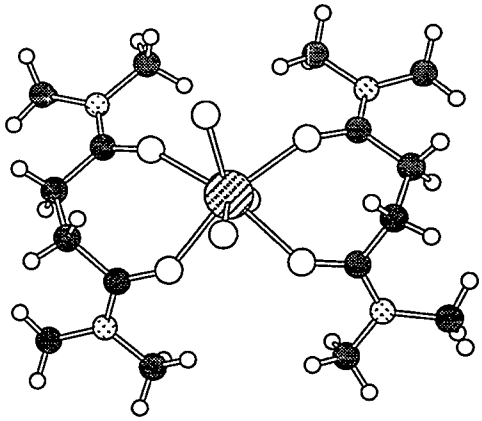

$[M(\mathbf{2})_2(H_2O)_3]^{3+}(CF_3SO_3)^-_3$ (M = Yb)

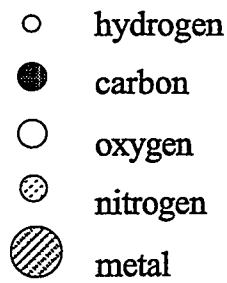

Figure 2. (contd)

nitrates with **1** or **3** are consistent with the formation of a 2:1 species in solution as evidenced by the FTIR spectra. No evidence for any higher L:M species is observed.

We have obtained a series of crystal structures for complexes of lanthanides with **2** (see Figure 2). These are the first crystal structures for any lanthanide succinamide complex and reveal that lengthening the bridge leads to a rich and varied coordination chemistry. TGA analyses revealed that a 2:1 ligand:metal species occurs only with the early lanthanides (La and Ce). Single crystal x-ray diffraction revealed a *polymeric* material with one chelating bidentate diamide bound solely to one metal and the second bridging between two metals. IR spectroscopic titration of lanthanide nitrates with **2** is consistent with the formation of a 2:1 species in solution with no evidence for any higher L:M species.

TGA analysis reveals a different stoichiometry, a 3:2 ligand to metal ratio, for complexes of **2** with the lanthanides Pr, Nd, Gd, Yb, and Lu. The structures of the Pr, Nd, Gd, and Yb compounds have been determined by single crystal x-ray diffraction and were found to be *dimeric*, with one bidentate diamide bound to a single metal and a bidentate diamide bridging two metals. Curiously, a

crystal containing this stoichiometry was also isolated for Ce. With the exception of La and Ce, IR spectroscopic titration of lanthanide nitrates with **2** or **4** is consistent with the formation of the 3:2 species in solution with no evidence for any higher L:M species.

Ce appears to be a special (and transitional) lanthanide in its reaction with **2**. Although IR and TGA analysis indicate it is predominantly the 2:1 ligand-to-metal product, crystals for both the 2:1 and 3:2 compound were isolated. No evidence was found for multiple stoichiometries with any of the other lanthanides.

If non-coordinating counteranions are present, such as triflate or perchlorate, TGA analysis of the products formed in the presence of excess **2** reveals a 4:1 ligand: metal complex with Eu and Nd. Single crystal x-ray diffraction revealed a monomeric species with four bidentate chelating diamides. IR spectroscopic titration of lanthanide perchlorates with **2** is consistent with the formation of a 4:1 species in solution with no evidence for any higher L:M species. However, this stoichiometry is very sensitive to the amount of water present. By controlling the concentration of water, it is possible to isolate mixed aquo/diamide complexes such as those shown in Figure 2.

Binding Affinities

A literature search was performed to locate any information regarding single-phase stability constants for amide complexes of lanthanides or actinides and solution structural information on such complexes. This search revealed that not only are there no existing structure-stability data sets but no stability constant data for f-block metal ions with pure amide ligands. Given that the amide group is neutral over a wide pH range, this situation reflects the general difficulty of determining stability constants for non-ionizable ligands. Generation of structure-function data require that the relative metal binding affinities should be determined under identical experimental conditions of solvent, counter ion, and temperature. A variety of methods for the determination of metal-amide binding constants were investigated in first year of this project. These methods include electronic spectroscopy, IR spectroscopy, use of ion selective electrodes, calorimetry, and solvent extraction. Of these methods, solvent extraction and calorimetry were found to be the most applicable.

Calorimetry has yielded the first measurements of diamide binding constants with any metal ion (presentations 4, 5, 18; publication 30). The formation constants for 1:1 ligand:metal complexes have been determined for $Eu(ClO_4)_3$ with **1**, **2**, **3**, **8**, **9**, and **14** in 10% DMSO/90% acetonitrile solution buffered to ionic strength 0.1 M at 25°C. The results are presented in Table 1. A decrease in the formation constant by a factor of 3.7 occurs on lengthening the bridge by one methylene group, as shown in the comparison of **1** and **2**. Comparing **3** and **8** demonstrates that dialkylation of the methylene bridge causes a drop in the formation constant of at least 2 orders of magnitude. Data for **1**, **3**, **9**, and **14** illustrate that the formation constant steadily decreases as the steric bulk of N-alkyl groups increases.

Table 1. Formation Constants for $Eu(ClO_4)_3$

Ligand	Formation Constant, M^{-1} ($\pm 3\ \sigma$)	
1	21.9	(1.1)
2	5.9	(1.2)
3	3.5	(1.3)
8	<0.1	
9	11.0	(1.2)
14	1.2	(1.2)

Solvent extraction has also yielded structure-function data for diamide complexes with europium and uranyl nitrates. We have developed a new computer program, the SX Solver, to analyze solvent-extraction equilibria (publication 8). The program operates out of Microsoft Excel® and uses the built-in "Solver" function to minimize the sum of the square of the residuals between measured and calculated distribution coefficients. This program has been used to analyze europium and uranyl extraction data, as discussed below.

The extraction of europium(III) nitrate from aqueous acidic nitrate solutions with a series of tetrahexylmalonamides in t-butylbenzene has been investigated (presentation 7, 21; publication 14). The tetrahexylmalonamides considered were **3**, **7**, and **8**. This series of ligands allowed for a systematic determination of the effects of alkyl substitution of the methylene carbon. Equilibrium modeling of the extraction data indicates that there is only one species present in all cases, $Eu(L)_3(NO_3)_3$. The extraction constant decreases by seven-fold in going from **3** to **7**. However, a precipitous drop in the extraction constant occurs on going from **3** to **8**, i.e., with substitution of a second methyl group on the methylene carbon (see Table 2). This drop is consistent with the calorimetry results suggesting that the effect is due to the metal ligand interaction rather than environmental factors such as counteranion, solvent, or concentration.

The extraction of uranyl nitrate aqueous acidic nitrate solutions with **3**, **7**, and **8** in t-butyl-benzene also has been investigated (presentation 21, publication 13). Equilibrium modeling of the extraction data indicates that there are up to three different species present. These are $UO_2(NO_3)_2L$, $UO_2(NO_3)_2L_2$, and $UO_2(NO_3)_2L_3$. The relative population of these species depends on the nitrate concentration and the identity of the ligand. Extraction constants for the $UO_2(NO_3)_2L_2$ species could be determined for all three ligands (see Table 2). The relative binding affinities parallel those observed for europium complexation.

Table 2. Malonamide Extraction Constants (3.0 M $NaNO_3$)

Ligand	K_{ex} (europium)	K_{ex} (uranyl)
3	0.041	50.4
7	0.0057	29.5
8	<0.0002	1.2

The stoichiometries $Eu(L)_3(NO_3)_3$ and $UO_2(NO_3)_2L_2$ are inconsistent with the generally accepted bidentate coordination of the diamides and nitrate counteranions. However, these stoichiometries are consistent with the formation of complexes with monodentate-bound diamides. Several lines of evidence support this supposition. First, we have found that the same extraction stoichiometries found with the malonamides also are observed with the monoamide N,N- dihexylbutamide. Second, in accord with the well-known chelate effect, a bidentate ligand should exhibit binding constants several orders of magnitude greater than a unidentate ligand. However, under identical experimental conditions the extraction constant for the diamides is only a factor of two greater than the mono-amide for both uranyl and europium. Third, although there are no structurally characterized exam-ples of diamide complexes with the observed extraction stoichiometries, there is ample precedent for these stoichiometries with monoamides. Finally, molecular modeling studies reveal that the trends observed following alkylation of the central methylene are inconsistent with bidentate coordination but are consistent with monodentate coordination by the diamide (*vide infra*).

Calix[4]arene Amides

A series of eight calixarene amide derivatives have been prepared and characterized in the laboratory of Professor D.M. Roundhill at Texas Tech (publications 2, 6). Solid-phase structures for two of these compounds have been determined by single crystal x-ray diffraction (publication 6). The use of these ligands as metal ion extractants is under investigation (presentations 8, 9, 22; publications 2, 6, 9, 19 - 21). For example, geometrically isomeric 1,2- and 1,3-tert-butylcalix[4] arene amides disubstituted with (dibutylcarbamoyl)methoxy groups have been structurally characterized by ^{1}H and ^{13}C nuclear magnetic resonance (NMR) spectroscopy. Two non-interconverting conformers of the 1,2-isomer have been isolated. The 1,3-isomer and the two 1,2-isomers have been used to extract the uranyl ion into toluene and isooctane. The degree of the extraction depended on the particular conformer of the calixarene. As highlighted in a science/ technology concentrate in C&E News, March 2, 1998, this is the first example in which such conformer effects on the extraction of the uranyl ion have been observed.

Modeling

Our approach uses a molecular mechanics model to relate ligand structure to metal ion binding affinity. Precedence for this approach is documented in an exhaustive review of applying molecular mechanics to obtain structure-function relationships in coordination chemistry (presentation 17, 18; publication 3, 18). Using a molecular mechanics model requires the development of an extended force-field to handle the specific system under study. In this case, force-field development has required the refinement of existing amide parameters and the generation of new parameters for the metal-amide interactions. This has been accomplished with the MM3 force field using both electronic structure calculations and experimental data (crystal structures).

To understand how ligand architecture affects metal ion complexation, it is imperative to first understand the structural features of the free ligand. Given the importance of the amide functional group in organic chemistry and biochemistry, we were surprised to discover how little was known about the shape of simple amides and diamides. We found that the widely used and extensively validated MM3 model failed to produce observed ligand conformations. To address this problem, we first performed ab initio density functional theory (DFT) and molecular orbital theory calculations to obtain the rotational potential surfaces for C_a-C bond rotation in acetamide, propanamide, 2-methylpropanamide, and 2,2-dimethylpropanamide (see Figure 3). These data were used to correct the MM3 model. The refined model now predicts the correct shapes for amides (presentation 10, publication 12).

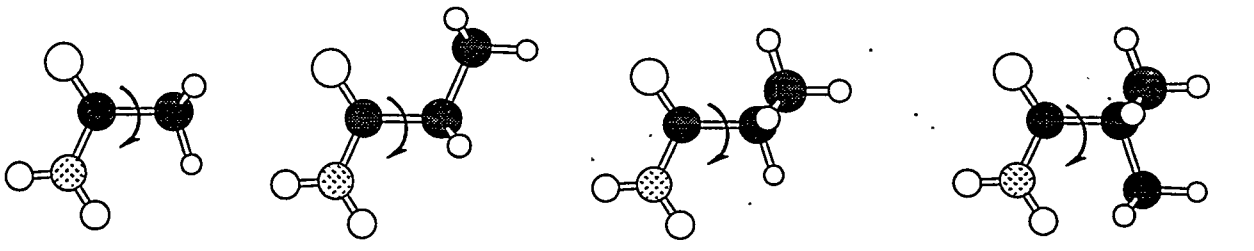

Figure 3. Illustration of the C_a-C Bond Rotations Investigated in Simple Amides

The MM3 force field did not contain torsional parameters needed to describe bond rotations present in malonamides. Therefore, we generated data needed to develop these parameters. This involved ab initio DFT and molecular orbital theory calculations to identify all stable conformations of malonamide, the three geometric isomers of N,N-dimethylmalonamide, and N,N,N',N'-tetramethylmalonamide, 1 (publication 17). Two stable conformations were identified for each malonamide derivative (see Figure 4). Only one of these ten structures had previously been reported. We then adjusted the MM3 model parameters to reproduce the structures and relative energies from the electronic structure calculations.

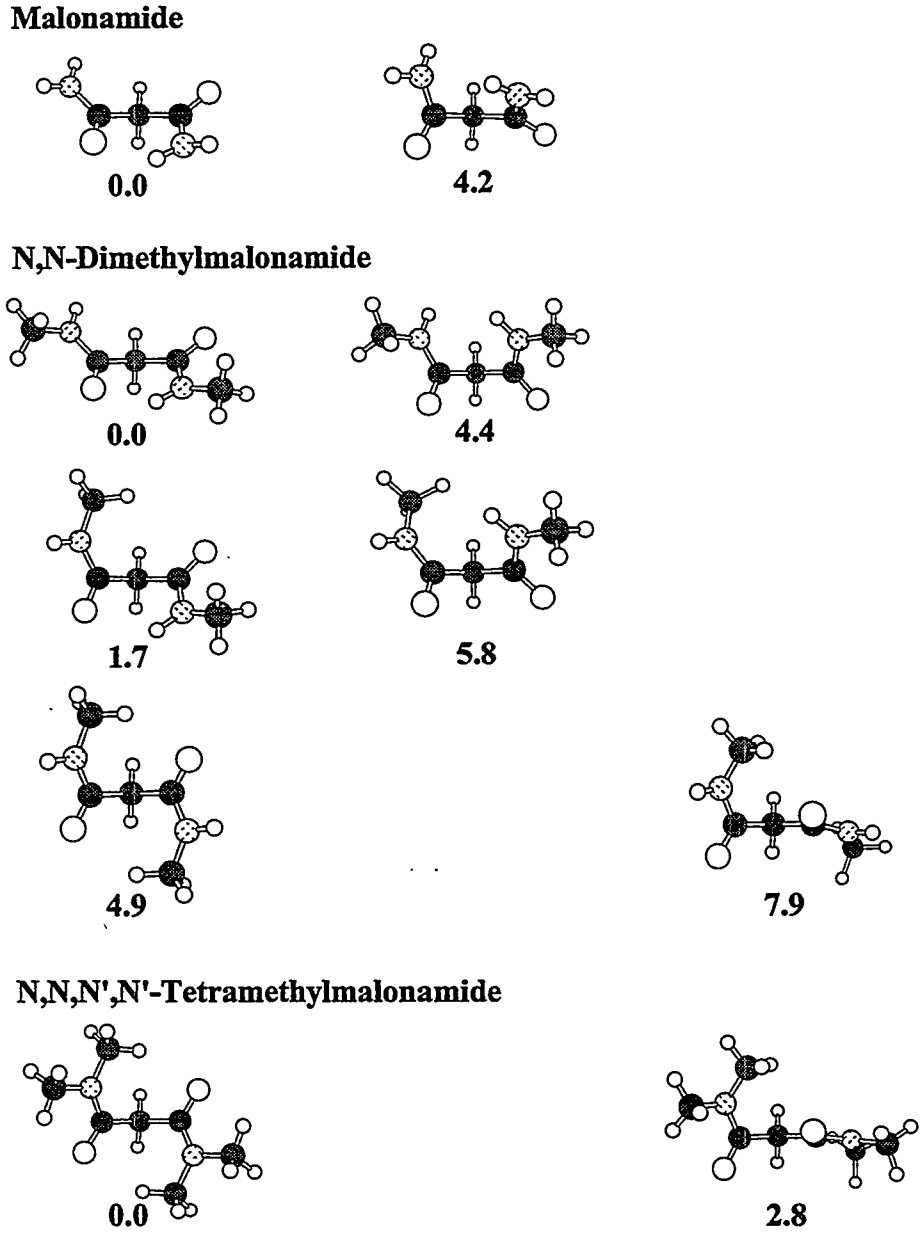

Figure 4. Malonamide Structures and Relative Energies (kcal/mol) from MP2/pTVZ Calculations

We also examined the conformations of N,N,N'N'-tetramethylsuccinamide, **2**, to identify the low energy shapes of this ligand and to provide a benchmark for the MM3 model performance (publication 23). Unlike the malonamide, **1**, which exhibits only two stable conformations, MM3 calculations revealed that **2** has at least 18 minima (see Figure 5). Electronic structure calculations were performed on these 18 minima. MM3 and DFT/DZVP structures and energies were in general agreement. However, the energies of several MM3 conformations were significantly different than those obtained by the electronic structure calculations. Examination of these cases led to the discovery of a previously unrecognized intraamide interaction.

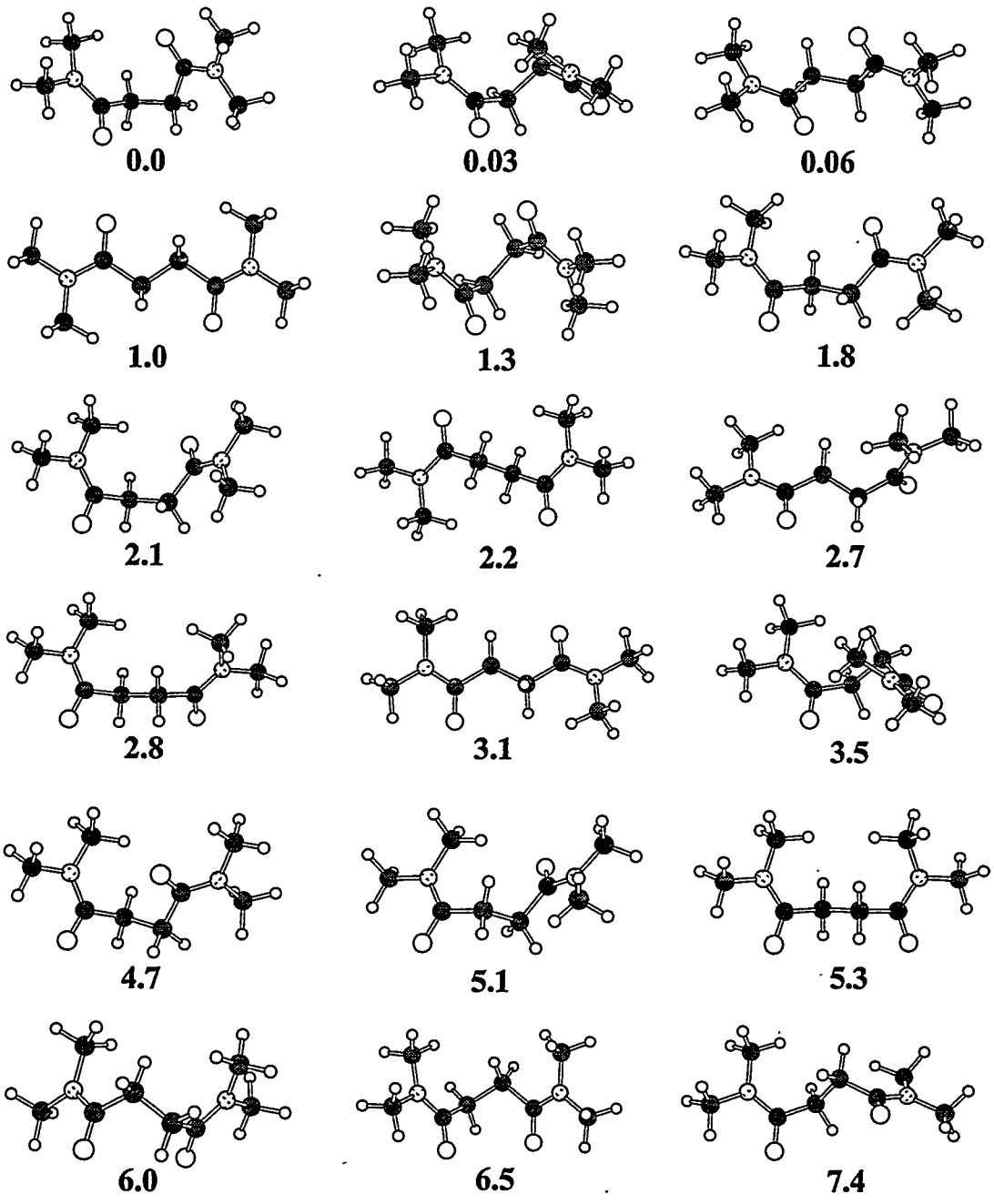

Figure 5. Succinamide Structures and Energies (kcal/mol) from BLYP/DZVP Calculations

We observed that the discrepancies between MM3 and DFT/DZVP energies in the succinamide structures occurred when there were close contacts (≤2.3 Å) between the methyl hydrogens and the oxygen atoms. This suggested the possibility of intramolecular hydrogen bonding between these groups. To test this hypothesis, calculations were performed on dimers of the dimethylformamide (see Figure 6). The results confirm the presence of C-H--O interactions. The energy per hydrogen bond, 1.6 kcal/mol, was unexpectedly strong. This previously unrecognized interaction may play an important role in controlling the shape of other polyamides, e.g., proteins (publication 22).

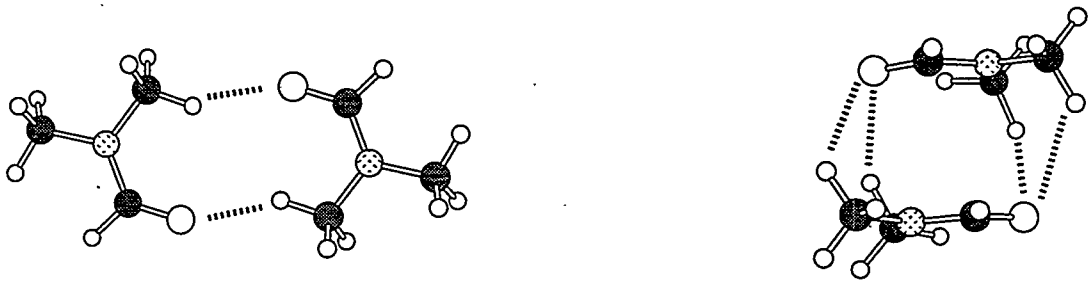

Figure 6. The C-H--O Interactions in Dimethylformamide Dimers

In addition to parameterization for free amides and diamides, we also have developed MM3 parameters for metal-amide interactions. Because the design of selectivity involves both an affinity for the target metal and a rejection of competing metal ions, the MM3 model needed to be applicable not only to f-block metals but also to other metals. For this reason, our model has been designed to evaluate amide complexes with metal ions throughout the periodic table. Ab initio DFT and molecular orbital theory calculations have been used to examine the structure, vibrational modes, and bonding of the various cations to simple unidentate and bidentate amides (publication 28 and 29). These calculations yielded ground state geometries and potential energy surfaces that provided a starting point for the refinement of the MM3 parameters through empirical fitting to crystal structure data, as described below. Because of their expense, the electronic structure calculations were focused on simple complexes of representative metal ions selected to cover a range of charge, size, and metal electronic configuration. Density functional theory has been used to calculate the structures of a variety of amides and metal ion complexes at local and nonlocal levels with at least polarized valence double zeta basis sets. Frequencies have been calculated for all species to determine if they are minima and as an aid in calibrating force field development. These calculations have been done with the computer codes NWChem and DGauss. This work has provided extensive testing of the new code NWChem developed at the William R. Wiley Environmental Molecular Sciences Laboratory (EMSL) at PNNL.

Initial parameters obtained through electronic structure calculations have been refined to give the best fit to crystal structures. An exhaustive survey of the Cambridge Structural Database identified suitable metal-amide structures for MM3 parameter refinement and validation. In addition, a statistical analysis of bond lengths, bond angles, and torsion angles was performed as a function of the degree of alkylation of the amide functional group and the type of metal ion in the amide complex. Geometric preferences of the coordinated amide ligand were evaluated in terms of M-O-C bond angles and M-O-C-N torsion angles. This evaluation led to the first recognition of the geometric requirements for amide binding (publication 4). A marked difference was observed in the structural features of covalent metals versus ionic metals (see Figure 7). In the covalent metals, the M-O-C angle is close to 120° as would be expected for optimal interaction with the oxygen sp2 orbital. In ionic metals, the M-O-C angle approaches 155°, consistent with an optimal orientation with the amide dipole. This structural difference suggests that ligand architecture can be manipulated to optimize selectivity for the actinides over the transition metals.

Figure 7. Illustration of Preferred Metal Ion Orientations with Respect to the Amide Donor

The performance of the extended MM3 model for metal-amide complexes has been validated by comparison of calculated and observed structural features. Fifty-six crystal structures, including those shown in Figure 2, were used in this comparison. In addition to f-block metal ions (lanthanides, Th(IV), U(IV), U(VI)), this set of structures included complexes with alkali, alkaline earth, and transition metals. We found that each metal ion requires a different set of parameters. A unique feature of this parameterization is that the metal-dependent parameters are correlated with the ionic radius, charge, and electronegativity of the metal ion. Therefore, the resulting MM3 model can be applied to any metal ion for which these properties are known. For the 56 crystal structures examined to date, the model computes a mean average deviation of ± 0.035 Å for M-O bond lengths, ± 5° for M-O-C angles, and ± 15° for M-O-C-X torsion angles (X = H, C, or N) (presentations 6, 11, 24; publication 11).

The MM3 model has been used to examine isolated malonamide metal ion chelates. Conformational analyses of complexes of **1** with a variety of metal ions reveal that this ligand forms three stable chelating conformers (see Figure 8). This result is consistent with x-ray crystal structure data that provide examples of all three of these forms. Ligand strain analyses have been performed for isolated chelate rings of **1**, **5**, and **6** with europium and uranyl cations. The results predict that the steric effects associated with methylation of the methylene bridge would give a binding affinity order of **5** > **1** > **6**. This order disagrees with the experimental results (**1** > **5** > **6**) suggesting that bidentate coordination is not occurring under the solvent extraction conditions (*vide supra*). On the other hand, MM3 calculations on complexes in which **1**, **5**, and **6** are monodentate-bound yield results that are consistent with the experimental ordering.

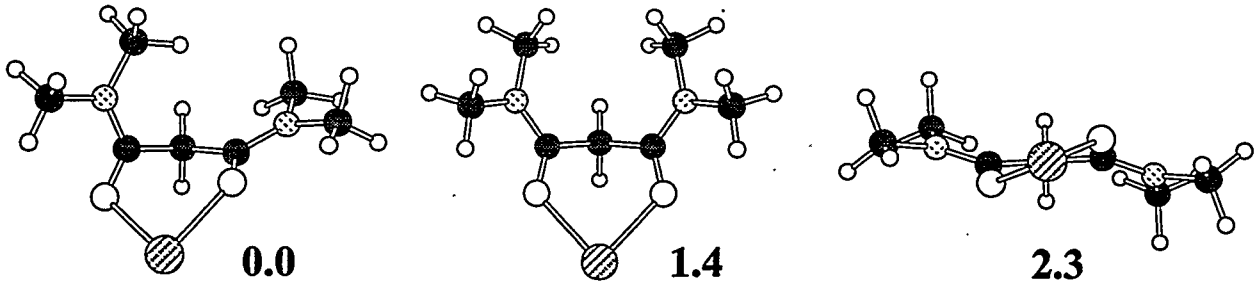

Figure 8. Structures and Energies (kcal/mol) for the Three Conformations of **1** with Am(III)

Examination of the chelate rings formed by **1**, **5**, and **6** in complexes with the f-block metal ions reveals that the oxygen donor atoms in the malonamide architecture are poorly organized for complexation. Significant structural reorganization is required to achieve a binding conformation and the binding conformation does not provide the optimal orientation of either amide with respect to the metal ion. This lack of preorganization and poor complementarity provides an explanation for why

these diamides would not form chelates under extraction conditions. Furthermore, these results suggest that alternative ligand architectures, in which the diamide was organized for chelation, could yield significant increases in metal ion binding affinity. Using ligand design criteria developed in this study, we have identified the diamide architecture **15** (Figure 9) that is preorganized for complexation and offers binding sites that are complementary for the trivalent actinides and lanthanides. Synthesis of **15** is in progress at the University of Oregon in the laboratory of Professor Hutchison.

Figure 9. Illustration of **1** and **15** Showing the Optimal Approach Vectors for Metal Complexation with the Amide Oxygens

Technology Transfer

Publications and presentations of our results have received international attention by scientists interested in f-element separations for nuclear fuel reprocessing. We have received two unsolicited invitations to collaborate. In November 1998, we were visited by Drs. J.-P. Dognon and M.-C. Charbonnel from the Macoule Facility of the Commissariat a L'Energie Atomique (CEA) in France. Dr. Dognon is the manager of the Theoretical and Structural Chemistry Laboratory responsible for the design and development of new extractants for radiochemical separation. This interaction led to the submission of a proposal to the DOE Nuclear Energy Research Initiative in which we would collaborate with the French researchers to develop improved sequestering agents for f-elements. In February 1999, we were visited by Dr. Shoichi Tachimori from the Tokai Research Establishment of the Japan Atomic Energy Research Institute (JAERI). Dr. Tachimori is the director of the Separations Chemistry Laboratory and supervises research on actinide separations. As a result of this visit, negotiations are underway to establish a collaboration interaction between JAERI and the EMSL.

Planned Activities

Our major focus for the remainder of this project is to complete the publication of our results (publications 22–30). In addition, we will attempt to synthesize (in progress at the University of Oregon) and test the preorganized diamide **15**. We also will collect and analyze data on several actinide diamide crystals (in progress at the University of Alabama).

Presentations

1. Rapko BM. April 1997. "Extraction of f-elements by phosphine oxide/pyridine N-oxide ligands." 213th American Chemical Society National Meeting, San Francisco.

2. Lumetta GJ, BK McNamara, and E Burgeson. June 1997. "Amide complexes of f-block elements." 21st Annual Actinide Separations Conference, Charleston, South Carolina.

3. Rao L, Y Xia, BM Rapko, and PL Martin. June 1997. "Synergistic extraction of Eu(III) and Am(III) by TTA and the neutral donor extractants CMPO and NOPOPO." 21st Annual Actinide Separations Conference, Charleston, South Carolina.

4. Zanonato PL, and L Rao. September 1997. "Complexation of Eu(III) by N,N,N',N'-tetra-alkyldiamides." 214th American Chemical Society National Meeting, Las Vegas.

5. Rapko BM, GJ Lumetta, BK McNamara, L Rao, and PL Zanonato. October 1997. "Determination of actinide and lanthanide binding constants with amides and diamides." Tenth Symposium on Separation Science and Technology for Energy Applications, Gatlinburg, Tennessee.

6. Clement O, G Sandrone, DA Dixon, and BP Hay. March 1998. "A MM3(96) force field for metal-amide complexes." 215th American Chemical Society National Meeting, Dallas.

7. Lumetta GJ, BK McNamara, and BM Rapko. April 1998. "Binding of amide ligands to f-block elements." 22nd Annual Actinide Separations Conference, Chattanooga, Tennessee.

8. Roundhill DM. May 1998. "New macrocycles for selective ion exchange." Metals Adsorption Workshop, Cincinnati.

9. Yordanov AT, NJ Wolf, HF Koch, and DM Roundhill. June 1998. "Sulfur and nitrogen derivatized calix[4]arenes as selective phase transfer extractants for heavy metals and oxyions." Second Fargo Conference on Main Group Chemistry, Fargo, North Dakota.

10. Hay BP, DA Dixon, and G Sandrone. June 1998. "A modified MM3(96) force field for simple amides and diamides." 53rd Northwest Regional American Chemical Society Meeting, Pasco, Washington.

11. Clement O, G Sandrone, DA Dixon, and BP Hay. June 1998. "A MM3(96) force field for metal-amide complexes." 53rd Northwest Regional American Chemical Society Meeting, Pasco, Washington.

12. Rapko BM, BK McNamara, RD Rogers, GJ Lumetta, and BP Hay. June 1998. "Coordination chemistry of lanthanide salts with N,N,N',N'-tetramethylsuccinamide and N,N,N',N'-tetrahexyl-succinamide." 53rd Northwest Regional American Chemical Society Meeting, Pasco, Washington.

13. Lumetta GJ, BK McNamara, and BM Rapko. June 1998. "Binding of diamide ligands to f-block elements." 53rd Northwest Regional American Chemical Society Meeting, Pasco, Washington.

14. Hay BP, DA Dixon, and G Sandrone. June 1998. "A modified MM3(96) force field for simple amides and diamides." West Coast Theoretical Chemistry Conference, Richland, Washington.

15. Clement O, BP Hay, DA Dixon, and G Sandrone. June 1998. "A MM3(96) force field for metal-amide complexes." West Coast Theoretical Chemistry Conference, Richland, Washington.

16. Hay BP. July 1998. "Architectural design criteria for f-block metal sequestering agents." Environmental Management Science Program Workshop, Chicago.

17. Hay BP. August 1998. "A points-on-a-sphere approach to model metal-ligand interactions with an extended MM3 model." Invited Talk, 216th American Chemical Society National Meeting, Boston.

18. Rao L, P Zanonato, and P Di Bernardo. August 1998. "Thermodynamics of europium(III) complexation with alkyl-substituted diamides in organic solvents." 216th American Chemical Society National Meeting, Boston.

19. Hay, BP. October 1998. "Ligand design with molecular mechanics." INEEL Science Integrated Workshop, Environmental Management Science Program, Idaho Falls, Idaho.

20. Rapko BM, BK McNamarra, RD Rogers, GJ Lumetta, G Broker, and BP Hay. March 1999. "Coordination chemistry of tetraalkyldiamides with f-block metal salts." 217th American Chemical Society National Meeting, Anaheim, California.

21. Lumetta GJ, BK McNamara, and BM Rapko. March 1999. "Equilibrium modeling of the extraction of f-block elements by diamides." 217th American Chemical Society National Meeting, Anaheim, California.

22. Roundhill DM. March 1999. "Calixarene amines and amides as extractants for oxyions." 217th National American Chemical Society National Meeting, Anaheim, California.

23. Rapko BM, BK McNamarra, RD Rogers, GJ Lumetta, G Broker, and BP Hay. June 1999. "Coordination chemistry of diamides with f-block metal salts." Metal Separation Technologies Beyond 2000: Integrating Novel Chemistry with Processing, United Engineering Foundation Conference, Turtle Bay, Oahu, Hawaii.

24. Hay BP. June 1999. "The Application of molecular mechanics in the design of metal ion sequestering agents." Invited Talk, Metal Separation Technologies Beyond 2000: Integrating Novel Chemistry with Processing, United Engineering Foundation Conference, Turtle Bay, Oahu, Hawaii.

Publications

1. Hay BP, DA Dixon, GJ Lumetta, and BM Rapko. 1997. *Science to Support DOE Site Cleanup: The Pacific Northwest National Laboratory Environmental Management Science Program Awards. Fiscal Year 1997 Mid-Year Progress Report.* PNNL-11589, Pacific Northwest National Laboratory, Richland, Washington.

2. Falana OM, HR Koch, DM Roundhill, GJ Lumetta, and BP Hay. 1998 "Synthesis and extraction studies of 1,2- and 1,3-disubstituted butylcalix[4]Arene amides with oxyions: Geometric and conformational effects." *Journal of the Chemical Society, Chemical Communications* 503.

3. Hay BP and O Clement. 1998. "Metal complexes," Invited Book Chapter In *The Encyclopedia of Computational Chemistry*, PvR Schleyer, NL Allinger, T Clark, J Gasteiger, PA Kollman, HF Schaefer III, and PR Schreiner, eds. John Wiley and Sons, Chichester.

4. Clement O, BM Rapko, and BP Hay. 1998. "Structural aspects of metal-amide complexes." *Coordination Chemistry Reviews* 170:203.

5. Rao L, Y Xia, BM Rapko, and PF Martin. 1998. "Synergistic extraction of Eu(III) and Am(III) by thenoyltrifluoroacetone and neutral donor extractants: Octyl(phenyl)-N,N-diisobutylcarbonyl-methylphosphine oxide and 2,6-bis(diphenylphosphino)methyl pyridine N,P,P trioxide." *Solvent Extraction and Ion Exchange* 16:913.

6. Yordanov A and DM Roundhill. 1998. "Solution extraction of transition and post-heavy and precious metals by chelate and macrocyclic ligands." *Coordination Chemistry Reviews* 170:93.

7. Hay BP, DA Dixon, GJ Lumetta, and BM Rapko. *1998. Science to Support DOE Site Cleanup: The Pacific Northwest National Laboratory Environmental Management Science Program Awards. Fiscal Year 1998 Mid-Year Progress Report.* PNNL-11899, Pacific Northwest National Laboratory, Richland, Washington.

8. Lumetta GJ, BM Rapko, and BK McNamara. 1999. *The SX solver: A New Computer Program for Analyzing Solvent Extraction Equilibria.* PNNL-12085, Pacific Northwest National Laboratory, Richland, Washington.

9. Yordanov AT, NJ Wolf, EM Georgiev, HF Koch, OM Falana, and DM Roundhill. 1999. "Derivatized calix[4]arenes as selective phase transfer extractants for heavy metal and oxyion salts." *Comments on Inorganic Chemistry* 20:163.

10. Hay BP, O Clement, G Sandrone, and DA Dixon. 1998. "A MM3(96) force field for metal amide complexes." *Inorganic Chemistry* 37:5887.

11. Hay BP, DA Dixon, GJ Lumetta, and BM Rapko. 1998. "Environmental management science program workshop." CONF-980736, Environmental Management Science Program, U.S. Department of Energy, Office of Science and Risk Policy EM-52, Washington, D.C.

12. Sandrone G, DA Dixon, and BP Hay. 1999. "$C(sp^2)$-$C(sp^3)$ rotational barriers in simple amides: H_2N-C(=O)-R, R = methyl, ethyl, i-propyl, t-butyl." *Journal of Physical Chemistry, A* 103:893.

13. Lumetta GL, BK McNamara, and BM Rapko. 1999. "Complexation of uranyl ion by tetrahexyl-malonamides: An equilibrium modeling and infrared spectroscopic study." *Inorganica Chimica Acta.* (in press).

14. McNamara BK, GJ Lumetta, and BM Rapko. 1999. "Extraction of europium(III) ion with tetrahexylmalonamides." *Solvent Extraction and Ion Exchange* (in press).

15. Wolf NJ, EM Georgiev, AT Yordanov, BL Whittlesey, HF Koch, and DM Roundhill. 1999. "Synthesis of lower rim amine and carbamoyl substituted calixarenes as transfer agents for oxyions between an aqueous and a chloroform phase." *Polyhedron* (in press).

16. Rapko BM, BK McNamara, GJ Lumetta, RD Rogers, and BP Hay. 1999. "Coordination chemistry of lanthanide nitrates with N,N,N,N-tetramethylsuccinamide." *Inorganic Chemistry* (in press).

17. Sandrone G, DA Dixon, and BP Hay. 1999. "Conformational analysis of malonamide, N,N'-dimethylmalonamide, and N,N,N',N'-tetramethylmalonamide." *Journal of Physical Chemistry, A*. (in press).

18. Hay BP. 1999. "The use of molecular mechanics in the design of metal ion sequestering agents." In *Metal separation technologies beyond 2000: Integrating novel chemistry with processing*; United Engineering Foundation, New York (in press).

19. Koch HF, NJ Wolf, and DM Roundhill. 1999. "A comparison between the picrate and inductively coupled plasma-atomic emission spectroscopy (ICP-AES) methods of metal assays in solution for calix[4]arene amides and amines as extractants." *Separation Science and Technology* (submitted).

20. Shen J, HF Koch, and DM Roundhill. 1999. "Polyethylene glycol as a selective biphasic phase transfer agent for the extraction of chromium(VI) from aqueous salt solutions." *Separation Science and Technology* (submitted).

21. Koch HF and DM Roundhill. 1999. "Lower rim amide and amine substituted calix[4]arenes as phase transfer extractants for oxyions between an aqueous and an organic phase." In *Calixarene Molecules for Separations, American Chemical Society Symposium Series*, American Chemical Society: Washington, D.C. (submitted).

22. Vargas R, J Garza, DA Dixon, and BP Hay. "The dimethylformamide dimer: Evidence for a strong C-H -- O interaction" (manuscript in preparation).

23. Vargas R, J Garza, DA Dixon, and BP Hay. "Conformational analysis of N,N,N',N'-tetramethylsuccinamide" (manuscript in preparation).

24. Hay BP. "Structural criteria for the rational design of selective ligands. III. Analysis of the malonamide chelate ring" (manuscript in preparation).

25. Rapko BM, BK McNamara, GJ Lumetta, RD Rogers, G Broker, and BP Hay. "Coordination of lanthanide ions containing non-coordinating counteranions with N,N,N',N'-tetramethylsuccinamide (TMSA). I. Preparation and characterization of $[(TMSA)_4Ln][A]_3$, $A = ClO_4^-$, $CF_3SO_3^-$" (manuscript in preparation).

26. Rapko BM, BK McNamara, GJ Lumetta, RD Rogers, G Broker, and BP Hay. "Coordination of lanthanide ions containing non-coordinating counteranions with N,N,N',N'-tetramethylsuccinamide (TMSA). II. Preparation and characterization of $[(TMSA)_{4-x}(H_2O)_x Ln][A]_3$, $A = ClO_4^-$, $CF_3SO_3^-$" (manuscript in preparation).

27. Rapko BM, BK McNamara, GJ Lumetta, RD Rogers, G Broker, and BP Hay. "The coordination of lanthanide nitrates with N,N,N,N-tetramethylmalonamide" (manuscript in preparation).

28. Dixon DA, G Sandrone, and BP Hay. "Computational studies of cation binding to amides. I. Proton binding affinity" (manuscript in preparation).

29. Dixon DA, G Sandrone, and BP Hay. "Computational studies of cation binding to amides. II. Metal ion binding affinity" (manuscript in preparation).

30. Rao L, P Zanonato, and P Di Bernardo. "Studies of europium(III) complexation with tetramethylmalonamide and tetramethylsuccinamide in organic solvents by calorimetry and optical spectroscopy" (manuscript in preparation).

Ionizing Radiation Induced Catalysis on Metal Oxide Particles

(First Year of Funding: 1996)

Principal Investigator

Michael A. Henderson
Pacific Northwest National Laboratory
P.O. Box 999, MSIN K8-93
Richland, WA 99352
(509) 376-2192 (phone)
ma.henderson@pnl.gov

Co-Investigators

Scott A. Chambers
Pacific Northwest National Laboratory
P.O. Box 999, MSIN K8-93
Richland, WA 99352
(509) 376-1766 (phone)
sa_chambers@pnl.gov

John L. Daschbach
Pacific Northwest National Laboratory
P.O. Box 999, MSIN K8-93
Richland, WA 99352
(509) 376-2467 (phone)
jl_daschbach@pnl.gov

Charles H.F. Peden
Pacific Northwest National Laboratory
P.O. Box 999, MSIN K8-93
Richland, WA 99352
(509) 376-1689 (phone)
chuck.peden@pnl.gov

Yali Su
Pacific Northwest National Laboratory
P.O. Box 999, MSIN K8-93
Richland, WA 99352
(509) 376-5290 (phone)
ya.su@pnl.gov

Yong Wang
Pacific Northwest National Laboratory
P.O. Box 999, MSIN K8-93
Richland, WA 99352
(509) 376-5117 (phone)
yongwang@pnl.gov

External Collaborators

Professor Miguel E. Castro (University of Puerto Rico)
Professor Abhaya K. Datye (University of New Mexico)
Professor Jürg Osterwalder (University of Zurich)

Research Objective

This project focuses on a novel approach for destroying organics found in high-level mixed waste prevalent at DOE sites. In this project, we propose that organics can be destroyed by using reduction/oxidation (redox) chemistry resulting from electron-hole (e^-/h^+) pairs generated in stable, wide bandgap semiconductors via interactions with ionizing radiation. Conceptually, this process is an extension of visible and near-UV (ultraviolet) photocatalytic processes known to occur at the interfaces of narrow bandgap semiconductors in both solution and gas phases. In these processes, an electron is excited across the energy gap between the filled and empty states in the semiconductor. The excited electron does reductive chemistry and the hole (whence the electron was excited) does oxidative chemistry. The energy separation between the hole and the excited electron reflects the redox capability of the e^-/h^+ pair, and is dictated by the energy of the absorbed photon and the bandgap of the material. The use of ionizing radiation overcomes optical transparency limitations associated with visible and near-UV illumination (γ-rays penetrate much farther into a solution than UV/Vis light), and permits the use of wider bandgap materials (such as ZrO_2), which possess potentially greater redox capabilities than those with narrow bandgap materials.

Planned experiments are aimed at extending the body of knowledge about e^-/h^+ pair chemistry of semiconducting metal oxide (MO) materials by examining the influence of surface structure, defects, and dopants on the photocatalytic activity of narrow bandgap materials (TiO_2), and by expanding these studies to wider bandgap materials (ZrO_2) that are virtually unexplored in terms of their e^-/h^+ pair chemistry. Experiments are being conducted in three areas: 1) γ-radiocatalysis of reactant-colloidal MO solutions, 2) photoelectrochemical studies at model MO electrodes, and 3) photochemical studies in ultra-high vacuum (UHV) and high pressures on model MO surfaces. An outcome of this proposed work will be a more thorough evaluation of the use of ionizing radiation in the catalytic remediation of organics (and other problem species) in high-level mixed waste.

Problem Statement

High-level radioactive waste storage tanks at DOE sites contain significant amounts of organic components (solid and liquid phases) in the form of solvents, extractants, complexing agents, process chemicals, cleaning agents, and a variety of miscellaneous compounds. These organics pose several safety and pretreatment concerns, particularly for the Hanford tank waste. All currently proposed tank waste cleanup alternatives encounter potential safety and/or pretreatment problems associated with organics, particularly Hanford tank waste. Remediation technologies are needed that significantly reduce the amounts of problem organics without resulting in toxic or flammable gas emissions and without requiring thermal treatments. These restrictions pose serious technological barriers for current organic destruction methods, which use oxidation achieved by thermal or chemical activation.

Research Progress

Probing the Mechanism of Radiocatalytic Oxidation and Reduction

In the first two years of this program, we examined in detail the radiocatalytic destruction of EDTA, a typical chelating agent found in DOE tank waste, over various TiO_2 catalysts. In the final year of this program, we have conducted similar studies on smaller probe organic molecules (such as

ethanol, formic acid, and acetic acid). Our results show that solution-phase radiolytic processes dominate those associated with the TiO_2 surface to the extent that any catalytic effects are not detected. This contrasts with the catalytic destruction of EDTA, which was greater than solution-phase radiolysis. UV-based experiments did show significant destruction of these small organics, in agreement with the literature. The presence of platinized TiO_2, however, significantly increased the production of hydrogen during the destruction of these small organics, presumably through the interaction of solution-phase radicals with the catalyst surface.

A comparison of radiocatalytic and photocatalytic methods for the reduction of noble metal cations and for the decomposition of water has also been conducted. Specifically, the experiments were performed by irradiating carboxylic acid solutions containing H_2PtCl_6/TiO_2 and Pt/TiO_2 with γ-rays from a ^{60}Co source and with UV light from a mercury lamp. The gas phase and liquid phase products were then analyzed using gas chromatography and high-performance liquid chromatography. Results show that the presence of the above catalysts and γ-irradiation significantly promotes the platinum ion reduction and hydrogen production. The γ-ray radiocatalytic generation of H_2 over platinized TiO_2 is consistent with those obtained from UV photocatalysis. These results show that γ-irradiation of TiO_2 can simultaneously promote both reduction and oxidation, further suggesting that the e^-/h^+ mechanism is in effect with γ-irradiation.

Along this line, we have also shown that radiocatalytic reductive deposition of noble metals, such as Pt, onto TiO_2 can explain the generation of benzene from tetraphenylborate (TPB) in Savannah River waste tanks. Our studies show that radiation (either ionizing or not) is not required for TPB decomposition on noble metal impregnated TiO_2; i.e., the thermal decomposition is highly facile even at room temperature. However, when noble metal ions, which are known to exist in the waste along with colloidal titanates, are irradiated they reductively precipitate on the titanates, opening the door for thermal decomposition of TPB.

Probing the Role of Surface Defects in Thermal and Photochemical Processes

To understand better on a molecular level how redox processes occur on TiO_2 surfaces and how surface structure influences these processes, we have conducted a variety of UHV studies on model TiO_2 surfaces focusing on the role of defects in surface chemistry.

Because molecular oxygen is key in photo-oxidation processes, we have examined the interaction of molecular oxygen with the $TiO_2(110)$ surface using temperature programmed desorption (TPD), isotopic labeling studies, sticking probability measurements, and electron energy loss spectroscopy (ELS). Molecular oxygen does not adsorb on the $TiO_2(110)$ surface in the temperature range between 100 and 300K unless surface oxygen vacancy sites are present. These vacancy defects are generated by annealing the crystal at 850K and can be quantified reliably using water TPD. Adsorption of O_2 at 120K on a $TiO_2(110)$ surface with 8% oxygen vacancies (about 4×10^{13} sites/cm^2) occurs with an initial sticking probability of 0.5 to 0.6 that diminishes as the surface is saturated. The saturation coverage at 120K, as estimated by TPD uptake measurements, is approximately three times the surface vacancy population. Coverage-dependent TPD shows little or no O_2 desorption below a coverage of 4×10^{13} molecules/cm^2 (the vacancy population), presumably due to dissociative filling of the vacancy sites in a 1:1 ratio. Above a coverage of 4×10^{13} molecules/cm^2, a first order O_2 TPD peak appears at 410K. Oxygen molecules in this peak do not scramble oxygen atoms with either the surface or with other co-adsorbed oxygen molecules. Sequential exposures of $^{16}O_2$ and $^{18}O_2$ at 120K indicate that each adsorbed O_2 molecule, irrespective of its adsorption sequence, has equivalent probabilities with respect to its neighbors to follow the two channels (molecular and dissociative) suggesting that O_2 adsorption is not only precursor-mediated, as the sticking probability measurements indicate, but that all O_2 molecules reside in this precursor state at 120K. This precursor state may be associated with a weak 145K O_2 TPD state observed at high O_2 exposures. ELS measurements suggest charge transfer from the surface to the O_2 molecule based on disappearance of the

vacancy loss feature at 0.8 eV and the appearance of a 2.8 eV loss that can be assigned to an adsorbed O_2^- species based on comparisons with Ti-O_2 inorganic complexes in the literature. Using results from recent spin-polarized DFT calculations in the literature, we propose a model in which three O_2 molecules are bound in the vicinity of each vacancy site at 120K. For adsorption temperatures above 150K, the dissociation channel completely dominates and the surface adsorbs oxygen in a 1:1 ratio with each vacancy site. ELS measurements indicate that the vacancies are filled, and the remaining oxygen adatom, which is apparent in TPD, is transparent in ELS. Based on the variety of oxygen adsorption states observed in this study, further work is needed to determine which oxygen-related species play important roles in chemical and photochemical oxidation processes on TiO_2 surfaces.

By means of postirradiation TPD, we have investigated further the states of oxygen adsorbed on rutile TiO_2. Previous work has shown that annealing the (110) surface in vacuum produces isolated bridging oxygen vacancies, and that these vacancies are intimately connected with molecular and dissociative oxygen adsorption channels. We find that, at 120K, illumination of the oxygen exposed surface with photons having energies above the band gap (>3.6 eV) results in photodesorption of the molecularly bound oxygen, in contrast to the remaining oxygen destined for the dissociative channel. An unusual effect of water overlayers on the O/TiO_2(110) system is explored. For thick overlayers (>2 mL), it is possible to generate via UV irradiation a previously unobserved oxygen TPD state.

We have also examined the interaction of these oxygen-related species with a simple organic species, methanol. The chemistry of methanol was explored on the vacuum-annealed TiO_2(110) surface, with and without the presence of co-adsorbed water and oxygen, using TPD, high-resolution electron energy loss spectroscopy (HREELS), SSIMS, and low-energy electron diffraction (LEED). The vacuum-annealed TiO_2(110) surface possessed about 8% oxygen vacancy sites, as determined with H_2O TPD. Although evidence is presented for CH_3OH dissociation to methoxyl groups on the vacuum-annealed TiO_2(110) surface using SSIMS and HREELS, particularly at vacancy sites, the majority of the adlayer was molecularly adsorbed, evolving in TPD at 295K. Although no evidence of irreversible decomposition was found in the TPD, dissociative CH_3OH adsorption at 135K on the vacuum-annealed TiO_2(110) surface led to recombinative desorption states at 350 and 480K, corresponding to methoxyls adsorbed at non-vacancy and vacancy sites, respectively. Co-adsorbed water had little or no influence on the chemistry of CH_3OH on the vacuum-annealed TiO_2(110) surface; however, new channels of chemistry were observed when CH_3OH was adsorbed on the surface after O_2 adsorption at various temperatures. In particular, O_2 exposure at 300K resulted in O adatoms (via dissociation at vacancies) that led to increased levels of CH_3O-H bond cleavage. The higher surface coverage of methoxyl then resulted in a disproportionation reaction to form CH_3OH and H_2CO above 600K. In contrast, low temperature exposure of the vacuum-annealed TiO_2(110) surface to O_2 resulted in low temperature state of O_2 (presumably an O_2^- species) that oxidized CH_3OH to H_2CO by C-H bond cleavage. These results provide incentive to consider alternative thermal and photochemical oxidation mechanisms that involve the interaction of organics and oxygen at surface defect sites. We have begun EPR studies on TiO_2 to characterize both surface and bulk defects resulting from radiation.

Working with Jürg Osterwalder at the University of Zurich, we have performed experiments mapping the 3-D Fermi surface of rutile TiO_2(110). Our recent investigations at Pacific Northwest National Laboratory suggest that the reduction of TiO_2 surfaces may be an important step in the radiation-induced chemistry that occurs under aqueous conditions. The reduction of TiO_2 results in the formation of a Fermi surface. The Fermi surface is an important quantity because it determines many of the properties of the material (e.g., the chemical properties, the electrical and thermal conductivities, etc.). Also, recent theoretical investigations suggest that reduced TiO_2 has a spin-polarized state that is stabilized at defect sites. These theoretical investigations may provide insight into the chemistry of paramagnetic molecules (e.g., NO, O_2) with the defective surface. For example, it was theoretically proposed, contrary to prior investigations, that the defect state for

reduced TiO_2 is not localized on a single site. This has led to proposed structural models that suggest these delocalized states may, in fact, help stabilize the adsorption of molecules at the surface.

Experiments were performed on reduced TiO_2 to determine the dispersion of the defect state and perform Fermi-surface mapping, ultraviolet photoelectron diffraction, and x-ray photoelectron diffraction. Our preliminary results suggest that point defects such as oxygen vacancy sites, although localized entities from a structural perspective, have longer-ranging influence on the electronic structure of the TiO_2 surface. This delocalization of electrons at point defects has significant influence on the adsorption and reaction of molecules and may also influence the trapping of photoexcited charge carriers. We have measured the dispersion of the defect state along several different directions to experimentally investigate this effect. Results show that although the highest intensity along $k_{//}$ is at nearly -0.8 eV, a significant shift occurs from -0.9 to -0.8 eV at $k_{//} = 1.2$ to 1.5. This small but significant dispersion in the defect state is the first experimental evidence for delocalization of this state for reduced TiO_2.

The intensity of the feature at the Fermi energy (E_f) can furthermore be monitored over the full 2π above the surface. Comparison of these results will be made to theoretical calculations. The calculations will provide information on the surface structure surrounding the defect state as well as the orbital that the electron occupies (i.e., which of the five 3-d orbitals).

Planned Activities

We are currently conducting EPR studies on the bulk and surface defects on TiO_2 rutile, analyzing results from the surface mapping of defects on $TiO_2(110)$, and conducting studies on aluminum-doped TiO_2. Other activities focus on writing (for publication) the results mentioned in this report before the end of this program in August of this year.

Publications

Epling WS, CHF Peden, MA Henderson, and U Diebold. 1998. "Evidence for oxygen adatoms on $TiO_2(110)$ resulting from O_2 dissociation at vacancy sites." *Surf. Sci.* 412-413:333.

Henderson MA, WS Epling, CL Perkins, CHF Peden, and U Diebold. 1999. "Interaction of molecular oxygen with the vacuum annealed $TiO_2(110)$ surface: Molecular and dissociative channels." *J. Phys. Chem.* (in press).

Henderson MA, S Oreto-Tapia, and ME Castro. 1998. "Electron induced decomposition of CH_3OH on the vacuum annealed surface of $TiO_2(110)$." *Surf. Sci.* 412-413:252.

Henderson MA, S Otero-Tapia, and ME Castro. 1999. "The chemistry of methanol on the $TiO_2(110)$ surface: The influence of vacancies and coadsorbed species." *Phys. Chem. Chem. Phys.* (submitted).

Herman GS, MA Henderson, KA Starkweather, and EP McDaniel. 1999. "Mass-spectrometry of recoiled ions and secondary ion mass spectrometry investigation of Y-stabilized $ZrO_2(100)$ and (110)." *J. Vac. Sci. Technol. A* (in press).

Perkins CL and MA Henderson. 1999. "Photoconversion of adsorbed oxygen states on $TiO_2(110)$" (in preparation).

Perkins CL and MA Henderson. 1999. "Reaction of molecular oxygen with bridging OH groups on TiO_2(110)" (in preparation).

Su Y, Y Wang, JL Daschbach, TB Fryberger, MA Henderson, J Janata, and CHF Peden. 1998. "Gamma-ray destruction of EDTA catalyzed by titania." *J. Adv. Oxid. Technol.* 3:63.

Taylor DP, WC Simpson, K Knutsen, MA Henderson, and TM Orlando. 1998. "Photon stimulated desorption of cations from yttria-stabilized cubic ZrO_2(100)." *Appl. Surf. Sci.* 102:4536.

Presentations

Henderson MA. 1999. "Activation of molecular oxygen on TiO_2(110) by reaction with bridging hydroxyls." First International Workshop on Oxide Surfaces, Elmau, Germany.

Henderson MA. 1998. "Ionizing radiation induced catalysis: Radiocatalytic degradation of organic contaminants in TiO_2 suspensions." Notre Dame Radiation Laboratory, University of Notre Dame, South Bend, Indiana (invited talk).

Henderson MA. 1998. "Coadsorption studies with water: A small step toward understanding the surface chemical and photochemical properties of TiO_2." 45th National Symposium of the American Vacuum Society, Baltimore (invited talk).

Henderson MA. 1998. "Coadsorption studies with water and oxygen: A small step toward understanding the surface chemical and photochemical properties of TiO_2." Department of Chemistry, University of Puerto Rico, Mayaquez, Puerto Rico (invited talk).

Su Y. May 2-6, 1999. "Radiocatalytic and photocatalytic studies of oxidation of organics and reduction of water." The 195th Meeting of the Electrochemical Society, Seattle.

Su Y. May 24-28, 1999. "Radiocatalytic and photocatalytic studies of metal ion reduction and water cleavage into hydrogen." The 5th International Conference on Advanced Oxidation Technologies for Water and Air Remediation, Albuquerque.

Electroactive Materials for Anion Separation – Technetium from Nitrate

(First Year of Funding: 1998)

Principal Investigators (Pacific Northwest National Laboratory)

Johanes H. Sukamto
Pacific Northwest National Laboratory
P.O. Box 999, MSIN K8-93
Richland, WA 99352
(509) 373-1473 (phone)
johanes.sukamto@pnl.gov

Scot D. Rassat
Pacific Northwest National Laboratory
P.O. Box 999, MSIN K6-28
Richland, WA 99352
(509) 376-1410 (phone)
sd.rassat@pnl.gov

Timothy L. Hubler
Pacific Northwest National Laboratory
P.O. Box 999, MSIN K8-93
Richland, WA 99352
(509) 373-0249 (phone)
tim.hubler@pnl.gov

Gregory M. Anderson
Pacific Northwest National Laboratory
P.O. Box 999, MSIN K8-93
Richland, WA 99352
(509) 376-1410 (phone)
Gregory.Anderson@pnl.gov

Michael A. Lilga
Pacific Northwest National Laboratory
P.O. Box 999, MSIN K2-12
Richland, WA 99352
(509) 375-4354 (phone)
mike.lilga@pnl.gov

Principal Investigator (University of Minnesota)

William H. Smyrl
Corrosion Research Center
Department of Chemical Engineering and Materials Science
University of Minnesota, Minneapolis
221 Church Street SE
Minneapolis, MN 55455
(612) 625-0717 (phone)
smyrl001@maroon.tc.umn.edu

Principal Investigators (Brookhaven National Laboratory)

James McBreen
Brookhaven National Laboratory
DAS, Bldg. 480
Upton, NY 11973
(516) 344-4513 (phone)
jmcbreen@bnl.gov

Research Objectives

The focus of the project is to develop a fundamental understanding of how the physical and chemical properties of electroactive ion exchange (EaIX) materials control their efficiency when used as mass separation agents. Specifically, the desirable characteristics of EaIX materials for separation applications are 1) high reversibility, 2) high selectivity, 3) acceptable physical and chemical stability, 4) rapid intercalation and de-intercalation rates, and 5) high capacity. Because of these requirements, EaIX materials share many properties in common with conventional ion exchangers and electroactive polymers. For example, EaIX materials require the selectivity typically found in ion exchangers; they also require the redox reversibility of electroactive polymers. The results of this work will allow the rational design of new materials and processes tailored for the separation of specific anions.

The specific objectives and their relevance are discussed. The first three objectives address specific material properties, and the last objective explores the scientific issues related to the preparation of high-capacity EaIX material.

1. Determine the effects of the distribution/concentration and mobility of electroactive sites. A high concentration of electroactive sites is favorable for high capacity and fast electronic propagation through the material. However, increased site-to-site interactions can also be expected, which may reduce the intercalation rate and the utilization efficiency. Increasing the mobility of the electroactive sites will enhance charge propagation rates without increasing the site concentration.

2. Determine the effects of branching/cross-linking. Cross-linking makes the polymer less prone to swell. This can increase the selectivity for anions with lower hydration energy. Less swelling may also enhance the stability to delamination. But increased cross-linking can also reduce the penetrability of the polymer to all anions in addition to restricting segmental motion, which will, in turn, reduce the capacity and transport rates.

3. Determine the effects of polymeric chain length or molecular weight. A higher molecular weight polymer has an overall lower free energy of sticking to the electrode surface (provided that each segment is hydrophobic), and therefore, it is more stable. On the other hand, long polymeric chain length may result in entanglements. Entanglements may lead to restricted segmental motion and reduced free volume required for counter-ion diffusion. Ultimately, the intercalation/de-intercalation rates are reduced. Restricted segmental motion can also result in increased site-to-site interactions, which, as before, may reduce the intercalation rate and utilization efficiency.

4. Prepare and characterize high-surface-area EaIX materials using aerogel and phase-inversion techniques. If high-surface-area (based on the geometric or projected surface area) materials can be prepared, increased efficiency can be realized.

Problem Statement

Many contaminants of interest to the U.S. Department of Energy (DOE) exist as anions. These include the high-priority pollutants chromate, pertechnetate, and nitrate ions. In addition, there are also industrial and urban applications where the separation of anionic species from aqueous streams is critical.

Examples include industrial water recycle and waste water treatment (e.g., chloride ion removal for the pulp and paper industry, borate ion in the chemical and nuclear industries) and drinking water and agricultural waste treatment (e.g., nitrate removal).

In the proposed research, technetium is chosen as the target pollutant. Because of its half-life of 213,000 years, technetium (^{99}Tc) presents a long-term hazard for waste disposal. Much of the ^{99}Tc in the tank wastes is present as pertechnetate (TcO_4^-), accounting for its high solubility and mobility in aqueous systems. Several sorbents are available for removing TcO_4^- from alkaline waste brines, but each has important drawbacks. The use of commercial ion exchange (IX) resins to extract TcO_4^-, e.g., Reillex™-HPQ (Reilly Industries) and ABEC 5000 (Eichrom Industries), generates significant secondary waste. The elution of TcO_4^- from Reillex™-HPQ resins requires either concentrated nitric acid or a concentrated caustic solution of ethylene-diamine containing a small amount of tin chloride. This eluant has a short shelf life requiring frequent preparation, and the ^{99}Tc is delivered in a complexed, reduced form. While TcO_4^- can be eluted from ABEC 5000 resins using de-ionized water, the much-reduced capacity of ABEC 5000 resins in comparison to the Reillex™-HPQ resins leads to a low column capacity. In general, unwanted secondary wastes are generated because 1) the only effective eluant happens to be hazardous and/or 2) the IX material has a low capacity or selectivity for the target ion, resulting in more frequent elution and column replacements.

Alternative IX materials that have high capacities, can be regenerated easily, and are highly selective for TcO_4^- would avoid these problems. EaIX media meet these criteria. Such an IX system uses electrically induced changes in the media to expel sorbed ions through a charge imbalance rather than requiring chemical eluants to "strip" them. Therefore, this medium eliminates the need to prepare, store, and dispose of many of the process chemicals normally required for IX operations.

Research Progress and Implications

The two main activities of the project are 1) synthesis and characterization of EaIX polymers and 2) determination of the resulting EaIX characteristics. Briefly, effects of electroactive site density and mobility, polymer chain length, and degree of cross-linking will be systematically explored by synthesizing 1) polymers of polyvinylferrocene (PVF) and 2) polymers obtained through the polymerization of vinyl ether monomers. PVF is chosen because it has been widely studied, it is widely accepted as one of the model redox polymers, and it promises to extract TcO_4^-. Both the molecular weight and cross-linking of PVF can be synthetically controlled. Copolymerization of PVF, e.g., with acrylonitrile and styrene, has also been reported, and this technique will be used to control the electroactive site density. The (vinyl ether)-based polymers are chosen because of the synthetic flexibility they afford to control the structural features listed above. High-surface-area electrodes will be prepared from both types of polymers using aerogel and phase-inversion techniques.

The EaIX characteristics of interest are reversibility, selectivity, stability, intercalation/de-intercalation rates, and capacity. Conventional electrochemical methods (e.g., cyclic voltammetry and impedance) will be used to provide macroscopic characterization. Selectivity will be further characterized by in situ Raman and x-ray absorption spectroscopy. Correlation with morphology will be determined by means of Scanning ElectroChemical Microscopy-Topography (SECM-Topography) and Atomic Force Microscopy (AFM).

Synthesis and Characterization of EaIX Polymers

Progress has been made in both the synthesis and characterization of EaIX polymers. To date, we have initiated work in synthesizing cross-linking agents, preparing EaIX materials containing electroactive sites with varying mobility, post-polymerization cross-linking using a nitrogen plasma, and making large-surface-area, porous EaIX assemblies. For characterization of the polymers, we are developing the proper analytical techniques. Primarily we are examining the use of gel permeation chromatography (GPC), which uses a triple angle light-scattering detector in series with a concentration detector (in this case UV/Vis). We are analyzing data to determine if we can obtain reproducible molecular weight data for PVF polymers. Additionally, we are incorporating an Fourier transform infrared (FTIR) probe as we analyze the crude polymer mixtures. Hence, the entire system consists of a liquid chromatographic separation using a GPC column, with subsequent FTIR, UV/Vis, and triple-angle light-scattering detection of the separated polymer fractions. The FTIR analysis is used to characterize the chemical functionality of the polymers (e.g., the number of unpolymerized vinyl groups in the polymer can be detected).

Synthetic routes leading to enhanced cross-linking in PVF polymers are in progress. One method involves the use of 1,1'-divinylferrocene as a cross-linking agent. Because the preparation of this material is plagued by poor yields, a similar cross-linking material is also being considered whereby 1,1'-diacetylferrocene undergoes a Wittig reaction producing the propenyl analogue of 1,1'-divinylferrocene. The methyl groups should not cause undue steric hindrance of polymerization and cross-linking of the vinylferrocene polymers and yet may be easier to produce in high yield than the 1,1'-divinylferrocene itself. We anticipate that we will produce polymers incorporating these cross-linking agents during the fourth quarter of this fiscal year. In addition to these chemical routes for preparing cross-linked PVF, the use of plasma for post cross-linking PVF is also pursued. Here, PVF is prepared using conventional means; after depositing the PVF on an electrode surface (e.g., by means of spin coating), the PVF/electrode assembly is exposed to a plasma that is known to induce cross-linking. Preliminary results using a nitrogen plasma will be discussed below; additional gases of interest include argon.

Work to synthesize EaIX materials based on (vinyl ether)-based polymers has been initiated. The initial target is to synthesize materials with varying electroactive site mobility. Monomers containing ferrocene tethered to reactive vinyl groups by carbon chains of varying length are being prepared. These monomers are designed to produce polymers with varying mobility of the electroactive group by altering their distance from the rigid backbone. Progress has been made in preparing the desired monomers, but yields have been low. The reason for the low yield is known, and modified synthetic strategies are now being evaluated.

Electrodeposition of PVF onto conductive porous nickel substrates produced stable films, which demonstrated the same current densities as films deposited on flat electrodes. The current scaled with the amount of available surface area. Phase inversion, a solvent/non-solvent exchange process commonly used in membrane manufacture, yielded a powdery film with poor physical stability. Spray coating of PVF and carbon particles and evaporative coating of PVF on conductive porous substrates also yielded less stable products than PVF spin-coated onto flat electrodes. Difficulties encountered with the solvent/non-solvent exchange process are caused by the insufficiently low viscosity of the starting polymer solution. Attempts to increase the initial solution viscosity by increasing the polymer concentration and using thickening agents were not successful. Another alternative is to increase the MW of the polymer. To date, only commercial PVF has been used; according to the vendor (Polysciences, Inc.), it has an average MW of 50,000. The MW can be increased by 1) increasing the chain length, 2) cross-linking

shorter chains, or 3) a combination of the two. Possible use of both post-polymerization plasma cross-linked PVF and cross-linked PVF obtained from using cross-linking agents during the actual polymerization to prepare porous EaIX materials will be considered.

Determination of EaIX Characteristics

To date, we have made progress in developing standard experimental and data analysis procedures that will allow appropriate comparison of different EaIX materials. In addition, this will also aid in furthering fundamental understanding of the structure/property relationships of EaIX materials. As noted earlier, the EaIX characteristics of interest are reversibility, selectivity, stability, intercalation/de-intercalation rates, and capacity.

Selectivity of PVF for ReO_4^- over NO_3^- has been verified. Electrochemical and gravimetric results of a PVF film potential cycled in solutions of 1) only NO_3^-, 2) only ReO_4^-, and 3) a mixture of NO_3^- and ReO_4^- are shown in Figures 1 and 2. The potential dependence of the current (CV), shown in Figure 1, shows that the oxidation and reduction of PVF is more facile in a solution of only ReO_4^- than in a solution of only NO_3^-. These results imply that ReO_4^- stabilizes the ferrocenium (Fc^+) cation to a higher degree than NO_3^-. Equivalently, the complex formation constant of the $(Fc^+)(ReO_4^-)$ salt is larger than that of the $(Fc^+)(NO_3^-)$ salt (see also Inzelt and Horányi 1986). Gravimetric measurement results shown in Figure 2 were obtained simultaneously with the electrochemical results shown in Figure 1. Comparison of the data shown in Figures 1 and 2 shows that oxidation of the PVF film is accompanied with an increase in mass loading (represented as a decrease in the fundamental frequency of the quartz crystal). Furthermore, more mass loading accompanies the oxidation of the PVF film in a solution of only ReO_4^-, which is consistent with the higher molecular weight of ReO_4^- as compared to NO_3^-. As detailed in Rassat et al. (1999), the data shown in Figures 1 and 2 can be used to calculate the separation factor, $\alpha_B^A = \dfrac{\overline{C}_A/\overline{C}_B}{C_A/C_B}$ with A = ReO_4^-, B = NO_3^-, C_i is the concentration in the bulk solution, and $\overline{C}_i$ is the concentration within the EaIX material. The average separation factor was determined to be $30 \pm 20\%$. The use of x-ray photoelectron spectroscopy (XPS) (Zeng et al. 1988) to measure the amount of ions intercalated into PVF will be pursued; this will provide additional verification of the electrochemical and gravimetric measurements presented here.

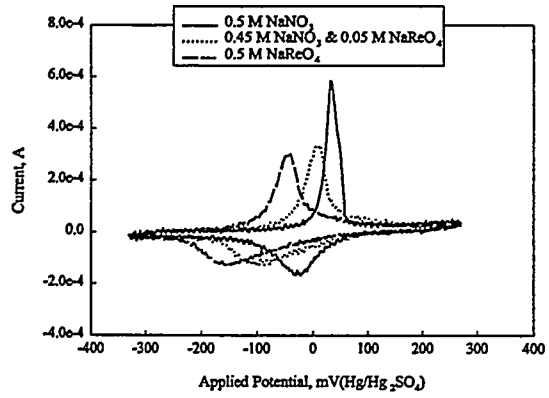

Figure 1. CVs of PVF in Different Solutions

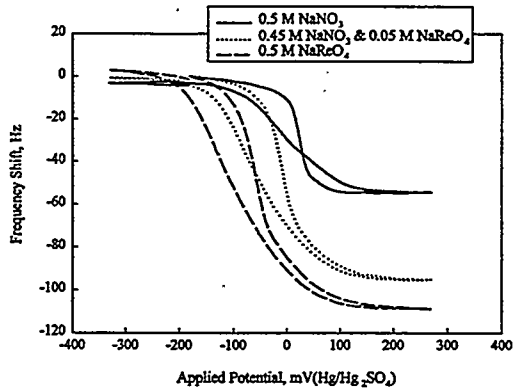

Figure 2. Measured Frequency Shifts Corresponding CVs in to Figure 1

To be of practical use, EaIX materials need to be both physically and chemically stable. Chemical instability of ferrocenes and possible means to overcome it under alkaline conditions have been reported (Chambliss et al. 1998, Clark et al. 1996), and we are currently investigating these issues as they pertain to PVF. Physical instabilities (e.g., caused by swelling/de-swelling of the PVF) during potential cycling are also issues that need to be addressed. The current-potential characteristics of a spin coated PVF film in 0.5 M $NaNO_3$ are shown in Figure 3 for the 3rd and 50th cycle. The integrated charge passed of the 50th cycle is 34% of that measured for the 3rd cycle. In contrast, a spin-coated PVF film that was exposed to a nitrogen plasma showed enhanced stability (see Figure 4); the charge measured in the 50th cycle is 62% of that measured for the 3rd cycle. The most likely explanation for the observed decrease in capacity with potential cycling (for both films) is the uncoiling and dissolution of individual PVF chains. PVF films typically swell during oxidation, and oxidation in the presence of highly hydrated anions, e.g., NO_3^-, will likely increase the degree of swelling. The degree of uncoiling and dissolution of individual PVF chains are likely to correlate directly with the degree of swelling. Exposure of a PVF film to a nitrogen plasma is expected to cross-link some of the chains, which, in turn, should reduce film swelling.

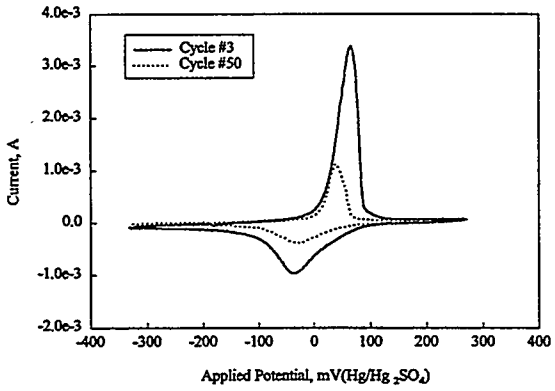

Figure 3. CVs of Spin-Coated PVF

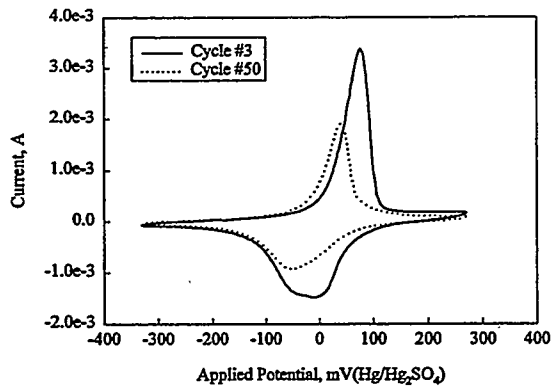

Figure 4. CVs of Plasma-Treated Spin-Coated PVF

Work has been initiated in developing techniques for obtaining good x-ray absorption (XAS) spectra for PVF under in situ conditions in an electrochemical cell. Early work was done on spin-coated films of PVF on sputtered platinum on glass slides. However, preliminary ex situ XAS studies on these films indicated that more concentrated samples were needed to obtain good XAS spectra. Electrochemical methods were developed to prepare samples with higher loadings per unit area. The most satisfactory method so far has been the electrodeposition of films on carbon cloth from solutions of 2 mM PVF in CH_2Cl_2 containing either 0.1 M tetrabutylammonium perchlorate or 0.1 M tetrabutylammonium perrhenate.

A special cell for in situ XAS was designed and built for XAS studies at both the Fe K edge and the Re L_3 edge. The cell materials were compatible with CH_2Cl_2, so electrode preparation could be done in the same cell. Both in ex situ and in situ XAS studies were done on PVF films that were electrodeposited on carbon cloth. Deposition was done, as noted earlier. Subsequent electrochemistry and in situ XAS were done in the same cell with 0.1 M NH_4ReO_4 or $LiCLO_4$ in water, or 0.1 M $TBAClO_4$ or $TBAReO_4$ in acetonitrile. Ex situ measurements were also done on films that were washed and dried after preparation.

Excellent in ex situ and in situ XAS spectra were obtained at the Fe K edge. Good ex situ XAS were obtained at the Re L_3 edge. However, soluble ReO_4^-, entrained in the electrolyte in the pores of the carbon cloth, interfered with the spectra. This problem requires a new design for the electrochemical cell that will permit electrolyte exchange while maintaining the electrode under potential control. XAS spectra were also obtained on several standard compounds such as various iron oxides, ferrocene, ferrocenium hexafluorophosphate, and ferrocenium tetrafluoroborate.

Figure 5 shows x-ray absorption near-edge spectrometry (XANES) spectra at the Fe K edge for ferrocene and ferrocenium hexafluorophosphate. The data show a shift in the absorption edge to higher energies for the ferrocenium hexafluorophosphate. The shift is due to an increase in the Fe oxidation state. The peak at about a step height of 0.7 was observed for both ferrocenium compounds. It is due to some electronic effect such as mixing of empty p and d states above the Fermi level.

Figure 6 shows in situ Fe XANES spectra for a PVF electrode in a 0.1 M solution of $TBAReO_4$ in acetonitrile at 0.0 V and 0.8 V vs. Ag/AgCl reference electrode. There is an edge shift at 0.8 V, indicating oxidation of the ferrocene moieties. However, the edge peak at a step height of 0.6 is less pronounced than that seen for the ferrocenium compounds. Figure 7 shows the FTIR of the Fe EXAFS at 0.0 and 0.8 V. The data have not yet been analyzed.

At present, we are trying to synthesize and purify ferrocenium perrhenate, which will be used as a model compound for analysis of the EXAFS.

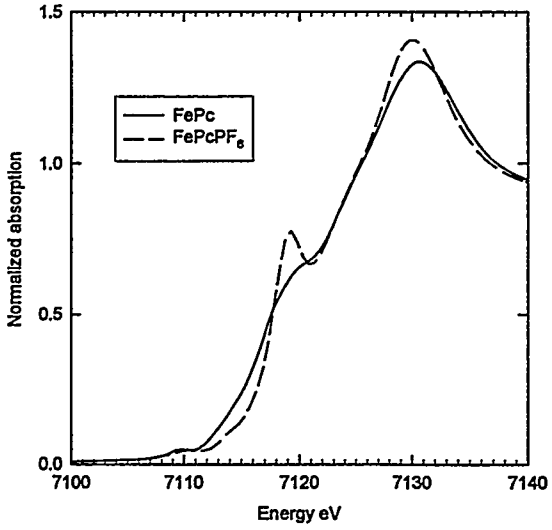

Figure 5. Fe XANES Spectra for Ferrocene and Ferrocenium Hexafluorophosphate

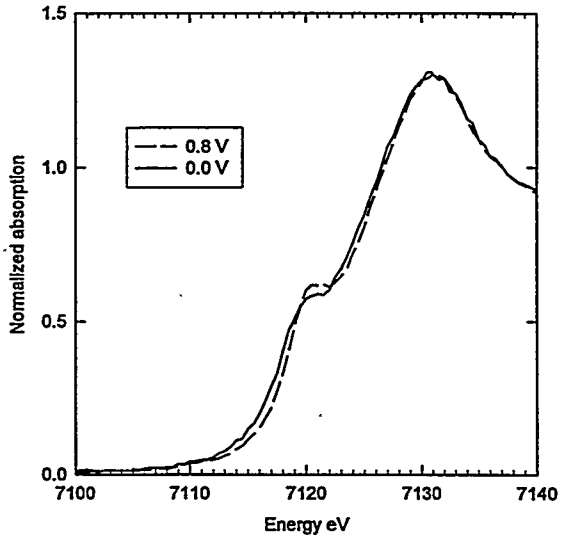

Figure 6. In situ Fe XANES Spectra for a PVFc Electrode in a 0.1 M Solution of $TBAReO_4$ in Acetonitrile at 0.0 V and 0.8 V Versus Ag/AgCl Reference Electrode

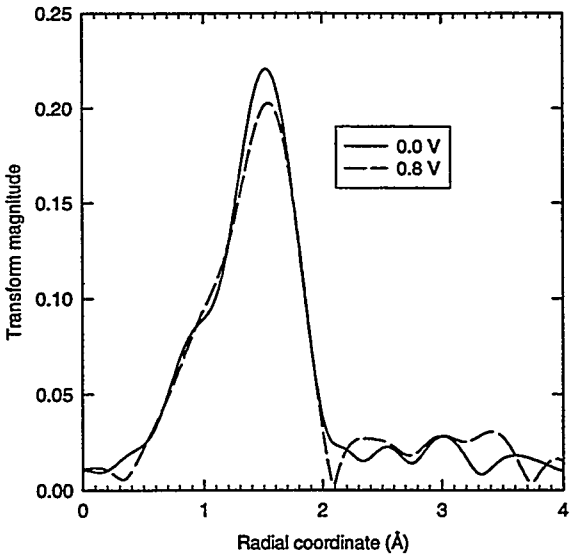

Figure 7. FTIR of In Situ Fe XANES Spectra for PVFc in 0.1 M Solution of $TBAReO_4$ in Acetonitrile at 0.0 V and 0.8 V Versus Ag/AgCl Reference Electrode

Planned Activities

As noted above, plasma and chemically cross-linked PVF will be prepared and characterized. Preparation of EaIX with varying electroactive site mobility will also continue. To understand better how the swelling/de-swelling processes (that accompany the oxidation/reduction processes) of the PVF films lead to uncoiling/delamination of the films, experimental methods that are more sensitive to morphological changes will be used (e.g., ellipsometry or AFM). Chemical stability studies of PVF in alkaline solutions will be undertaken. More specifically, the degradation mechanism/products of PVF caused by potential cycling in alkaline solutions need to be determined. If PVF degrades in the same manner as ferrocenes, then stabilization strategies (e.g., alkylation) that have been successful for ferrocenes can be expected to work for PVF as well. XANES analysis will also be pursued, as outlined.

Publications and Presentations

Hubler TL, GM Anderson, JH Sukamto, MA Lilga, and SD Rassat. "Polyvinylferrocene (PVF) polymers as electroactive ion-exchange materials for separation of pertechnetate ion from high nitrate ion containing wastes: Issues and synthetic strategies." Abstract submitted to the 218th ACS National Meeting, August 22-26, 1999, New Orleans.

Gronda AM and WH Smyrl. "High capacity electroactive polymers for radioactive waste removal." Abstract submitted to the 196th Electrochemical Society Meeting, October 17-22, 1999, Honolulu.

References

Chambliss CK, MA Odom, CML Morales, CR Martin, and SH Strauss. 1998. "A strategy for separating and recovering aqueous ions: Redox-recyclable ion-exchange materials containing a physisorbed, redox-active, organometallic complex." *Analytical Chemistry* 70:757.

Clark JF, DL Clark, GD Whitener, NC Schroeder, and SH Strauss. 1996. "Isolation of soluble ^{99}Tc as a compact solid using a recyclable, redox-active, metal-complex extractant." *Environmental Science & Technology* 30:3124.

Inzelt G, and G. Horányi. 1986. "Combined cyclic voltammetric and radiometric study of polymer film electrodes." *Journal of Electroanalytical Chemistry and Interfacial Electrochemistry*, 200:405.

Rassat SD, JH Sukamto, RJ Orth, MA Lilga, and RT Hallen. 1999. "Development of an electrically switched ion exchange process for selective ion separation." *Separation and Purification Technology* 15:207.

Zeng X, S Moon, S Bruckenstein, and AR Hillman. 1998. "XPS study of counterion incorporation into poly(vinylferrocene)." *Analytical Chemistry* 70:2613.

Removal of Technetium, Carbon Tetrachloride, and Metals from DOE Properties

(First Year of Funding: 1997)

Principal Investigators

Thomas E. Mallouk
The Pennsylvania State University
(814) 863-9637 (phone)

John G. Darab
Pacific Northwest National Laboratory
P.O. Box 999, MSIN K3-59
Richland, WA 99352
(509) 375-6608 (phone)
john.darab@pnl.gov

PNNL Contributors

AB Amonette
DS Burke
RD Orr

External Contributors

S Ponder (The Pennsylvania State University)
DK Shuh (Lawrence Berkeley National Laboratory)
(510) 486-6937; dkshuh@lbl.gov)
JJ Bucher (Lawrence Berkeley National Laboratory)
DL Caulder (Lawrence Berkeley National Laboratory)
IM Craig (Lawrence Berkeley National Laboratory)
P Liu (Lawrence Berkeley National Laboratory)
WW Lukens (Lawrence Berkeley National Laboratory)
NM Edelstein (Lawrence Berkeley National Laboratory)

Research Objective

The objective of this research is to prepare, characterize, and evaluate new materials for the removal of technetium compounds, carbon tetrachloride, and other troublesome metals from DOE waste streams and contaminated areas. The work performed at PNNL focuses on the removal of technetium from DOE tank wastes using these materials.

Research Statement

Current estimates of Hanford tank waste inventories indicate that the amount of technetium in the waste will need to be reduced substantially to be able to prepare low-activity waste (LAW) glass with sufficiently low radioactivity. One option is to remove some of the technetium in the waste using ion exchanging or absorbing materials. For such an application, the use of very fine particulates of zero-valent iron supported on an appropriately stable material has considerable potential. The iron metal particles, i.e., Fe(0), on the support material can react with pertechnetate, TcO_4^-, in the waste, forming iron oxide and reduced forms of technetium (e.g., TcO_2), which are immobilized in the support. Judicious choice of the support to particular inorganic materials can enable the technetium-loaded absorbant/support system to be stabilized directly (e.g., through vitrification) into a separate waste form without the need for first isolating the separated technetium.

Research Progress

Introduction

We have been studying the use of nanophase iron supported on a variety of base-stable inorganic materials, such as ZrO_2 and ZnO, in removing pertechnetate from simulated aqueous tank wastes. Support materials have included both commercially available products as well as high surface area (>200 m^2/g), nano-crystalline (<10 nm crystallite diameter) zirconium oxide (predominantly of the cubic form) particulates prepared by a patented PNNL technology (Matson et al. 1997), rapid thermal decomposition of solutes (RTDS). The nanophase iron was applied to these support materials using a proprietary process developed by our collaborators at The Pennsylvania State University.

These materials were tested for technetium uptake under a variety of conditions. The nanophase iron on RTDS ZrO_2 supports both before and after contact with simulant solutions was characterized using x-ray absorption fine structure (XAFS) spectroscopy. The speciation of the technetium absorbed onto the support after contact was also studied using XAFS. Finally, nanophase iron supported on RTDS ZrO_2 after contact with ReO_4^- spiked simulants (where Re is being used as surrogate for Tc [Darab and Smith 1996]) was mixed with a glass frit and heat treated to different temperatures to evaluate the potential for encapsulating the loaded absorbant/support material into a waste form.

Removal of Pertechnetate by Supported Nanophase Iron

A simplified Hanford double-shell slurry feed (DSSF) simulant consisting of 7.4 M Na^+, 3.1 M NO_3^-, 3.8 M OH^-, and 0.27 M CO_3^- of pH ~13-14 was used as a basis for these experiments. A stock solution of $NaTcO_4$ was used to spike this base simulant to various concentrations of TcO_4^-.

Samples of the supported nanophase iron materials to be studied were weighed and placed in pre-weighed centrifuge tubes. To each centrifuge tube, an aliquot of Tc-spiked simulant was added using a plastic syringe, and the tube weighed again. A blank spike and a blank were also carried throughout the experiment. All centrifuge tubes were placed on an orbit shaker for 24 hours, after which each tube was weighed, then centrifuged at 1500 rpm for 10 minutes. Using individual plastic 5-mL syringes for each sample, approximately 4 drops of each solution filtered through a 0.2 μm filter was placed in a pre-weighed glass scintillation vial and weighed again to determine the aliquot mass. The technetium remaining in solution after batch contact with the supported nanophase iron material was determined by several methods, including liquid scintillation.

The results of the pertechnetate removal experiments for various starting concentrations of TcO_4^- and phase ratios (defined as the volume of solution in contact with a given mass of absorbant) are summarized in Table 1 in the form of K_d values (which is defined as the ratio of the amount of a particular species—technetium in this case—absorbed onto the absorbant to the amount left in solution). Absorbent/support materials that provide high K_d values are most desirable. Although we have not yet optimized the class of materials being studied in this project, the results summarized in Table 1 indicate that we are achieving reasonable pertechnetate K_d values. As a comparison, using an experimental phase ratio of 100 L/kg, the commercially available organic ion exchange resins, Reillex™-HPQ and ABEC-5000, were determined to have pertechnetate K_d values of 380 and 160 L/kg, respectively (Blanchard et al. 1997). To put these results in a different light, nanophase iron on RTDS ZrO_2 supports evaluated with a phase ratio of 645 absorbed 11 kg of TcO_2) (the form the technetium is believed to be in after reacting with the iron) per 100 kg of absorbant/support material.

Table 1. Pertechnetate Removal by Nanophase Iron Supported on Different Materials

Support Material	Iron Present? (Y/N)	Starting $[TcO_4^-]$ (mM)	Phase Ratio (L/kg)	K_d (L/kg)
RTDS ZrO_2	N	9.7	153	2
RTDS ZrO_2	Y	12.4	150	80
RTDS ZrO_2	Y	9.0	645	160
Commercial ZrO_2	Y	12.4	150	16
Commercial ZrO_2	Y	9.0	624	68
Commercial ZnO	Y	12.4	150	6

XAFS Characterization of Supported Nanophase Iron

XAFS experiments on the starting nanophase iron supported on RTDS ZrO_2 were performed at the National Synchrotron Light Source (NSLS). Initial analyses of the results indicate that a considerable fraction of the iron occurs as Fe(0) with the balance being Fe(II/III). After contacting this same material in the simplified Hanford DSSF simulant discussed above, but containing NH_4ReO_4 instead of $NaTcO_4$ (where Re is being used as surrogate for Tc [Darab and Smith 1996]), the iron became more oxidized, although a small fraction of Fe(0) still remained. A more detailed analysis of these results is ongoing.

XAFS Characterization of Technetium

XAFS analyses of the technetium contained on the nanophase iron/RTDS ZrO_2 material after being contacted with pertechnetate-containing solution were performed at the Stanford Synchrotron Radiation Laboratory through our collaborations with Lawrence Berkeley National Laboratory. Initial analyses of the results indicate that the technetium occurs most likely as TcO_2. A more detailed analysis of these results is ongoing.

Encapsulation of Used Absorbant/Support Materials

An alkali borosilicate-based glass frit previously developed at PNNL for the encapsulation of plutonium-containing ash was used to attempt to encapsulate the used solid material obtained after contacting nanophase iron supported on RTDS ZrO_2 with simplified DSSF simulant (see above) containing ReO_4^-. The used solids were mixed with this glass frit (10-20 wt% loading) and heat treated to various temperatures up to 800°C. Foaming was observed in some cases, but in one instance, a dense sintered pellet of encapsulated material was successfully prepared.

Planned Activities

Further testing will be performed to evaluate the technetium removal efficiency of new absorbant/support materials. Additional studies on encapsulating the used absorbant/support material, including those obtained from tests performed with TcO_4^-, are planned. Characterization and evaluation of the starting absorbant/support materials, the technetium after contact with the materials, and the stabilized materials will continue.

References

Blanchard DL, GN Brown, SD Conradson, SK Fadeff, GR Golcar, NJ Hess, GS Klinger, and DE Kurath. 1997. *Technetium in Alkaline, High-Salt, Radioactive Tank Waste Supernate: Preliminary Characterization and Removal.* PNNL-11386, Pacific Northwest National Laboratory, Richland, Washington.

Darab JG and PA Smith. 1996. "Chemistry of technetium and rhenium species during low-level radioactive waste vitrification." *Chem. Mater.* 8:1004.

Matson DW, JL Fulton, JC Linehan, RM Bean, TD Brewer, TA Werpy, and JG Darab. 1997. "Catalysts material and method of making." United States Patent No. 5,652,192.

Modeling of Spinel Settling in Waste Glass Melter

(First Year of Funding: FY 1998)

Principal Investigator

Dr. Pavel Hrma
Pacific Northwest National Laboratory
P.O. Box 999, MSIN K6-24
Richland, WA 99352
(509) 376-5092 (phone)
(509) 372-0682 (fax)
pavel.hrma@pnl.gov

Co-Principal Investigator

Dr. Petr Schill
Glass Service, Ltd.
Vsetin, Czech Republic
+420-657-611-439 (phone)
+420-657-611-430 (fax)
research@gsl.cz

University Collaborators

Professor Lubomir Nemec
Institute of Inorganic Chemistry
Czech Academy of Sciences
Prague, Czech Republic
+420-2-24-310-371 (phone)
nemec@uach.iic.cas.cz

Dr. Jaroslav Klouzek
Institute of Chemical Technology
Prague, Czech Republic
jaroslav.klouzek@vscht.cz

Dr. Martin Mika
Institute of Chemical Technology
Prague, Czech Republic
martin.mika@vscht.cz

Contributors

Pavel Izak (Post Master Research Associate)
Trevor Plaster (Undergraduate Student Fellow)

Research Objective

Each 1% increase of waste loading (W), defined as the high-level waste (HLW) mass fraction in glass, can save the U.S. Department of Energy (DOE) over a half billion U.S. dollars for vitrification and disposal. For a majority of Hanford and Savannah River waste streams, W is limited by spinel precipitation and settling in waste glass melters. Therefore, a fundamental understanding of spinel behavior is crucial for economy and the low-risk operation of HLW vitrification.

The goal of this research is to develop a basic understanding of the dynamics of spinel formation and motion in velocity, temperature, and redox fields that are characteristic for the glass-melting process. This goal is being achieved by directly studying spinel formation and settling in molten glass and by developing a mathematical tool for predicting the spinel behavior and accumulation rate in the melter.

The main potential benefit of this study is achieving a lower waste-glass volume, which translates into a shorter cleanup time, a smaller processing facility, a smaller repository space, and, hence, a reduced investment of time and money to reach acceptable technical risks. Additional benefits include 1) more accurately assessing sensible limits for problem constituents (such as chromium) in the melter feed, 2) reducing the blending requirements, and 3) comparing cost and risk with other options (pretreatment, blending or diluting the waste) to determine the best path forward. The results of this study will allow alternate melter designs and operating conditions to be evaluated. The study will also address the option of removing the settled sludge from the melter.

Problem Statement

Accumulation of insoluble phases interferes with melter operation and shortens melter lifetime. The current HLW vitrification strategy is to minimize insoluble phases and to avoid crystallization in the melter by imposing on glass formulation the requirement that the liquidus temperature (T_L) is below the minimum temperature of the glass in the melter (T_L <1050°C). This restriction avoids the risk of spinel formation in the melter at a very high cost. An adequate constraint of crystallization behavior of HLW glass may result in an increase of W by several mass per cents.

This project is generating essential thermodynamic, kinetic, hydrodynamic, and rheological data to assess the rate that spinel forms and settles. These data include physical and geometric parameters of the melter, glass properties, spinel equilibria in HLW glass, spinel crystallization kinetics, the rate of spinel settling in high-viscosity melts (subjected to complex velocity, temperature, and redox fields), and the rheological characteristics of spinel sludge in molten glass. The rate of spinel settling and accumulation on the melter bottom will be estimated using mathematical modeling. In addition, the study will address spinel formation during the melter feed reactions, spinel agglomeration, and spinel interaction with gas bubbles.

Research Progress and Implications

Melter Selection

The slurry-fed ceramic melter (SFCM) designed and operated at Pacific Northwest National Laboratory (PNNL) (Goles and Nakaoka 1990) was selected for the modeling work.

Glass Selection

Based on previous studies (Mika et al. 1997, Hrma et al. 1999), nine glasses were formulated with different content of spinel-forming oxides (NiO, Cr_2O_3, Fe_2O_3, and MnO). Glass compositions and their liquidus temperatures (T_L) are listed in Table 1.

Table 1. Compositions (in Mass Fractions), Estimated Viscosity, and Measured T_L of Glasses

	MS-1	MS-2	MS-3	MS-4	MS-5	MS-6	MS-7	MS-8	MS-9
Al_2O_3	0.080	0.080	0.080	0.080	0.080	0.0800	0.0800	0.0800	0.0800
B_2O_3	0.070	0.070	0.070	0.070	0.070	0.0700	0.0700	0.0700	0.0700
Cr_2O_3	0.007	0.005	0.005	0.005	0.005	0.0035	0.0030	0.0035	0.0100
Fe_2O_3	0.130	0.145	0.115	0.089	0.115	0.1250	0.1150	0.1250	0.1100
Li_2O	0.045	0.040	0.040	0.045	0.041	0.0300	0.0454	0.0300	0.0400
MgO	0.006	0.006	0.006	0.006	0.006	0.0060	0.0060	0.0060	0.0060
MnO	0.005	0.005	0.005	0.005	0.005	0.0036	0.0050	0.0036	0.0036
Na_2O	0.157	0.153	0.153	0.153	0.153	0.1573	0.1530	0.1573	0.1573
NiO	0.020	0.012	0.012	0.012	0.007	0.0140	0.0095	0.0075	0.0100
SiO_2	0.450	0.424	0.454	0.475	0.458	0.4600	0.4531	0.4600	0.4531
ZrO_2	0.030	0.060	0.060	0.060	0.060	0.0506	0.0600	0.0571	0.06
η (Pa·s)[a]	4.19	4.10	5.37	5.37	5.37	7.62	4.43	7.62	5.08
T_L (°C)[b]	1247	1215	1185	1139	1171	1225	1114	1125	1199
T_L (°C)[c]	1221	1223	1188	1144					

(a) Estimated value at 1150°C.
(b) Measured value at PNNL.
(c) Measured value at the Institute of Chemical Technology, Prague.

MS-4 glass was chosen as an internal standard for T_L. MS-7 and MS–9 glasses are used as model glasses for this study.

Glass and Spinel Properties

The viscosity (η) data of MS-7 glass and electrical conductivity (ε) data for MS-7 and MS-9 glasses are listed in Table 2. Viscosity versus temperature for MS-7 glass has been fitted as $\ln(\eta) = -6.00155 + 6072/(540.9 + T)$. The specific heats of molten glasses measured by a differential scanning calorimeter (DSC) within the temperature interval from 850°C to 1250°C are $c_p = 1.35\ J \cdot g^{-1} \cdot K^{-1}$ for MS-7 glass and

$c_p = 1.860 - 1.00\times10^{-4}T - 1.508\times10^{5}T^{-2}$ (T is in K) for MS-9 glass. The preliminary estimate for the effective heat conductivity of MS glasses at 1150°C is $k_{ef} = 3.31$ $W\cdot m^{-1}\cdot K^{-1}$. This estimate is based on measured values for welding glasses with a similar iron content.

Table 2. Viscosity Data for MS-7 Glass and Electrical Conductivity Data for MS-7 and MS-9 Glasses

MS-7				MS-9	
T (°C)	η (Pa·s)	T (°C)	ε (S/m)	T (°C)	ε (S/m)
1251	1.14	1245	67.87	1250	62.14
1210	1.59	1206	59.98	1201	54.97
1171	2.11	1157	51.89	1152	47.30
1140	2.67	1109	44.17	1104	40.02
1094	3.76	1059	36.80	1055	33.29
1049	5.93	1011	30.13	1006	27.19
1000	9.83	963	24.04	958	21.70
950	17.78	913	18.59	908	16.72
902	35.81	864	13.80	859	12.51
853	79.78				

Spinel was separated from SS-AA glass designed to produce a large fraction of spinel while the glass was sufficiently fluid to allow settling. SS-AA glass composition in mass% oxides is SiO_2 44.94, B_2O_3 6.84, Na_2O 15.37, Li_2O 2.93, MgO 2.11, Al_2O_3 7.82, Fe_2O_3 14.93, Cr_2O_3 1.50, MnO 0.35, and NiO 3.21. This glass was heated for five days at 1100°C to generate spinel sludge for rheological studies and for isolating spinel. To separate spinel, the solid sludge was dissolved in HNO_3 at 60°C for four days. A magnet was used to remove spinel from the residue. The density of this spinel was estimated from the x-ray diffraction (XRD)-lattice parameters to be 5.1 to 5.2 $g\cdot cm^{-3}$; its volume expansion coefficient is approximately 6.5×10^{-5} K^{-1}. Spinel composition was measured indirectly by calibrated scanning electron microcopy with energy-dispersive spectroscopy (SEM-EDS), and directly by separating spinel from the glass and using energy dispersive x-ray fluorescence (EDXRF).

Spinel Equilibria

The effect of the concentration of spinel-forming components in glass on the equilibrium fraction of spinel is shown in Figure 1. The effect of HLW components on T_L with the spinel primary phase is shown in Table 3 (Hrma et al. 1999).

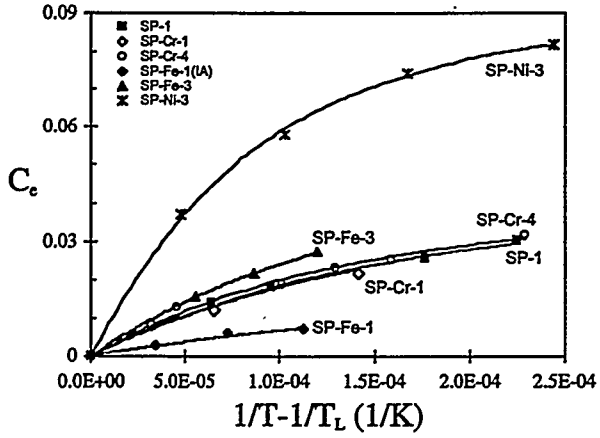

Figure 1. Equilibrium Fractions of Spinel in the Baseline Glass SP-1 and Glasses with Varied Spinel-Forming Components Displayed as a Function of Temperature (Stachnik and Hrma 1999). The content of spinel-forming oxides (in mass%) was Cr_2O_3 0.22, NiO 0.52, and Fe_2O_3 12.50 in SP1; Cr_2O_3 0.00 in SP-Cr-1 and 1.20 in SP-Cr-4; NiO 3.00 in SP-Cr-3; Fe_2O_3 6.00 in SP-Fe-1 and 15.00 in SP-Fe3. The remaining components were in the same proportions as in SP-1.

Table 3. Partial Specific T_L Values (T_{Li}) for Glass Components (in °C)

Al_2O_3	B_2O_3	CaO	Cr_2O_3	Fe_2O_3	K_2O	Li2O	MgO	MnO	Na_2O	NiO	SiO_2	TiO_2	U_3O_8	Others
2866	403	1757	20592	2685	-980	-1367	3820	1312	-1736	9530	1010	4925	1633	3583

The spinel equilibrium fraction (C_e) is measured by heat-treating the glass long enough at a constant temperature to reach equilibrium, quenching the melt and using quantitative XRD. The results are checked by optical microscopy with an image analyzer. Spinel equilibrium as a function of temperature can be fitted by the equation (Reynolds and Hrma 1997)

$$C_e = C_{\max}\left\{1-\exp\left[-B_L\left(\frac{1}{T}-\frac{1}{T_L}\right)\right]\right\}. \tag{1}$$

where $C_{\max}$, and B_L are composition-dependent coefficients.

Spinel Precipitation Kinetics

Reynolds and Hrma (1997) have shown that spinel nucleates readily, without a measurable incubation period, and crystallizes rapidly (Figure 2). Spinel crystallization kinetics can be represented by the equation

$$\frac{dC}{dt} = nk(C_e - C)\left[-\ln\left(1-\frac{C}{C_e}\right)\right]^{(n-1)/n} \tag{2}$$

where C is the spinel fraction in molten glass, n the Avrami number, the value of which is $n = 1.5$ for spinel crystallization in a HLW borosilicate glass and

$$k = k_0 \exp\left(-\frac{B_k}{T}\right) \tag{3}$$

is the crystallization rate coefficient; k_0, and B_k are composition-dependent coefficients. Equation (2) can be solved for a T = constant to yield the Kolmogorov-Mehl-Avrami-Johnson equation:

$$C = C_e\left\{1-\exp\left[-(kt)^n\right]\right\} \tag{4}$$

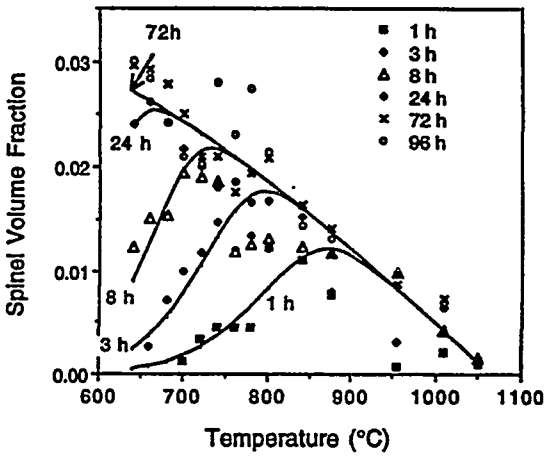

Figure 2. Volume Fraction of Spinel Precipitated from a HLW Glass under Isothermal Conditions as a Function of Temperature and Time (Reynolds and Hrma 1997)

For spinel formation under a more complex temperature history, Equation (2) needs to be verified. Casler and Hrma (1999) made the first step in this direction by solving Equation (2) for a constant rate of cooling and for the temperature history typical for a HLW glass canister.

The dependence of the equilibrium and kinetic coefficients, i.e., C_{max}, B_L, k_0, and B_k, on glass composition provides an opportunity for optimization guided by mathematical modeling. This dependence is most conveniently represented by partial specific coefficients defined by the equation (Hrma 1998)

$$P = \sum_{i=1}^{N} P_i g_i \tag{5}$$

where P is a composition-dependent coefficient, P_i is the i-th component partial specific coefficient (also called component coefficient), g_i is the i-th component mass fraction in glass, and N is the number of the key components. Composition coefficients for T_L are listed in Table 3.

The composition effects (including glass redox) on spinel equilibrium and the rate of crystallization in MS-7 glass are being measured as a function of temperature. We use ultraviolet-visible-near infrared (UV-VIS-NIR) and Mössbauer spectroscopy to measure the iron redox ratio in glass and spinel. To control the oxygen pressure, we equilibrate glass with CO/CO_2 atmosphere.

Spinel Dissolution Kinetics

Spinel forms during the batch melting reactions, dissolves as temperature increases, and precipitates again as the melt temperature decreases below T_L. The spinel dissolution rate determines how much, if any, of the original spinel survives in the stream of molten glass and subsequently grows at colder sections of the melter. Because spinel dissolution occurs near T_L, where glass has a low viscosity, settling of crystals interferes with the measurement. The same is true about crystallization kinetics near T_L. Preparations for the dissolution study are in progress.

Spinel Formation in the Cold Cap

Melting reactions in HLW glass batches were investigated previously (Anderson et al. 1994a, b; Smith et al. 1995; Vienna et al. 1999). However, little is known about spinel formation during the initial melting reactions. A quantitative description of spinel formation during melting reactions is needed for

realistic modeling. Spinel formation during the batch melting reactions is being investigated using a time-temperature function that is close to the temperature history of feed within the cold cap.

Melter feed slurries were prepared for MS-7 and MS-9 glasses. Spinel-forming components in the form of Fe, Ni, Cr, and Mn nitrates were dissolved in deionized water and co-precipitated by mixing the solution with enough 10 M NaOH at 40°C to supply the Na_2O of the glass. Other feed components, $ZrO(NO_3)_2 \cdot 2H_2O$, $Mg(NO_3)_2 \cdot 6H_2O$, Li_2CO_3, SiO_2 sand (≤190 μm), Al_2O_3, and H_3BO_3 were stirred into the co-precipitate to prepare the slurry feed. The slurry was dried in an oven at 90°C for two days. Approximately 1.3-g samples were ramp-heated in platinum crucibles at 4°C/min starting from 200°C. Crucibles were removed from the furnace at different temperatures, quenched, and analyzed by XRD and SEM.

The semi-quantitative mass fractions of crystalline phases in MS-7 glass are plotted against temperature in Figure 3. Nitrates decomposed and quartz dissolved by 750°C. Spinel appeared above 400°C, peaked at 650°C, and dissolved by 1150°C. A yellow-green chromate melt occurred at 700°C to 900°C. Feed volume increased several times at temperatures above 700°C and collapsed at above 900°C. Interestingly, carnegieite was observed above 700°C and persisted up to 1150°C. The work is ongoing.

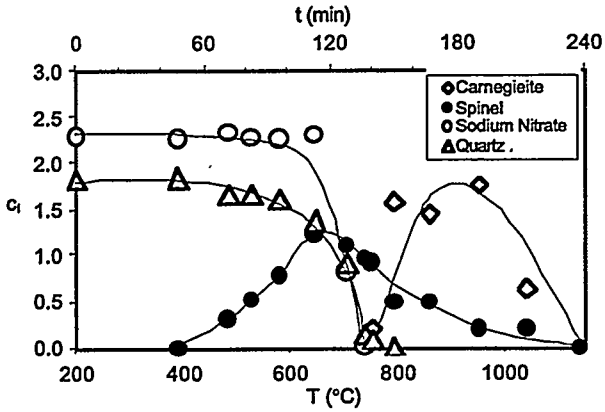

Figure 3. Evolution of Crystalline Phases During Ramp Heating of MS-7 Glass Feed (c_i is crystal fraction in mass%)

Spinel Agglomeration and interaction with Gas Bubbles

Agglomeration and interaction with bubbles may influence spinel settling in melters. LaMont and Hrma (1998) observed these phenomena in laboratory crucibles. Spinel agglomerates by the shear flocculation mechanism in steep velocity (Cobb and Hrma 1991, LaMont and Hrma 1998, Schweiger et al. 1998). LaMont and Hrma (1998) observed the interaction of spinel with bubbles in silica crucibles as a result of silica dissolution in the melt. Evidence exists (Kim and Hrma 1994) that a large concentration of bubbles produced by redox reactions affects the melt flow under the cold cap. Mathematical modeling of the redox field will show the degree to which bubbles and spinel can interact within the melter.

Spinel Settling

The hydrodynamics of spinel settling in a high-viscosity liquid entails a two-phase mixture of spinel and molten glass. LaMont and Hrma (1998) have shown that spinel particles in molten glass behave as a swarm rather than individual bodies even when their concentration is low and distances between them are large. Spinel settling produced a single flow-cell within the crucible, indicating that in a larger volume of melt, a cellular convection pattern will probably evolve.

We conducted preliminary experiments with corundum particles suspended in a model liquid of the same viscosity as molten glass. The suspension was dyed and placed on top of pure model liquid. Settling was recorded by camera (Figure 4). The corundum particles did not settle individually; the suspension plunged into the less dense liquid below. The maximum velocity, measured at the tip of the plume, was nearly time-independent and increased nearly linearly with corundum concentration (Figure 5). These results will be used for model verification.

Mathematical Model

Mathematical modeling adopted in this study is based on a numerical solution of field equations on a system of three-dimensional discrete grids by the control-volume method that enables proper balances of all quantities. We modified the glass model code to accept specific features of the SFCM geometry, the slurry and cold cap regions, the electrode arrangement, special input and output, and material properties. After tuning, the code was modified to incorporate density variation caused by spinel and to describe spinel settling. The first stage of the project is focused on mathematical simulation of the temperature, electric, and velocity fields in the melt and the cold-cap of a test SFCM under various operation conditions. This simulation is based on literature data and PNNL staff communication (Peters et al. 1990; Goles and Nakaoka 1990).

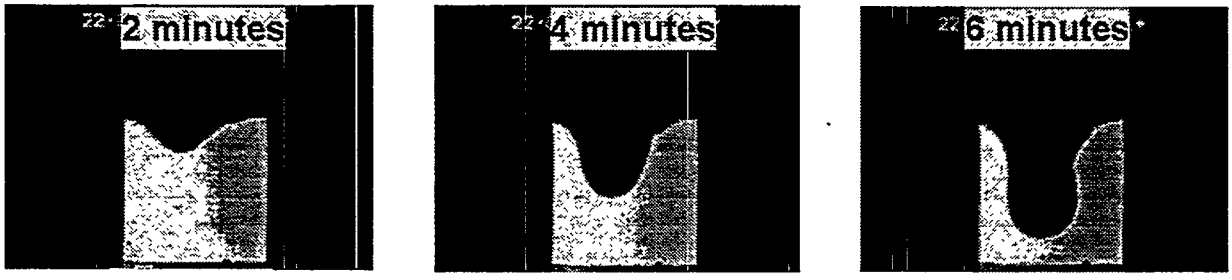

Figure 4. Motion of the Boundary between the Liquid with Suspended Corundum Particles (10 μm, 5 g·m^{-3}) and the Pure Liquid

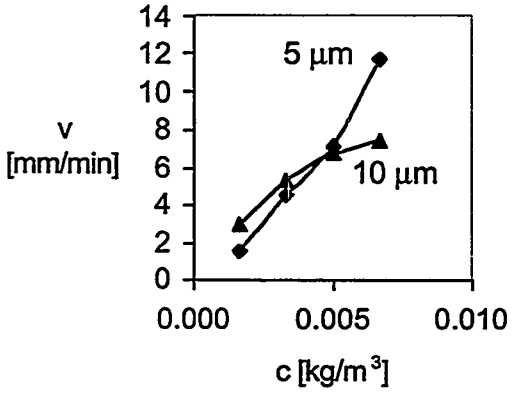

Figure 5. The Settling Velocity Versus Corundum Concentration

The glass model code was adapted to 1) accept a batch blanket composed from two parts (the slurry pool and the cold cap), 2) approximate the plenum space, and 3) enable glass density dependence on other than temperature variables. The SFCM geometry was set up by the Glass Service GS-CAD program using PNNL blueprints. The model melter has the 0.79-m nominal glass depth, 2.0-m^2 surface area

(1.15×1.73 m), and 0.67-m plenum space height above the glass. Two electrode walls have a 30° slope, and the remaining two walls have a 66° slope against the horizontal level. The melt was Joule-heated by single-phase electric current from three submerged bock electrodes (Elliott et al. 1994).

The nonuniform net, automatically generated by the GS-CAD program, involved 79×91×84 grid nodes. Measured MS-7-glass properties were used when available; other melt properties (Table 4) were taken from the literature (Peters et al. 1990, Palmer 1991, Eyler et al. 1991). The batch-to-glass conversion degree was estimated from gradient-furnace experiments (Anderson et al. 1994a).

The operation parameters and boundary conditions were set up as follows (Peters et al. 1990; Palmer 1991; Choi 1991):

glass pull:	1080 kg/day
electrode voltage:	-56.8 V (bottom electrode), +28.4 V (side electrodes)
total electric supply:	96 kW
surface temperature:	900°C (glass), 100°C (slurry), 500°C (cold cap)
melter operating temperature:	1150°C

The Joule heat distribution (Figure 6, upper left) shows unusually high values in the middle-lower part and low values in the middle-upper part. This Joule heat distribution can by changed by modifying electrode voltages if necessary. The temperature and flow in both cuts (cross and longitudinal) show the good mixing ability of this type of melter.

Table 4. Glass Properties as Function of Temperature (in K)

Property	Formula
Density [kg/m^3]	$\rho(T) = 2497 - 0.2300T$
Kinematic Viscosity [m^2/s]	$\nu(T) = \exp[-20.02 + 19880/(4.663\times10^{-4} + T)]$
Specific Heat [J/(kg·K)]	$c = 2512$
Thermal Conductivity [W/(m·K)]	$\lambda(T) = 1.78 + 0.0004T$ at $300<T<1000$
	$\lambda(T) = 2.737 - 0.0024214T + 1.86384\times10^{-6}T^2$ at $1000<T<1800$
Electrical Conductivity [S/m]	$\sigma(T) = \exp[6.921 - 2844/(-475.0 + T)]$

For the spinel settling model, we treated spinel as a mixture component characterized by the pure-component density (ρ_0), particle diameter (d), and mass concentration (c). For spinel-melt interaction, we postulate the constitutive equation

$$F^g = -A(c,d)v^g\left(u^g - u\right) \tag{6}$$

where F^g is the force from particles to glass, υ^g is the liquid kinematic viscosity, u^g is the liquid velocity, u is the velocity of particles, and A is a coefficient that depends on c and d, such that $A(0) = 0$. For small c and d, $A = A_0cd$, where A_0 is a shape factor.

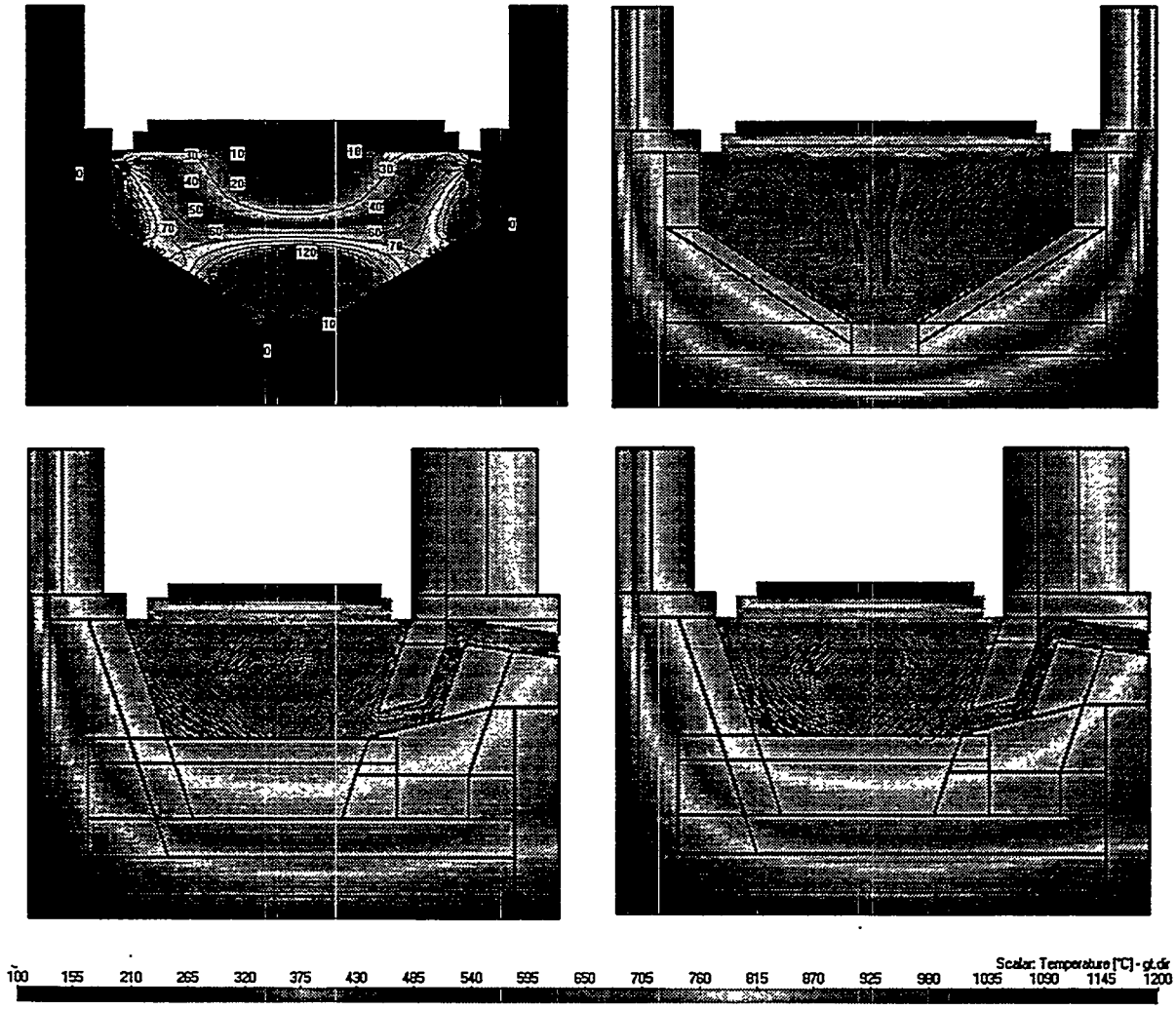

Figure 6. Examples of Electric (in kW/m^3), Temperature, and Flow Fields

We used the particle mass balance and the balance of force

$$u \cdot \nabla c = D\Delta c + E(c) \tag{7}$$

$$\frac{d}{dt}(cu) = -F^g + \frac{\pi}{6}(\rho^g - \rho)gd^3 \tag{8}$$

where D is the diffusion coefficient (estimated from the Stokes-Einstein equation), E(c) is the source term, and g is gravity. Equations (6) to (8) constitute the basis for modeling experiments, currently in progress.

Spinel Sludge Rheology

Spinel sludge was prepared by the method described above. Its behavior was tested using a rotatind spindle viscometer. Preliminary results indicate that spinel sludge behaves as a pseudoplastic rheopectic liquid.

Planned Activities

We will continue to measure the kinetics of spinel crystallization and dissolution under both isothermal and nonisothermal conditions and to evaluate component coefficients for spinel equilibrium and kinetics. The study of the redox effect on spinel formation will also continue.

We will study the spinel settling mode and rate in molten glass and also pay attention to spinel agglomeration and interaction with bubbles. We will finish the study of spinel sludge rheology as a function of temperature, shear rate, and aging. Physical modeling will be further developed to verify mathematical models.

The modified mathematical model will be used to predict the rate of spinel settling in the melter. A parametric study of mathematical simulation will be performed, focusing on identifying the potential for glass formulation optimization and melter design and operation optimization with respect to waste vitrification economy (maximum waste loading) and minimum risk (minimum spinel accumulation and melter disturbances).

References

Anderson LD, T Dennis, ML Elliott, and P Hrma. 1994a. "Waste glass melting stages." *Ceram. Trans.* 39:213-220.

Anderson LD, T Dennis, ML Elliott, and P Hrma. 1994b. "Noble metal behavior during melting of simulated high-level nuclear waste feeds." *Ceram. Trans.* 39:213-222.

Casler DG and P Hrma. 1999. "Nonisothermal kinetics of spinel crystallization in a HLW glass." *Scientific Basis for Nuclear Waste Management* (eds.), Material Research Society, Pittsburgh, Pennsylvania. (In print)

Choi IG. 1991. "Mathematical modeling of radioactive waste glass melter." *Ceram. Trans.* 23:385-394.

Cobb WT and P Hrma. 1991. "Behavior of RuO_2 in a glass melt." *Ceram. Trans.* 23:233-237.

Elliott ML, LL Eyler, LA Mahoney, MF Cooper, LD Whitney, and PJ Shafer. 1994. *Preliminary melter performance assessment report.* PNL-9822, Pacific Northwest Laboratory, Richland, Washington.

Eyler LL, ML Elliott, DL Lessor, and PS Lowery. 1991. "Computer modeling of ceramic melters to assess impacts of process and design variables on performance." *Ceram. Trans.* 23:395-407.

Goles RW, and RK Nakaoka. 1990. *Hanford Waste Vitrification Program Pilot-Scale Ceramic Melter.* PNL-7142, Pacific Northwest Laboratory, Richland, Washington.

Hrma P. 1998. "Empirical models and thermodynamic constitutive functions for high-level waste glass properties." *Ceram. Trans.* 87:245-252.

Hrma P, JD Vienna, M Mika, JV Crum, and GF Piepel. 1999. *Liquidus Temperature Data for DWPF Glass.* PNNL-11790, Pacific Northwest National Laboratory, Richland, Washington.

Kim DS and P Hrma. 1994. "Laboratory studies for estimation of melting rate in nuclear waste glass melters." *Ceram. Trans.* 45:409-419.

LaMont MJ and P Hrma. 1998. "A crucible study of spinel settling in a high-level waste glass." *Ceram. Trans.* 87:343-348.

Mika M, MJ Schweiger, and P Hrma. 1997. "Liquidus temperature of spinel precipitating high-level waste glass." WJ Gray and IR Triay (eds.), *Scientific Basis for Nuclear Waste Management*, 465:71-78, Material Research Society, Pittsburgh, Pennsylvania.

Palmer RA. 1991. "West Valley strategy for meeting waste acceptance preliminary specifications." *Ceram. Trans.* 23:475-490.

Peters RD, ML Elliott, and CC Chapman. 1990. "Proposed noble metals-compatible melter: Preliminary modeling results." *Ceram. Trans.* 9:567-580.

Reynolds JG and P Hrma. 1997. "The kinetics of spinel crystallization from a high-level waste glass." WJ Gray and IR Triay (eds.), *Scientific Basis for Nuclear Waste Management* 465:65-69, Material Research Society, Pittsburgh, Pennsylvania.

Schweiger MJ, MW Stachnik, and P Hrma. 1998. "West Valley high-level waste glass crystallization in canisters." *Ceram. Trans.* 87:335-341.

Smith PA, JD Vienna, and P Hrma. 1995. "The effect of melting reactions on laboratory-scale waste vitrification." *J. Mat. Res.*, 10[8]:2137-2149.

Stachnik MW, P Hrma, and H Li. 1999. "Effects of high-level waste glass composition on spinel precipitation." *Ceram. Trans.* 107 (to be published).

Vienna JD, DK Peeler, JG Darab, JR Zamecnik, H Li, and JE Mara. 1999. "Chemistry of rare earth oxalate vitrification" (to be published).

Publications and Presentations

Mika M, P Hrma, and MJ Schweiger. "Rheology of spinel sludge" (in preparation).

Stachnik MW, P Hrma, and H Li. 1999. "Effects of high-level waste glass composition on spinel precipitation." *Ceram. Trans.* 107 (to be published).

Izak P, P Hrma, and MJ Schweiger. "Nonisothermal crystallization of spinel from a high-level waste feed" (submitted to American Ceramic Society 1999 meeting).

Hrma P, P Izak, J Klouzek, M Mika, L Nemec, and P Schill. "Chemistry and hydrodynamics of spinel settling in molten glass" (submitted to ACS 1999 meeting).

Schill P. "A three-dimensional mathematical model of radioactive waste glass melter" (submitted to American Ceramic Society 1999 meeting).

Ion-Exchange Processes and Mechanisms in Glasses

(First Year of Funding: 1997)

Principal Investigator

Dr. B. P. McGrail
Pacific Northwest National Laboratory
P.O. Box 999, MSIN K6-81
Richland, Washington 99352
(509) 376-9193 (phone)
(509) 376-2210 (fax)
pete.mcgrail@pnl.gov

Contributors and Collaborators

D. R. Baer (PNNL)
J. G. Darab (PNNL)
M. H. Engelhard (PNNL)
J. P. Icenhower (PNNL)
D. K. Shuh (LBNL)
S. Thevusathan (PNNL)

Research Objective

Recent performance assessment calculations (Mann et al. 1998) of a disposal system at Hanford, Washington, for low-activity waste (LAW) glass show that a sodium ion-exchange reaction can effectively increase the radionuclide release rate by over a factor of 1000 and so is a major factor that currently limits waste loading. However, low-temperature ion exchange has not been thought to be important in recent analyses of waste-glass durability. The objective of this work is to develop an understanding of the processes and mechanisms controlling alkali ion exchange and to correlate the kinetics of the ion-exchange reaction with glass structural properties. The fundamental understanding of the ion-exchange process developed under this study is targeted at developing lower ion-exchange-rate glasses that would remain durable at higher alkali waste loading.

Research Statement

This multidisciplinary research program involves two primary tasks to develop an understanding of the processes and mechanisms that control ion exchange, specifically sodium ion exchange, in waste glass materials: 1) reaction mechanisms and 2) glass structure correlations. The objective of the reaction mechanisms task is to identify specific ion-exchange mechanism(s) by using surface analytical techniques to probe the distribution of selected elements in the hydrated layers on glass surfaces. Differences in the uptake and distribution of selected isotopes will provide a signature characteristic of specific ion-exchange reactions. The objective of the glass structure task is to determine whether differences in key structural properties, such as the number of nonbridging oxygens (NBO), bonding of alkali to other elements in the glass, and alkali coordination, can be correlated with differences in measured rates of alkali exchange. The reaction mechanisms and glass structure tasks are discussed in detail in the following sections.

An overview of the proposed research plan is given in Figure 1. To simplify interpretation of the kinetics measurements and glass structure analyses, three series of simple glasses in the Na_2O-Al_2O_3-B_2O_3-SiO_2 family will be examined where the amounts of sodium, aluminum, boron, and silicon are systematically varied along compositional joins. Selective substitutions of network modifiers such as CaO, ZrO_2, and La_2O_3, will also be made in the base glass to change the bonding coordination of Na^+ with network intermediate sites. Differences in the structural properties of these glasses will then be correlated with observed changes in the sodium ion-exchange kinetics. It is the *combination* of the glass structure correlations with the identification of the ion-exchange reaction mechanism(s) that provides the underpinning scientific basis for formulation of glasses with lower rates of alkali ion exchange. This new understanding of ion-exchange processes and mechanisms will be evaluated at the conclusion of this research project in the formulation and testing of a low ion-exchange rate glass with a 25 wt% Na_2O loading.

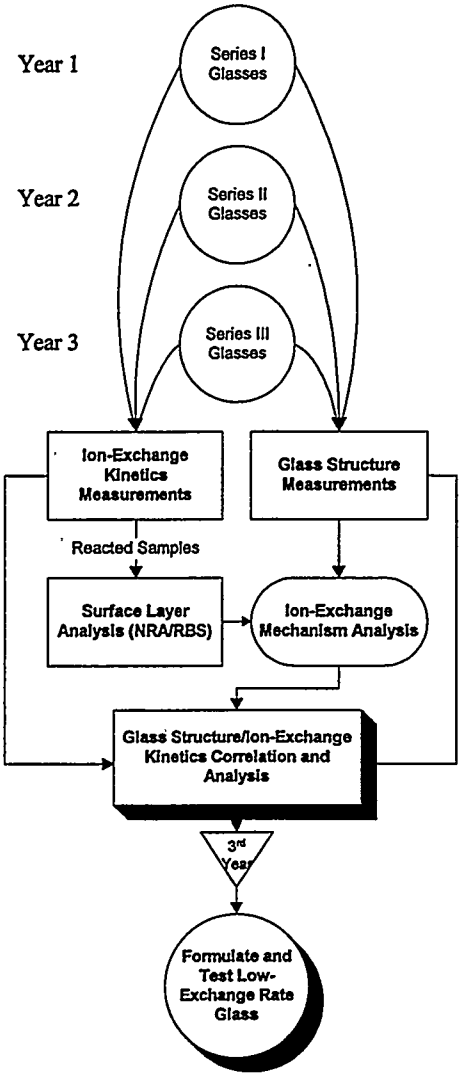

Figure 1. Research Plan Flow Chart

Research Progress

Project Status

This project was initiated in FY 1998 and is being performed cooperatively between Pacific Northwest National Laboratory (PNNL) and Lawrence Berkeley National Laboratory (LBNL). Progress has primarily focused on three activities: 1) developing and manufacturing the Series I glasses and formulating Series II glasses, 2) characterizing these glasses, and 3) conducting flow-through tests for measuring sodium ion-exchange kinetics. A few scoping measurements of isotope distributions have also been completed using nuclear reaction analysis (NRA) and elemental depth profiles using Rutherford backscattering spectroscopy (RBS).

Technical Progress

Current plans for immobilizing low-activity radioactive wastes include vitrification followed by subsurface storage. All scenarios for waste disposal include the provision that groundwater will eventually breach the outer containment and interact with the vitrified material. In many cases, high alkali loading in the glass is a concern because exchange of alkalis in the glass for hydrogen species in solution will cause a rise in solution pH with a concomitant rise in glass dissolution rates. Glass compositions that are vulnerable to alkali leaching may have significantly higher release rates of radioactive elements. Accordingly, our investigation is aimed at understanding the link between glass structure and alkali H-species exchange reactions. These studies will serve the dual purpose of providing decisive information for fashioning alkali leach-resistant glass compositions and probe fundamental glass structure-solution interactions.

The vitrification of LAW streams into durable glass waste forms will be limited by the ability of the glass to accommodate the sodium in the waste. In Na_2O-SiO_2 glasses, for example, the Na_2O enters the glass structure through the formation of and association with NBO sites (e.g., $^{Q3}SiO_{2.5}Na$), making the glass more susceptible to chemical attack. Adding Al_2O_3, for example, to a Na_2O-SiO_2 glass formulation decreases the concentration of NBO sites through the formation of tetrahedrally coordinated AlO_2Na species.

Current models of glass interactions with aqueous solutions state that alkali H-species exchange occurs at small values of reaction progress. However, as we demonstrate, this exchange process continues to occur at high values of reaction progress. This previously unrecognized behavior of glass-solution interactions is important to modeling long-term release rates of radioactive elements in vitrified waste.

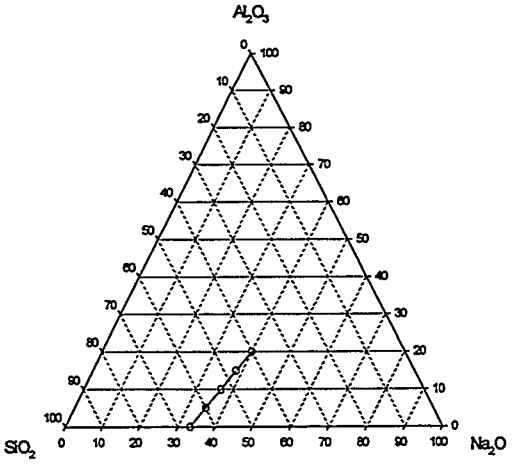

Figure 2. Ternary Diagram Illustrating Compositions of Series I Glasses

Glass System Development

For our initial alkali leaching investigations, we have selected Na-Al-Si glass compositions designed to keep the fraction of metals in the glass that are network formers (f_M^N) constant at 0.50 while varying the distribution of Na^+ between association with ^{Q3}Si non-bridging oxygen sites (f_{Na}^{Q3}) and four-coordinated Al sites (f_{Na}^{Al}) (see Figure 2). Based on a 33.33 Na_2O-66.67 SiO_2 composition, which was given the nomenclature NaSiO-X, five Na_2O-Al_2O_3-SiO_2 glasses were formulated with the concentration of Al_2O_3 ranging from 0 to 20 mol%. Each glass was also doped with 0.1 wt% MoO_3 for use as a tracer of glass matrix dissolution. The glasses were batched in 100+ gram quantities using Na_2CO_3, Al_2O_3 and SiO_2, melted at 1500°C for one hour in air, then quenched on a stainless steel plate. All melts except the NaSiO-20.0Al glass were visually homogeneous and readily pourable and yielded a clear, visibly homogenous glass. Table 1 summarizes the target composition of these glasses. The selected Series II set of glasses consists of a set of Na-B-Si and Na-Al-B-Si glasses as shown in Table 1. Molybdenum was not added to these glasses because boron provides an equivalent tracer element for glass matrix dissolution.

Table 1. Target Compositions (in wt% oxide component), MAS-NMR ^{29}Si Chemical Shift Values (δ), and Normalized 7-Day PCT Mass Loss of Boron (NL_B) for the Glasses Studied in this Work

	Oxide Component					δ (ppm)	NL_B
Glass	SiO_2	B_2O_3	Al_2O_3	Na_2O	Other	^{29}Si[a]	(g/m^2)
Bas-1	74.0	6.0	-	20.0	-	-99±1	[b]
B-3	77.0	3.0	-	20.0	-	-99±1	[b]
B-16	64.0	16.0	-	20.0	-	-97±1	11.70
B-24	56.0	24.0	-	20.0	-	-94.5±0.5	12.13
Al-4	70.0	6.0	4.0	20.0	-	-96±1	6.908
Al-8	66.0	6.0	8.0	20.0	-	-95±1	1.267
Al-16	58.0	6.0	16.0	20.0	-	-92.0±0.5	0.145
Al-24	50.0	6.0	24.0	20.0	-	-90.3±0.5	0.151
NaSiO-X	65.9	-	-	34.1	-	-87±1	NA
NaSiO-5Al	57.3	-	8.1	34.6	-	-86±1	NA
NaSiO-10Al	49.3	-	15.7	35.0	-	-80±1	NA
NaSiO-15Al	41.8	-	22.8	35.4	-	-78±1	NA

(a) Chemical shift reported with respect to TMS (tetramethylsilane).
(b) The Bas-1 and B-3 glasses completely dissolved during the test.
NA = Not applicable.

NMR Characterization

Magic angle-spinning nuclear magnetic resonance (MAS-NMR) spectroscopy is a sensitive technique for studying the structure and chemical environment of many of the nuclei contained in LAW glass (^{11}B, ^{27}Al, ^{29}Si, ^{31}P). We are building on our previous structural characterization work (Darab et al. 1997) to develop a model to predict the ^{29}Si MAS-NMR chemical shift value, δ, for a particular glass, which we then use to describe the chemical nature of the glass network. By using δ as an indicator of the bonding characteristics within a glass network, we take into account the effects of primary bond strengths (Darab et al. 1997) as well as secondary effects, such as partial covalent bonding, which are not accounted for in other models. To date, we have focused on sodium borosilicate, sodium boro-aluminosilicate, and sodium aluminosilicate glasses as well as more complex simulated LAW glasses (see Table 1).

Room temperature ^{29}Si, ^{27}Al, and ^{11}B MAS-NMR spectra were obtained on a Varian VXR-300 spectrometer at 7.05 T using high-speed probes manufactured by Doty Scientific, Inc. Silicon nitride rotors (5 mm diameter) or sapphire rotors (7 mm diameter) with Vespel polymer end caps were used to spin the samples at 5 kHz. In addition to the long-term corrosion studies, a product consistency test (PCT) was used to determine the leachability of the prepared glasses. Powdered glass samples were immersed in distilled/deionized water at 90°C for seven days and the leachate analyzed chemically. Details are summarized in Darab et al. (1997); the relevant MAS-NMR and PCT results are given in Table 1.

For the Bas-1, B-, and Al- series glasses (Table 1), there is a rudimentary relationship between the ^{29}Si chemical shift (δ) and the normalized release of boron (NL_B); for δ less than -99 ppm the glass completely dissolves during PCT evaluation, while relatively durable glasses give rise to δ values greater than about -92 ppm. Glasses with intermediate δ values are indicative of intermediate durability. We have discussed this relationship in more detail in a recent publication (Darab et al. 1999) and plan on testing this approach with the ion-exchange kinetics measurements obtained under this project. The first step in this approach, however, is measuring or predicting the ^{29}Si chemical shift value as a function of glass composition.

The resonance line shapes of the ^{27}Al MAS-NMR spectra obtained from the glasses studied here (not shown) are nearly identical for all the glasses and are indicative of predominantly (>98%) tetrahedral coordination to four oxygens (Darab et al. 1997), which we designate as Al^{iv}, presumably occurring as network forming units. For simplicity, we have assumed that 100% of the Al in these glasses occurs as Al^{iv} units. The environment of the boron in relevant glasses is a combination of both tetrahedrally (B^{iv}), and trigonally (B^{iii}) coordinated sites, the relative amounts of each depending on the composition of the glass (Yun and Bray 1978). MAS-NMR is very sensitive to the coordination symmetry of the boron (spectra not shown), allowing for the quantitative determination of the relative amounts of B^{iv} and B^{iii} in these glasses (Darab et al. 1997; Kirkpatrick 1988).

The tetrahedrally coordinated Al^{iv} (chemically represented by AlO_2^-) and B^{iv} (BO_2^-) sites identified in these glasses need to be charge-compensated through association with alkali (Na^+) cations. Any excess Na^+ then most likely become associated with NBO sites such as ^{Q3}Si (e.g., $SiO_{2.5}Na$) and ^{Q2}Si (e.g., SiO_3Na_2). Based on the summary by Eckert (1992) and the concentration of the sodium-gettering Al_2O_3/B_2O_3 components in the glasses examined in this work, the distribution of silicon species will occur predominantly between ^{Q4}Si and ^{Q3}Si with much less than 10% as ^{Q2}Si and close to zero ^{Q1}Si. For simplicity, we have assumed that in the glasses discussed here, silicon occurs as ^{Q4}Si and ^{Q3}Si species only. The Na^+ in these glasses is thus distributed between the ^{Q3}Si NBO, B^{iv}, and Al^{iv} sites.

The glass composition and the distribution of structural units within a glass are important factors that dictate the ^{29}Si NMR chemical shift values. For example, as the relative Na_2O content in Na_2O-SiO_2 glasses is increased, the average ^{29}Si MAS-NMR chemical shift value, δ, becomes less negative as more ^{Q3}Si sites are generated at the expense of ^{Q4}Si sites (Kirkpatrick 1988; Eckert 1992). Increasing the relative amount of Al_2O_3 in Al_2O_3-SiO_2 glass compositions causes δ for ^{29}Si to become less negative due to changes in the electron density in the vicinity of the silicon.

Darab et. al. (1999) found that the overall ^{29}Si MAS-NMR chemical shift value for glasses typical of those studied here can be predicted ($r^2 = 0.9915$) using the following expression:

$$\delta = -111 + 51\, f_{Al}^{N} + 44\, f_{B4}^{N} + 22\, f_{Q3}^{N} \quad (1)$$

where

$$f_{Al}^{N} = [Al]/([Si] + [B] + [Al]) \quad (2)$$

$$f_{B4}^{N} = [B^{iv}]/([Si] + [B] + [Al]) \quad (3)$$

$$f_{Q3}^{N} = [^{Q3}Si]/([Si] + [B] + [Al]) \quad (4)$$

X-Ray Absorption Spectroscopy Characterization

The modeling of the near-edge x-ray absorption fine structure (XAFS) spectra at the sodium K-edge has been initiated using the FEFF7 computer code. A series of theoretical calculations of the sodium K near-edge spectrum for the reference sodium compounds were performed and are shown in Figure 3, along with the smoothed near-edge spectrum of Glass #2, a specialty glass for plutonium immobilization (Mann et al. 1998), for comparison. The sodium K-edge XANES structure calculations were done using FEFF7 program and all energies were calibrated to sodium K-edge at 1067 eV (Ankudinov et al. 1992). These results illustrate that there is a significant difference in the structures of sodium K-edge spectra for sodium ions in different crystal environments. Qualitative interpretation of the spectra in Figure 3 suggests that the local structural environment of sodium in Glass #2 resembles that found in Na_2O and Na_2SiO_3.

The theoretical calculations using the FEFF7 methodology form an essential component of the XAFS structural characterization program and will be used extensively throughout to maximize the information obtained from the experimental measurements. FEFF7 will continue to be used to model the sodium K-edge spectra in the near-edge region and in the extended-XAFS region to extract structural parameters. Furthermore, FEFF7 simulations will be used to evaluate model compounds before experimentation to maximize the utility of beam time. For instance, theoretical calculations of sodium K-edge from $Na_4Si_4O_9$ and well-characterized glasses ($Na_{0.17}Al_{0.03}Si_{0.23}O_{0.56}$ and $Na_{0.17}Al_{0.15}B_{0.04}Si_{0.09}O_{0.56}$) will be performed to obtain an improved basis to interpret structural information from the experimental spectra. Because the glass materials have a substantial component of disorder, a method to include this in the calculations beyond what is currently available is being examined.

The initial experimental sodium XAFS investigations have shown that Beamline 8.0 at the Advanced Light Source (ALS) is the best beamline to make these measurements on before the commissioning of the new Beamline 6 facility designed for 1-2 keV science. Efforts to collect sodium XAFS on Beamline 9.3.2 have been slowed by the availability of the high-energy monochromator diffraction grating,

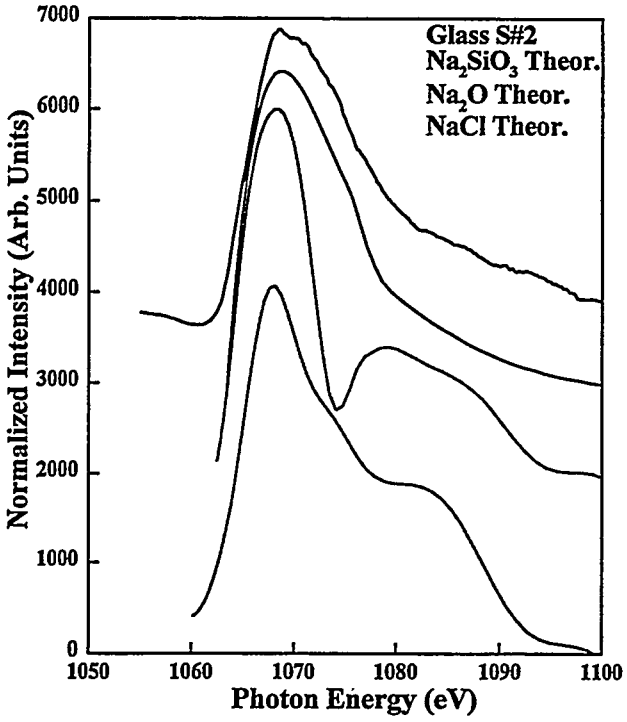

Figure 3. NEXAFS Spectrum of Glass #2 (smoothed) and Results of Theoretical Calculations of the Sodium K-Edge for Reference Sodium Compounds. The traces are from top to bottom; the experimental spectrum of Glass #2 and the simulated edges from the sodium reference materials Na_2SiO_3, Na_2O, and NaCl, respectively. Intensities are normalized to the intensity of the main peak of the sodium XAFS and the spectra are aligned to 1067 eV. A linear background also has been subtracted from the experimental near-edge spectrum.

which has been sent out for repair. An Independent Investigator Program proposal was submitted to the ALS to obtain the beam time necessary on Beamline 8.0 to collect the XAFS from the glass materials (Ivanov et al. 1998). The experimental equipment to make the measurements on Beamline 8.0 has been assembled and tested during the most recent beam run at the ALS on Beamline 7.0.

Ion-Exchange Kinetics

An accurate measurement of the rate of sodium ion exchange from the test glasses is one of the key challenges on this project. The experiments must be performed under controlled conditions of constant pH, temperature, and solution composition. The kinetics of Na-Al-Si glass dissolution and ion exchange were determined with a unique single-pass flow-through (SPFT) system. Glass coupons (up to five) were placed into columns fashioned from polyetheretherketone containing five individual cells. The cells are interconnected by a narrow tunnel that passes from the bottom to the top of the column, allowing solutions to flow from the reservoir, past each glass coupon, and out of the column to the sample collection vial. In this manner, the solution reacts with the samples, and individual coupons can be removed from the column for analysis of reaction layers without disrupting the other coupons (see Figure 4).

Solutions were made up by adding THAM (tris hydroxymethyl aminomethane) to deionized water to bring the concentration up to 0.01 or 0.05 M. Ultra pure nitric acid was then added to the solution to bring the solution pH to the desired value (8 or 9). We found that the maximum buffering capacity of this weak buffer solution is at pH values of 8. We additionally added silicon to the solution (2.3×10^{-3} M) in the form of amorphous silica. The solutions were heated to 90°C to facilitate the dissolution of silica into solution. The high concentrations of silicon in solution correspond to oversaturated conditions, which simulates high reaction progress and minimizes glass matrix dissolution. In summary, the solutions are designed to maintain a uniform pH and fix the reaction affinity at a constant high level, conditions that are lacking in previous investigations.

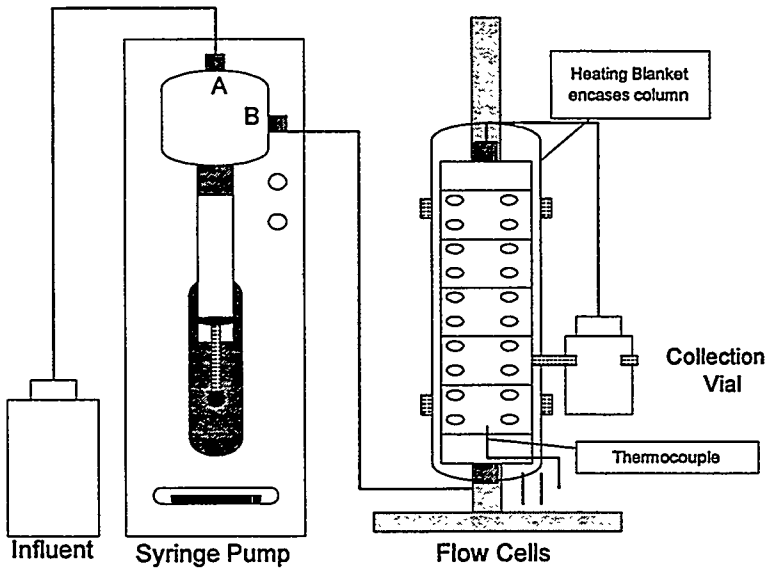

Figure 4. Schematic of Multichamber Flow-Through Column for Ion-Exchange Kinetics Tests

Flow-through rates varied depending on the glass composition. To maintain constant pH, even when the solutions are buffered, we found that flow-through rates of 20 mL/day were necessary for the 5 mol% Al_2O_3 glass. In contrast, flow-through rates of 1 to 3 mL/day were adequate for the 10 and 15 mol% Al_2O_3 glasses. Relatively low flow-through rates, such as those used in these experiments, are necessary to yield concentrations of elements in solution high enough to be detected during chemical analysis (ICP-MS). Typical run durations varied from 6 hours to 28 days, depending on the information sought. Short run times (6 to 72 hours) were necessary to detect differences in sodium depletion profiles as a function of time with RBS. In contrast, longer-duration experiments are necessary to establish steady-state dissolution rates, as explained in the next section. All experiments have been conducted at room temperature.

A typical concentration (sodium and molybdenum) profile versus time in an experiment with low flow-through rates is illustrated in Figure 5; in this case, 2 mL/day. The concentrations of sodium and molybdenum at steady-state conditions were then used to calculate normalized release rates, as shown in Figure 5. For each glass composition, the apparent dissolution rates based on sodium and molybdenum differ by a factor of ~100. These disparities in apparent dissolution rates indicate that two distinctly different glass-solution reactions are operating. Sodium concentrations in solution are due to two distinctly different processes: 1) dissolution of the glass into aqueous components and 2) exchange of Na^+ in glass with H_3O^+ (or H^+) in solution. In contrast, the presence of Mo(VI) in solution is probably due solely to dissolution of the glass framework (see Figure 6). Calculations suggest that the proportion of Na^+ to Mo(VI) in solution is much greater (80 to 120X) than the proportion of these cations in glass, indicating that the alkali for hydronium exchange is operating even when the solution is supersaturated with respect to amorphous silica (i.e., affinity term maximized). Therefore, a major postulate of this investigation appears to have been confirmed; alkali exchange is an important mechanism of glass/solution reactions even when reaction progress is high.

The number of sodium atoms in the leached layer was determined by comparing the RBS spectra for the reacted with those of non-reacted ("blank") coupons. Spectra were collected by accelerating 2.04 MeV helium ions at the target coupons. The accumulated charge was 60°C and the scattering angle 170 degrees. Hydrogen uptake profiles in the leached layer were determined by NRA by comparing spectra between reacted and non-reacted samples. The analyses were performed using ^{19}F ions with energies between 6.4 to 9.0 MeV. A typical RBS spectra plot is illustrated in Figure 7 for a leached and a non-reacted coupon. This illustration plots channel versus counts, which is roughly equivalent to plotting energy versus concentration. The number of counts in this illustration has been normalized to

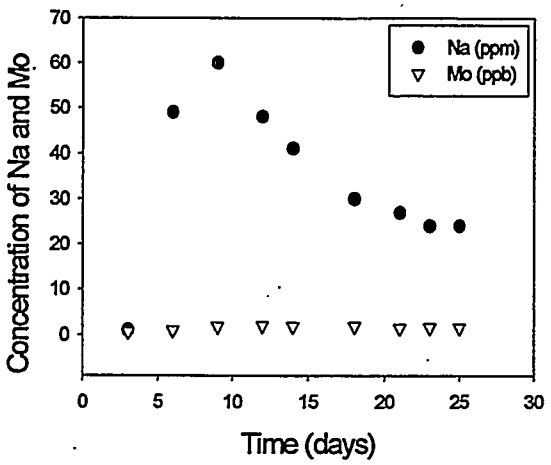

Figure 5. Concentrations of Sodium and Molybdenum Versus Time for 10 mole% Al_2O_3 Glass, T = 15 C, pH = 8

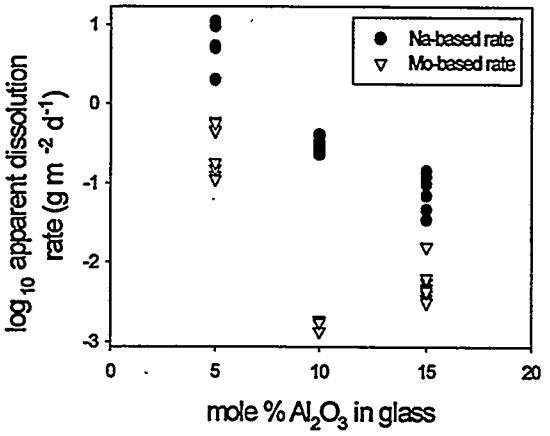

Figure 6. Plot of Apparent Dissolution Rates Versus Aluminum-Content of Glass T = 15°C, pH = 8-9

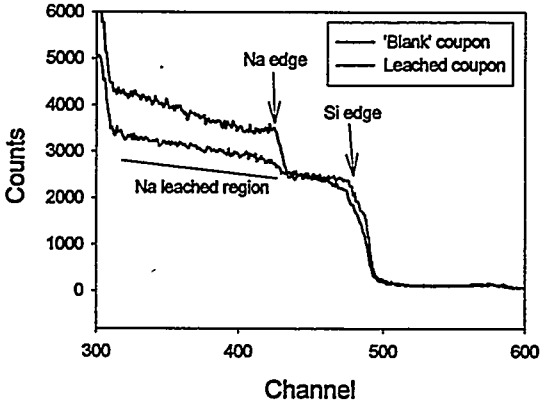

Figure 7. RBS Spectra Illustrating Channel (= energy) Versus Counts for Glass Coupons, Normalized to Silicon Atoms

the number of silicon atoms so the two spectra can be compared. Several features of the spectra should be noted, beginning with the sharp rise in the number of counts from the left of the diagram (towards low "channels" or energy). This feature represents the silicon edge, and the sodium edge is evident in the blank coupon spectra further to the right of the diagram. The smaller number of counts in the energy region corresponding to sodium in the leached compared with the blank coupon represents sodium loss from the glass. The approximate depth of sodium depletion is estimated to be between 2000 and 3000 Å. The depth of sodium depletion roughly corresponds to the depth of hydrogen uptake, as illustrated in Figure 8. Comparing leached and blank glass coupons, Figure 8 shows that hydrogen concentrations are relatively enriched in a region approximately 500 to 1000 Å.

Future Research Directions

Dissolution experiments using D_2O and $D_2{}^{18}O$ have been initiated, but the results are not available for this report. Measurement of D and ^{18}O uptake in the glass coupons will provide crucial information on the exact mechanism of alkali H-species exchange. Additional experiments will be carried out to establish the temperature dependence of alkali exchange and matrix dissolution. We expect that the activation energy of ion exchange will be much lower than matrix dissolution, underscoring the importance of alkali exchange at the lower temperatures (10°C to 20°C) that will prevail in a disposal vault.

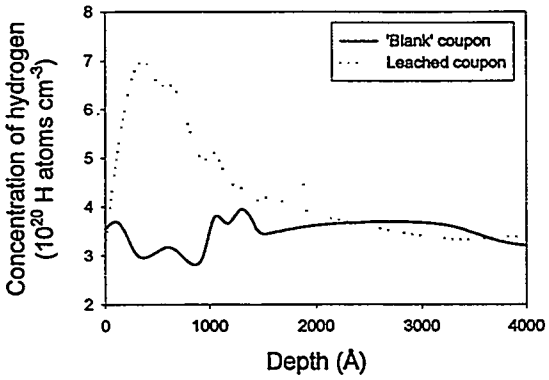

Figure 8. Plot of Depth Versus Hydrogen Concentration for Leached and Unleached Coupons Based upon Fluorine RBS Spectra

References

Ankudinov KL, SI Zabinsky, JJ Rehr, and RC Albers. "Ab initio multiple-scattering x-ray absorption fine structure and x-ray absorption near edge structure code." (Copyright 1992, 1993, 1994, 1996) University of Washington, Seattle.

Darab JG, X Feng, JC Linehan, PA Smith, and I Roth. 1997. "Composition-structure relationships in model Hanford low-level waste glasses." *Ceram. Trans.* 72:103-110.

Darab JG, JC Linehan, and BP McGrail. 1999. *Mat. Res. Soc. Symp Proc.* (in press).

Eckert H. 1992. *Progress in NMR Spectroscopy* 24:159.

Ivanov KE, P Liu, DK Shuh, BP McGrail, JG Darab, and D Baer. 1998. "Investigation of sodium structure in waste form glasses by Na K-edge x-ray absorption fine structure." ALS Independent Investigator Proposal (ALS-00177).

Kirkpatrick RJ. 1988. In *Spectroscopic Methods in Mineralogy and Geology*, FC Hawthorne, ed., Mineralogical Soc. of America, Washington, D.C., pp. 341-403.

Mann FM, RP Puigh II, CR Eiholzer, Y Chen, NW Kline, AH Lu, BP McGrail, and PD Rittmann. 1998. *Hanford immobilized low-activity tank waste performance assessment.* DOE/RL-97-69 Rev. 0, U.S. Department of Energy, Richland, Washington.

Yun YH, and PJ Bray. 1978. *J. Non-Cryst. Solids* 27:363.

Radiation Effects in Nuclear Waste Materials

(First Year of Funding: 1996)

Project Manager and Principal Investigator

Dr. William J. Weber
Pacific Northwest National Laboratory
P.O. Box 999, MSIN K2-44
Richland, WA 99352
(509) 375-2299 (phone)
(509) 375-2186 (fax)
bill.weber@pnl.gov

Co-Investigator

Dr. L. René Corrales
Pacific Northwest National Laboratory
P.O. Box 999, MSIN K1-96
Richland, WA 99352
(509) 375-6410 (phone)
(509) 375-6631 (fax)
rene.corrales@pnl.gov

PNNL Contributors

N.J. Hess
R.E. Williford
H.L. Heinisch
G.D. Maupin
M.J. Schweiger
S. Thevuthasan
Y. Gao
J.P. Icenhower
B.P. McGrail
J. Song (Post Doctoral Fellow)
B. Park (Post Doctoral Fellow)
R. Devanathan (Post Doctoral Fellow)
W. Jiang (Post Doctoral Fellow)
B. Begg (Visiting Scientist)
R.M. VanGinhoven (Ph.D. Student)

External Contributors

R.B Bircher (ANL)
X. Chen (ANL – Post Doctoral Fellow)
S.D. Conradson (LANL)

External Collaborators

R.C. Ewing (University of Michigan)
S.X. Wang (University of Michigan)
A. Meldrum (ORNL)
L.A. Boatner (ORNL)
D.E. Day (University of Missouri)
J.D. Gale (Imperial College)
A.N. Cormack (Alfred University)
H. Jónsson (University of Washington)
D.L. Griscom (Naval Research Laboratory)

Research Objective

The objective of this multidisciplinary, multi-institutional research effort is to develop a fundamental understanding of radiation effects in glasses and ceramics at the atomic, microscopic, and macroscopic levels. Current research addresses many of the scientific issues identified in the reports of two recent DOE panels (Weber et al. 1997, 1998). The goal of this effort is to provide the underpinning science and models necessary to assess the performance of glasses and ceramics designed for the immobilization and disposal of high-level tank waste, plutonium residues, excess weapons-grade plutonium, and other highly radioactive waste streams. Studies are focused on the effects of ionization and elastic collisions on defect production, defect interactions, diffusion, solid-state phase transformations, and gas accumulation using actinide-containing materials, gamma irradiation, ion-beam irradiation, and electron-beam irradiation to simulate the effects of α-decay and β-decay on nuclear waste materials. This program exploits a variety of structural, optical, and spectroscopic probes to characterize the nature and behavior of defects, defect aggregates, and phase transformations. Computer simulation techniques are also used to determine defect production processes, defect energies, and defect/gas diffusion and interactions. A number of irradiation facilities and capabilities are used, including user facilities at other national laboratories, to study the effects of irradiation under different conditions.

Problem Statement

A significant challenge facing the environmental management and restoration activities at DOE facilities is the stabilization and immobilization of high-level tank waste, high-level sludge in fuel storage basins, and plutonium residues/scrap. In addition, the immobilization and disposal of surplus weapons-grade plutonium is becoming a growing technological and political issue that is historically and politically tied to environmental management and restoration activities. These high-level wastes will be converted to glass or glass-ceramic waste forms for permanent disposal in a geologic repository. A key challenge is to develop predictive strategies and models, based on sound scientific understanding, to fully assess long-term performance. Self-radiation effects from α-decay and β-decay can significantly impact long-term performance. Waste forms for the disposal of plutonium residues/scrap, surplus weapons-grade plutonium, and other high-actinide waste streams may differ significantly in composition from the waste forms for high-level tank wastes and will produce significantly higher radiation doses and helium. The current baseline data and scientific understanding of radiation effects in glasses, glass-ceramics, and crystalline phases are critically lacking. Without a fundamental understanding of radiation effects at the molecular, microscopic, and macrosopic levels, meaningful predictions of performance are not possible. This lack of understanding of the radiation damage processes that occur in nuclear waste materials makes it impossible to extrapolate the limited existing data bases to larger doses, lower dose rates, longer time periods, different temperature regimes, and different glass compositions or ceramic structures.

Research Progress

There has been extensive progress under this project, and work to date has resulted in a number of publications, which are listed at the end of this report. Highlights of the research over the past year are presented below.

Theory, Simulations, and Modeling

Oxygen Vacancy Migration in Silica

The migration pathway and energy of an oxygen vacancy were calculated in quartz, stishovite, and cristobolite using empirical potentials. For comparison, the minimum energy pathway in quartz was calculated using a density functional theory (DFT) interatomic potential. The differences between the two potentials' types show that although the energies of both approaches are similar, the pathways and hence the mechanisms of diffusion are different.

The migration pathway calculations for the oxygen vacancy in quartz show similar energetics for the barrier energy using DFT and the BKS (Van Beest, Kramer, and Van Santen) (Van Beest et al. 1990) potentials. However, the underlying mechanism for diffusion is clearly different. The BKS potential has as its initial and final states a puckered structure for the vacancy defect. Although DFT also predicts the puckered configuration as the lowest energy state, it also shows that there is a barrier of 0.6 eV towards a metastable planar configuration. The lowest lying migration pathway is that in which both the initial and final states are the planar state. Thus, distinct differences in the pathway, the degree of network relaxation, and path length are seen between the two calculation methods.

The migration pathway calculations in stishovite and cristobolite reveal similarities (and also some differences) when compared with the quartz calculations. These were calculated using only the BKS potential. The existence of backbonding structures, which is a signature of the puckered configuration, persists in all three crystalline structures. It would thus be valuable to carry out more detailed DFT calculations of the vacancy defect in these crystal structures to determine the stable and metastable structures, as in quartz.

Calculations of the Self-Trapped Exciton in Silica

Density Functional Theory. The existence of intrinsic defects in silica can complicate the understanding of how electronic excitations can lead to the formation of point defects. The formation of electron-hole pairs, where the excited electron occupies the lower edge of the conduction band, can lead to a self-trapped exciton state in α-quartz where the lattice (or bond) is distorted. In such a state, the hole is trapped at an oxygen center and the excited electron at a silicon center. The presence of a point defect, such as the oxygen vacancy, can change how the electron-hole pair interacts with the lattice depending upon the oxidation states of the vacancy. Moreover, the presence of the electron-hole pair can lead to significant changes in the migration pathways and energetics of the point defect.

Recent work under this project has revealed that there are several self-trapped exciton (STE) states in quartz, one of which is the same as that first determined by ab initio calculations of Fisher et al. (1990). In addition to the lowest-energy-oxygen-distorted STE, there is a silicon-distorted STE at an energy of 0.23 eV higher. These two states appear to luminesce at significantly different energies; however, the absolute energies cannot be calculated with this DFT method. Instead, new methods are being developed to determine the absolute energies and carry out ab initio calculations to verify these DFT findings.

The excited state configurations and luminescence energies of several oxygen vacancy and interstitial states have also been characterized, as given in Table 1. The luminescent energies for these states overlap those of the oxygen and silicon-distorted STEs, which also show two distinct energy bands. When a Frenkel defect pair is excited, the emission energy is strictly from the oxygen vacancy. In fact,

Table 1. Self-Trapped Exciton Absorption (E_a), Lattice Relaxation (E_{LR}), Luminescent (E_e), and Non-Radiative (E_{NR}) Energies

	E_a	E_{LR}	E_e	E_{NR}
O STE	6.00[(a)]	-0.47[(b)]	3.72	2.70
Si STE	6.00[(a)]	-0.70[(b)]	0.90	5.80
O neutral vacancy	5.73	2.14	1.09	2.50
O charged vacancy	4.91	0.33	3.12	1.46
O neutral interstitial	4.09	2.80	-	-
O charged interstitial	5.77	0.91	4.14	0.72
Defect pair	4.12	2.50	0.95	0.67

(a) This is the delocalized Free Exciton State (FES) of the perfect lattice without distortion.
(b) The negative sign indicates that these states are higher in energy than the FES.

upon exciting the peroxy interstitial, the system undergoes a non-radiative decay back to the ground state with an apparent curve crossing, as the oxygen interstitial system undergoes a configuration relaxation of the ions. This work will be submitted for publication.

Ab Initio Calculations of Excitons in Silica Clusters. To verify the results of the DFT calculations for STE in silica, and to more fully characterize the newly discovered STE state, ab initio calculations are being performed on silica clusters. Significant improvements have been obtained over the results from previous calculations of Fisher et al. (1990) by increasing the level of theory, the quality of basis set used in the calculation, and the size of the cluster. The basis set and cluster size dependence for this system is being investigated. The minimum cluster size to adequately describe the new STE state is $Si_5O_{16}H_{12}$. The minimum level of theory required is second-order Moller-Plesset Perturbation (MP2) with a 6-31G* basis set. Calculations of the required size will take some additional time to complete.

Semi-Empirical Simulation Methodology for Excitons Coupled with Phonons. A novel simulation method that couples the motion of the excited electron and hole with the ionic motion of network atoms has been developed and tested for the crystalline and amorphous states of pure silicon. However, because the application of this method to silica depends on including the proper mechanisms for the formation of the excitons, the work has been put on hold while the silica systems are better characterized using ab initio methods. In the work on silicon, which is being submitted for publication, coupling of the electronic states with the ionic motion has been successfully implemented.

The time scales for relaxing the electronic states into their lowest energy states happens at a rate comparable to the time steps of the ionic motion, which is about 1.5 to 2 fs. Thus, the method is viable for use in silica systems but requires further development.

Defect Energetics in Crystalline Ceramics

Activities under this task are focused on using state-of-the-art computational methodologies to determine fundamental defect energetics in complex crystalline oxides relevant to nuclear waste applications. The most fundamental energy parameters important to radiation effects are the threshold displacement energies, E_d, for the various cations and anions and the migration energies, E_m, of radiation-induced

defects (e.g., interstitials and vacancies). These energies, which are not easy to determine experimentally, particularly for multication ceramics, are the fundamental parameters controlling irradiation-induced defect production, defect migration, and the kinetics of microstructure growth and phase transformations. Also important is the energy change associated with the incorporation of radionuclides, such as plutonium, in the host crystal structure. Both static energy-minimization methods and molecular dynamics (MD) simulations are being employed under this project to determine these energies.

Threshold Displacement Energies in MgO and $ZrSiO_4$. Molecular dynamics simulations are used to obtain threshold displacement energies of atoms along specified directions in MgO and $ZrSiO_4$. The MD code, DL_POLY (a general purpose, parallel molecular simulation package developed by Daresbury Laboratory, UK) has been modified to implement irradiation phenomena. Ziegler-Biersack-Littmark (ZBL) and Buckingham-type potentials represent the short-range interactions. The long-range Coulombic interactions are evaluated by an Ewald method.

MgO was chosen as an initial test case because it is one of the simplest oxides and has been extensively studied by both experimental and computational methods. The simulation cell consists of 13,824 atoms with periodic boundary conditions in all three directions. The simulations are carried out at 10K. An atom in the center of the cell is given kinetic energy along a specific direction, and the positions and kinetic energies of all neighboring atoms are monitored as a function of time. The threshold displacement energy is the kinetic energy at which a permanent displacement (interstitial or replacement) is produced. Several directions have been investigated, and the minimum displacement energies in MgO are 90 eV for Mg and 65 eV for oxygen. The MD simulations have revealed the dynamic nature of atomic displacement processes in MgO, and the results of this study will be submitted for publication.

Compared with MgO, $ZrSiO_4$ is a rather complex oxide in terms of structural features (open network, directional bonding, multiple cation sites, and distinct bond types), and it is a challenge to develop viable empirical potentials. A new potential parameter set for $ZrSiO_4$ based on the rigid ion model has been developed under this project. The total number of atoms used in the displacement simulations for $ZrSiO_4$ is 12,288, and the computational procedures are the same as for MgO. A larger number of directions is needed to account for the anisotropic nature of $ZrSiO_4$. A total of 15 different directions have been examined to date. The minimum displacement energies are 98 eV for zirconium, 48 eV for silicon, and 23 eV for oxygen; however, there is a very strong directional dependence for the displacement energies.

Vacancy Migration in $ZrSiO_4$. Based on this project's previous experience in computing displacement energies in zircon (Williford et al. 1998), two sets of interatomic potentials were selected to study the migration of zirconium, silicon, and oxygen vacancies in zircon: one with O-Si-O three-body terms for the SiO_4, and one without. Results show that both zirconium and oxygen vacancies can migrate on fully connected three-dimensional networks within the zircon lattice. The lowest-energy pathway for the zirconium vacancy is between nearest-neighbor zirconium sites, with an activation energy of 1.2 or 1.4 eV, depending on the potential used. The lowest-energy pathway for the oxygen vacancy is along the unshared ZrO_8 dodecahedra edges, with an activation energy of 1.2 or 1.0 eV, depending on potential. The experimental activation energy (Cherniak et al. 1997) for self-diffusion on the zirconium sublattice (7.5 to 8.7 eV) is consistent with the sum of the zirconium vacancy formation (6.2 eV) and migration (1.2 to 1.4 eV) energies. Similarly, the activation energy (Watson and Cherniak 1997) for self-diffusion on the oxygen sublattice (4.6 eV) is consistent with the sum of the oxygen vacancy formation (3.3 eV) and migration (1.0 to 1.2 eV) energies. Results for silicon were inconclusive, but are consistent with the structural stability of the SiO_4 tetrahedra.

Stable Defect Configuration for Plutonium Substitution in $ZrSiO_4$. X-ray absorption spectroscopy (XAS) experiments (Hess et al. 1998) on plutonium-containing zircons studied under this project have confirmed that the plutonium in the originally prepared and radiation-damaged samples occurs as Pu^{3+} because of the original preparation under reducing conditions. More recent XAS studies, as discussed below, have revealed that by annealing the samples in air the Pu^{3+} state is oxidized to Pu^{4+}. Energy minimization methods have been used to determine the energetics of Pu^{3+} and Pu^{4+} incorporation in zircon (as interstitials or as substitutions on zirconium sites) to identify the most stable defect configuration for each oxidation state and to assist in the interpretation of XAS data. The lowest-energy configuration for Pu^{4+} was as a substitution on a zirconium site, which is consistent with the recent XAS data. The lowest-energy configuration for Pu^{3+} incorporation was as a defect cluster consisting of two closely associated Pu^{3+} ions on zirconium sites and an oxygen vacancy for charge compensation. The resulting polarized defect cluster has a lower energy than isolated Pu^{3+} on zirconium sites and charge-compensating oxygen vacancies. In the lowest-energy cluster (Figure 1), the two Pu^{3+} ions are arranged in a right angle configuration with the oxygen vacancy at the center. Incorporation of Pu^{3+} or Pu^{4+} as interstitials is energetically prohibited. Mean-field calculations of the unit-cell volumes using these lowest energy configurations for 8% Pu^{3+} or Pu^{4+} substitution for zirconium (as in actual samples) are in good agreement with recent x-ray diffraction data on these samples.

Evolution of Damage from Alpha-Recoil Cascades in $ZrSiO_4$

Kinetic Monte Carlo (KMC) simulations are being used to study the evolution of radiation damage at the atomic scale over times and distances well beyond those possible with MD simulations. In principle, KMC simulations can be used to study self-radiation effects, such as amorphization, in nuclear waste materials over laboratory to geologic time scales. Our current approach uses cascades generated by the binary simulation code MARLOWE as the defect production input. Single vacancies and interstitials representing the cascade-generated defects are inserted into the simulation. The kinetics of individual defects hopping on the crystal lattice are followed, but interactions of individual atoms are not dealt with explicitly. Defects are assumed to migrate only on their own sublattices. When a vacancy and interstitial defect become nearest neighbors (on their own sublattice), they are recombined. Same-type

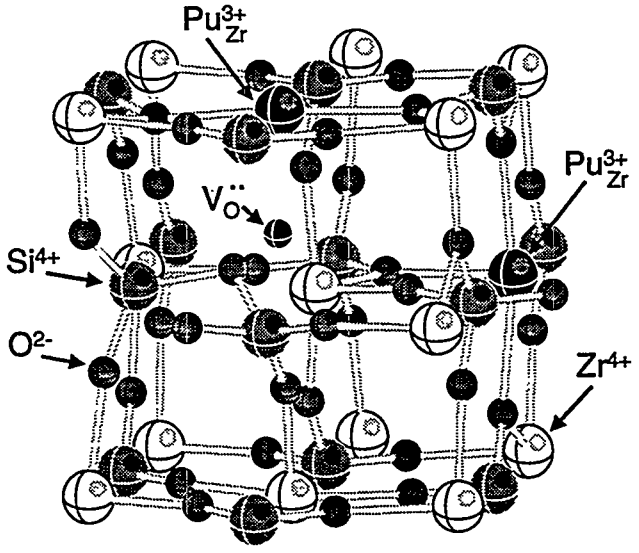

Figure 1. The Defect Cluster $2Pu^{3+}{}_{Zr}{}' + V_O{}^{\bullet\bullet}$ in Zircon, Viewed Along the [001] Direction

defects associated with nearest neighboring sites are assumed to form an immobile cluster. Collision cascades are inserted into the simulation volume randomly in space and time at a predetermined average rate. After each cascade occurs, the cascade region is searched for amorphization based on defect density, and regions with a defect density above a critical value are assumed "amorphous."

Defect accumulation and amorphization in zircon doped with plutonium have been simulated in a rectangular simulation volume, 72 lattice parameters on a side, using 1000 MARLOWE cascades for 94 keV ^{234}U recoils. This represents a cumulative dose of about 2.2×10^{18} alpha decays/g (or 0.093 dpa). The simulation results for the amorphous fraction as a function of dose are in excellent agreement with experimental results (Weber et al. 1994), as shown in Figure 2. The effects of recoil spectra, dose, and dose rate are being explored to examine the differences between amorphization of plutonium-doped, natural and ion-irradiated zircon using this model.

Experimental Studies

Plutonium-Containing Glasses and Ceramics

Studies have continued on polycrystalline zircon samples containing either 10 wt% ^{238}Pu or 10 wt% ^{239}Pu and a suite of compositionally identical plutonium-doped (1 wt%) waste glasses prepared with different α-activities by varying the $^{239}Pu/^{238}Pu$ isotopic ratio. The zircon and glass samples were prepared 17 and 16 years ago, respectively. The ^{238}Pu zircons (5.6×10^{10} Bq/g) have achieved an accumulated dose of 2.8×10^{19} α-decays/g, while the ^{239}Pu zircons (2.5×10^{8} Bq/g) have a relatively low accumulated dose of 1.2×10^{17} α-decays/g. The plutonium glasses, with α-activities ranging from 1.9×10^{7} to 4.2×10^{9} Bq/g, have accumulated doses between 8.8×10^{15} to 1.9×10^{18} α-decays/g.

Swelling measurements for the plutonium-zircon are summarized in Figure 3. The results show that the swelling is totally saturated at high doses and that the saturation swelling increases with decreasing porosity. When compared with the results for natural zircons (Weber 1993), the saturation swelling increases from 16.6% at 5.5% porosity to 18.4% at 0% porosity. In all cases, the swelling can be accurately modeled based on the contributions from crystalline and amorphous components.

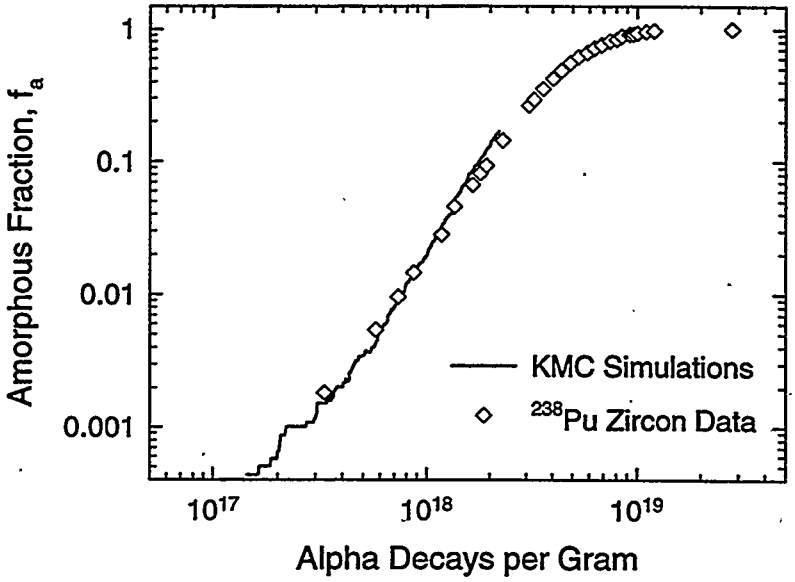

Figure 2. Comparison of KMC Simulations with Experimental Results of Weber et al. (1994)

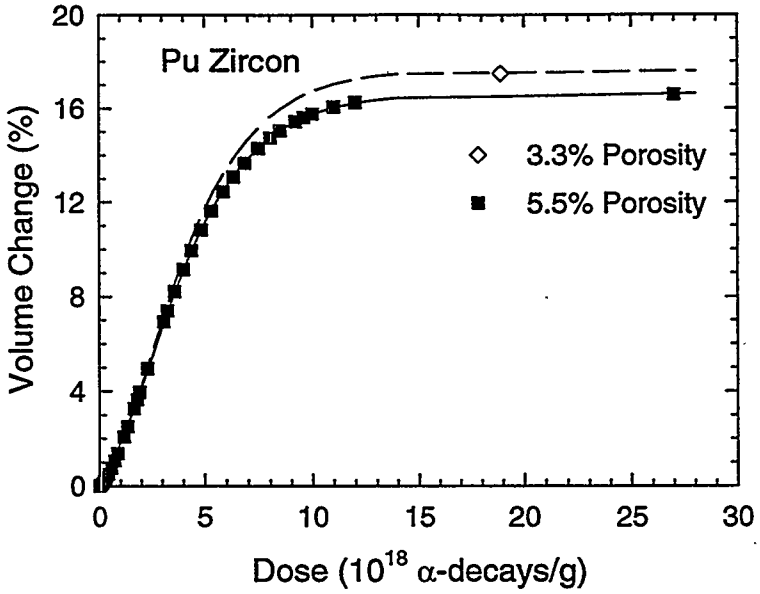

Figure 3. Swelling in Plutonium-Doped Zircon

The multicomponent composition of the plutonium-containing glasses and zircons permitted XAS investigations at six absorption edges for the borosilicate glasses and at three absorption edges for the polycrystalline plutonium-zircons. For all materials, analysis of extended x-ray absorption fine structure (EXAFS) spectra indicates that the local environment around the cations exhibits different degrees of disorder as a result of the accumulated α-decay dose. In general, cations with short cation-oxygen bonds show little effect from self-radiation, whereas cations with long cation-oxygen bonds show a greater degree of disorder with accumulated α-decay dose. The plutonium L_{III}-edge x-ray absorption near-edge structure (XANES) data for the zircon samples indicate that plutonium is present as Pu^{3+} as a result of the reducing conditions (argon atmosphere) under which the plutonium-zircon was synthesized. The plutonium L_{III}-edge EXAFS data are consistent with Pu^{3+} substitution of Zr^{4+} in the zircon lattice, as also predicted by the computer simulation results discussed above.

Diffuse x-ray scattering measurements have been performed on the identical samples on which the earlier XAS studies were conducted. Initial scattering results of the glass samples indicate no change in the silica tetrahedral unit. However, the pair distribution function (PDF) reveals the sharpening of a feature at 0.21 nm with increasing α-decay dose, which suggests an increase in order for octahedrally coordinated cations. In addition, a feature at 0.27 nm broadens with accumulated α-decay dose. This distance corresponds to the O-O distance of the silica tetrahedra, suggesting that O-Si-O bond angle changes may be occurring. The PDF of the zircon diffuse scattering shows strong structure to a distance of 0.5 nm, suggesting that there is significant short-range order in the fully amorphous zircon. Distinct PDF peaks occur at 0.16, 0.21, and 0.37 nm. These distances correspond to the Si-O, Zr-O, and both Zr-Zr and Zr-Si crystallographic distances in crystalline zircon. As a result, the 0.5 nm unit most likely represents a zirconium center coordinated by first and second-nearest neighbor zirconium atoms and silica tetrahedra. These recent results provide additional insight into the phenomenon of self-radiation damage in glass and ceramic waste forms.

An initial series of annealing studies under oxidizing conditions has been conducted on the zircon samples to determine the distribution of Pu^{4+} in the amorphous and crystalline structure. The amorphous ^{238}Pu-doped zircon was annealed in air at 1000 and 1200°C for 12 hours. The crystalline ^{239}Pu-doped zircon was annealed in air at 1200°C for 12 hours. XANES, EXAFS, and PDF analysis were used to

determine the oxidation state, local structure, and radial distribution of the zirconium, plutonium, and uranium cations. Analysis of the plutonium L_{III}-edge XANES indicates oxidation of Pu^{3+} to Pu^{4+} in all the annealed zircon samples. Analysis of zirconium K-edge and plutonium L_{III}-edge EXAFS of the ^{238}Pu-doped zircon annealed at 1000°C are inconsistent with the zircon structure and suggest the formation of a ZrO_2-phase. The analysis of zirconium K-edge EXAFS of the ^{238}Pu- and ^{239}Pu-doped zircons annealed at 1200°C indicates highly crystalline zircon. However, the plutonium L_{III}-edge EXAFS of the ^{238}Pu- and ^{239}Pu-doped zircon annealed at 1200°C indicates the formation of both separated PuO_2 and the substitution of plutonium for zirconium in zircon structure. This result suggests that the solubility of plutonium in zircon at 1200°C is less than the 10 wt% that was originally incorporated in the zircon samples at 1465°C.

In collaboration with Drs. Ankudinov and Rehr at the University of Washington, the plutonium L_{III}-edge XANES has been modeled using FEFF8 and the atomic distributions based on the defect calculations discussed above. The experimental XANES of the unannealed zircons are well matched with the ab initio calculations based on the coupled substitution of two Pu^{3+} for two Zr^{4+} plus an oxygen vacancy in the zircon structure. The experimental XANES of the annealed zircons are best matched by the calculated XANES based on the PuO_2 structure. These results are consistent with those derived from the EXAFS calculations.

Gamma-Irradiation Studies

Temperature-controlled capsules have been used for irradiation studies within the PNNL (^{60}Co) gamma-irradiation facility. Samples of seven different glasses have been irradiated at four different temperatures (50, 100, 150, and 200°C) over the past two years. Glasses exposed to dose levels of about 2.5×10^7 Gy and 7.5×10^7 Gy at each temperature have been extensively characterized. Density measurements indicate no significant changes in volume. Raman, polarized Raman, UV-Vis-NIR, and FTIR spectroscopies have been carried out on these glass samples. Electron paramagnetic resonance (EPR) and transmission electron microscopy (TEM) characterization of these samples are planned. The highest dose glass samples, 1.5×10^8 Gy, have just been removed from the gamma-irradiation facility for characterization. This dose is equivalent to about 25 years of storage time for DWPF glasses.

The Raman, polarized Raman, UV-Vis-NIR, and FTIR spectra from each of the glass compositions exhibit significant differences as a result of the chemical variation in the glass samples and the resulting effect on the silicate glass structure. However, initial spectroscopic analyses indicate only minor changes in the Raman, polarized-Raman, or FTIR spectra between the nonirradiated samples and those with 2.5×10^7 Gy accumulated dose. Significant differences are observed between the nonirradiated samples and those with 2.5×10^7 Gy and 7.5×10^7 Gy accumulated dose in the 400 to 700 nm region of the UV-Vis-NIR optical absorption spectra of the sodium-borosilicate glass compositions. Furthermore, these radiation-induced variations display systematic dependencies on the irradiation temperature. At this time, the change in optical absorption in the 400 to 700 nm region are believed to originate from electronic defects, and D. Griscom (Naval Research Laboratory) will fully characterize the nature of these defects using EPR spectroscopy.

Electron and Ion Irradiation Studies

Amorphization in Zircon. Single crystals of synthetic zircon ($ZrSiO_4$) have been irradiated with different ions (from neon to bismuth) over a wide range of temperatures. The results of these studies (Weber et al. 1999), as illustrated in Figure 4, show that amorphization in zircon is controlled by a variety of parameters and is a more complex process than previously thought. The critical temperature

(975K) for amorphization appears to be relatively independent of ion mass, and irradiation-induced decomposition is observed above this temperature (Meldrum et al. 1998), as indicated in Figure 4. The critical amorphization dose (in dpa) in zircon exhibits a two-stage dependence on irradiation temperature and increases with temperature. However, the critical dose for amorphization is significantly higher at lower temperatures (below 500K) for very heavy ions, such as lead and bismuth. This increase in critical dose with the damage energy density has not been observed previously in other materials and is generally inconsistent with direct-impact amorphization as the dominant amorphization process. The data suggest that irradiation with light ions (helium through xenon) may not provide accurate simulation of the dose dependence of amorphization due to α-decay events.

Amorphization in Pyrochlore Structures. The temperature dependence of the critical dose to completely amorphize $A_2Ti_2O_7$ pyrochlore structures (A=Y, Sm, Gd, Lu) under irradiation with 0.6 MeV Bi^+ ions is shown in Figure 5. There is no significant effect of A-site ion mass on the temperature and dose dependence of amorphization. The amorphization dose exhibits a distinct two-stage dependence on temperature, with a transition temperature between stages at about 500K. Above 950K, the dose for amorphization rises rapidly as the rate of recovery becomes similar to the rate of amorphization. At room temperature, the dose to completely amorphize all the samples is on the order of 0.18 dpa.

Several $A_2Ti_2O_7$ pyrochlores were irradiated with 2 MeV Au^+ ions to produce a fully amorphous surface layer to depths of 300 to 400 nm. Leach testing (at pH 2) of as-prepared and irradiated samples was conducted to evaluate the effect of amorphization on dissolution rates and relative reactivities. The leach rates for the amorphous state of $Gd_2Ti_2O_7$ and $Lu_2Ti_2O_7$ were at least an order of magnitude higher than for the crystalline state. The increase in leach rate for $Y_2Ti_2O_7$ was less apparent, but the leach rate for the crystalline state of this composition is significantly higher (factor of 10) than for the crystalline

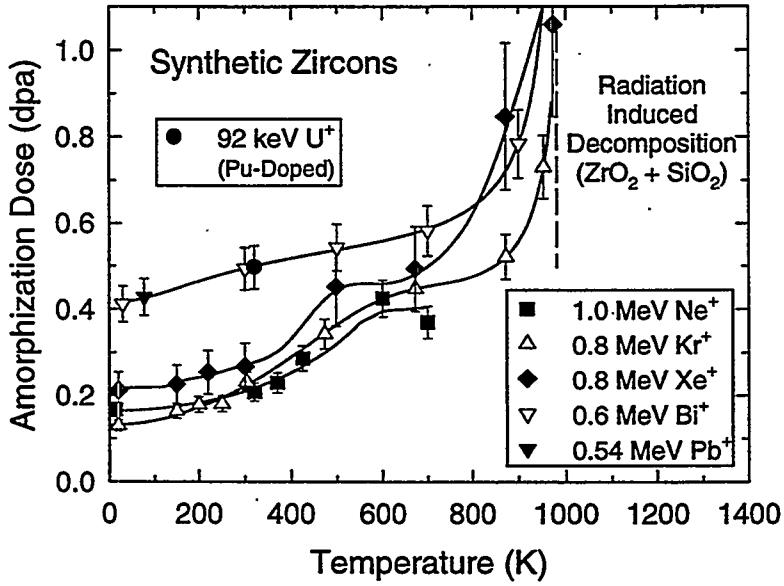

Figure 4. Temperature Dependence of Amorphization Dose in Zircon under Irradiation with Different Ions and from α-Decay in Plutonium-Doped Zircon (Weber et al. 1999). Also indicated is the radiation-induced amorphization that occurs above 950°C (Meldrum et al. 1998).

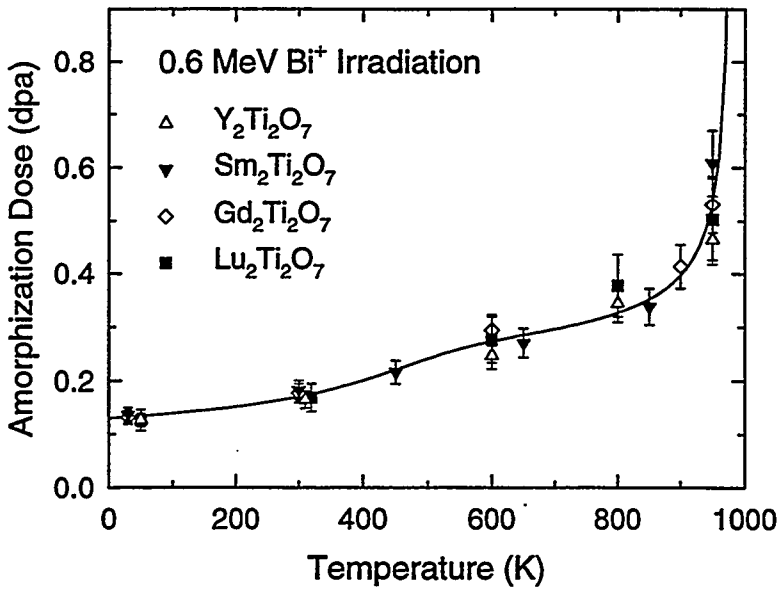

Figure 5. Temperature Dependence of Amorphization in Several Rare-Earth Titanates with the Pyrochlore Structure

state of either $Gd_2Ti_2O_7$ or $Lu_2Ti_2O_7$. For all three materials, the results suggest incongruent enhanced leaching of the gadolinium, lutetium, and yttrium relative to titanium. The measured order of magnitude increase in leach rate for the amorphous material relative to the crystalline material is consistent with the 20- and 50-fold increase in curium and plutonium release, respectively, measured in amorphous curium-doped $Gd_2Ti_2O_7$ relative to the fully crystalline state (Weber et al. 1985).

Bubble Formation in Glasses. Gas bubble formation in glasses has been studied in situ by ion implantation. Alkali silicate glass and sodium-borosilicate glass were implanted with 50 keV xenon ions at 200°C in a Hitachi-9000 electron microscope, and the formation of bubbles was studied by TEM during interruptions of the ion beam after discrete ion fluence steps. The results show that the alkali silicate glass has a larger volumetric swelling than sodium-borosilicate glass for the same implanted xenon ion fluence. The results also infer that xenon behaves like a perfect gas inside equilibrium bubbles. The difference in bubble growth in these two glasses is attributed to the difference in glass network structure.

Systematic studies of ion implantation in a simple sodium-borosilicate glass have been carried out using helium, krypton, argon, xenon, and oxygen ions. No oxygen bubbles were observed to form up to a fluence of 1×10^{17} ions/cm^2 during oxygen implantation; however, gas bubbles were observed for all the noble gas implantations. The average bubble size increased with atomic mass of the gas species. These results indicate that oxygen bubbles do not readily form for the simple sodium-borosilicate glass composition. This may be due to the large fraction of modifiers in this glass composition. Electron irradiation studies also showed no evidence of bubble formation in this glass composition, in agreement with the oxygen ion implantation study. This result, however, contradicts previous claims that electron irradiation can cause oxygen bubble formation in more complex glasses. One notable difference is that in the current studies under this project electrochemical polishing is used for sample preparation to avoid possible damage to the sample by ions; in previous studies, ion milling was used to prepare TEM samples.

Simultaneous electron irradiation during xenon ion implantation was found to increase the average bubble size in the sodium-borosilicate glass. This is attributed to ionization-enhanced diffusion and not to any thermal effect. It is postulated that STEs generated by high-energy electron bombardment in the glass distort local structures and open channels for ion migration. Clusters that were observed in electron-irradiated glasses also indirectly support this speculation. Bubbles formed under only implantation with xenon implantation were observed to shrink when exposed to subsequent electron irradiation. There is no decrease in the xenon content in the samples, indicating that the xenon inside the bubbles diffused into the matrix but was not released from the samples.

Planned Activities

All the above research efforts will be phased out over the next few months as this project is terminated. As much work as possible will be brought to completion and written up for publication. Unfortunately, some of the most impactful work will neither be completed nor published. No follow-on funding has been identified at this time. Many team members will move on to other project or jobs. Samples will be temporarily archived in hopes that some of the needed additional studies can be funded in the future. Some of the computer simulation codes and expertise will find use under other projects. Other expertise and capabilities will be lost.

References

Cherniak DJ, JM Hanchar, and EB Watson. 1997. *Chem. Geol.* 134:289.

Fisher AJ, W Hayes, and AM Stoneham. 1990. *Physical Review Letters* 64:2667.

Hess NJ, WJ Weber, and SD Conradson. 1998. *J. Nuclear Materials* 254:175.

Meldrum A, LA Boatner, WJ Weber, and RC Ewing. 1998. *Geochim. et Cosmochim. Acta* 62:2509.

Van Beest BWH, GJ Kramer, and RA Van Santen. 1990. *Phys. Rev. Letters* 64:1955.

Watson EB and DJ Cherniak. 1997. *Earth and Planetary Science Letters* 148:527.

Weber WJ, JW Wald, and Hj Matzke. 1985. *Materials Letters* 3:173.

Weber WJ. 1993. *J. American Ceramic Society* 76:1729.

Weber WJ, RC Ewing, and LM Wang. 1994. *J. Materials Research* 9:688.

Weber WJ, RC Ewing, CA Angell, GW Arnold, AN Cormack, JM Delaye, DL Griscom, LW Hobbs, A Navrotsky, DL Price, AM Stoneham, and MC Weinberg. 1997. *J. Materials Research* 12:1946.

Weber WJ, RC Ewing, CRA Catlow, T Diaz de la Rubia, LW Hobbs, C Kinoshita, H Matzke, AT Motta, M Nastasi, EKH Salje, ER Vance, and SJ Zinkle. 1998. *J. Materials Research* 13:1434.

Weber WJ, R Devanathan, A Meldrum, LA Boatner, RC Ewing, and LM Wang. 1999. "Microstructural processes in irradiated materials," SJ Zinkle, RC Ewing, GE Lucas, and JS Williams, eds. *Mater. Res. Soc. Symp. Proc. 540*, Warrendale, Pennsylvania (in press).

Williford RE, R Devanathan, and WJ Weber. 1998. "Computer simulation of displacement threshold energies for several ceramic materials." *Nuclear Instruments and Methods* B 141:98.

Publications

Begg BD, NJ Hess, and WJ Weber. 1999. "XAS and XRD characterization of annealed Pu-doped zircon," *Proc. of the CEA Meeting on HLW and Pu Immobilization*, C Meis and J Carpena, eds. CEA/Saclay (in press).

Begg BD, WJ Weber, R Devanathan, JP Icenhower, S Thevuthasan, and BP McGrail. 1999. "Heavy-ion irradiation effects in rare-earth titanates." *Journal of Nuclear Materials* (submitted).

Begg BD, WJ Weber, R Devanathan, JP Icenhower, S Thevuthasan, and BP McGrail. 1999. "Heavy-ion irradiation effects in pyrochlores." *Waste Management Science and Technology in the Ceramic and Nuclear Industries*, GL Smith, GT Chandler, and B Mobasher, eds. The American Ceramic Society, Westerville, Ohio (in press).

Chen X and RC Birtcher. 1999. "Bubble formation and growth in nuclear waste glasses." *Microstructural Processes in Irradiated Materials*, SJ Zinkle, RC Ewing, GE Lucas, and JS Williams, eds. *Mater. Res. Soc. Symp. Proc. 540*, Warrendale, Pennsylvania (in press).

Chen X and RC Birtcher. 1999. "Electron irradiation enhanced bubble growth in sodium borosilicate glass." *Applied Physics Letters* (to be submitted).

Chen X and RC Birtcher. 1999. "Ion implantation and bubble formation in sodium borosilicate glass." *Journal of Nuclear Materials* (to be submitted).

Corrales LR and J Song. 1998. "Semi-empirical methodology to simulate exciton processes in glasses." *Proc. of the CEA/VALRHO Summer School on Glass: Scientific Research for High Performance Containment.* CEA/Valrhô, Bagnols-sur-Cèze, France, pp. 218-227.

Corrales LR, J Song, RM VanGinhoven, and H Jónsson. 1999. "Vacancy migration and excitons in silica polymorphs." *Waste Management Science and Technology in the Ceramic and Nuclear Industries*, GL Smith, GT Chandler, and B Mobasher, eds. The American Ceramic Society, Westerville, Ohio (in press).

Corrales LR, RM VanGinhoven, J Song, and H Jónsson. 1999. "Vacancy migration barrier energetics and pathways in silica." *Multiscale Modeling of Materials*, VV Bulatov, T Diaz de la Rubia, R Phillips, E Kaxiras, and N Ghoniem, eds. *Mater. Res. Soc. Symp. Proc. 538*, Warrendale, Pennsylvania, pp. 317-321.

Devanathan R, WJ Weber, and LA Boatner. 1998. "Response of zircon to electron and Ne^+ irradiation." *Phase Transformations and Systems Driven far from Equilibrium*, E Ma, P Bellon, M Atzmon, and R Trivedi, eds. *Mater. Res. Soc. Symp. Proc. 481*, Warrendale, Pennsylvania, pp. 419-424.

Fortner JA, JM Hanchar, Y Badyal, DL Price, and WJ Weber. 1999. "Structural analysis of a completely amorphous ^{238}Pu-doped zircon by neutron diffraction." *Microstructural Processes in Irradiated Materials*, SJ Zinkle, RC Ewing, GE Lucas, and JS Williams, eds. *Mater. Res. Soc. Symp. Proc. 540*, Warrendale, Pennsylvania (in press).

Gorretta KC, ML Burdt, MM Cuber, LA Perry, D Singh, AS Wagh, JL Routbort, and WJ Weber. 1999. "Solid-particle erosion of Portland cement and concrete." *Wear* 224:106-112.

Heinisch HL, RE Williford, and WJ Weber. 1999. "Kinetic monte carlo simulations of irradiation-induced amorphization in zircon." *Journal of Nuclear Materials* (to be submitted).

Hess NJ, BD Begg, WJ Weber, and SD Conradson. 1999. "X-ray absorption fine structure and x-ray diffraction analyses of Pu^{3+} and Pu^{4+} substitutions in aged and annealed zircon." *Journal of Nuclear Materials* (submitted).

Hess NJ, GD Maupin, D Griscom, and WJ Weber. 1999. "Spectroscopic investigations of gamma-irradiation effects in complex glasses." *Journal of Non-Crystalline Solids* (to be submitted).

Hess NJ, WJ Weber, and SD Conradson. 1998. "U and Pu L_{III} XAFS of Pu-doped glass and ceramic waste forms." *J. Alloys and Compounds* 271-273:240-243.

Hess NJ, WJ Weber, and SD Conradson. 1998. "X-ray absorption fine structure of aged, Pu-doped glass and ceramic waste forms." *Journal of Nuclear Materials* 254:175-184.

Hess NJ, WJ Weber, and SD Conradson. 1998. "X-ray absorption fine structure of aged, Pu-doped glass and ceramic waste forms." *Scientific Basis for Nuclear Waste Management XXI*, IG McKinley and C McCombie, eds. *Mater. Res. Soc. Symp. Proc. 506*, Warrendale, Pennsylvania, pp. 169-176.

Song J, LR Corrales, and H Jónsson. 1999. "Exploring the excited states of vacancy defects in silica." *Microstructural Processes in Irradiated Materials*, SJ Zinkle, RC Ewing, GE Lucas, and JS Williams, eds. *Mater. Res. Soc. Symp. Proc. 540*, Warrendale, Pennsylvania (in press).

Song J, H Jónsson, and LR Corrales. 1999. "Multiple self-trapped excitons in quartz." *Physical Review Letters* (to be submitted).

Song J, RM VanGinhoven, E Apra, H Jónsson, and LR Corrales. 1999. "Ab initio study of triplet self-trapped excitons in silica: Density functional and Hartee-Fock theory." *Journal of Chemical Physics* (to be submitted).

Song J, RM VanGinhoven, H Jónsson and LR Corrales. 1999. "Vacancy migration in silica polymorphs." *Physical Review B* (to be submitted).

Thevuthasan S, W Jiang, DE McCready, and WJ Weber. 1999. "Damage accumulation and thermal recovery in $SrTiO_3$ implanted with various ions." *Microstructural Processes in Irradiated Materials*, SJ Zinkle, RC Ewing, GE Lucas, and JS Williams, eds. *Mater. Res. Soc. Symp. Proc. 540*, Warrendale, Pennsylvania (in press).

Weber WJ. 1999. "Radiation effects in zircon." *Journal of Nuclear Materials* (to be submitted).

Weber WJ and LR Corrales. 1997. "Radiation effects in nuclear waste materials." *Science to Support DOE Site Cleanup: The Pacific Northwest National Laboratory Environmental Management Science Program Awards.* PNNL-11589, Pacific Northwest National Laboratory, Richland, Washington, pp. 43-52.

Weber WJ and LR Corrales. 1998. "Radiation effects in nuclear waste materials." *Science to Support DOE Site Cleanup: The Pacific Northwest National Laboratory Environmental Management Science Program Awards.* PNNL-11889, Pacific Northwest National Laboratory, Richland, Washington, pp. 1.107-1.126.

Weber WJ, R Devanathan, A Meldrum, LA Boatner, RC Ewing, and LM Wang. 1999. "The effect of temperature and recoil spectra on amorphization in zircon." *Microstructural Processes in Irradiated Materials,* SJ Zinkle, RC Ewing, GE Lucas, and JS Williams, eds. *Mater. Res. Soc. Symp. Proc. 540,* Warrendale, Pennsylvania (in press).

Weber WJ, RC Ewing, and A Meldrum. 1997. "The kinetics of alpha-decay-induced amorphization in zircon and apatite containing weapons-grade plutonium or other actinides." *J. Nuclear Materials* 250:147-155.

Weber WJ and NJ Hess. 1999. "Radiation effects in defense reference borosilicate glass containing plutonium." *Journal of Nuclear Materials* (to be submitted).

Weber WJ, NJ Hess, SD Conradson, and JD Vienna. 1997. "Self-radiation effects in glass and ceramic waste forms for the stabilization and disposition of plutonium." *Plutonium Futures - The Science.* LA-13338-C, Los Alamos National Laboratory, Los Alamos, New Mexico, pp. 25-26.

Williford RE, BD Begg, WJ Weber, and NJ Hess. 1999. "Computer simulation of Pu^{3+} and Pu^{4+} substitutions in zircon." *Journal of Nuclear Materials* (submitted).

Williford RE, R Devanathan, and WJ Weber. 1998. "Computer simulation of displacement threshold energies for several ceramic materials." *Nuclear Instruments and Methods* B 141:98-103.

Williford RE, WJ Weber, R Devanathan, and AN Cormack. 1999. "Native vacancy migrations in zircon." *Journal of Nuclear Materials* (in press).

Presentations

Begg BD, NJ Hess, and WJ Weber. April 22-23, 1999. "XAS and XRD characterization of annealed Pu-doped zircon." CEA Meeting on HLW and Pu Immobilization, Saclay, France.

Begg BD, WJ Weber, R Devanathan, JP Icenhower, S Thevuthasan, and BP McGrail. April 25-28, 1999. "Heavy-ion irradiation effects in pyrochlores." The 101st Meeting of The American Ceramic Society, Indianapolis, Indiana.

Chen X, RC Birtcher, and SE Donnelly. November 30-December 4, 1998. "Bubble formation and growth in nuclear waste glasses." Materials Research Society Annual Meeting, Boston.

Corrales LR. October 1997. "Lattice theories and molecular dynamics simulations of glasses." Department of Chemistry, University of Maryland, College Park, Maryland.

Corrales LR. October 1997. "Molecular dynamics simulations of defects and excitons in glasses." American Ceramics Society, Glass and Optical Materials Division Meeting, Williamsburg, Virginia.

Corrales LR and J Song. September 1997. "Molecular dynamics simulations of excitons in glasses." CEA/VALHRO Summer School, Mejannes le Clap, France.

Corrales LR, J Song, RM VanGinhoven, and H Jónsson. March 21-25, 1999. "Migration of oxygen vacancy radical defects and self-trapped excitons in silica." American Chemical Society National Meeting, Anaheim, California (invited paper).

Corrales LR, J Song, RM VanGinhoven, and H Jónsson. April 25-28, 1999. "The formation and migration energetics of radical defects in silica polymorphs." The 101st Meeting of The American Ceramic Society, Indianapolis, Indiana (invited paper).

Corrales LR, RM VanGinhoven, J Song, and H Jónsson. November 30-December 4, 1998. "Vacancy migration barrier energetics and pathways in silica." Materials Research Society Annual Meeting, Boston.

Devanathan R, WJ Weber, and LA Boatner. December 1-5, 1997. "Response of zircon to electron and Ne^{+} irradiation." Materials Research Society Annual Meeting, Boston.

Devanathan R, WJ Weber, and RE Williford. November 30-December 4, 1998. "Amorphization of $Gd_2Ti_2O_7$ by energetic heavy ion irradiation." Materials Research Society Annual Meeting, Boston.

Fortner JA, JM Hanchar, Y Badyal, DL Price, and WJ Weber. November 30-December 4, 1998. "Structural analysis of a completely amorphous ^{238}Pu-doped zircon by neutron diffraction." Materials Research Society Annual Meeting, Boston.

Heinisch HL, RE Williford, and WJ Weber. November 30-December 4, 1998. "Computer simulations of irradiation-induced defect accumulation and amorphization in zircon." Materials Research Society Annual Meeting, Boston.

Hess NJ, GD Maupin, and WJ Weber. November 30-December 4, 1998. "Spectroscopic studies of gamma-irradiated glass waste forms." Materials Research Society Annual Meeting, Boston.

Hess NJ, WJ Weber, and SD Conradson. September 21-26, 1997. "U and Pu L_{III} XAFS of Pu-doped glass and ceramic waste forms." International Conference on *Actinides '97*, Baden-Baden, Germany.

Hess NJ, WJ Weber, and SD Conradson. September 28-October 3, 1997. "X-ray absorption fine structure of aged, Pu-doped glass and ceramic waste forms." MRS Symposium, *Scientific Basis for Nuclear Waste Management XXI*, Davos, Switzerland.

Song J and LR Corrales. March 16-20, 1998. "Simulation of exciton processes in networked materials." March APS National Meeting, Anaheim, California.

Song J, LR Corrales, and H Jónsson. November 30-December 4, 1998. "Exploring the excited states of vacancy defects in silica." Materials Research Society Annual Meeting, Boston.

Thevuthasan S, W Jiang, DE McCready, and WJ Weber. November 30-December 4, 1998. "Damage accumulation and thermal recovery in $SrTiO_3$ implanted with various ions." Materials Research Society Annual Meeting, Boston.

Weber WJ. February 20, 1997. "Radiation effects from the incorporation of plutonium in glasses and ceramics." Los Alamos National Laboratory, Los Alamos, New Mexico (invited seminar).

Weber WJ. December 1, 1997. "Radiation effects in glass and ceramic waste forms." Massachusetts Institute of Technology, Cambridge, Massachusetts (invited seminar).

Weber WJ. December 11, 1997. "Radiation effects in glass waste forms." Argonne National Laboratory, Argonne, Illinois (invited seminar).

Weber WJ. January 8, 1998. "Radiation effects in crystalline waste form phases." Idaho National Engineering and Environmental Laboratory, Idaho Falls, Idaho (invited seminar).

Weber WJ. April 3-4, 1998. "Radiation effects from alpha decay in nuclear waste ceramics." American Nuclear Society Northern Student Conference, Ann Arbor, Michigan (invited plenary lecture).

Weber WJ. April 19-22, 1998. "Effects of radiation on solid nuclear waste forms." DOE Workshop on Research Needs and Opportunities in Radiation Chemistry, Chesterton, Indiana (invited plenary lecture).

Weber WJ. July 27-30, 1998. "EMSP projects in materials science." DOE Environmental Management Science Program Scientific Workshop, Rosemont, Illinois.

Weber WJ and LR Corrales. July 27-30, 1998. "Radiation effects in nuclear waste forms." DOE Environmental Management Science Program Scientific Workshop, Rosemont, Illinois.

Weber WJ and R Devanathan. May 4-6,1998. "Effects of alpha decay on crystalline ceramic waste forms." American Ceramic Society Meeting, Cincinnati, Ohio.

Weber WJ, R Devanathan, A Meldrum, LA Boatner, RC Ewing, and LM Wang. November 30-December 4, 1998. "The effect of temperature and recoil spectra on amorphization in zircon." Materials Research Society Annual Meeting, Boston.

Weber WJ, RC Ewing, and A Meldrum. March 30-April 3, 1998. "Radiation effects in nuclear waste ceramics." American Chemical Society Annual Meeting, Dallas.

Weber WJ, NJ Hess, SD Conradson, and JD Vienna. August 25-27, 1997. "Self-radiation effects in glass and ceramic waste forms for the stabilization and disposition of plutonium." Topical Conference on Plutonium Futures - The Science, Santa Fe, New Mexico.

Williford RE and WJ Weber. April 25-28, 1999. "Defect formation and migration energetics in disordered $Gd_2Ti_2O_7$." The 101st Meeting of The American Ceramic Society, Indianapolis, Indiana.

Williford RE, R Devanathan, and WJ Weber. September 14-19, 1997. "Computer simulation of displacement threshold energies for several ceramic materials." 9th International Conference on Radiation Effects in Insulators, Knoxville, Tennessee.

Williford RE, WJ Weber, R Devanathan, and JD Gale. November 30-December 4, 1998. "Oxygen vacancy migration in $Gd_2(Ti,Zr)_2O_7$ pyrochlores." Materials Research Society Annual Meeting, Boston.

Spent Nuclear Fuel and Nuclear Materials

Microbially Promoted Solubilization of Steel Corrosion Products and Fate of Associate Actinides

(First Year of Funding: 1998)

Principal Investigator

Dr. Yuri A. Gorby
Pacific Northwest National Laboratory
P.O. Box 999, MSIN P7-54
Richland, WA 99352
(509) 373-6177 (phone)
(509) 376-1321 (fax)
ya_gorby@pnl.gov

Co-Principal Investigator

Dr. James K. Fredrickson
Pacific Northwest National Laboratory
P.O. Box 999, MSIN P7-54
Richland, WA 99352
(509) 375-3908 (phone)
(509) 376-1321 (fax)
jk_fredrickson@pnl.gov

University Co-Investigator

Dr. Gill Geesey
Center for Biofilm Engineering
Montana State University
P.O. Box 173980 (409 Cobleigh Hall)
Bozeman, MT 59717-3890
(406) 994-4770 (phone)
(406) 994-6098 (fax)
gill_g@erc.montana.edu

Research Objectives

This project will probe fundamental scientific issues regarding a microbial process with potential for decontaminating corroding metal surfaces. We hypothesize that dissimilatory iron-reducing bacteria (DIRB), via anaerobic respiration, can quantitatively dissolve amorphous and crystalline iron oxides and thereby release oxide-associated radionuclide contaminants. Associated actinides will be sorbed by cell surfaces or precipitated within biofilms that can be removed and recovered by enzymatic digestion of microbial attachment factors. This environmentally benign, enzymatic process avoids the use of hazardous or toxic chemicals, minimizes the volume and toxicity of secondary wastes, and could be applied in situ. Although an increasing body of scientific literature supports this working hypothesis, a basic understanding is needed of the biological and chemical processes that impact 1) attachment and detachment of iron-reducing bacteria to oxide surfaces; 2) the rate, extent, and products of iron reduction; and 3) the fate of radionuclides following enzymatic reduction of corroding steel (which is needed to evaluate and develop effective biological approaches for decontamination of aging metallic structures and piping). The goal of this project is to provide the scientific underpinnings for the development of biologically based approaches for the removal of contaminants from corroding steel surfaces. Specifically, this research will accomplish the following:

- determine the role of oxide structure, topology, and composition on bacterial attachment and subsequent reductive dissolution of Fe(III) oxide corrosion products that form on stainless and mild steels
- identify how soluble electron "shuttles" can facilitate the rate and extent of microbial reductive dissolution of iron oxide corrosion products, including surface features and pores inaccessible to bacteria
- determine the distributions of radionuclides released during reductive dissolution of oxide films on metal surfaces as a function of aqueous geochemical composition.

This project uniquely couples PNNL's expertise in microbial metal reduction and biogeochemistry with Montana State University's Center for Biofilm Engineering's expertise and capabilities in biofilm analysis, engineering, and corrosion. In addition, this research project will take advantage of the capabilities and expertise at PNNL in actinide chemistry and advanced instrumentation for probing the distribution and chemical nature of surface-associated radionuclides and metals associated with the William R. Wiley Environmental Molecular Sciences Laboratory (EMSL).

Problem Statement

Contaminated surfaces of various metals, including stainless steel, copper, nickel, iron, and carbon steel, pose significant problems to the ongoing efforts of the U.S. Department of Energy (DOE). Contamination consisting of nuclear fuel components contaminated with plutonium, uranium, etc., constitutes the most significant problems at DOE facilities and is commonly associated with the surfaces of metal piping, tanks, gloveboxes, and other structures. Current technologies for removing the contaminants are costly and produce large volumes of secondary waste; hence, the bulk of contaminated metal

is commonly disposed of as radioactive waste. Also, interior surfaces of the piping are inaccessible to many standard decontamination methods. DOE recognizes that new or significantly improved techniques are needed for decontaminating stainless steel, iron, copper, and other metals with surface-associated radionuclides and metals.

Processing and disposal of radionuclides has contaminated metallic surfaces throughout the DOE complex. Currently, DOE estimates that nearly 180,000 metric tons of contaminated stainless and mild steel structures and piping will be disposed of as radioactive solid waste because current technologies for dealing with these wastes are inadequate and costly. DOE is faced with meeting decommissioning and decontamination obligations at many of its facilities by the year 2019. If decontamination to levels required for free release could be achieved, some of this material could be released as scrap into the commercial sector for reuse or recycling. The estimated value of scrap metal across the DOE complex was estimated to be greater than $1 billion in 1993. Thus, if effective and economic approaches were developed for decontaminating metal surfaces, they could result in considerable savings by reducing the volume of radioactive waste requiring disposal and by rendering the metals useful and as a potentially valuable commodity.

Microbial enzymatic dissolution of post-corrosional oxide scales has considerable potential for environmentally benign and economic treatment of contaminated metallic surfaces. However, fundamental scientific information is lacking in key areas that prevent the development of such approaches. These areas include the mechanisms involved in the attachment, colonization, and detachment of iron-reducing bacteria from corrosion scales; the quantitative reductive dissolution of mineralogically, morphologically, and compositionally diverse metal oxides that make up the scales; and the post-reduction solubility and distribution of the scale-associated contaminants.

This research project will investigate the microbial reductive dissolution of mild and stainless steel corrosion products and the fate of associated radionuclide and metal contaminants. The general goals are as follows:

- develop an improved understanding of microbial reductive dissolution of iron oxide scales that form on corroding steel and act as highly efficient scavengers of radionuclides, as a function of oxide form and composition

- evaluate approaches for promoting the attachment to and colonization of surfaces by iron-reducing bacteria and the biological and chemical factors that promote the formation of iron-reducing biofilms

- identify the potential for actinide binding to cells and/or precipitation within biofilms as a function of solution chemistry.

To this end, the proposed research will address fundamental scientific questions regarding the microbial dissolution of corrosion products and associated radionuclide and metal contaminants. These questions include the following:

- How do the mineralogy, morphology, and contaminant composition of oxide minerals formed on corroded steel influence the attachment and colonization by iron-reducing bacteria and the subsequent reductive dissolution reactions?

- How does aqueous chemical composition influence the rate and extent of microbial reductive dissolution of corrosion products and the subsequent solubility of associated contaminants?

- What is the fate of radionuclides associated with corrosion products that are dissolved via microbial reductive dissolution? Are the contaminants selectively accumulated or biosorbed by the cells or biofilms, released into solution, or repartitioned to the surface of the metal or into secondary mineral phases?

- Can soluble quinones, such as anthraquinone disulfonate (AQDS), facilitate dissolution of oxides and oxide films, including surface features and pores inaccessible to the bacteria, via electron "shuttling" from cell to oxide surfaces with subsequent bonded electron transfer, and thereby enhance removal of contaminants from the surface?

Research Progress and Implications

The research is structured into four primary tasks. Task 1 will investigate the factors controlling the attachment to and release from oxide scale that forms on corroding mild and stainless steel by metal-reducing bacteria to Fe(III). Task 2 will probe the effects of iron oxide composition and surface properties on cell attachment and biofilm formation. Task 3 will examine and quantify the reductive dissolution of synthetic iron oxide thin films deposited on internal reflective elements as well as the reductive dissolution of iron oxide scale on corroding steel in the presence and absence of soluble electron shuttles that can enhance the rate and extent of enzymatic iron reduction. Oxygen concentration gradients throughout the developing biofilm will be measured and the impact of aerobic conditions external to the biofilm on the rate and extent of iron reduction will be evaluated. Task 4 will determine the distribution of actinides released from Fe oxides during reductive dissolution of scales that are colonized by metal-reducing bacteria. Particular attention will be given to the processes that direct the incorporation of actinides into the biomass.

Work has begun on all four tasks with contributions from each of the three collaborating laboratories. Frank Caccavo at the University of New Hampshire has been addressing Task 1 by investigating the attachment of iron-reducing bacteria to a variety of iron oxide minerals that are typical components of corroding steels. Dr. Caccavo found that the attachment of cells to minerals is influenced by the mineral form and by the ionic strength of the aqueous medium. For brevity, only selected data are presented. Figure 1 shows the impact of ionic strength on the attachment of the iron-reducing bacterium *Shewanella alga* strain BrY to a synthetic hydrous ferric oxide (HFO). The data illustrate that bacterial attachment is reduced as the ionic strength of a synthetic groundwater medium increases.

These results have important implications for the application and attachment of bacteria to contaminated corrosion of mild and stainless steels. First, they define the operational conditions that optimize the attachment of cells to contaminated, corroded steel. Second, they provide insight into potential approaches for removing and recovering bacterial cells once they have extracted radionuclides from the contaminated surfaces.

Dr. Gill Geesey at Montana State University has begun work on Tasks 2 and 3. Dr. Geesey and his coworkers have purchased and recently installed a Raman microscopic imaging system. When fully functional, this Raman microscope will offer a powerful alternative to high vacuum surface chemical analysis where reaction product stability is strongly influenced by the presence of water or where

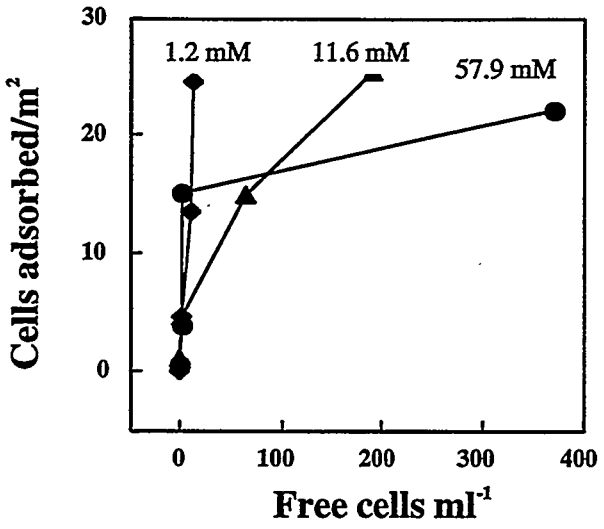

Figure 1. Effect of Ionic Strength on the Attachment of Iron Reducing Bacteria to HFO

chemical transformations in fully hydrated iron oxide films during colonization by DIRB in a nondestructive, real-time mode. They will 1) establish the role of the film-associated DIRB in iron transformation and 2) determine the influence of such transformations on the stability of sorbed actinide ions, which can also be detected by Raman scattering. Because the spatial resolution of this imaging spectroscopic technique is on the order of a few micrometers, localized reactions at the individual bacterial cell or microcolony level will be resolved. This will allow discrimination of biotically and abiotically mediated iron transformations that occur over the duration of bacterial attachment and biofilm formation on the iron oxide film.

Researchers at PNNL are addressing Task 4 by evaluating the effect of soluble electron shuttle compounds on the rate and extent of reduction of iron oxides typically associated with corroding steels as well as the effects of these compounds on the fate of actinides entrained or sorbed to the corrosion products. The majority of the work has focused on the chemistry of the redox-reactive compound anthroquinone disulfonate. This chemical can serve as an electron shuttle between iron-reducing bacteria and solid-phase iron oxides that the organisms reduce as a mode of respiration.

Dr. Fredrickson, co-principal investigator on this project, has demonstrated that microbially reduced AQDS can increase the rate and extent of iron oxides reduction, such as HFO. Figure 2 illustrates that reduction of HFO proceeds more rapidly and to a greater extent in the presence of AQDS than in its absence.

We have begun to evaluate the effect of microbially reduced AQDS on the valence transformation and solubility of plutonium. Pu(IV) is exceedingly insoluble at pH values above 2 and reaches levels of detection ($10^{-8.5}$) at around pH 3. In contrast, Figure 3 illustrates that plutonium, initially added as Pu(IV), remained dissolved at pH values between 0.5 and 5.5 in the presence of microbially reduced AQDS. The marked increase in dissolved plutonium is attributed to reduction of Pu(IV) to Pu(III), which is soluble to pH values approaching neutrality. This conclusion will soon be confirmed by spectroscopic analyses that discriminate between the various valence states of plutonium. The results have important implications for evaluating the potential of AQDS as part of a biological strategy for removing plutonium from corroded steel while avoiding acidic conditions necessary for dissolving Pu(IV) solids.

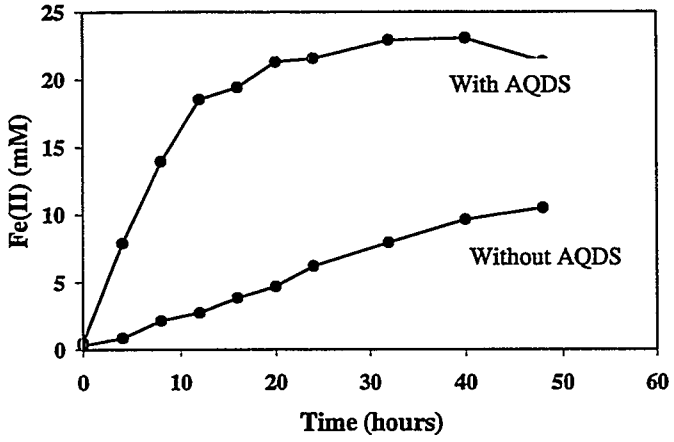

Figure 2. Effect of Dissolved AQDS on the Rate and Extent of HFO Reduction by Iron-Reducing Bacteria

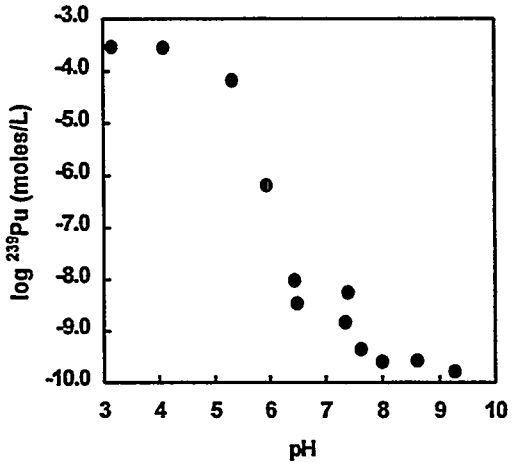

Figure 3. Solubility of Plutonium in the Presence of Microbially Reduced AQDS

Planned Activities

Progress will continue on all aspects of the proposed research. Collaborators at the University of New Hampshire will continue to investigate conditions that promote the attachment and detachment of bacterial cells on iron oxides associated with corrosion scales. Researchers at the University of Montana will monitor and describe the bacterial colonization of oxide minerals using infrared spectroscopy by following the intensity of the amide I and amide II bands. Dissolution or sloughing of the oxide film due to bacterial colonization and enzymatic reduction will be evaluated by monitoring increases in the water adsorption bands compared with that obtained from sterile controls run in parallel. Bacterial colonization of the oxide film will be simultaneously characterized by reflectance differential interference contrast light microscopy or scanning confocal laser microscopy via a specially designed shuttle that translocates the flow channel reactor between the microscope stage and the optical bench of the

spectrometer without disrupting flow or disturbing the biofilm. Through this approach, we will be able to relate structural and chemical changes in the oxide film by attenuated total reflectance/Fourier Transform infrared to the microbiological properties, such as cell density and biofilm structure on the film. The infrared technique averages spectral information gathered from the entire surface of the oxide film. Specific biofilm features will be investigated using the newly installed Raman imaging capability. Because Raman is sensitive to chemical changes in the inorganics located on the surface and insensitive to the solvent, the complementary visual and chemical imaging techniques of the coupled system will provide vital information on the inorganic chemistry occurring in the biofilm, visual information of the biofilm, and changes in the oxide film beneath the biofilm. Raman spectroscopy is very valuable for distinguishing between bonding environments of the partially oxidized iron species. Spectra will be collected with integration times of about 30 seconds, which makes the process ideal for the identification of kinetic products and intermediates on the time scale of iron oxidation.

PNNL researchers will continue to investigate the fate of actinides during reductive dissolution of contaminated corrosion scale. Total alpha activity to evaluate the amount of plutonium and uranium that is released into solution, partitioned into reduced secondary mineral phases, or incorporated into microbial biomass in the presence and absence of the soluble electron shuttle AQDS. Oxidation states of the actinides will be determined by x-ray adsorption near-edge spectroscopy by requesting beam time at Stanford Synchrotron Research Laboratory. When applicable (i.e., under low pe conditions imposed by the bacteria), Nd(III) will be used as a non-radioactive analog for Pu(III).

Because the phosphoryl substituents of lipopolysaccharides on the outer membrane of gram-negative bacteria exhibit a high affinity for polyvalent cations, experiments will be conducted to determine what role these components may play in accumulation of uranium and plutonium by DIRB under aerobic and iron-reducing conditions. Similar bioaccumulation experiments will be conducted using cells in which the production of exopolysaccharide has been induced. Exopolysaccharide, an extracellular component implicated in the long-term attachment of DIRB to iron oxides, may be an important sink for actinides during reduction of oxide scale and should therefore receive experimental attention. Together, topics addressed in Task 4 will provide information vital for evaluating the fate of actinides during and following the reduction of contaminated corrosion products.

Schedule and Milestones

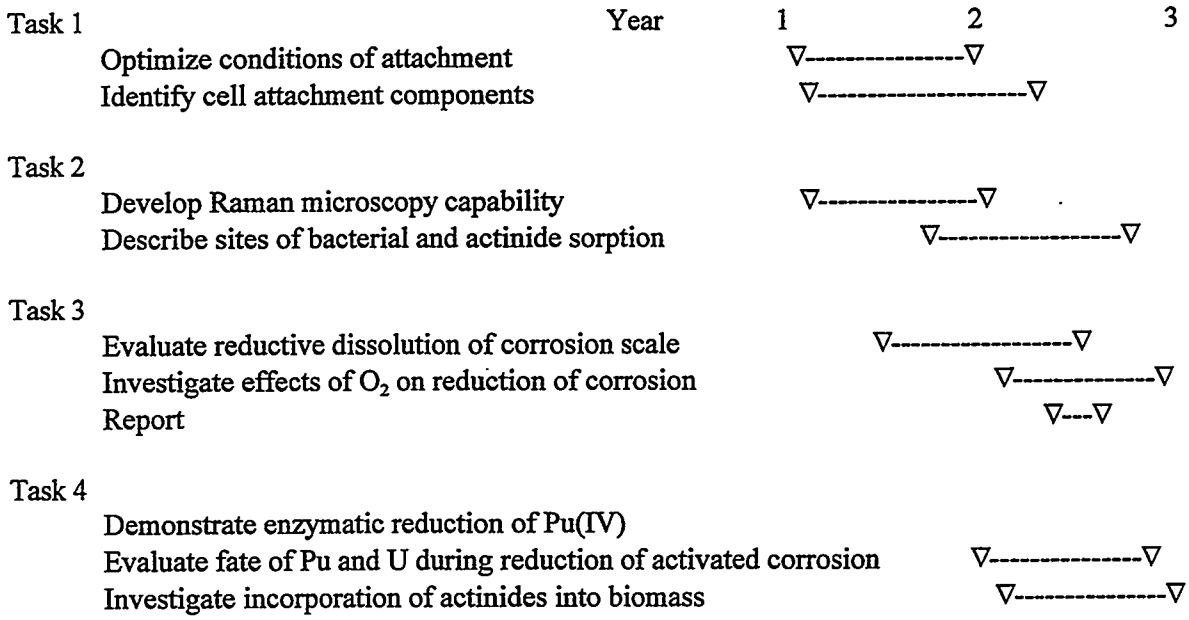

Publications and Presentations

To date no publications or presentations have resulted from this work. Publications are expected within the second and third years of the project's duration.

Contaminant-Organic Complexes, Their Structure and Energetics in Surface Decontamination Processes

(First Year of Funding: 1998)

Principal Investigator

Dr. Calvin C. Ainsworth
Pacific Northwest National Laboratory
Biogeochemistry Resources
P.O. Box 999, MSIN K3-61
Richland, WA 99352
(509) 375-2670 (phone)
(509) 375-6954 (fax)
cc_ainsworth@pnl.gov

Co-Principal Investigators

Dr. Donald M. Friedrich
Pacific Northwest National Laboratory
Environmental Dynamics & Simulation
P.O. Box 999, MSIN K8-96
Richland, WA 99352
(509) 376-9637 (phone)
(509) 376-3650 (fax)
dm_friedrich@pnl.gov

Dr. Benjamin P. Hay
Pacific Northwest National Laboratory
Theory, Modeling, and Simulation
P.O. Box 999, MSIN K1-83
Richland, WA 99352
(509) 372-6239 (phone)
(509) 375-6631 (fax)
bp_hay@pnl.gov

Dr. Samuel J. Traina
Ohio State University
School of Natural Resources
2021 Coffey Road
Columbus, OH 43210
(614) 292-9037 (phone)
(614) 292-7432 (fax)
traina.1@osu.edu

Dr. Satish C. B. Myneni
Lawrence Berkeley National Laboratory
Earth Sciences Division
Mail Stop 50E
Berkeley, CA 94720
(510) 486-4591 (phone)
(510) 486-5105 (fax)
smyneni@lbl.gov

Project Objectives

There are a wide variety of compounds that are naturally occurring biodegradable organic chelates (siderophores) that appear to be more effective at oxide dissolution and actinide complexation than EDTA or other organic acids now used in decontamination processes. These chelates bind hard acids [Fe(III) and actinides(IV)] with extraordinarily high affinities. For example, the binding constant for the siderophore enterobactin with iron is about 10^{50}, and its binding constant for Pu(IV) is estimated to be as high. Hence, this project is investigating the efficacy of using siderophores (or siderophore-like chelates) as decontamination agents of metal surfaces. The specific goals of this project are as follows:

1. develop an understanding of the surface interaction between siderophores (and their functional moieties), iron, and actinide oxides; their surface chemical properties that foster their dissolution; and the conditions that maximize that dissolution

2. develop the computational tools necessary to predict the reactivity of different siderophore functional groups toward oxide dissolution and actinide(IV) solubilization

3. identify likely candidate chelates for use in decontamination processes.

To meet these objectives, the project combines molecular spectroscopy and computational chemistry to provide basic information on the structure and bonding of siderophore functional groups to metal (iron and uranium) oxide specimens common to corrosion products and scales on carbon steel and stainless steel encountered in U.S. Department of Energy (DOE) facilities. The project explores fundamental scientific aspects of oxide mineral surface chemistry and dissolution related to chelate-induced solubilization. The spectroscopic and computational aspects of this project are complemented by macroscopic dissolution and solubilization studies of oxides and associated contaminants. From this combination of molecular, macroscopic, and computational studies, structure-function and structure-reactivity relationships will be developed.

Problem Statement

DOE must decontaminate and decommission a large number of surplus facilities. At present there are about 7,000 contaminated facilities that require deactivation and decommissioning. A major need associated with this effort is improvement of metal surface decontamination. DOE is responsible for the disposal of approximately 180,000 metric tons of metal (mostly steel) associated with their nuclear facilities. Much of this metal is steel and iron, which develops a passivity layer where radionuclides and other contaminants are retained. Continued deposition of corrosion products on the steel surfaces allows radioactive materials to be continually sorbed to these secondary oxide layers, incorporated into their structure, or occluded by overgrowth.

Oxides of the type important to steel passivity layers and secondary scale layers are found in nature and have been shown to sorb foreign ions (such as actinides) to their surface, incorporate them into their structure, and occlude them from the bathing solution via overgrowth mechanisms. Contaminants associated with steel surface films, corrosion pits, and cracks are present as mixed solids or surface sorbed species. Regardless of where they reside, the critical step in decontamination is the dissolution of the oxide surface film. As dissolution of the oxide film occurs, solubilization of radioactive contaminants will follow. DOE-EM led surveys and workshops focused on understanding decontamination and

decommissioning (D&D) needs at its production and processing sites and concluded that new, more effective decontamination techniques for metal surfaces and equipment are a high priority. The candidate facilities include gaseous diffusion plants, reactors, isotope processing plants, fuel reprocessing plants, hot cells, gloveboxes, and waste/storage processing facilities. Equipment ranges from highly contaminated tanks, extraction columns, and piping to surfaces with trace amounts of radioactive contamination such as gloveboxes, piping, and other surfaces.

Research Progress

This research program, which began in late FY 1998, is separated into four activities on siderophore chemistry (Table 1). These tasks are centered on central investigative themes 1) macroscopic dissolution studies (C. Ainsworth, PNNL), 2) optical spectroscopy (D. Friedrich and C. Ainsworth, PNNL), 3) x-ray absorption spectroscopy (XAS) (S. Traina, OSU, and S. Myneni, LBNL), and 4) computational chemistry (B. Hay, PNNL). All studies use the same set of solids that were prepared in bulk and whose surface and chemical properties have been determined (i.e., surface area, electrophoretic mobility, etc.). Dr. Sam Traina (Ohio State University) produced, characterized, and distributed the solids. In addition, to focus the effort, a series of siderophores and siderophore analogs is being used throughout the planned research (Table 2). These chelates represent the three major classes of biologically produced chelates and will allow the spectroscopic and macroscopic researchers to build a data set relating reactivity to molecular scale information on ligand surface structure and orientation that will be broadened using computational tools. The chelates (or siderophores) are purchased, synthesized, or isolated from specific bacterial or fungal cultures.

Macroscopic Dissolution Studies

Initially, this task is directed at obtaining the specific compounds listed in Table 2. To date, two hydroxamates, Desferrioxamine B and ferrichrome, have been purchased from Sigma. Both of these siderophores are trihydroxamates but have different structures. A dihydroxamate, rhodotorulic acid, is being collected from culture growth of *Rhodotorula pilimanae* (ATCC 26423). Likewise, a catecholate (agrobactin) siderophore and an aminocarboxylate (rhizoferrin) siderophore are being collected from culture growth of *Agrobacterium tumefaciens* (ATCC 23308) and *Rhizopus microsporus* var. rhizopodiformis (ATCC 66276). These three organisms have been received from the American Type Culture Collection and are currently being cultured in iron-free media.

This task's primary objective centers on determining solubilization of iron and uranium from oxide sols under a range of environmental variables (i.e., pH, ionic strength, ionic composition, ligand and solid type and concentrations). The goal of this task is to develop kinetic dissolution data that can be used in calculating structure-reactivity relationships relating solution complexation data to dissolution rates and finally to ligand surface structure.

Preliminary oxide dissolution investigations have begun. These studies are centering on 1) determining the effectiveness of batch systems versus stirred-flow cell systems, 2) detection options for iron and the reactive ligand, and 3) time dependence. We are working with acetohydroxamate, Desferrioxamine, and a well-characterized goethite. Preliminary data suggest that, by varying the residence time, solid solution ratio, and pH in a stirred-flow cell system, dissolution rates can be readily obtained with minimal waste of siderophore.

Table 1. Objectives, Initial Hypotheses, and Experiments Governing Investigations in the Four Tasks

	Task 1	Task 2	Task 3	Task 4
Objectives	Determine the dissolution rate of oxides as a function of pH, ligand concentration, chromium content, and ionic composition	Identify dominant surface species responsible for oxide dissolution and its time-resolved spectra	Identify the structure and coordination chemistry of sorbed metals and their interaction with ligands	Using molecular mechanics, correlate aqueous structure function data to oxide dissolution rate data
Hypotheses	pH of maximal dissolution rate will be > the oxide zpc for catecholate ligands and < the oxides zpc for hydroxamate ligands; surface speciation is critical to rate	Mononuclear bidentate surface complex primarily responsible for dissolution but mechanism will have multiple species and parallel reaction paths	Metal surface speciation will vary with surface concentration, time, and oxide phase and will affect ligand's ability to desorb metals and dissolve oxide	Aqueous binding affinities for ligands with iron and f-block metals will correlate to the maximal oxide dissolution rate
Experiments/Results	Dissolution rate studies of oxide phases at variable pH, ligand concentration, and chromium content • identification of optimum dissolution rates and conditions • mechanisms and ligand binding structure suggested • presence/absence of incongruent dissolution • rates of reaction vary with extent	Static and time-resolved studies with different oxide phases in varying conditions • identify surface speciation of ligands • species vary with chemical conditions but a primary species responsible for dissolution • reactions are related to surface charge and site density	Determine ability of ligands to promote metal desorption and the metals effect on ligand promoted oxide dissolution • metal clusters form with increasing surface metal concentration and time • as metal concentration increases ligand promoted desorption rate decreases • ligand reacts with stable metal surface species	Extend the MM3 parameter set to treat ligands with catechol and hydroxamate and their iron and f-block metal complexes • extended MM3 model reproduces features of known compounds • model correctly locates observed configurations of ligands and metal complexes • correlates ligand structure/reactivity and dissolution rates

Table 2. Set of Siderophores and Siderophore Analogs To Be Used in the Planned Research

Class	Siderophore	Representative Model Ligand
Hydroxamates	Desferrioxamine B	Acetohydroxamate, benzohydroxamate
Catecholates	Enterobactin	Catechol, 3-hydroxysalicylate
Aminocarboxylates	Rhizoferrin	EDTA, glycine

Optical Spectroscopy

Task 2 (optical spectroscopy) will investigate the bonding and structure of ligands and the surface speciation under conditions similar to those in the macroscopic dissolution studies. The goal of this task is to develop the fundamental basis by which we can refine macroscopic reactivity interpretations and relate them to aqueous structure-function relationships.

Preliminary studies have centered on collecting infrared spectra of acetohydroxamic acid that were obtained from 400 to 4000 cm^{-1} using horizontal attenuated total reflectance (HATR) measurements. An ATR trough cell was obtained that is compatible with the low pHs of the solutions and suspensions of interest. The ATR cell was installed and aligned in a Bruker IFS66/VS. This spectrometer has conventional N_2 gas purge and the ability to evacuate the bench and sample chamber, thereby eliminating absorbances from CO_2 and water.

Spectra of lyophilized goethite agreed well with published analyses. Signal to noise of the spectra was greatly enhanced when the goethite powder was pressed against the ATR crystal using a powder press. Solutions and suspensions of acetohydroxamic acid at pH 3 and pH 6, with and without goethite, were obtained under vacuum. However, to obtain vacuum spectra, the samples were placed in the trough cell and a cover clamped to the cell. This clamping caused undetected movements of the ATR and its mount, thereby causing some spectral artifacts. Generally, spectra of these solutions and suspensions agreed with previous published work, but subtle spectral features were masked. Subsequent analyses will be performed either using conventional nitrogen gas purge or by use of a flow-cell cover plate. The cover plate allows atmospheric isolation thereby enabling evacuation of the bench and eliminates cell misalignment due to clamping and unclamping.

X-Ray Absorption Spectroscopy

Task 3 (XAS) will work closely with Task 2 as these two spectroscopies approach the structure and bonding issues from different aspects; they are complementary (hence confirmatory to one another) and noninvasive. Hence, a consistent model of oxide-chelate adsorption/dissolution may be obtained. However, before initiating these studies, a series of oxides were required for Tasks 1 through 3. These oxides have been prepared and sent to the principal investigators of the other tasks. Dr. Sam Traina, as a university collaborator, has a separate contract with the EMSP and has developed a report of this project under his DOE contract (DE-FG07-98ER14926). For more detailed information on this task, see Dr. Traina's annual report.

Chromium substitution for iron in maghemite and hematite can occur during the corrosion of chromium-containing steels. The goal of this study was to characterize the effects of chromium substitution on some fundamental properties of hematite and maghemite and the substitution's effect on ligand adsorption and oxide dissolution. Hematite (α-Fe_2O_3) was synthesized using Fe(III) perchlorate instead of Fe(III) nitrate. Eskolaite (α-Cr_2O_3) was synthesized from Cr(III) perchlorate in a manner analogous to that used for hematite. The resulting chromium-precipitate was heated at >600°C. Samples of α-$Fe_{2-x}Cr_xO_3$ were synthesized by mixing solutions of Cr(III) and Fe(III) nitrate in an $(NH_4)_2CO_3$ buffer. Calcination of these materials at 400°C produced the mixed-metal oxides. Maghemite (γ-Fe_2O_3) was synthesized by heating synthetic magnetite to 250°C. Mixed-metal maghemites (γ-$Fe_{2-x}Cr_xO_3$) were generated in a like fashion from synthetic Cr(III) magnetites.

To date, 11 solids have been synthesized, with hematite and maghemite synthesized in substantial quantities. The hematite-eskolaite series contains the following members: hematite, 95% iron, 90% iron,

75% iron, 50% iron, 25% iron, and eskolaite. Also a partial series of maghemite-eskolaite has been produced. Members of this series include maghemite, 90% iron, 75% iron, and eskolaite. In addition, magnetite has been synthesized.

X-ray diffraction (XRD) identification has been performed on each of the synthesized minerals. The hematite-eskolaite series shows that with increasing chromium content the characteristic peaks gradually shift from hematite to eskolaite. The XRD also shows changes in crystallinity within the series. The same XRD changes are seen in the maghemite-eskolaite series. In both series the degree of peak shift and changes in crystallinity will be determined by further XRD analysis using an appropriate internal standard. This will allow for peak positions and intensities to be known relative to the internal standard.

Infrared and thermal analysis has been performed on all samples. This data are still being analyzed. Color analysis was accomplished for each sample. This shows differences in the color of the mineral with changes in the ratio of iron:chromium. Color analysis also shows that more drastic color changes can be attributed to chromium substitution than with iron substitution.

Surface area measurements were performed on all the minerals. The hematite-eskolaite series exhibits the following trend with respect to surface area: 90% iron hematite> 95% iron hematite> 75% iron hematite> hematite> eskolaite> 50% iron hematite> 25% iron hematite. Similarly, the maghemite-eskolaite series data shows the following: 75% iron maghemite> 90% maghemite> maghemite> eskolaite. From these data, it appears that small substitutions of chromium increase surface area, but as the chromium substitution increases, the surface area is lowered to less than that of the end members.

Molecular Modeling

The goal of Task 4 is to correlate siderophore structure to metal oxide dissolution rates. As a first step toward this goal, we are attempting to correlate siderophore structure with metal ion binding affinity in aqueous solution. This will be accomplished through a molecular mechanics (MM3) approach that has proven successful with other types of ligands. The approach requires the development of an extended force field to handle the specific system under study. We have focused initially on a series of catecholamide ligands and their complexes with Fe(III). This system was chosen because (a) the catechol functional group is important in siderophore chemistry and (b) Fe(III) binding constant data are available for a series of seven structurally varied tris-catecholamide ligands, thus providing an experimental benchmark for the model.

Force-field development for catecholamides and their Fe(III) complexes is in progress. This task involves the development of new MM3 parameters for interactions that are exclusive to catecholamide structure as well as for interactions between the metal ion and the catecholamide. The parameterization is being accomplished using both experimental data (crystal structures) and electronic structure calculations. A survey of the Cambridge Structural Database has been carried out to gather statistical data on the geometric features of the basic catecholamide subunit in its two stable conformations, shown in Figure 1. This ligand subunit contains several interactions that are not included in the current version of MM3, such as the rotational potential surface for the C-C bond connecting the phenyl ring to the amide and the strength of the intramolecular hydrogen bonds. These interactions are being investigated with ab initio density functional theory and molecular orbital calculations. The potential surface for the C-C bond rotation has been obtained at the RHF/6-31G*, BLYP/DZVP2, and MP2/DZVP2 levels. These data will be used to fit the required torsional parameters. The hydrogen bond interaction is under investigation at the MP2/DZVP2 level. The Cambridge Structural Database has also been used to identify the geometric features of catechol when chelated with first row transition metals. A preliminary set of parameters for Fe(III) dependent interactions has been derived by fitting to the crystal structure data.

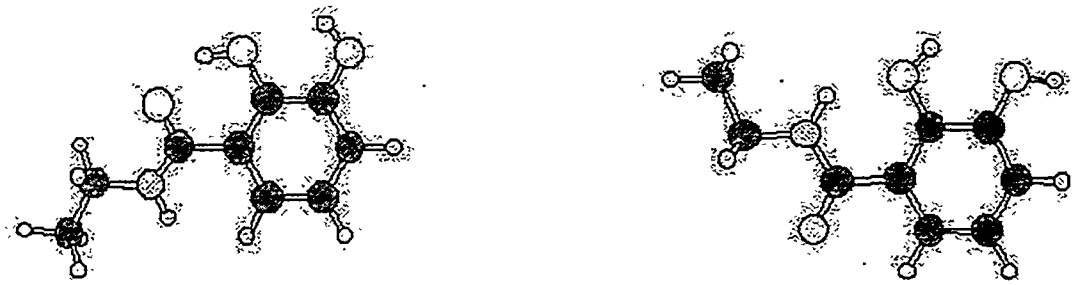

Figure 2. The Two Conformers of Catecholamide. The one on the left is stabilized by an intramolecular O--HO hydrogen bond; the one on the right is stabilized by an intramolecular O--HN hydrogen bond.

Planned Activities

Future efforts will focus on the primary objectives of each task. All tasks have received at least some of the oxides. In addition, each task has the same representative model ligands and the siderophores that could be purchased. Below is a brief description of the next year's efforts in each task.

Task 1 will continue to produce and disseminate siderophores as they are collected and purified from microbial culture. Dissolution studies will focus on developing rate data for the model ligands and siderophores using oxides distributed by Task 3.

Task 2 efforts in the coming year will focus on developing the bonding and structure of the representative model ligands at the water-oxide interface using those oxides developed for this project. In addition, specific attention will be centered on synthesizing and collecting spectra on a di-functional group model ligand. This compound will have two different reactive moieties that will allow spectral differentiation between the groups and hence a clearer picture on multi-moiety compound surface binding.

Future efforts in Task 3 will focus on determination of the surface charge properties of these solids followed by macroscopic sorption studies and x-ray absorption measurements of Eu(III) sorption by these solids.

Efforts in Task 4 will center on completing the MM3 parameterization for catecholamides and their iron complexes. Efforts will also benchmark the model by determining its ability to predict known solid-state structures. Once this is deemed reasonable, the model will be used to correlate siderophore structure with metal ion binding affinity in aqueous solution.

Decommissioning and Decontamination

Radiolytic and Thermal Processes Relevant to Dry Storage of Spent Nuclear Fuel

(First Year of Funding: 1997)

Principal Investigator

Dr. Steven C. Marschman
Pacific Northwest National Laboratory
P.O. Box 999, MSIN P7-27
Richland, WA 99352
(509) 376-3569 (phone)
steve.marschman@pnl.gov

Co-Investigators

Dr. Theodore E. Madey
Rutgers University
Department of Physics
136 Frelinghuysen Rd.
Piscataway, NJ 08854-8019
(732) 445-5185 (phone)
madey@physics.rutgers.edu

Dr. Peter E. Haustein
Brookhaven National Laboratory
Department of Chemistry
P.O. Box 5000
Upton, NY 11973
(516) 344-4340 (phone)
haustein@bnldag.ags.bnl.gov

Dr. Thomas M. Orlando
Pacific Northwest National Laboratory
P.O. Box 999, MSIN K8-88
Richland, WA 99352
(509) 376-9420 (phone)
Thomas.Orlando@pnl.gov

Dr. James P. Cowin
Pacific Northwest National Laboratory
P.O. Box 999, MSIN K8-88
Richland, WA 99352
(509) 376-6330 (phone)
jp.cowin@bnldag.ags.bnl.gov

Collaborators

Dr. Nikolai Petrik
All-Russian Project and Research Institute of
Complex Power Technology ìVINIPIETÎ
St. Petersburgh, Russia

Prof. Jory Yarmoff
Department of Physics
University of California
Riverside, CA

R. Dobrozemsky
Department of Physics
Technical University of Vienna
Vienna, Austria

Research Objective

This project involves basic research in chemistry and physics aimed at providing information pertinent to the safe long-term dry storage of spent nuclear fuel (SNF), thousands of tons of which remain in water storage across the DOE complex. The Hanford Site K-Basins alone hold 2300 tons of spent fuel, much of it severely corroded, and similar situations exist at Savannah River and Idaho National Engineering and Environmental Laboratory. DOE plans to remove this fuel and seal it in overpack canisters for "dry" interim storage for up to 75 years while awaiting permanent disposition. Chemically bound water will remain in this fuel even after the proposed drying steps, leading to possible long-term corrosion of the containers and/or fuel rods themselves, generation of H_2 and O_2 gas via radiolysis (which could lead to deflagration or detonation), and reactions of pyrophoric uranium hydrides. No thoroughly tested model is now available to predict fuel behavior during preprocessing, processing, or storage. In a collaborative effort among Rutgers University, Pacific Northwest National Laboratory, and Brookhaven National Laboratory, we are studying the radiolytic reaction, drying processes, and corrosion behavior of actual SNF materials and of pure and mixed-phase samples. We propose to determine what is omitted from current models: radiolysis of water adsorbed on or in hydrates or hydroxides, thermodynamics of interfacial phases, and kinetics of drying. A model will be developed and tested against actual fuel rod behavior to ensure validity and applicability to the problems associated with developing dry storage strategies for DOE-owned SNF.

Research Progress

Several oxide surfaces, which are present on SNF (i.e., UO_2, ZrO_2, and Al_2O_3), have been prepared and studied using a variety of surface science methods. Specific emphasis is on understanding the interaction of water with these surfaces as it relates to the kinetics of drying. Studies on the electronic structure and mechanisms of non-thermal dissociation/damage of the materials and interfacial water have also been carried out in an effort to assess the non-thermal mechanisms and cross-sections for producing molecular hydrogen and oxygen from interfacial water. Though these tasks are correlated, they are described separately for the sake of clarity.

Photon- and Electron-Stimulated Desorption of O^+ From Zirconia

The breakdown of zirconia films (important to the integrity of Zr-alloy fuel-rod cladding) under extreme radiation conditions has been systematically studied using low-energy electron and photon bombardment of well-characterized ZrO_2 surfaces. These studies have clarified the mechanism of oxygen removal from such surfaces, which involves the ionization of shallow metal cation core levels followed by interatomic Auger decay. This results in the formation and rapid ejection of O^+ ions (Simpson et al. 1999). Simpler one- and two-electron processes can lead to the desorption of neutral and molecular oxygen.

Controlled radiolysis of water-covered ZrO_2 surfaces has begun to clarify the interaction of adsorbates with secondary electrons, electronhole pairs, and excitons near the surface. A related study of the radiolysis of water adsorbed on a series of powdered oxides using ^{60}Co gamma irradiation reveals that the hydrogen yield from radiolysis can be significantly greater, approximately equal to, or significantly less than the yield from pure gas-phase water. This depends on the specific oxide involved and can be

correlated with the band-gap of the oxide particles as well as the adsorbate-substrate interaction. A mechanism has been proposed that accounts for these differences, based on the migration of excitons to the surface and their resonant coupling with the water adsorption complex (Petrik et al. 1999a).

Laser-Stimulated Luminescence of Yttria-Stabilized Cubic Zirconia Crystals

The kinetics of laser-stimulated luminescence (LSL) of yttria-stabilized cubic zirconia (YSZ) single crystals was investigated (Petrik et al. 1999b). These experiments were carried out to probe the valence band structure and defect states of zirconia; specifically, excitation of ZrO_2·9.5%Y_2O_3 (100) and (110) using nsec pulses of 213 nm (5.82 eV), 266 nm (4.66 eV), and 355 nm (3.49 eV) photons produce LSL bands with Gaussian profiles and peak maxima at 460 nm (2.69 eV), 550 nm (2.25 eV) and 600 nm (2.07 eV), respectively. LSL involves a single-photon process for energy densities below ~1.0 MW/cm^2. Decay times vary from 0.1 to 100 μs depending on the excitation energy and temperature. Decay kinetics are hyperbolic indicating that all LSL bands result from recombination. The LSL quenches with increasing temperature and activation energies obtained using the Mott approximation are 0.10 ± 0.01, 0.20 ± 0.02, and 0.45 ± 0.04 eV for the 2.69, 2.25, and 2.07 eV LSL bands, respectively.

The various activation energies, decay kinetics, and excitation/emission energies correspond to the presence of several emission centers which can be associated with anion vacancies. We tentatively assign these centers to intrinsic F-centers and extrinsic F-type centers. The latter are associated with one and two Y^{3+} ions in the nearest neighborhood positions. Since the normalized temperature dependencies of the decay coefficients are similar for all the LSL bands, we suggest that recombination primarily involves electrons, trapped at intrinsic and extrinsic defect sites, and mobilized holes.

Nuclear-Stimulated Desorption at the Surfaces of Model SNF Materials

Radiolytic degradation of the integrity of spent nuclear fuel (SNF) is an important concern for these highly radioactive materials, which have been in storage for a number of years awaiting reprocessing and interim isolation. Nuclear stimulated desorption (NSD) methods have been applied to models of SNF materials to assess the importance of various degradation mechanisms. These include the microscopic damage from the initially energetic nuclear recoil event, as well as secondary damage from the usually nonradioactive atoms, which are dislodged in the initial event. Interfacial nuclear decay and radiolysis processes that evolve flammable gases have also been studied on Al_2O_3 and ZrO_2 surfaces using intense radioactive sources with radiochemical tracer techniques.

Interaction of Water with UO_2 (001)

Uranium oxide exists in a range of stochiometries, from UO_2 to UO_3. In the present work, the interaction of water with UO_2 (001) using low-energy electron diffraction (LEED), x-ray photoelectron spectroscopy (XPS), low-energy electron ion scattering (LEIS) and electron-stimulated desorption (ESD) has been studied. The clean UO_2(001) exhibits ordered c(2x2) LEED patterns in excellent agreement with previous published data. The x-ray photoelectron spectrum of the U 4f peaks exhibits a clear single satellite at 6.8 eV on the high binding energy side of U 4f5/2 , which has been assigned to a shake-up excitation of an electron from the O 2p-U bonding band to partially occupied or unoccupied localized metal 5f levels. Electron stimulated desorption (ESD) measurements of clean UO_2 indicate the desorption of H^+ and O^+; the O^+ desorption threshold is at ~22 eV, and the kinetic energy distribution is peaked at 3.5 eV. The O^+ desorption threshold is correlated to the ionization threshold of the oxygen 2s level, rather than the U 6p levels. Upon exposure to D_2O^{18} at 300K, the XPS and ESD results show no

evidence of OD formation after water exposure. However an ESD O^{18+} signal appears. Both O^{16+} and O^{18+} signals reach a saturation value after 20 Langmuir exposure. Further, LEIS spectra show an O^{18} peak after water dosage. These results indicate that the water is completely dissociated on UO_2 (001) and that O^{18} atoms are incorporated in the surface. The results also suggest a diffusion of oxygen in the bulk.

Desorption of Tritiated Water from Uranium Oxide Films Under Atmospheric Conditions

In preliminary experiments in the laboratory of R. Dobrozemsky and T.U. Vienna, we have measured the desorption rate of tritiated water, HTO, from UOx films using radiotracer techniques. Our preliminary results indicate that the HTO desorption rate is considerably faster in atmospheric air than in vacuum. This interesting observation suggests that HTO desorption is accelerated by coadsorption of atmospheric molecules. More measurements are planned on new films to confirm and quantify this effect.

Electron-Bombardment of Spent Nuclear Fuel Elements

An ultrahigh vacuum system has been designed and modified to permit electron-bombardment studies of actual SNF material in a hot-cell facility. This will allow us to look at the role electronic excitation and hydride damage play in the production of hydrogen gas from actual fuel samples. We have obtained a Gatan Precision Ion Milling System (originally designed for milling TEM samples) to perform these electron bombardment studies. Electron-stimulated desorption (ESD) tests on metallic uranium spent nuclear fuel specimens are underway and the gases generated and released will be monitored in real time using a mass spectrometer.

Planned Activities

Measurements of the thermal and electron-stimulated desorption kinetics of water from well-characterized UO_2 and U-metal surfaces will continue. Studies using thin-films and radiotracer techniques with tritiated water will also be continued. The surface radiolysis studies with radioactive sources will be extended to uranium oxide systems and actual fuel materials using a hot-cell facility at PNNL. Finally, the mechanism of nonthermal production of hydrogen from water covered zirconia surfaces will be examined using state-resolved laser detection schemes.

Information Access

This project involves three organizations: Pacific Northwest National Laboratory, Rutgers University, and Brookhaven National Laboratory. The information is shared with DESH and Numatec. In addition, we participate in national and international meetings of scientific societies, such as the American Chemical Society, the Electrochemical Society, the American Physical Society, the American Nuclear Society, and the IEEE. We also publish essentially all of our work in the open literature. The following is a list of publications and conference presentations for the project.

References

Petrik NG, AB Alexandrov, AI Vall, and TM Orlando. 1999a. *Gamma radiolysis of water on oxide surfaces: Parameters controlling the energy transfer* (in press).

Petrik NG, DP Taylor, and TM Orlando. 1999b. "Laser-stimulated luminescence of yttria-stabilized cubic-zirconia crystals." *J. Appl. Phys.* 85:6770.

Simpson WC, WK Wang, JA Yarmoff, and TM Orlando. 1999. "Photon- and electron-stimulated desorption of O^+ from zirconia." *Surf. Sci.* 423:225.

Publications

Hedhili MN, BV Yakshinskiy, and TE Madey. "Interaction of water with UO_2 (001)." *Surf. Sci* (in preparation).

Haustein P. "Nuclear stimulated desorption studies of oxides relevant to spent fuel material." *J. Nucl. Materials* (in preparation).

Petrik NG, AB Alexandrov, AI Vall, and TM Orlando. 1999a. *Gamma radiolysis of water on oxide surfaces: Parameters controlling the energy transfer* (in press).

Petrik NG, DP Taylor, and TM Orlando. 1999b. "Laser-stimulated luminescence of yttria-stabilized cubic-zirconia crystals." *J. Appl. Phys.* 85:6770.

Simpson WC, WK Wang, JA Yarmoff, and TM Orlando. 1999. "Photon- and electron-stimulated desorption of O^+ from zirconia," *Surf. Sci.* 423:225.

Presentations

Haustein P. August 22-26, 1999. "Nuclear stimulated desorption at the surfaces of model SNF materials: Experiment and computer simulation." Annual Symposium on "First Accomplishments of the Environmental Management Science Program," Annual Meeting, Am. Chem. Soc., New Orleans (invited talk).

Hedhili MN, BV Yakshinskiy, and TE Madey. March 21-25, 1999. "Interaction of water with UO_2 (001)." National American Physical Society Meeting, Atlanta.

Hedhili MN, BV Yakshinskiy, TE Madey, R Dobrozemsky, and J Yarmoff. August 22-26, 1999. "Interaction of water with uranium oxide surfaces." Annual Symposium on "First Accomplishments of the Environmental Management Science Program," Annual Meeting, Am. Chem. Soc., New Orleans.

Orlando TM. March 21-25, 1999. "Quantum-resolved studies of condensed phase reactions." Symposium on "Free radicals in the Condensed Phase," Annual Meeting, Am. Chem. Soc., Anaheim, California (invited talk).

Orlando TM, N Petrik, S Marshman, and DM Camaioni. November 14-18, 1999. "Nonthermal surface processes in the generation of gas in mixed wastes." Annual Meeting, Am. Nuclear Soc., Long Beach, California (invited talk).

Orlando TM, NG Petrik, AB Alexandrov, and WC Simpson. February 24, 1999. "Nonthermal processes on oxide surfaces and interfaces." Los Alamos National Laboratory, Los Alamos, New Mexico (invited talk).

Orlando TM, NG Petrik, AB Alexandrov, and WC Simpson. February 24-25, 1999. "Nonthermal processes on oxide surfaces and interfaces." DOE Laboratory Catalysis Research Symposium, Albuquerque, New Mexico.

Orlando TM, NG Petrik, AB Alexandrov, and WC Simpson. February 26, 1999. "Nonthermal processes on oxide surfaces and interfaces." Department of Chemistry, University of Utah, Salt Lake City (invited talk).

Petrik N, S Marshman, DM Camaioni, and TM Orlando. August 22-26, 1999. "Nonthermal surface and interface processes in the storage of spent nuclear fuel and mixed wastes." Annual Symposium on "First Accomplishments of the Environmental Management Science Program." Annual Meeting, Am. Chem. Soc., New Orleans.

Distribution and Solubility of Radionuclides and Neutron Absorbers in Waste Forms for Disposition of Plutonium Ash and Scraps, Excess Plutonium, and Miscellaneous Spent Nuclear Fuels

(First Year of Funding: 1997)

Principal Investigator

Denis M. Strachan
Pacific Northwest National Laboratory
P.O. Box 999, MSIN K6-24
Richland, WA 99352
(509) 376 0677 (phone)
denis.strachan@pnl.gov

PNNL Contributors and Collaborators

JG Darab (509 375 6608; john.darab@pnl.gov)
LL Davis (509 372 1635; linda.davis@pnl.gov)
H Li (509 373 0256; hong.li@pnl.gov)
L Li (509 373 7502; liyu.li@pnl.gov)
MJ Schweiger (509 376 3245; michael.schweiger@pnl.gov)
Z Wang (509 376 6119; zheming.wang@pnl.gov)

External Contributors and Collaborators

DK Shuh (Lawrence Berkeley National Laboratory; 510 486 6937; dkshuh@lbl.gov)
PG Allen (Lawrence Berkeley National Laboratory; 510 486 5427; pgallen@lbl.gov)
JJ Bucher (Lawrence Berkeley National Laboratory; 510 486 4484; jjbucher@lbl.gov)
DL Caulder (Lawrence Berkeley National Laboratory; 510 486 5377; dlcauder@lbl.gov)
IM Craig (Lawrence Berkeley National Laboratory; 510 486 5377; imcraig@lbl.gov)
NM Edelstein (Lawrence Berkeley National Laboratory; 510 486 5624; nmedelstein@lbl.gov)
P Liu (Lawrence Berkeley National Laboratory; 510 486 5141; lliu@lbl.gov)
WW Lukens (Lawrence Berkeley National Laboratory; 510 486 4305; wwlukens@lbl.gov)
H Nitsche (Lawrence Berkeley National Laboratory; 510 486 5615; hnitsche@lbl.gov)
L Rao (Lawrence Berkeley National Laboratory; 510 486 5427; lrao@lbl.gov)
RC Ewing (University of Michigan; 734 647 8529; rodewing@umich.edu)
LM Wang (University of Michigan; 734 647 8530; lmwang@umich.edu)
D Zhao (University of Michigan; 734 763 4774; dzhao@umich.edu)
ER Vance (Australian Nuclear Science and Technology Organization; 61 2 9717 3019; erv@ansto.gov.au)

Research Objective

The objective of this research is to develop a basic understanding of the distribution and solubility of radionuclides and neutron absorbers in waste forms and their release from waste forms by studying the local structural environments of these constituents in representative materials.

Research Statement

Crucial to the near-term DOE/EM mission of developing waste forms for the disposal of specific plutonium-containing wastes is a fundamental understanding of the radionuclide and neutron absorber solubility in glasses and ceramics. This understanding is empirically based, making it difficult to provide a defensible position on issues such as waste-form selection and development, assessment of waste form criticality safety, stability, long-term performance, and waste-form qualification for repository acceptance. The elucidation of the fundamental relationship between the local structure of radionuclides and neutron absorbers and their solubility in waste forms will advance material science and provide depth to the defense.

Research Progress

Introduction

We have been examining the solubility of surrogate oxides in a suite of baseline glasses that allow us to vary the glass melt chemistry. Over the past year, we have found evidence to suggest that the solubility of metal oxides in sodium boro-aluminio-silicate glasses is facilitated by the formation of nanometer heterogeneities that we refer to as "clusters" of the metal-oxide moiety. We are uncertain as to the exact composition of these clusters, but they appear to be rich in the metal being dissolved. In this report, we discuss the results from several spectroscopic techniques. The presence of clusters appears to be pervasive from very low metal oxide concentrations and appears to be a metastable condition for the metal oxide.

We have also examined uranium- and plutonium-containing glasses and found that the oxidation state has an important effect on the solubility with the lower oxidation state of plutonium being more soluble. Crystalline waste forms too have been investigated. Here, again, the oxidation state of the surrogate metal plays an important role. We have looked at the crystal chemistry of pyrochlore, zirconolite, and perovskite.

We discuss the baseline glasses that we reported last year and the new glasses that we made this year. We then discuss our results for gadolinium and hafnium glasses, followed by a discussion of the nuclear magnetic resonance (NMR) and transmission electron microscopy (TEM) results. We then discuss our results from our investigations of the uranium- and plutonium-containing glasses. We finish with a discussion of crystalline materials as potential waste forms.

Glasses Studied

Baseline Glasses

The compositions of the baseline glasses[1] are designed according to a simplified Pu16MC3 sodium-alumino-borosilicate glass developed for plutonium immobilization (Darab et al. 1997). More complicated baseline glasses are used in our uranium and plutonium studies (Feng et al. 1998). Normally, baseline glasses were prepared from well-mixed oxide and carbonate powders. Radionuclide surrogates (HfO_2, Gd_2O_3, La_2O_3, Nd_2O_3) and neutron absorbers (HfO_2 or Gd_2O_3) were then added to ground baseline glasses and melted at 1450-1560°C. The melt was quenched in water. Resulting glasses or glass-crystal mixtures were analyzed with different techniques to develop an understanding of the solution mechanisms.

Clear glasses resulted from the melting of the majority of the baseline compositions at or below 1450°C. Glasses did not form from compositions such as PA0, PB0, PC0, and PA20, below 1450°C. However, glasses could be formed when surrogate oxides were added to the melt. Characterization of the baseline glasses has been carried out with NMR on $60SiO_2$-aB_2O_3-bNa_2O-cAl_2O_3 glasses and TEM on the B20 baseline glass.

Rare Earth Element Solubility in Glasses

We reported Gd_2O_3 solubilities in $60SiO_2$-aB_2O_3-bNa_2O-cAl_2O_3 baseline glasses in our last annual report. Recently, we found that the solution behavior of La_2O_3 in the baseline glasses is very similar to that of gadolinium. A study of the La_2O_3 solubility was needed because we could not analyze gadolinium-containing glasses with NMR (gadolinium has a strong magnetic moment). Our results show that there is a one-for-one substitution of La_2O_3 for Gd_2O_3 in both the glass and the crystals that precipitate from the glass melt. A complete solid solution was observed in the B15 glass for the system $Na_{1-x}(Gd, La)_{9+x/3}Si_6O_{26}$ ($0<x<1$).

Our results indicate that there is a small temperature dependence of the Gd_2O_3 solubility. Between 1400°C and 1550°C, the Gd_2O_3 solubility in the B15 glass increases less than 7 mass%. Our results indicate an enthalpy change of Gd_2O_3 dissolution in this baseline glass is about 40 kJ/mol.

Figure 1 shows Gd_2O_3 ($GdO_{1.5}$) solution behavior in $60SiO_2$-$15B_2O_3$-xNa_2O-$(25-x)Al_2O_3$ glass system. Similar results were found for La_2O_3 and Nd_2O_3, which indicates that they have similar solubility. The Gd_2O_3 solubility changed rapidly with the $Na_2O/(Na_2O + Al_2O_3)$ ratio in the glass. At $Na_2O/(Na_2O + Al_2O_3)$ equal to 0.50, its solubility reaches a minimum. As the $Na_2O/(Na_2O + Al_2O_3)$ ratio increases from 0.50 to 1.00 or decreases from 0.50 to 0, Gd_2O_3 solubility increases from 5 to 46 and from 5 to 63 mass%, respectively. When $Na_2O/(Na_2O + Al_2O_3)$ is ≤ 0.35, Gd_2O_3 additions to the baseline glass aid glass formation. In this case, there are two solubility limits—a lower and an upper.

---

1 Glasses are labeled and named in the following fashion: in the system $60SiO_2 \cdot aB_2O_3 \cdot bNa_2O \cdot cAl_2O_3$ where a = 5 to 20; b = 10 to 30; c = 2 to 15; glass B15 has a = 15, b = 20, and c = 5; in the system $60SiO_2 \cdot 15B_2O_3 \cdot xNa_2O \cdot (25-x)Al_2O_3$, x was varied from 0 to 25 and designated PLr, PAr, PBr, and PCr, where r = $Na_2O/(Na_2O + Al_2O_3)$; in the system $\alpha SiO_2 \cdot \beta Na_2O \cdot \gamma Al_2O_3$, α was varied from 38.33 to 66.67, β 15 to 33.33, and γ 0 to 46.67.

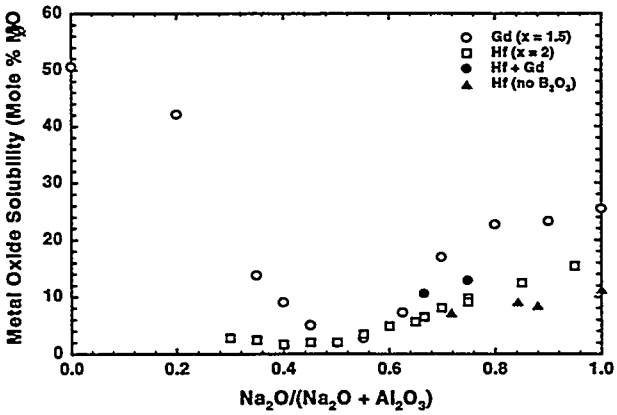

Figure 1. The Dependence of Gadolinium and Hafnium Oxide Solubility on Glass Composition

The lower solubility limit is defined by the existence of mullite ($Al_6Si_2O_{13}$, ideal formula). Increasing the Gd_2O_3 causes mullite to dissolve. The lower solubility decreases from 28 to 0 mass% as $Na_2O/(Na_2O + Al_2O_3)$ increases from 0 to 0.35. For $Na_2O/(Na_2O + Al_2O_3)$ between 0 to 0.20 and 0.70 to 1.00, $Na_{1-x}Gd_{9+x/3}Si_6O_{26}$ (x=0 to 1) crystals (upper solubility) and mullite [$(Al_4SiO_8)_{1.2}$ (formula for XRD), lower solubility] were identified with XRD. For $Na_2O/(Na_2O + Al_2O_3)$ in range 0.35 to 0.625, the glasses exhibit opalescence, indicating liquid-liquid phase separation. When examined in the TEM, the average size of the dispersed phases was about 50 nm. We found that the dispersed phase was gadolinium rich compared with the continuous phase. Another much smaller dispersed phase (several nm) was found for both in the liquid phases.

In the B20 glass, as the concentration of Gd_2O_3 increases from 0 to 47 mass%, the glass density increases from 2.4 g/cm^3 to 3.7 g/cm^3. We used the density, composition, and published ionic radii to calculate the vacancy volume for each glass. The vacancy volume reaches a maximum when Gd_2O_3 concentration is about 5 mass%. Further increasing the Gd_2O_3 concentration causes the vacancy volume ration to decrease. This has implications about the structure surrounding the gadolinium. These samples were also studied with laser-induced, time-resolved fluorescence spectroscopy and lifetime measurement. The intensity of the emission bands was found to increase from 1 to 20 mass% Gd_2O_3 and then to decrease at higher Gd_2O_3 concentrations. In parallel, the fluorescence lifetime decreased rapidly when the concentration of Gd_2O_3 was greater than 20 mass%. This indicated that a significant decrease in Gd-Gd distance occurred. Under TEM, we observed that a small dispersed phase, as seen in the phase-separated glasses discussed above, increased as the Gd_2O_3 concentration increased.

In our efforts to find another spectroscopic tool to examine the nature of these gadolinium-containing clusters, we determined that small additions of Nd_2O_3 for Gd_2O_3 could be used as a probe of the gadolinium site(s). The presence of Nd_2O_3 in these glasses allows us to use UV-Vis spectroscopy to examine these glasses. While the resulting spectra are complex, there is one peak that is uncomplicated, i.e., it appears to be a single peak whereas the others appear to be composed of several overlapping peaks. We are able to see some differences in the peak position and the maximum width at half height. We are still trying to interpret these data. The solubility behavior of Nd_2O_3 is similar to that observed for Gd_2O_3 and La_2O_3.

Glasses B20La5, B20La20, and B20La47 (peralkaline) were analyzed with ^{11}B and ^{27}Al solid-state nuclear magnetic resonance (NMR). In all of these glasses, the aluminum occurs in predominantly four-fold (tetrahedral) coordination, while boron occurs as a mixture of three-fold (trigonal planar) and four-fold (tetrahedral) coordinated species. It was found that, as more La_2O_3 was added to the B20 base glass, the boron environment became more three-fold coordinated.

Hafnia Solubility in Glasses

Solubility studies of HfO_2 in sodium boro-alumino-silicate glasses have been extended from the peralkaline [$Na_2O/(Na_2O + Al_2O_3) > 0.5$; molar ratio] to the peraluminous [$Na_2O/(Na_2O + Al_2O_3) < 0.5$]. compositional range (Figure 1). Optical microscopy, scanning electron microscopy (SEM), NMR, and x-ray absorbance fine structure (EXAFS) have been used to document morphological, mineralogical, compositional, and atomic-level structural differences for the glasses. Results from electron microprobe quantitative microanalyses of selected HfO_2 glasses compare favorably with our target glass compositions. These results also confirm that sodium was lost during the preparation of high Na_2O-containing glasses. Four sodium alumino-silicate glasses without boron have been prepared to help elucidate the role of boron in HfO_2 solubility. We also prepared mixed Gd_2O_3-HfO_2 glasses to evaluate the possible competition between the two absorbers/surrogates.

Hafnia (HfO_2) has been identified as a precipitate in both peralkaline and peraluminous glasses with x-ray diffraction (XRD). The only other crystalline phase found is mullite, and it occurs only in peraluminous glasses and in Na10Gd2Hf19. Hafnia in peraluminous glass occurs as pinacoidal prismatic crystals that are compositionally zoned or twinned with sections that are mainly HfO_2 and others that contain hafnium, aluminum, oxygen, and perhaps sodium. Only a limited number of peraluminous glasses could be made (Figure 1) because these compositions could not be melted at the upper limit of the furnace (1600°C). In the peralkaline glasses, crystals are also zoned or twinned, but with respect to hafnium, silicon, sodium and oxygen, not aluminum: one sector is essentially hafnia, while the other that appears epitaxial contains little hafnium and significant silicon and sodium.

We have performed TEM analyses on three Na10Hf10 glasses, homogenized for one, three, and seven hours, and for the B20 glass series, homogenized for two hours. There appears to be a similarity between B20 glasses with varying amounts of HfO_2 and Na10Hf10. All samples examined exhibit a similar feature: light and dark "spots," approximately 5 nm in diameter, randomly but seemingly homogeneously distributed throughout the material studied. As with the gadolinium-containing glasses, we have tentatively identified these as clusters. The density of the clusters does not seem to change with increasing HfO_2 content, although a more rigorous examination is needed. Some of our results (see the discussion below) suggest that the hafnium-containing clusters may be compositionally different than the gadolinium-containing clusters. Stereoscopic TEM photographic pairs from the gadolinium-glasses illustrate that the clusters are spherical and separated. They occur throughout the glass volume. Results from our TEM examination of the glasses annealed for various durations indicate that the grains of HfO_2 are residual from the glass batch. The existence of the clusters persists throughout the annealing. Our TEM analyses also show that the glasses are inhomogeneous with respect to hafnium. Locally, energy dispersive spectroscopy (EDS) of B20Hf5 (5 mass% HfO_2) gives a scaled hafnium peak area very similar to that for B20Hf31 (31 mass% HfO_2). The composition and structure of the clusters remains to be determined.

Analyses with EXAFS spectroscopy have been completed, and the data have been modeled successfully for two series of glasses. We examined the effect of changing HfO_2 content with the series Na10Hf5 through Na10Hf20 (10 mol% Na_2O, 5 to 20 mass% HfO_2). We looked at the effect of changing the $Na_2O/(Na_2O + Al_2O_3)$ while holding B_2O_3 and SiO_2 in the same molar proportions. The EXAFS data indicate a distinct difference between peralkaline and peraluminous glasses, with the sample representing the boundary between the two compositional ranges [$Na_2O/(Na_2O + Al_2O_3) = 0.5$] being distinct from or intermediate between the others. Changes in the calculated hafnium coordination are found as the boundary is crossed. While these data are preliminary, they indicate that the hafnium in peraluminous glasses has oxygen near neighbors and oxygen and aluminum as next nearest neighbors. On the other

hand, the peralkaline glasses are best modeled without aluminum as next nearest neighbors. None of the XAFS spectra from the glasses resemble HfO_2 (actual) or $HfSiO_4$ (simulated) reference spectra.

Glasses Na10Hf5 through Na10Hf20 (peralkaline), and PL50Hf6 through PL30Hf8 (peraluminous) have been examined with solid-state NMR (^{11}B, ^{27}Al). The preponderance of aluminum is in four-fold coordination for both peraluminous and peralkaline glasses, while the boron coordination is a mixture of three-fold (trigonal planar) and four-fold (tetrahedral). In general, it was found that peraluminous glasses contain far less boron in tetrahedral coordination than in trigonal coordination, whereas the opposite is true for peralkaline glasses. In both the Na10 series and Na30 series peralkaline glasses, the boron coordination changes similarly with the addition of hafnium: the more HfO_2 added to the same base glass, the more three-coordinate boron is found.

Interpretation of Solubility, NMR, and EXAFS Data

For the Na10 and Na30 peralkaline glass series, the boron environment was found with NMR to become more three-fold coordinate with increasing additions of HfO_2. Likewise, for the B20 peralkaline glass series, the boron environment was also found to become more three-fold coordinate with increasing additions of La_2O_3. As association of sodium with the boron is required to maintain the boron in four-fold coordination, an immediate conclusion one might be tempted to draw from these results is that Hf(IV) or La(III) require some sort of association with sodium during the dissolution process and that Hf(IV) and La(III) compete more strongly for the available sodium than does boron. Hence, as more HfO_2 or La_2O_3 is added, sodium that in the absence of these oxides, would stabilize four-coordinate boron, instead aids in the dissolution of Hf(IV) or La(III) and the boron becomes more three-fold coordinate. One might also contend that some equilibrium might eventually be reached where the boron will not give up any more sodium to the Hf(IV) or La(III) and the solubility limit of the system is reached.

If the above model were true, however, the solubility limit of HfO_2 in these glasses should increase with increasing "free sodium." The free sodium is the total sodium in the glass minus the concentration of aluminum, which very strongly achieves four-fold coordination by association with sodium, minus the concentration of four-fold coordinated boron at equilibrium. Thus, glasses with no aluminum or boron and high concentrations of sodium (e.g., NaSiO-X) should show maximum HfO_2 solubility. As a matter of fact, the NaSiO-X along with the other glasses with no boron, in spite of their high concentrations of "free sodium" exhibit less-than-expected HfO_2 solubilities (Figure 1).

Thus, we believe that the boron is playing an important role in the dissolution of the HfO_2, perhaps by allowing a more energetically favorable route through which sodium can become associated with Hf(IV). We are currently developing chemical equilibrium-based models to calculate the solubility of HfO_2 from the relative amounts of B_2O_3, Al_2O_3 and Na_2O in these glasses.

As the composition of the base glass approaches that where the concentration of Na_2O and Al_2O_3 are equal, i.e., the boundary between peralkaline and peraluminous regions, the concentration of free sodium approaches zero. At this point, regardless of the mechanism by which sodium could become associated with Hf(IV) there is little free sodium and the solubility of HfO_2 approaches a minimum.

Finally, in the peraluminous region, there is less Na_2O than Al_2O_3 and it is difficult to maintain four-fold coordinate aluminum. Theoretically then, NMR characterization of peraluminous glasses containing, for example HfO_2, should indicate that the aluminum environment becomes more six-fold

coordinate as more Na_2O is removed. In actuality, the NMR results show that the aluminum environment maintains four-fold coordination and there is very little four-fold coordinated boron in the hafnium-containing peraluminous glasses. Additionally, the EXAFS results indicate that aluminum is associated with the hafnium as a second nearest neighbor. One interpretation is that, in order to maintain four-fold coordination, one or more aluminum become associated with a Hf(IV) as more sodium is removed in the peraluminous region. This would explain the NMR data, the EXAFS data, and the increase in HfO_2 solubility, as more Na_2O is removed in peraluminous glass compositions.

Since the trends in solubility for HfO_2 and for $(La/Gd/Nd)_2O_3$ are similar, but different in magnitude, perhaps similar mechanisms with different equilibrium constants can be used to describe the solubilities of these and other types of cations (such as actinides or other troublesome transition elements) in glass.

Microprobe Analyses

Electron microbeam techniques, such as electron microprobe analysis (EMPA), backscattered electron (BSE) EDS, and x-ray mapping, have been used to characterize distributions of each individual element and actual contents of elements in the glass products. The gadolinium- and hafnium-glasses studied are homogeneous in composition except for the sample containing a precipitated gadolinium-bearing crystal phase. Good agreement was obtained between the analyzed compositions and the target compositions. The gadolinium-containing crystals took more gadolinium from the glass matrix and made it heterogeneous in composition.

In the gadolinium-containing glass that is above saturation, the separated crystals are up to 200 μm in length. Backscattered electron images of the samples showed that the crystals are elongated, acicular, prismatic, or dendritic. Cross-sections of the crystals are often hexagonal, sometimes with hollow hexagonal features (Figure 2). The different shapes of the crystals indicate that they were probably formed during the different stages of crystallization as the glass cooled. Chemical compositions of precipitated crystals are more enriched in gadolinium than in the glass matrix. Crystals of different shapes have the same composition, and each crystal is homogeneous in composition. The composition of the crystals is consistent with the XRD results described above. The glass composition near the precipitated crystals was depleted in gadolinium and richer in the other glass components. This is consistent with the composition of the crystals.

Figure 2. Backscattered Electron Images of the Crystalline Phase in the Gadolinium-Containing Glass Matrix

Solubility and Local Structure of Uranium in Silicate Glass

A standard soda-lime silicate, SRM 1830, was obtained from National Institute of Standards and Technology and selected for our studies of the uranium solubility and local structure under oxidizing and reducing conditions. This glass contains (in mass%) 73.1 SiO_2, 13.8 Na_2O, 8.6 CaO, 3.9 MgO, 0.1 Al_2O_3, 0.1 Fe_2O_3, plus small quantities of K_2O, TiO_2, and SO_3. This glass was selected for its good chemical durability and its relatively high concentration of Na_2O. The high Na_2O favors high uranium solubility.

The uranium solubility study was previously summarized (Feng et al. 1998). The results are briefly summarized here: under oxidizing conditions, the solubility was 30 mass% UO_3 at 1500°C based on optical, XRD, and TEM studies. At 31

at 1500°C based on optical, XRD, and TEM studies. At 31 mass% UO_3 and above, uranium crystallizes as U_3O_7 in the oxidized glasses. Under reducing conditions, the solubility was less than 30 mass% and UO_2 precipitated.

The XAFS have been collected on these glasses at room temperature at the Stanford Synchrotron Radiation Laboratory. The U L_{III} near edge of the oxidized and reduced glasses doped with uranium was reported (Feng et al. 1998). From these analyses, we determined that, on the average, U(V) was present in oxidized glasses above 10 mass% and U(IV) in reduced glasses. The axial and equatorial U-O parameters can be derived, but the extraction of the structural parameters beyond these shells, except for the identification of U-U scattering, which is clearly evident in some of the U40 materials (~4Å), is not practical. The respective trends in coordination number and bond distances with increasing uranium content are consistent prior to formation of U(IV).

The bond-valence model (Brese and O'Keefe 1991) was use to calculate the valence from the U-O bond distance and U to O coordination number. Good agreement was found suggesting the majority of the U is U(VI) in the oxidized glasses, with 10 and 20 mass% UO_3 and U(IV) in the reduced glasses. The bond-valence model results further suggest a trend that U(V) increases as UO_3 increases above 20 mass% in the oxidized glasses. Combining the uranium solubility data with results of the XAFS, bond-valence model, XRD, and TEM results, the uranium oxidation state that favors the uranium stability in the melt is in the order U(VI)> U(V)> U(IV).

Plutonium Solubility and Local Structure in Borosilicate Glasses

A reference borosilicate composition (Pu16MC3) developed under a previous DOE/MD project for Pu immobilization was chosen to study plutonium solubility under oxidizing and reducing conditions. The Pu16MC3 glass contains (in mass%) 42.8 SiO_2, 13.2 B_2O_3, 4.1 Al_2O_3, 4.1 Li_2O, 5.1 Na_2O, 1.5 K_2O, 1.0 Cs_2O, 11.3 Gd_2O_3, 2.1 P_2O_5, and 4.7 Fe_2O_3 in which Gd_2O_3 functions as a neutron absorber.

Preliminary results of the plutonium solubility study were reported in Feng et al. (1998). The results are briefly summarized here: under oxidizing conditions, the solubility was less than 10 mass% PuO_2 at 1450°C; plutonium precipitated as PuO_2. Under reducing conditions, the PuO_2 solubility limit was greater than 40 mass%.

Near-edge and XAFS investigations have been completed for these plutonium glasses. The Pu L_{III} near-edge spectra indicate that, in these glasses, plutonium is either Pu(III) or Pu(IV) depending primarily on the oxidation conditions. In these glasses, Pu(IV) dominates when the conditions are oxidizing and Pu(III) when reducing. As shown in Figure 3c, there exists a broad diffraction peak near 30° two-theta that is also seen in a borosilicate glass containing 47 mass% Gd_2O_3 (insert in Figure 3c). For the Gd_2O_3 glass, we have tentatively identified clusters of approximately 5 nm in diameter (see discussion above). Hence, the high solubility of Pu(III) in the borosilicate glass may be related to the formation of Pu(III)-bearing clusters.

With the XAFS of the plutonium in these glasses, in addition to the near-edge information, we are able to discern trends in the local environment surrounding the plutonium. We do need to provide the caveat that the limited order in these glasses results in metrical parameters (coordination number and distances) with significant uncertainty from all but the nearest shells. This is additionally complicated by

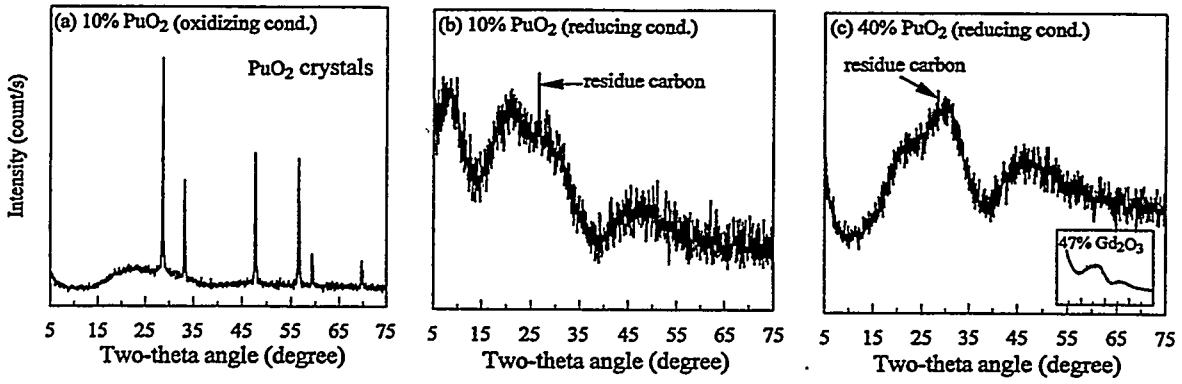

Figure 3. XRD Patterns for the Oxidized (a) and Reduced (b, c) Pu16MC Glasses with Plutonium

the possibility that a significant quantity of the plutonium resides in clusters. We are interpreting the XAFS results with this possibility in mind. The results of the XAFS structural determinations and curve fitting are in the process of being finalized along with the experimental EXAFS results.

Crystalline Waste Forms

This work is directed toward understanding (a) solid solubility limits of plutonium, associated uranium, and the neutron absorbers gadolinium and hafnium, and (b) plutonium and uranium valences in crystalline phases which have had serious consideration for immobilizing waste plutonium and uranium. These phases are zirconolite, $CaZrTi_2O_7$; pyrochlore, $(Ca,An)_2Ti_2O_7$; monazite, $REPO_4$; perovskite, $CaTiO_3$; titanite, $CaTiSiO_5$; apatite, $(Ca,RE,An)_{10}(P,Si)_6O_{26}$; zircon, $ZrSiO_4$; and brannerite, $AnTi_2O_6$, where RE = rare earths and An = actinides.

Uranium in Zirconolite

Sintered $CaZr_{(1-x)}U_xTi_2O_7$ samples were prepared with x varied at 0.1 intervals. From XRD, SEM, and TEM, the zirconolite 2M-4M transition was found to be at x = 0.15 and the pyrochlore/zirconolite boundary near x = 0.65. Synthesis of the end-member $CaUTi_2O_7$ phase is still proving difficult, but hot pressing at 1275°C gave a pyrochlore yield of ~90%, the rest being UO_2. The pyrochlore phase in $CaUTi_2O_7$ samples melted in argon at 1500 and 1550°C was deficient in uranium, having an approximate $Ca_{1.1}U_{0.9}Ti_2O_7$ stoichiometry. Results from x-ray absorption near-edge structure (XANES) measurements at SSRL and diffuse reflectance spectra (DRS) on $CaU_{0.2}Zr_{0.8}Ti_{1.8}Al_{0.2}O_7$ and $CaU_{0.2}Zr_{0.8}Ti_{1.8}Mg_{0.2}O_7$ fired in air and in which the uranium was targeted as U(V) and U(VI), respectively, showed that both the argon- and air-fired samples contained both U(IV) and U(V). The solubility limit of U(IV) on the calcium site was found to be ~0.3 formula units.

Uranium in Perovskite

A perovskite, $Ca_{0.9}U_{0.1}Ti_{0.9}Al_{0.1}O_3$, was fired at 1400°C in argon and H_2/N_2 to target uranium as U(IV) and U(III), respectively. In spite of these attempts, only U(IV) was found in perovskite. Perovskite can incorporate 0.06 formula units of uranium on the calcium site.

Incorporation of Neutron Absorbers and Uranium

Less than 0.02 formula units of hafnium were found to enter the monazite lattice. Brannerite has been found to incorporate ~0.2 formula units of hafnium. Approximately 0.5 formula units of gadolinium can be incorporated in air-fired brannerite, but only 0.1 formula units in argon-fired material. The enhanced gadolinium solubility is consistent with DRS observations indicating U(V) in the gadolinium-doped, but not the undoped material. Titanite was found to incorporate ~0.3 and 0.5 formula units of gadolinium and hafnium, respectively. The incorporation of U(IV) in titanite did not exceed 0.05 formula units.

Summary

We have discussed the results from a variety of microscopic and spectroscopic techniques that we have used in attempts to identify the metal-oxide moiety in the glass. The metastable clusters that appear to form in these glasses form rapidly as the glass cools. Their concentration appears to be dependent on the metal oxide concentration, but our results are inconclusive in this regard. While clusters appear to be metastable, we have no information to suggest that they would alter over a finite time to a more stable form, presumably crystalline in nature. The metastability of these clusters, should they be definitively shown to exist, should be a study that is carried out in some future program.

Several gaps have been filled in our understanding of the solid solubility of plutonium, uranium, and the neutron absorbers hafnium and gadolinium in candidate crystalline waste form phases and, so far, the valences of uranium. This knowledge will be ultimately valuable for repository licensing.

Planned Activities

If clusters exist for metal oxides in glass, it will be one of the major findings for this project. Understanding the nature of these clusters will be the key to the solubility mechanisms for high-valence metal cations such as lanthanide (gadolinium, lanthanum, neodymium) and actinide elements (uranium, plutonium). Electron energy-loss (EELS) and electron energy loss fine structure (ELFS) studies have been started for both plutonium- and gadolinium-doped glasses. We will begin a systematic study of the solubility of Gd_2O_3/HfO_2 mixtures in sodium-alumino-borosilicate glasses to determine the effect of each on the solubility of the other. The solubility of Pu(III) and Pu(IV) will also be investigated. Experiments on selected peralkaline base glasses will be completed. Glasses will continue to be analyzed with EXAFS to determine local glass structures.

To substantiate the U(V) observed in the uranium glasses, a U(V) solid was measured. The uranium XAFS from the glasses is much different than we have seen in several uranates. This leads us to believe that the uranium in the glasses is U(V). Theoretical calculations using FEFF will be performed to model the EXAFS response from U_3O_7 to compare to the uranium glass XAFS while a suitable U(V) material is obtained or prepared for measurement.

The crystalline phases that form as the surrogate oxide become saturated in these glasses will be studied with XRD, SEM, and TEM. The results will help in the understanding of the structure of the crystalline phases and the correlation, if any, to the structure in the glass melt.

The incorporation of hafnium, uranium, and plutonium in the rare-earth apatite with the $Ca_9Gd_{0.33}(Hf, U)_{0.33}(P0_4)_5SiO_4O_2$ stoichiometry and associated whitlockite are currently being studied. The Pu^{3+} and Pu(IV) solubility on the calcium site of sphene and of perovskite will be completed. We will initiate leaching of a selected crystalline phases doped with plutonium, uranium, gadolinium, and hafnium. We will investigate the possible collaboration to determine the uranium oxidation states in glass with DRS.

References

Begg BD, ER Vance, and SD Conradson. 1998. "The incorporation of plutonium and neptunium in zirconolite and perovskite." *J. Alloys and Compounds*, vol 271-273, 221-6.

Brese NE and M O'Keeffe. 1991. "Bond-valence parameters for solids." *Acta Cryst.*, B47, 192-197.

Brown ID. 1992. "Chemical and steric constraints in inorganic solids." *Acta Cryst. B48,* 553-572.

Darab JG, H Li, MJ Schweiger, JD Vienna, PG Allen, JJ Bucher, NM Edelstein, and DK Shuh. 1997. "Chemistry of plutonium and plutonium surrogates in vitrified nuclear wastes." *Plutonium Futures The Science Conference Transactions*. LA-13338-C, Los Alamos National Laboratory, Los Alamos, New Mexico.

Feng X, H Li, LL Davis, L Li, JG Darab, DK Shuh, RC Ewing, LM Wang, ER Vance, PG Allen, JJ Bucher, NM Edelstein, IM Craig, MJ Schweiger, JD Vienna, DM Strachan, and BC Bunker. 1998. "Distribution and Solubility of Radionuclides and Neutron Absorbers in Waste Forms for Disposition of Plutonium Ash and Scraps, Excess Plutonium, and Miscellaneous Spent Nuclear Fuels." In *Science to Support DOE Site Cleanup: The Pacific Northwest National Laboratory Environmental Management Science Program Awards*. PNNL-11899, Pacific Northwest National Laboratory, Richland, Washington.

Feng X, H Li, LL Davis, L Li, JG Darab, MJ Schweiger, JD Viena, and BC Bunker. 1999. "Distribution and solubility of radionuclides in waste forms for distribution of plutonium and spent nuclear fuels." *Ceramic Transactions*, Vol. 93, JC Marra and GT Chandler, eds. American Ceramic Society, Westerville, Ohio.

Publications and Presentations

Publications

Davis LL, L Li, JG Darab, H Li, DM Strachan, PG Allen, JJ Bucher, IM Craig, NM Edelstein, and DK Shuh. 1998. "The effects of Na_2O, Al_2O_3, and B_2O_3 on HfO_2 solubility in borosilicate glass." In *Scientific Basis for Nuclear Waste Management XXII*. Materials Research Society, Pittsburgh, Pennsylvania.

Feng X, H Li, LL Davis, L Li, JG Darab, MJ Schweiger, JD Vienna, BC Bunker, PG Allen, JJ Bucher, IM Craig, NM Edelstein, DK Shuh, RC Ewing, LM Wang, and ER Vance. 1999. "Distribution and solubility of radionuclides in waste forms for disposition of plutonium and spent nuclear fuels: Preliminary results." *Ceramic Transactions 93*, JC Marra and GT Chandler, eds., American Ceramic Society, Westerville, Ohio, p.409-419.

Li L, DM Strachan, LL Davis, H Li, and M Qian. 1998. "Gadolinium solubility limits in sodium-alumino-borosilicate glasses." In *Scientific Basis for Nuclear Waste Management XXII*, Materials Research Society, Pittsburgh, Pennsylvania (in press).

Li L, DM Strachan, H Li, LL Davis, and M Qian. 1999. "Peraluminous and peralkaline effects on Gd_2O_3 and La_2O_3 solubilities in sodium-alumino-borosilicate glasses." *Ceramic Transactions*. American Ceramic Society, Westerville, Ohio (in press).

Presentations

Davis LL, L Li, JG Darab, H Li, DM Strachan, PG Allen, JJ Bucher, IM Craig, NM Edelstein, and DK Shuh. December 1998. "The effects of Na_2O, Al_2O_3, and B_2O_3 on HfO_2 solubility in borosilicate glass." Materials Research Society, Boston.

Feng X, H Li, LL Davis, L Li, JG Darab, MJ Schweiger, JD Vienna, BC Bunker, PG Allen, JJ Bucher, IM Craig, NM Edelstein, DK Shuh, RC Ewing, LM Wang, and ER Vance. May 1998. "Distribution and solubility of radionuclides in waste forms for disposition of plutonium and spent nuclear fuels: Preliminary results." *Symposium of Waste Management Science and Technology in the Ceramic and Nuclear Industries*. 100th Am. Cer. Soc. Annual Meeting, Cincinnati.

Li L, DM Strachan, LL Davis, H Li, and M Qian. December 1998. "Gadolinium solubility limits in sodium-alumino-borosilicate glasses." Materials Research Society Meeting, Boston.

Li L, DM Strachan, H Li, LL Davis, and M Qian. April 24-29, 1999. "Peraluminous and peralkaline effects on Gd_2O_3 and La_2O_3 solubilities in sodium-alumino-borosilicate glasses." American Ceramic Society Meeting, Indianapolis.

Shuh DK, PG Allen, JJ Bucher, NM Edelstein, IM Craig, X Feng, DM Strachan, H Li, JG Darab, LL Davis, L Li, RC Ewing, LM Wang, ER Vance, MJ Schweiger, and JD Vienna. July 28, 1998. "Distribution and solubility of radionuclides and neutron absorbers in forms for disposition of plutonium ash and scraps, excess plutonium, and miscellaneous spent nuclear fuels." Environmental Management Science Program Workshop Plenary Address, Chicago.

Shuh DK, PG Allen, JJ Bucher, NM Edelstein, IM Craig, X Feng, DM Strachan, H Li, JG Darab, LL Davis, L Li, RC Ewing, LM Wang, ER Vance, MJ Schweiger, and JD Vienna. July 9, 1998. "Investigations of actinide materials chemistry utilizing synchrotron radiation methods." Chemical and Analytical Sciences Division, Oak Ridge National Laboratory, Oak Ridge, Tennessee.

Vance ER, JN Watson, ML Carter, RA Day, GR Lumpkin, KP Hart, Y Zhang, PJ McGlinn, MWA. Stewart, and DJ Cassidy. April 28. "Crystal chemistry, radiation effects and aqueous leaching of brannerite, UTi_2O_6." S-I-059-99, Materials Division, ANSTO, Menai, NSW 2234, Australia.

Soil and Groundwater Cleanup

Dynamics of Coupled Contaminant and Microbial Transport in Heterogeneous Porous Media

(First Year of Funding: 1996)

Principal Investigators

Timothy R. Ginn
172 Everson Hall
Department of Civil and Environmental Engineering
University of California, Davis
Davis, CA 95616-5294
(916) 752-1707 (phone)
trginn@ucdavis.edu

Madilyn M. Fletcher
Belle W. Baruch Institute for Marine Biology and Coastal Research
University of South Carolina
Columbia, SC 29208
(803) 777-5288 (phone)
fletcher@biol.sc.edu

Ellyn M. Murphy
Environmental and Health Sciences Division
Pacific Northwest National Laboratory
P.O. Box 999, MS K3-61
Richland, WA 99352
(509) 375-5914 (phone)
em_murphy@pnl.gov

John H. Cushman
Department of Mathematics & Department of Agronomy
Purdue University
West Lafayette, IN 47907
(317) 494-8040 (phone)
jcushman@math.purdue.edu

Collaborators

Zheming Wang
Environmental Molecular Sciences Laboratory
Pacific Northwest National Laboratory
P.O. Box 999, MS K8-96
Richland, WA 99352
(509) 376-9637 (phone)
dm_friedrich@pnl.gov

David R. Boone
Department of Environmental Biology
Portland State University
P.O. Box 751
Portland, OR 97207-0751
(503) 725-3865 (phone)
boone@ese.ogi.edu

Research Objectives

Dynamic microbial attachment/detachment occurs in subsurface systems in response to changing environmental conditions caused by contaminant movement and degradation. Understanding the environmental conditions and mechanisms by which anaerobic bacteria partition between aqueous and solid phases is a critical requirement for designing and evaluating in situ bioremediation efforts. This interdisciplinary research project is providing fundamental information on the attachment/detachment dynamics of anaerobic bacteria in heterogeneous porous media under growth and growth-limiting conditions. An iterative approach using experimentation and theoretical development is used to describe the attachment/detachment mechanisms used by growing anaerobes capable of reductive dechlorination. Theoretical representations of these attachment/detachment mechanisms have been incorporated into existing flow and transport models that include heterogeneity effects and can be used to predict behavior at field scales. These mechanistic-based models will be tested this summer against experimental data provided through controlled laboratory experiments in heterogeneous porous media in large (meter-scale) 2-D flow cells. In addition to a mechanistic-based predictive model, this research will lead to new theories for the transient spatial distribution of microbial populations and contaminant plumes in heterogeneous porous media, improving our capability for designing staged remediation strategies for dealing with mixed contaminants.

Problem Statement

The central challenge of in situ remediation strategies is the control of the transient spatial distribution of contaminants and remediation reagents (e.g., nutrients or microorganisms) in the presence of natural physical and chemical heterogeneities. Available predictive tools rely almost exclusively on the representation of passive attachment/detachment processes (e.g., filtration, sedimentation) with the bacterium treated as an inert biocolloid. One of the most intractable aspects of bioreactive transport, however, is active microbial partitioning (e.g., attachment/detachment) under growth and transport in physically and chemically heterogeneous systems. Active attachment/detachment is associated with microbial physiologic response to changes in local aqueous concentrations of nutrients and electron-acceptors: this process is treated rarely in field-scale bacterial transport theories and not at all in available predictive tools.

Understanding coupled contaminant and bacterial transport in real media is critical to the success of potential future bioremediation/biobarrier strategies at DOE sites. Disposal of chlorinated hydrocarbons has generated extensive contaminant plumes in sand/gravel aquifers at DOE's Savannah River Site (SRS) in South Carolina and Paducah Gaseous Diffusion Plant (PGDP) in Kentucky, and such organic solutes interact with natural environments in coupled complex ways that have serious ramifications for remediation. For example, during the SRS in situ bioremediation demonstration, 90% of the increase in methanotroph biomass arising from degradation of trichloroethylene (TCE) partitioned into the aqueous phase. Initially, this methanotroph population was primarily attached to solid surfaces. If this partitioning behavior during bioremediation were understood and could be predicted, the knowledge could be exploited to effectively distribute the biomass across a contaminated area and to plan an injection network to minimize costly well construction and dampen or eliminate microbially induced reductions in hydraulic conductivity. This basic knowledge on the transport response of microorganisms is required for any subsurface remediation involving microbes, including staged approaches that sequentially degrade and immobilize multiple contaminants.

The purpose of the proposed research is to address the limitations in understanding reactive contaminant transport and dynamic bacterial attachment/detachment under growth and growth-limiting conditions in natural porous media. This research will assess the coupled degradation and transport processes involving biological agents, with focus on the active and passive attachment/detachment and transport processes of anaerobic microorganisms involved in TCE degradation, including their persistence under transient variations in substrate and electron-acceptor availability. Experiments will be performed in natural geologic materials that display general physical and chemical heterogeneity patterns representative of TCE-contaminated sandy media at SRS and at PGDP. The goals of the research are to develop basic knowledge of the fundamental relationship between contaminant transport and active bacterial transport and attachment/detachment under transient local chemical conditions. This knowledge will afford a quantitative understanding of the transient spatial distribution of contaminants and microbial populations during contaminant degradation and microbial growth in physically and chemically heterogeneous media. To accomplish this end, the proposed research includes an integrated effort toward the development of predictive models of contaminant transport and degradation in heterogeneous media through a combined multiscale experimental and theoretical approach.

Research Progress

The work on this project is being coordinated among six different investigators at five different institutions, Madilyn Fletcher (University of South Carolina), John Cushman (Purdue University), Timothy Ginn (University of California, Davis), David Boone (Portland State University), and Ellyn Murphy and Zheming Wang (Pacific Northwest National Laboratory). In addition, numerous post doctoral students and students have been supported by this project. Dr. Paula van Schie (USC) and Chris Brugato (UCD) made significant contributions to the research in the project over the last year.

Adhesion Behavior of Anaerobes

The investigation of bacterial adhesion has focused on three species of anaerobic bacteria, *Desulfomonile tiedjei, Syntrophomonas wolfei* and *Desulfovibrio* sp. G11, which together can constitute a theoretical tetrachloroethylene and trichloroethylene-degrading consortium. An experimental method was developed for which only small volumes of bacterial culture were needed and in which passive attachment of cells via sedimentation was prevented by continuous rotation of the test vials. Several environmental conditions that affect bacterial adhesion were investigated: the presence of nutrients for growth (i.e., the growth phase of the cells), the influence of physicochemical properties of the substratum, and exposure to air. Adhesion of the microorganisms was evaluated by microscopic determination of the numbers of bacteria that attached to glass surfaces exposed to cell suspensions under anaerobic conditions.

The three species adhered to clean glass surfaces to different degrees, with *S. wolfei* adhering in the largest numbers. In suspensions of 1×10^9 cells/mL, typically 15 ± 3 *S. wolfei* cells attached per 100 μm^2. At equal suspension density, only 2.2 ± 0.3 *D. tiedjei* cells were shown to adhere. *Desulfovibrio* sp. G11 cells adhered in even lower numbers. The growth phase of the tested species, which is influenced by the presence of nutrients, had a significant effect on the ability of *S. wolfei* and *Desulfovibrio* sp. G11 cells to adhere to solid surfaces. The ability of *S. wolfei* cells to attach decreased with culture age and became negligible when growth substrates were depleted (Figure 1). Similarly, *Desulfovibrio* sp. G11 cells attached only when they were actively growing. In contrast, the presence or absence of nutrients did not significantly affect the adhesion of *D. tiedjei* cells.

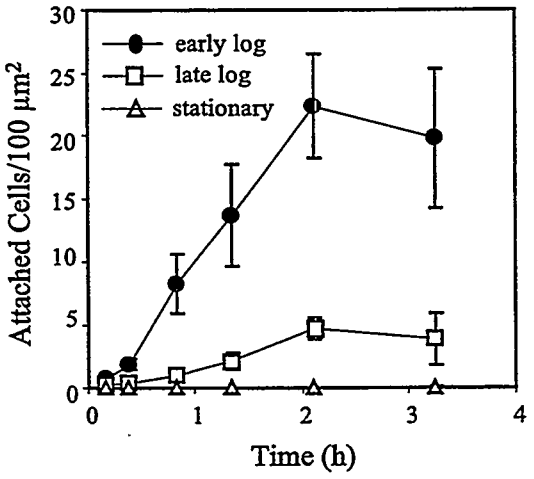

Figure 1. Effect of the Growth Phase of *S. Wolfei* Cells on Adhesion to Solid Surfaces. Clean glass surfaces were exposed to anaerobic suspensions of *S. wolfei* cells (density 5 x 10^8 cells/mL) for 3.5 hours. The log phase cells were provided with 20 mM carbon source for growth (crotonate). Attached cells were fixed with formalin and counted microscopically. Standard deviations are indicated by error bars.

The presence of electropositive groups on the surface, in the form of Fe^{3+}, greatly increased the attachment of *S. wolfei* cells. Typically, in suspensions of 1 x 10^9 cells/mL, iron-coated surfaces became entirely covered with *S. wolfei* cells, which corresponds to 65 ± 5 cells/100 µm^2. Iron coatings also increased the numbers of attaching *D. tiedjei* cells but had no significant effect on the adhesion of *Desulfovibrio* sp. G11 cells. The presence of hydrophobic groups on the surface, in the form of silicone, significantly decreased the number of attached cells of all three species.

Aerobic conditions during adhesion decreased the ability of *S. wolfei* and *Desulfovibrio* sp. G11 cells to attach to solid surfaces. Interestingly, exposure to air did not significantly affect the adhesion of *D. tiedjei* cells.

Detachment experiments performed by exposing surfaces with attached bacteria to cell-free solutions showed that cells of the different species detach from solid surfaces at different rates. *Desulfovibrio* sp. G11 cells detach rapidly. More than 60% of the attached cells detached after an eight-minute incubation in cell-free medium; and within one hour, 85% of the initially attached cells had detached (Figure 2a). *S. wolfei* cells detached at a much slower rate (Figure 2b), and, on average, only 17% of the cells detached during an incubation period of up to 44 hours. Aerobic conditions during the detachment experiment did not result in altered detachment rates (Figure 2b). *D. tiedjei* cells also detached slowly when exposed to cell-free solution.

Recently, a flow chamber device was developed to enable microscopic observation of bacterial attachment kinetics in a flow field. The chamber was made out of glass slides and silicone sealant and contained a microscope coverslip, which can be coated with iron if desired, as the test surface. The device is small and transparent, and yields clear phase contrast images. Using a digital camera connected to the microscope, and image analysis software, the accumulation of bacterial cells onto the test surface can be monitored. Anaerobic conditions in this flow system can most likely be obtained and maintained by flushing the chamber with sodium-sulfide-containing liquid medium before use, using adequate sodium-sulfide concentrations in the cell suspension, and storing the flow chamber under anaerobic

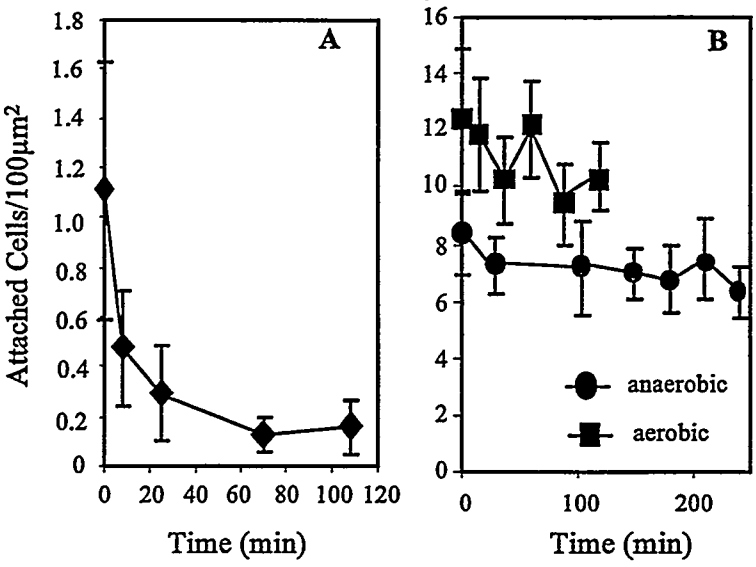

Figure 2. Detachment of Anaerobic Bacteria. Clean glass surfaces were exposed to anaerobic suspensions of *Desulfovibrio* sp. G11 (a) or *S. wolfei* cells (b) (density 5 x 10^8 - 1 x 10^9 cells/mL) for three hours. After the attachment period, the control surfaces were fixed with formalin. All other surfaces were rinsed with anaerobic mineral solution and left in this solution for varying periods of time under anaerobic (A, B circles) or aerobic (B squares) conditions. At chosen time points, remaining attached cells were fixed with formalin and counted microscopically.

conditions before use. Preliminary experiments have been performed with *D. tiedjei* cells, whose adhesive characteristics were shown not to be significantly affected by aerobic conditions. Results of these experiments show that *D. tiedjei* cells attach rapidly to the test surface in the flow chamber and do not readily detach when cell-free solution is pumped through the system. Experiments aimed to corroborate the results of the adhesion assays in test vials (see above) are planned for the near future.

Modeling of Biodegradation Reaction Kinetics

Modeling research at the University of California at Davis has focused on the specification of the anaerobic consortium for use in the laboratory and on the representation of the kinetics of growth and degradation for the experimental consortium selected in a reactive transport model. This has involved in-depth characterization of the microbial degradation characteristics and formulation of a consortium degradation kinetics model that is approached using reaction energetics. These two topics are summarized in the following subsections. A final subsection summarizes the incorporation of the degradation and growth kinetics into a reactive transport model.

Coculture Characteristics

The anaerobic coculture under study is composed of two bacterial species, *Syntrophomonas wolfei* (*S. wolfei*) and *Desulfomonile tiedjei* (*D. tiedjei*). These species have received much attention in the microbiology literature. *S. wolfei* has been repeatedly used to study details of syntrophic fatty acid oxidation, while *D. tiedjei* is well known for its ability to reductively dehalogenate a wide variety of halocarbon compounds. As a result of this attention, the metabolism and physiology of these species has

been fairly well characterized. The active partitioning behavior of these bacteria, however, has only recently been studied by researchers at USC under this project.

S. wolfei is an obligate proton-reducing bacteria that beta-oxidizes 1) even-numbered saturated fatty acids (butyrate through octanoate) producing hydrogen and acetate and 2) the odd-numbered saturated fatty acids (pentanoate and heptanoate) producing hydrogen, acetate, and propionate (McInerney et al. 1981; Beaty and McInerney 1987). Fatty acid fermentation by *S. wolfei* requires low hydrogen partial pressures for these reactions to be energetically favorable. Therefore, fatty acid fermenting *S. wolfei* populations are typically grown in syntrophic association with a hydrogen-scavenging sulfate reducer or methanogen. *S. wolfei* can be grown in pure culture with crotonate as the sole substrate (Beaty and McInerney 1987). For the present work, butyrate was supplied as the primary substrate for *S. wolfei*. Low hydrogen and acetate concentrations are required for the oxidation of butyrate to be an exergonic reaction. For example, at standard conditions with neutral pH, the free energy change for butyrate degradation is 48.3 kJ. For these conditions the reaction is endergonic and bacterial growth is theoretically impossible. However, if the concentrations of hydrogen and acetate are low relative to the concentration of butyrate, the reaction becomes exergonic and growth is possible. Thus, the sensitivity of *S. wolfei* growth rates to hydrogen and acetate are the result of unfavorable energetics of the growth reaction.

D. tiedjei, a strict anaerobe, uses the hydrogen produced by *S. wolfei* to reduce sulfate. However, under certain conditions *D. tiedjei* has been demonstrated to reductively dechlorinate PCE, producing predominately cis-DCE, carbon dioxide, and chloride ion. Together, these bacteria syntrophically convert butyrate and sulfate to acetate and sulfide. The dehalogenation activity in *D. tiedjei* is not constitutive but requires induction. As with the electron acceptors, a wide range of compounds exist that are capable of inducing dehalogenation. While many inducers are also substrates, inducers exist that are not substrates, and substrates that are not inducers. Inducers must be meta-substituted benzoates, benzamines, or phenols, with chlorine, bromine, fluorine, CH_3, or CF_3 in the meta position (Mohn and Tiedjei 1992). Therefore, neither PCE nor TCE alone will induce dehalogenation activity. However, as demonstrated by Fathepure et al. (1987), once induced, cultures of *D. tiedjei* will continue to dehalogenate PCE even in the absence of the inducer. Consequently, for the design of the experiments in this project, cultures of *D. tiedjei* will be pretreated with a suitable inducer, or an inducer will be included in the experimental system. Potential complications could arise from inclusion of inducing agents in the experiment. For example, Townsend and Suflita (1996) demonstrated that, in the presence of both 3-chlorobenzoate and PCE or TCE, the former was preferentially dehalogenated.

Degradation and Growth Model Formulation via Reaction Energetics

The energy available to organisms from substrate utilization is much less in anaerobic than aerobic environments. For example, the free energy change from the conversion of butyrate to acetate under sulfate-reducing conditions is approximately 7% of that available from the aerobic conversion of butyrate to acetate.

$$CH_3CH_2CH_2COO^- + 0.5\ SO_4^{2-} \Leftrightarrow CH_3COO^- + 0.5\ HS^- + 0.5\ H^+ \quad (\Delta G^{o\prime} = -27.8\ kJ/rxn)$$

$$CH_3CH_2CH_2COO^- + O_2 \Leftrightarrow 2CH_3COO^- + H^+ \quad (\Delta G^{o\prime} = -426.1\ kJ/rxn)$$

This relative lack in available energy generally results in slower overall growth rates and lower biomass yields for anaerobic bacteria. In addition, a number of supplementary complications tend to influence bacteria growth and substrate utilization for anaerobic systems. Among these are the effects of end-product inhibition and minimum substrate thresholds.

End-product inhibition results when one or more reaction products accumulate to concentrations that render the overall reaction no longer energetically favorable. This effect can be demonstrated for the butyrate fermentation to acetate performed by *S. wolfei*. Under standard conditions with a neutral pH, the free energy change for this reaction is positive.

$$CH_3CH_2CH_2COO^- + 2\,H_2O \Leftrightarrow 2CH_3COO^- + 2\,H_2 + H^+ \quad (\Delta G^{\circ\prime} = 48.3 \text{ kJ/rxn})$$

Thus, under standard conditions with neutral pH the reaction is endergonic and bacterial growth resulting solely from this conversion is theoretically impossible. However, under reactant and product concentrations more typical of those encountered in natural environments or anaerobic digesters, the free energy change for the butyrate conversion to acetate can be shown to be negative, thus rendering the reaction exergonic and explaining the observed bacterial growth and butyrate degradation.

Schink and Thauer (1988) estimated that for a steady-state methanogenic reactor, concentrations of butyrate, acetate, and hydrogen were 1 mM, 1 mM, and $10^{-4.6}$ atm, respectively. Using these concentrations and assuming neutral pH, the free energy change from the conversion of butyrate to acetate and hydrogen becomes -21.3 kJ/rxn. Clearly, the addition of acetate or hydrogen will shift the reaction to the left, or toward equilibrium, and the energy available to organisms mediating this reaction will decrease. In this way, acetate and hydrogen are said to act as end-product inhibitors to the conversion of butyrate. End-product inhibition occurs for all reactions including aerobic reactions. However, because aerobic reactions are highly exergonic, and therefore aerobic environments are far from equilibrium, the effect is diminished to the point of being insignificant. For the coculture studied herein, the growth of *S. wolfei* resulting from butyrate conversion to acetate and hydrogen will not only be limited by the availability of substrate but also inhibited by the accumulation of acetate and hydrogen. Experimental work demonstrating this effect was discussed above.

For similar energetic reasons, minimum substrate thresholds are routinely observed in anaerobic environments. Thresholds are defined as the minimum concentration to which a particular substrate can be degraded. In anaerobic environments, hydrogen acts as the primary interspecies electron carrier. For example, in the coculture studied here, *S. wolfei* produces hydrogen as a result of butyrate degradation. *D. tiedjei* subsequently uses this hydrogen as an electron donor for sulfate reduction. Therefore, in anaerobic environments as well as in the present coculture, hydrogen thresholds are of particular interest. Unique hydrogen thresholds have been observed for the various terminal electron-accepting reactions, including manganese(IV) reduction, nitrate reduction, iron(III) reduction, sulfate reduction, and methanogenesis (Cord-Ruwisch et al. 1988; Stams 1994; Schink 1997; Yang and McCarty 1998). In the present work, the hydrogen threshold is the minimum concentration of hydrogen that will support growth and metabolism of *D. tiedjei*. Hydrogen threshold values are generally believed to result from low energy yields from catabolic reactions (Cord-Ruwisch et al. 1988; Stams 1994; Schink 1997; Yang and McCarty 1998). This can be demonstrated for the sulfate reduction performed by *D. tiedjei*:

$$SO_4^{2-} + H^+ + 4H_2 \Leftrightarrow HS^- + 4H_2O$$

The Gibbs free-energy change for this reaction under standard conditions with a neutral pH is -151.9 kJ. Assuming equilibrium conditions, or a Gibbs free energy change equal to zero, a hydrogen concentration of 0.016 nM can be calculated. This equals the theoretical hydrogen threshold for sulfate reduction. Observed hydrogen thresholds for sulfate reduction have been reported to be in the range of 1–1.5 nM (Yang and McCarty 1998), indicating that the reaction may not be carried completely to equilibrium. Thus, for the current work, hydrogen will never be completely consumed but rather reduced to some threshold level that will depend on the energetics of the sulfate reduction reaction.

To account for the effects of end-product inhibition and substrate thresholds, the model proposed by Hoh and Cord-Ruwisch (1995) was used to simulate bacterial growth. This model was originally developed as a modification to the Michaelis-Menton substrate utilization model (refer to the original work for a derivation). The original model was modified to describe bacterial growth rather than substrate utilization by replacing v_{max} with $\mu_i C_i$ where μ_i is the maximum specific growth rate for bacteria i, and C_i is the aqueous concentration of bacteria i. This results in the following term for the bacterial growth rate:

$$\frac{\partial C_i}{\partial t} = \frac{\mu_{max} C_i S_j (1 - \Gamma/K)}{K_s + S_j (1 + \Gamma/K)}$$

Here, S_j is the limiting substrate concentration and K_s is the half saturation constant for that substrate. In the present work, the substrates limiting the growth of *S. wolfei* and *D. tiedjei* were butyrate and hydrogen, respectively. Γ is the mass action ratio at each time step, and K is the mass action ratio at equilibrium. The ratio Γ/K is thus a measure of the driving force for the reaction. For $\Gamma/K << 1$, the growth reaction is very energetically favorable, and growth occurs unimpeded by energetic effects. As Γ/K approaches unity, the growth reaction approaches equilibrium and growth ceases. Therefore, both the effects of end-product inhibition and minimum substrate thresholds are included in the model because Γ/K can be driven toward unity by either product addition or substrate removal. Clearly, situations may arise in which $\Gamma/K > 1$. For such cases the model would predict the conversion of biomass to substrates. To avoid such absurdities, biomass formation was assumed to be irreversible, and the growth rate was set equal to zero for $\Gamma/K > 1$.

Reactive Transport System Formulation

The present reactive transport system included quantifying the transport of and interactions between eight chemical species and the two microbial populations described above as well as *Desulfovibrio G11*, a sulfate reducer that provides competition for sulfate with *D. Tiedjei* in some natural environments. (The reaction system reduces to the experimental consortium outlined above by simply zeroing the concentration of this microbe in the model). The reaction system is illustrated in the schematic of Figure 3. The chemical components considered are TCE, DCE, butyrate, formate, acetate, sulfate, sulfide, and a bromide tracer. The results of the microchamber bacterial transport studies in progress at M. Fletcher's lab by P. Van Schie suggested two of the three microbial populations, *S. Wolfei* and *D. G11*, were inclined to partition between the solid and aqueous phases in a manner dependent upon metabolic activity. Thus, for modeling purposes, each of these two species was divided into aqueous and solid-phase subpopulations with transfer between the two, as described below. As previously discussed, *D. tiedjei* was shown to attach irreversibly to the solid phase; therefore, *D. tiedjei* was assumed to be a solid-phase population only. In the end, a total of thirteen components make up the reaction system. These included ten mobile aqueous components comprising the chemical species described above combined with the aqueous populations of *S. wolfei* and *D. G11*, and the three immobile solid-phase components resulting from the attached populations of *S. wolfei*, *D. G11*, and *D. tiedjei*. Sorption of all solute species was allowed; however, solid-phase species were not included in the reactions.

All aqueous phase components are assumed to be subject to the transport processes of advection, molecular diffusion, and mechanical dispersion. The porous media are composed primarily of sandy material, and a high Peclet flow regime is presumed. Under such conditions convection dominates mixing, and mechanical dispersion rather than molecular diffusion is the dominant mixing process. However, the distinction between these two processes becomes blurred in experimental or field settings. As such, quantification of mechanical dispersion and molecular diffusion is typically achieved through a single lumped dispersion coefficient. Convective velocity nonuniformity is induced by simulating the

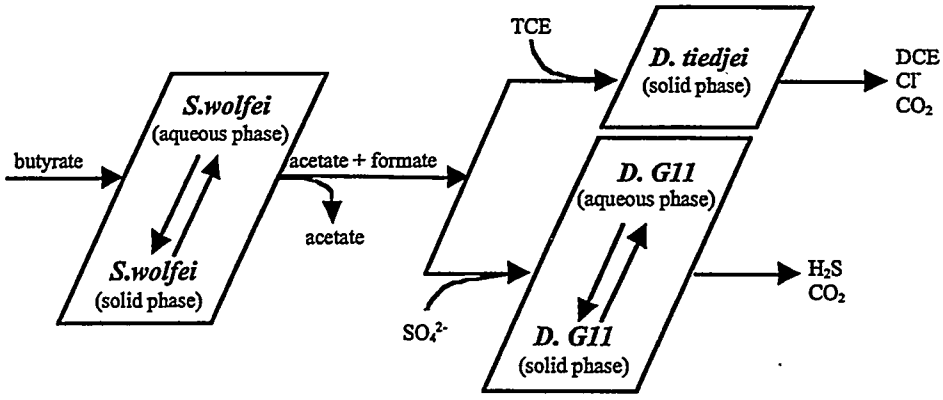

Figure 3. Reaction System

packed intermediate-scale flow cell with layers of different grain-sized sands. Seven of the ten aqueous components (TCE, DCE, butyrate, formate, acetate, sulfate, and sulfide) are assumed to undergo equilibrium sorbtion with the solid phase. Therefore, a linear sorption isotherm was incorporated into the mass balance equations for these components.

Biodegradation of the various substrates and the subsequent product formation is incorporated into the model, using the energetics of reactions approach summarized above. This included the biological processes of growth, metabolic lag, substrate utilization, product formation, and metabolic inhibition. Finally, the effects of bacterial partitioning are being considered in the mass balance equations for the aqueous and solid-phase biological components, using the results of the microchamber experiments ongoing at USC. The coupled effects of metabolic lag on the degradation with active bacterial adhesion is being incorporated using an exposure-time approach.

References

Ahring BK and P Westermann. 1988. "Product inhibition of butyrate metabolism by acetate and hydrogen in a thermophilic coculture." *Appl. Environ. Microbiol.* 54:2393-2397.

Beaty PS and MJ McInerney. 1987. "Growth of Syntophomonas wolfei in pure culture on crotonate." *Arch. Microbiol.* 147:389-393.

Beaty PS and MJ McInerney. 1989. "Effects of organic acid anions on the growth and metabolism of Syntrophomonas wolfei in pure culture and in defined consortia." *Appl. Environ. Microbiol.* 55:977-983.

Cord-Ruwisch R, H-J Seitz, and R Conrad. 1988. "The capacity of hydrogenotrophic anaerobic bacteria to compete for traces of hydrogen depends on the redox potential of the terminal electron acceptor." *Arch. Microbiol.* 149:350-357.

Fathepure BZ, JP Nengu, and SA Boyd. 1987. "Anaerobic bacteria that dechlorinate perchloroethene." *Appl. Environ. Microbiol.* 53:2671-2674.

Faust SD and JV Hunter. 1971. *Organic compounds in aquatic environments*. Marcel Dekker Inc., New York, chapter 21.

Hoh C and R Cord-Ruwisch. 1995. "A practical kinetic model that considers endproduct inhibition in anaerobic digestion processes by including the equilibrium constant-I. model formulation." *Biotechnol. Bioeng.* 51:597-604.

Hoh C-Y and R Cord-Ruwisch. 1997. "Experimental evidence for the need of thermodynamic considerations in modeling of an aerobic environmental bioprocesses." *Water Sci. Tech.* 36:109-115.

McInerney MJ, MP Bryant, RB Hespell, and JW Costerton. 1981. "Syntrophomonas wolfei gen. nov. sp. nov., an anaerobic, syntrophic, fatty acid-oxidizing bacterium." *Appl. Environ. Microbiol.* 41:1029-1039.

Mohn WW and JM Tiedje. 1992. "Microbial reductive dehalogenation." *Microbiol. Rev.* 56:482-507.

Schink B. 1997. "Energetics of syntrophic cooperation in methanogenic degradation." *Microbiol. and Molec. Biol. Rev.* 61:262-280.

Schink B and RK Thauer. 1988. "Energetics of syntrophic methane formation and the influence of aggregation." In G. Lettinga et al. (ed.), *Granular Anaerobic Sludge: Microbiology and Technology*, pp. 5-17, Pudoc, Wageningen, The Netherlands.

Stams AJM. 1994. "Metabolic interactions between anaerobic bacteria in methanogenic environments." *Antonie van Leeuwenhoek* 66:271-294.

Townsend GT and JM Suflita. 1996. "Characterization of chloroethylene dehalogenation by cell extracts *Desulfomonile tiedjei* and its relationship to chlorobenzoate dehalogenation." *Appl. Environ. Microbiol.* 62:2850-2853.

Yang Y and PL McCarty. 1998. "Competition for hydrogen within a chlorinated solvent dehalogenating anaerobic mixed culture." *Environ. Sci. Technol.* 32:3591-3597.

Publications and Presentations

Cushman JH and BX Hu. 1997. "Solutions to the stochastic transport problem of $O(\dot{t})$ for conservative solutes." *Stochastic Hydrology and Hydraulics*, 11:297-302.

Ginn TR. 1998. Comment on "Stochastic analysis of oxygen-limited biodegradation in three-dimensionally heterogeneous aquifers," by F. Miralles-Wilhelm et al. *Water Resources Research* (in press).

Ginn TR and EM Murphy. 1998. "The influence of subsurface heterogeneity on biodegradation." Invited Review for *Soil Science Society of America Journal.*

Murphy EM, TR Ginn, FJ Brockman, and DR Boone. 1997. "Growth effects on the partitioning and transport of bacteria." American Geophysical Union Fall Meeting, *EOS Transactions*, 78(46), p. F231.

Murphy EM and TR Ginn. 1996. "The role of passive and active partitioning in microbial transport in natural and contaminated systems," American Geophysical Union Fall Meeting, *EOS Transactions*.

van Schie PM, DR Boone, and M Fletcher. May 1998. "Adhesion of biodegradative anaerobic bacteria to solid surfaces." 98th general meeting of the American Society for Microbiology, Atlanta.

van Schie PM and M Fletcher. 1999. "Adhesion of anaerobic bacteria." *Applied and Environmental Microbiology* (in review).

Genetic Analysis of Stress Responses in Soil Bacteria for Enhanced Bioremediation of Mixed Contaminants

(First Year of Funding: 1996)

Principal Investigator

Kwong-Kwok Wong, Ph.D.
Pacific Northwest National Laboratory
P.O. Box 999, MSIN P7-56
Richland, WA 99352
(509) 375-5097 (phone)
kk.wong@pnl.gov

PNNL Contributors

Rita S. Cheng (Scientist Associate)
William B. Chrisler (Scientist Associate)
Lye Meng Markillie (Scientist Associate)

Research Objective

The purpose of this project is to provide fundamental knowledge on environment stress response of subsurface bacteria and a radiation-resistant bacterium *(Deinococcus radiodurans)*. This information will be particularly useful in the development of successful bioremediation strategies. These organisms represent two phylogenetically distinct groups of soil bacteria, each of which has specific features of interest for bioremediation. The subsurface bacteria, *Sphingomonas* spp (Savannah River Site), have unique degradative capabilities of organic waste (Fredrickson et al. 1995). The study of subsurface bacteria will serve as a model for bioremediation using indigenous bacteria. *D. radiodurans* exhibits high resistance to external stress (Battista 1997) such as ionizing radiation and organic solvent. The study of *D. radiodurans* will serve as a model for the use of genetically engineered bacteria for bioremediation.

Problem Statement

To realize the full potential of bioremediation, an understanding is needed of microbial community and individual bacterial responses to the stresses encountered at contaminated sites. Knowledge about the responses of soil and subsurface bacteria to environmental stresses, which include low nutrients and mixed pollutants, will allow extrapolation of basic principles to field applications using either indigenous bacteria or genetically engineered microorganisms. Defining bacterial responses to those stresses presents an opportunity for improving bioremediation strategies both with indigenous populations and genetically engineered microbes and should contribute to environmental management and restoration actions that would reduce the cost and time required to achieve OEM's cleanup goals.

Enhanced in situ removal of hazardous wastes by stimulating growth of indigenous bacteria with nutrients has been only demonstrated. However, how much and how often to apply these supplements has been determined empirically. As a result, a controlled, reproducible degradation of pollutants in the environment is difficult to achieve. The study of how different bacteria respond to different levels of nutrients is important in devising remediation strategies.

Research Progress

Growth Response of Subsurface Bacteria to Different Levels of Nutrient Supply

Insufficient nutrient in the environment is one of the reasons limiting the degradative ability of microbial communities. Enhanced in situ removal of hazardous wastes by stimulating growth of indigenous bacteria with nutrients has been demonstrated. However, the effect of adding nutrient has to be monitored. Four subsurface bacteria, *Terrabacter* sp. B511, *Arthrobacter* sp. B518, *Sphingomonas aromaticivorans* B522, and *Acinetobacter* sp. B525, were chosen for the study. Strain B522 is an organic degrader; the other strains are not. The rationale of this study is to test whether we can preferentially stimulate the expansion of organic degrader by supplying different amounts of nutrient. Can we predict the relative expansion of each bacterium by nutrient stimulation if we know the growth rate of each bacterium in different media?

Figures 1 and 2 show the growth curves of subsurface bacteria in the presence of 1% PTYG (low nutrient supply) and 10% PTYG (high nutrient supply) media. Under low nutrient supply (Figure 1),

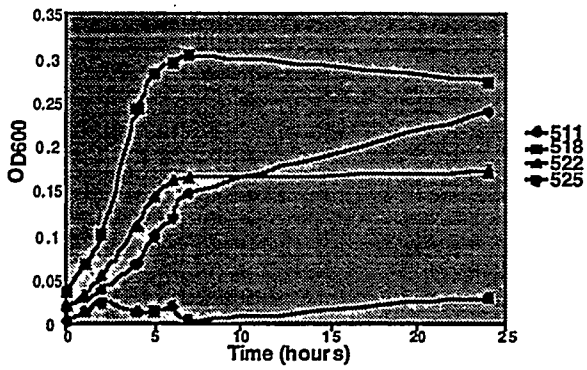

Figure 1. Growth Curves of Subsurface Bacteria in 1% PTYG Medium

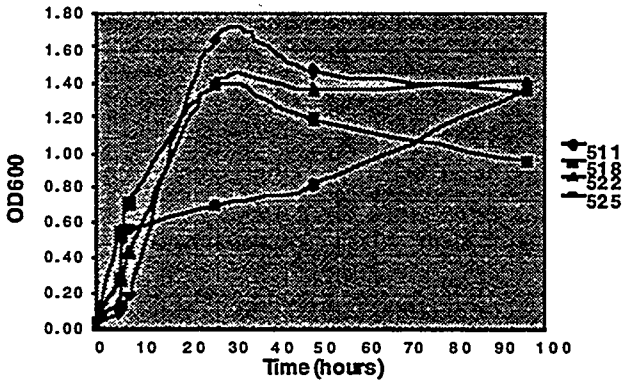

Figure 2. Growth Curves of Subsurface Bacteria in 10% PTYG Medium

strain B518 had the highest growth rate, but strain B525 was not able to grow. Strain B511 and B522 (organic degrader) have intermediate growth rates. On the other hand, under high nutrient supply (Figure 2), all the strains have similar growth rates except B525. These results indicate the heterogeneity in growth rates of subsurface bacteria. We hypothesize that, by stimulating the growth of starved cocultures (two or more bacteria strains mixed together) with different levels of nutrient supplies, we can manipulate the microbial community structure to enhance bioremediation.

To test this hypothesis, we carried out two experiments to study the effect of starvation and nutrient supply on the relative expansion of bacteria existing as cocultures. Strain B518 (bacterium with the highest growth rate in low nutrient supply) and strain B522 (organic waste degrader) were both grown in 10% PTYG medium, and then equal numbers of each bacterium were mixed together. Nutrient was stripped from the cocultures by washing the bacterial cells with minimal salt water (10 mM $CaCl_2$ and 10 mM $MgCl_2$). After 24 hours of starvation, viable cell numbers of each bacterium were obtained by serial dilutions of the cocultures. B518 appeared as white colonies, and B522 appeared as yellow colonies. We observed that the viable cell numbers of B522 have decreased from 9.3×10^5 to 6.8×10^5, while B518 has increased from 9.75×10^5 to 2.14×10^6 (Figure 3). Then a different amount of nutrient was added to the starved cocultures.

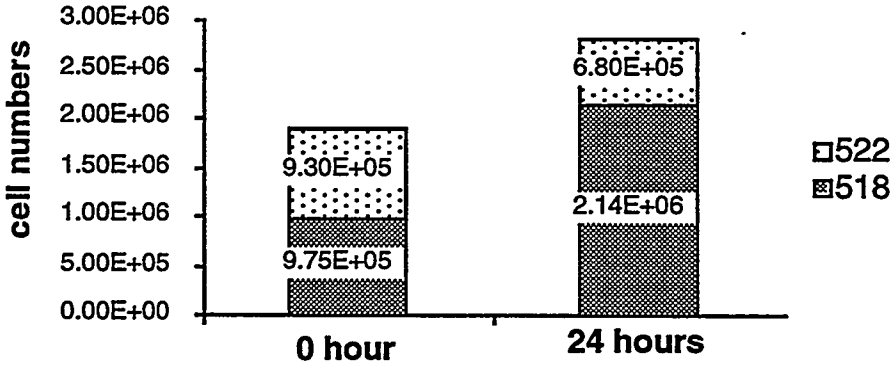

Figure 3. Survival of B518 and B522 Cocultures after Starvation for 24 Hours

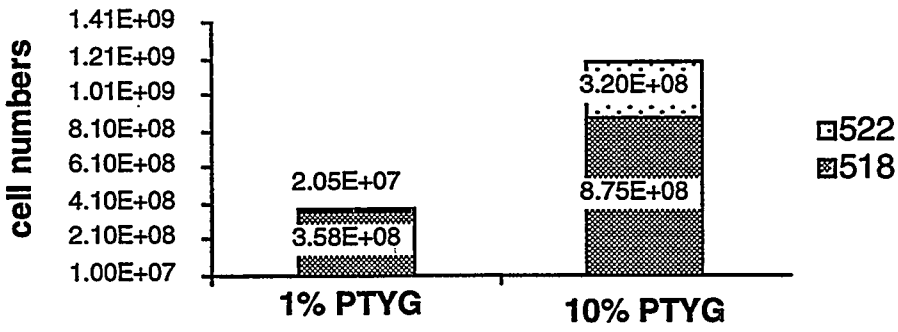

Figure 4. Effect of Nutrient Supplies on Starved B518 and B522 Cocultures

After 24 hours of nutrient supply, the number of viable cells of each bacterial strain was obtained by serial dilutions. With low nutrient supply, the number of organic degrader B522 represents less than 6% in the final bacterial populations. On the other hand, with high nutrient supply, the number of organic degrader (B522) still maintained about 30% of the total populations. This result indicates that the biodegrader may be eliminated if low nutrient supply is used repeatedly for enhancing bioremediation when there is a fast-growing bacterial strain in the microbial communities, such as the B518 in our case. However, further in situ experiments are required to support this hypothesis.

Solvent Responses of *Deinococcus radiodurans*

Soil bacteria with enhanced metal and solvent resistance will be desirable at mixed-contaminant sites with relatively higher contaminant levels. *D. radiodurans* can tolerate a relatively high level of organic solvent; however, the molecular mechanism of its tolerance is still unknown. By deciphering the solvent tolerance of *D. radiodurans*, we might be able to use those identified genes to enhance the solvent tolerance of other bacteria useful for bioremediation. Moreover, the promoters of such genes will be useful for expressing biodegradative genes from other bacteria into *D. radiodurans*.

It has been demonstrated that overexpressing *pspA* genes in *E. coli* can enhance its tolerance to metal and organic solvent. We carried out a genetic experiment to test the role of *pspA* gene in the solvent tolerance of *D. radiodurans*. We have developed a targeted mutagenesis method in *D. radiodurans* (Markillie et al. 1999), and a similar method was used to generate a *pspA* mutant. The sensitivity of the mutant and the parent strain R1 were measured by their survival in the presence of 0.5% toluene. Figure 5 shows that the *pspA* mutant was very sensitive to toluene. Thus, *pspA* plays an important role in the solvent tolerance of *D. radiodurans*. We are trying now to overexpress the *pspA* gene in subsurface bacterium F199 (organic waste degrader) to enhance the solvent tolerance of the subsurface bacteria.

To identify other solvent-inducible genes, total RNA was extracted from *D. radiodurans* that have been treated with xylene, trichloroethylene, or toluene. A RNA fingerprinting technique (Figure 6) was used to identify the RNA transcripts that were induced by solvent. Four putative solvent-inducible genes were identified and were cloned. Two of these genes were found to be rhamnosyl transferase and methyl transferase by sequencing analysis; the other two genes were unknown. These genes were disrupted by duplication insertion mutagenesis, and we are testing the solvent sensitivities of these mutants.

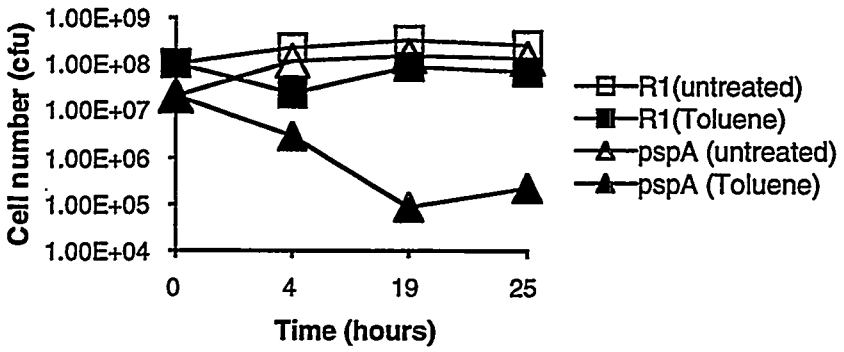

Figure 5. Solvent Sensitivities of pspA Mutant and the Wild-Type Strain R1

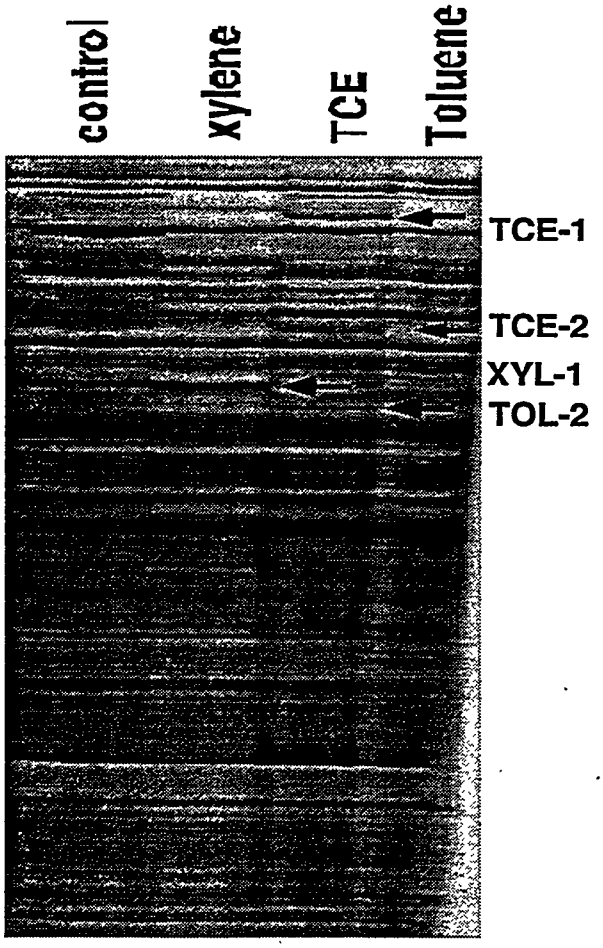

Figure 6. RNA Fingerprinting by Arbitrarily Primed PCR. Arrows indicate solvent-inducible genes.

Besides looking at the RNA transcript expression, total cellular proteins extracted from *D. radiodurans* after solvent stress or ionizing radiation irradiation were analyzed by SDS gel electrophoresis (Figures 7 and 8). A protein about 35 KD was detected one hour after solvent exposure, and the protein was maintained even after 24 hours. We are pursuing identification of this protein.

D. radiodurans is one of the most radiation-resistant bacteria and has recently been engineered to degrade toluene (Lange et al. 1998). This bacteria is one of the candidates for bioremediation of mixed waste with radioactivity. We have identified that both catalase and superoxide dismutase are partly required for the radiation resistance. The identification of radiation-inducible genes will allow us to define the promoter for radiation-inducible expression of biodegradative genes in *D. radiodurans*. By exposing logarithmic growing cells to a dose of 12 K Gy ionizing radiation, we were able to detect a radiation-inducible protein about 18 KD in size. We are trying mass spectrometry to identify this protein.

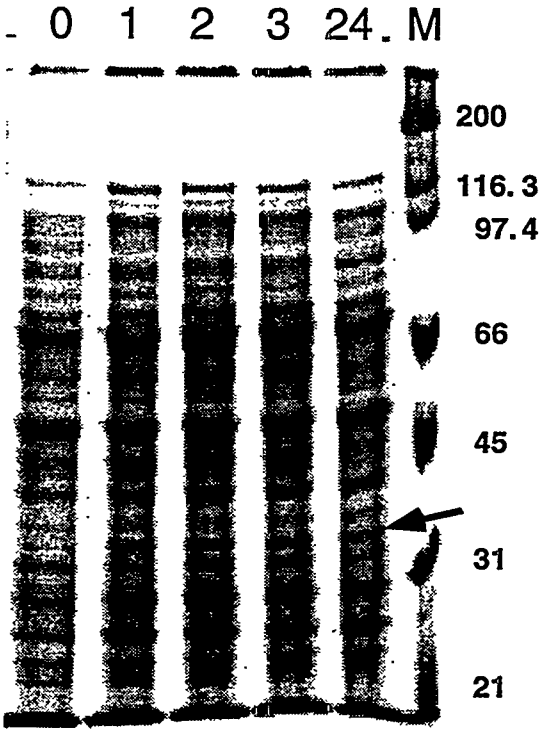

Figure 7. SDS Polyacrylamide Gel Electrophoresis Analysis of Total Cellular Proteins Extracted from *Deinococcus radiodurans* after Exposure to 0.5% Xylene for Different Lengths of Time (1 to 24 h). An arrow indicates a xylene-inducible protein.

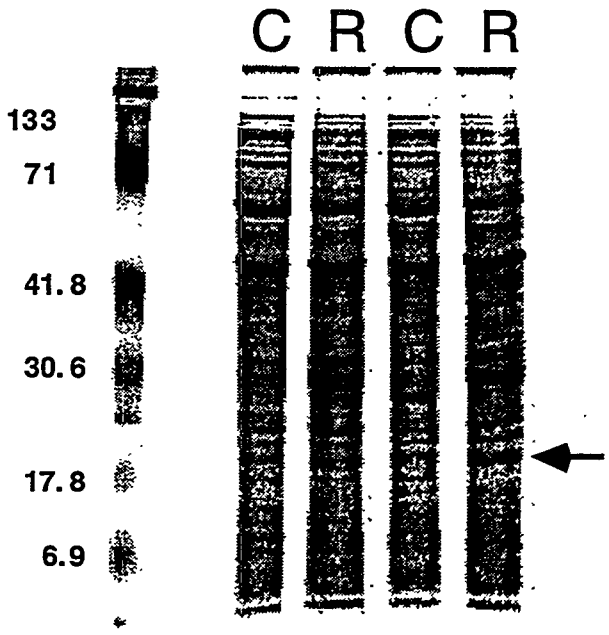

Figure 8. SDS polyacrylamide gel electrophoresis analysis of total cellular proteins extracted from *Deinococcus radiodurans* after exposure to a dose of 12 K Gy ionization radiation. C, unexposed control; R, cells exposed to radiation. An arrow indicates an identified protein.

Planned Activities

1. To overexpress *pspA* gene in subsurface bacterium *Sphingomonas aromaticivorans* to enhance its solvent resistance.

2. To identify xylene and radiation-inducible proteins detected by SDS gel electrophoresis.

References

Battista JR. 1997. "Against all odds: The survival strategies *of Deinococcus radiodurans*." *Annual Review of Microbiology*, 51:203-224.

Fredrickson JK, DL Balkwill, GR Drake, MF Romine, DB Ringelberg, and DC White. 1995. "Aromatic-degrading *Sphingomonas* from the deep subsurface." *Applied Environ. Microbiol.* 61:1917-1922.

Lange CC, LP Wackett, KK Minton, and MJ Daly. 1998. "Engineering a recombinant *Deinococcus radiodurans* for organopollutant degradation in radioactiave mixed waste environments." *Nature Biotechnology*, 16:929-933.

Publications

Wong KK, LM Markillie, and WB Chrisler. 1999. "PSPA is required for solvent tolerance of *Deinococcus radiodurans*." (manuscript in preparation).

Markillie LM, S Varnum, P Hradecky, and KK Wong. 1999. "Targeted mutagenesis by duplication insertion in the radioresistant bacterium *Deinococcus radiodrans*: radiation sensitivities of catalase (*katA*) and superoxide dismutase (*sodA*) mutants." *Journal of Bacteriology*, 181:666-669.

Molecular-Level Processes Governing the Interaction of Contaminants with Iron and Manganese Oxides

(First Year of Funding: 1996)

Principal Investigators

SA Chambers
Pacific Northwest National Laboratory
P.O. Box 999, MSIN K8-93
Richland, WA 99352
(509) 376-1766 (phone)
sa.chambers@pnl.gov

GE Brown, Jr.
Stanford University
Department of Geological and Environmental Sciences
Stanford, CA 94305-2115
(650) 723-9168 (phone)
gordon@pangea.stanford.edu

PNNL Contributors

JE Amonette
DA Dixon
NS Foster-Mills
SA Joyce
TJ Kendelewicz
JR Rustad
S Thevuthasan

PNNL Postdoctoral Associates

D Grolimund
P Liu
SI Yi

Research Objective

The central tenet of this program is that a fundamental understanding of specific mineral surface-site reactivities will substantially improve reactive transport models of contaminants in geologic systems, and will allow more effective remediation schemes to be devised. To this end, we are carrying out a program of research that focuses on the fundamental mechanisms of redox chemistry of contaminants on mineral surfaces. As much of this chemistry in sediments involves the iron(III)/iron(II) couples, we are focusing on mineral phases containing these species. Our approach is to conduct carefully controlled experiments on model, single-crystal iron oxide mineral surfaces grown by molecular beam epitaxy, natural iron oxide single crystals, and synthetic mineral powders. We use the results from the model surfaces, which are very well defined in terms of surface composition, structure, and defect densities, to understand the results obtained on more complex mineral specimens. We are using a variety of experimental probes, along with molecular modeling theory, to determine clean mineral surface structure, details of the chemisorption and decomposition of water, and the interface structure and redox chemistry of important contaminants such as CrO_4^{-2} on these surfaces.

Problem Statement

Contamination of subsurface sediments with radionuclides, organic solvents, and Resource Conservation and Recovery Act (RCRA) metals is one of the many challenging environmental problems at DOE weapons sites. Addressing this problem requires 1) an accurate assessment of the risks associated with these subsurface contaminants (in particular, a prediction of transport rates and degradation products in the subsurface) and 2) the development of reliable and economical remediation schemes. These two activities, in turn, critically depend on an adequate understanding of the chemistry that occurs when contaminants encounter the solid surfaces (largely minerals) present in the subsurface. In addition to adsorption and precipitation at these surfaces, many of the contaminants (e.g., plutonium, uranium, chromium(VI), CCl_4, TCE, and perchloroethylene) can undergo electron-transfer reactions that can substantially alter the species and thereby either help or hinder the remediation process. Predicting the movement of redox-sensitive contaminants through subsurface materials poses a difficult challenge, made more difficult by a lack of fundamental knowledge about the mechanisms and rates of redox reactions with exposed mineral phases. Manipulation of the redox status of aquifers, and the contaminants they contain, by the in situ reduction of iron-bearing minerals or the addition of elemental iron are two examples of proposed remediation techniques that take advantage of redox chemistry at solid surfaces to remove contaminants from groundwater. Although these remediation techniques have shown some success in laboratory-, intermediate-, and field-scale demonstrations, this success has been somewhat fortuitous in that little is actually known about the manner in which they work and the manner by which they might fail. Clearly, both risk-assessment and remediation activities can benefit from a better understanding of the molecular-level mechanisms of redox reactions at well-defined mineral surfaces.

Research Progress and Implications

Surface Structure of Clean and Hydroxylated Magnetite Surfaces

The first step in gaining a molecular-level understanding of redox-active contaminant interactions with model minerals is to understand the structure of the clean mineral surfaces with which contaminants interact. To this end, we have combined scanning tunneling microscopy (STM) with x-ray photoelectron diffraction (XPD) and molecular dynamics (MD) simulations to understand the surface structure of $Fe_3O_4(001)$ (magnetite), one of the most important iron oxide surfaces from the point of view of redox chemistry. The most fundamental surface structural property of materials such as $Fe_3O_4(001)$ is surface termination, i.e., which layer is outermost on the stable surface. There are essentially two choices within the inverse spinel structure of $Fe_3O_4(001)$: 1) the tetrahedral iron(III) layer (termination A) and 2) the octahedral iron(II,III)/tetrahedral O layer (termination B). A guiding principle that can be used to predict surface termination is that of surface autocompensation, which states that the most stable surface(s) is (are) those for which the cation (anion)-derived dangling bonds are completely empty (full) (Gibson and LaFemina 1996). Both of the aforementioned terminations of $Fe_3O_4(001)$ can be made to be autocompensated-model A by removal of every other tetrahedral iron(III) cation (Tarrach et al. 1993) and model B by creation of oxygen vacancies and modification of octahedral iron oxidation states (Voogt 1998). Both surfaces predict a $(\sqrt{2}x\sqrt{2})R45°$ surface reconstruction, which is observed (Chambers and Joyce 1999). We have found by STM that both terminations are stable and can be prepared by different surface preparation methods. Termination A (B) is obtained by preparing the surface under more reducing (oxidizing) conditions. We show in Figures 1a and 1b STM images and associated surface structural diagrams for the two terminations A and B, respectively. The bright spots are iron atoms. The different surface symmetries associated with the two terminations are clearly visible. The images in Figures 1a and 1b were obtained at PNNL by Dr. Steve Joyce and at Tulane University by graduate student Barbara Stanka and Professor Ulrike Diebold, respectively.

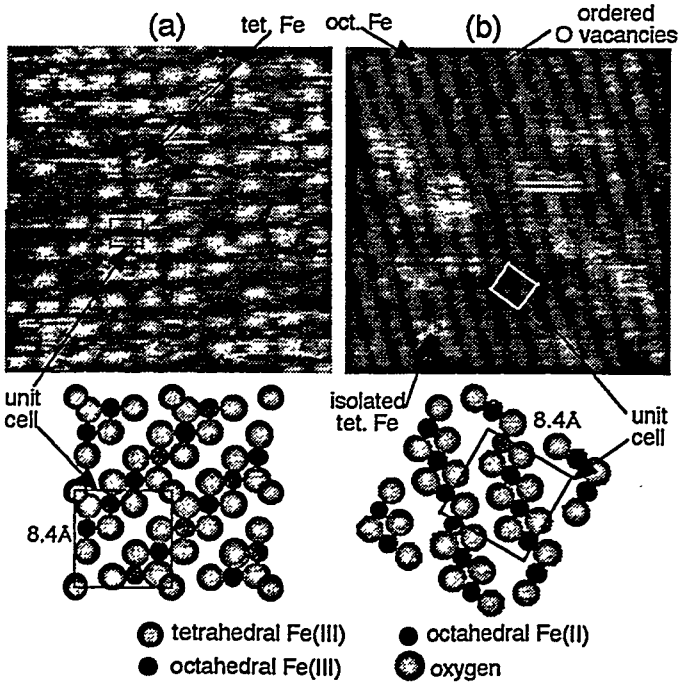

Figure 1. STM Images and Surface Structural Models for $Fe_3O_4(001)$ with (a) A and (b) B Terminations

The second most important set of surface structural parameters is the interlayer relaxations that result from creating the surface in the first place. We are currently analyzing XPD data obtained for $Fe_3O_4(001)$ to determine these parameters. Although the analysis is still in progress, it appears thus far that the best agreement between theory and experiment for termination A occurs for interlayer relaxations of -38%, -23%, -29%, +67%, and +48% for the first five interlayer spacings, respectively.

MD simulations predict termination B to be lower in energy than termination A. Also, MD predicts that yet another structure is more stable than either A or B (Rustad et al. 1999a). This structure is shown in Figure 2. In this structure, tetrahedrally coordinated iron(III) ions in the top layer of an autocompensated A termination rotate downward to occupy a vacant half-octahedral site in the plane of the second layer. At the same time, half of the tetrahedrally coordinated iron(III) ions in the third layer are pushed upward to occupy an adjacent octahedral vacancy in the second layer. The other half of the third-layer tetrahedral Fe(III) ions remain roughly in their original positions. This surface exhibits the $(\sqrt{2}x\sqrt{2})R45°$ surface reconstruction seen experimentally, and is autocompensated. The driving force for the formation of this surface can be thought of as a rearrangement of surface iron ions to achieve the maximum possible coordination number and to keep the Pauling bond order at the surface oxygens close to the bulk value of 2. However, XPD simulations of this surface do not match experiment at all well. This puzzling result is still under investigation.

In addition, MD simulations have been used to predict the structure of the hydroxylated $Fe_3O_4(001)$ surface. Hydroxylation represents the next step in understanding the structure of minerals in aqueous environments. The A-terminated surface becomes lower in energy upon hydroxylation, although hydrating the MD-predicted surface (Figure 2) also results in a metastable minimum. Either surface appears to be consistent with temperature programmed desorption (TPD) data for water in that water desorption peaks were observed at three distinct temperatures (225K, 260K, and 325K), corresponding to three distinct iron binding sites on either surface (unpublished results by I Ismagilov and CHF Peden). However, the binding energy of water on tetrahedral Fe(III) sites of termination A (45 kcal/mol) is much closer to that found previously for Fe_2O_3, which has a large TPD state at 325K (Henderson et al. 1998). In contrast, the binding energy for water on the MD-predicted surface (25 kcal/mol) is about half of that value. Therefore, MD predicts that upon hydroxylation, the surface should revert to termination A if indeed the surface departs from this geometry at all. Hydroxylated structures were also computed for the

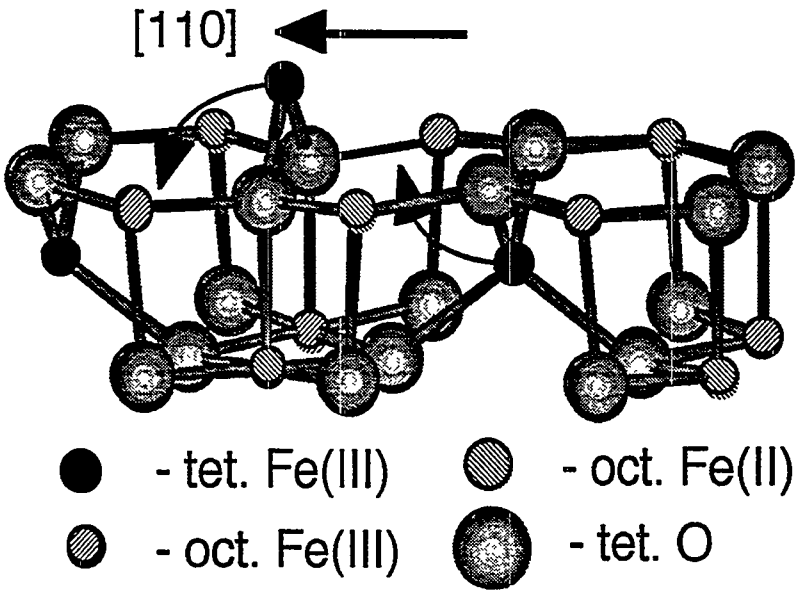

Figure 2. Surface Structure of $Fe_3O_4(001)$ Predicted by MD Simulations

B termination. The binding energy for water is nearly the same for each surface, but the A termination has a slightly higher capacity for water than the B termination. Thus, the binding energy of water on a per molecule basis is slightly higher on the B termination. But the effect is relatively small.

Experimentally, it is found that exposure of Fe_3O_4(001) and (111) to water vapor results in only marginal hydroxylation at pressures up to ~$1x10^{-5}$ torr (Kendelewicz et al. 1999a). Increasing the dosing pressure to higher values results in a marked increase in extent of hydroxylation. These results are similar to those obtained earlier on hematite surfaces (Liu et al. 1998) and are interpreted in the same way. The initial hydroxylation occurs at relatively low pressure as dissociative chemisorption of water occurs at steps. Hydroxylation occurs at terraces above a threshold pressure of ~10^{-5} torr. Our simulations for hydroxylated A and B terminations for Fe_3O_4(001) give 50 to 60% molecular dissociation, less than the 75% dissociation found for α-Fe_2O_3(012) (Henderson et al. 1998; Rustad et al. 1999) but greater than the 30% dissociation, mediated by hydrogen bonding within the water adlayer, as predicted by recent total energy calculations on MgO (Giordano et al. 1998).

Interface Structure of Adsorbed Aqueous Chromium on Iron Oxide Surfaces – Comparison with Chromium on Corundum

We have used chromium K-edge grazing-incidence x-ray absorption fine structure (GI-XAFS) spectroscopy to investigate the local structure of surfaces complexes formed when aqueous chromium(VI) and chromium(III) react with (0001)-oriented α-Al_2O_3 (corundum), α-Fe_2O_3 (hematite), and reduced α-Fe_2O_3 which contains magnetite surface domains in the (111) orientation. The studies of chromium sorption on corundum and unreduced hematite surfaces provide valuable model system data with which data for chromium species on magnetite surface domains can be compared. Our objective is to provide information about the mechanisms of chemical reactions responsible for the speciation and reduction of chromium at the aqueous solution-iron oxide interface.

Samples consisted of α-Al_2O_3(0001) substrates and MBE-grown α-Fe_2O_3films on synthetic single crystal hematite thin films (~350 Å) in the (0001) orientation were grown on α-Al_2O_3(0001) substrates. Partially reduced hematite surfaces were produced by annealing thin-film hematite samples at ~500°C in vacuum. These surfaces were exposed to chromium(III) or chromium(VI) containing solutions in a N_2-filled glovebox and analyzed by GI-XAFS under ambient conditions (i.e., with several monolayers of water present and T ≈ 23°C). Experimental conditions (pH, total chromium concentrations, and background electrolyte) were chosen to avoid the formation of multinuclear chromium complexes or supersaturation of chromium species in solution with respect to known hydroxides, carbonates, or basic salts (Smith and Martell 1976; Baes and Mesmer 1976). X-ray photoelectron spectroscopy (XPS) was used to ensure surface cleanliness prior to the experiment and to estimate surface coverage after reaction.

GI-XAFS experiments were performed at the Stanford Synchrotron Radiation Laboratory (SSRL) (with the SPEAR ring operating at 3 GeV and 60-100 mA) on beamlines 4-2 and 6-2. GI-XAFS data were collected using the SSRL grazing-incidence apparatus in the specular geometry with the incident angle set slightly below the critical angle of the corresponding substrate (≈0.2°). GI-XAFS data analysis was performed using EXAFSPAK (George and Pickering 1995). Phase and amplitude functions were calculated with FEFF7 (Rehr et al. 1991) and verified by comparison with phases and amplitudes extracted from EXAFS data from model mineral compounds.

The results obtained in this study emphasize the unique capabilities of GI-XAFS for identifying the structure of adsorbed species. An increased surface sensitivity is one advantage of this technique, which allows one to probe surface coverages well below 0.1 monolayer. In addition, the polarization

dependence and the well-defined structure of the single crystal substrate leads to additional constraints that simplify the interpretation of GI-XAFS data compared with conventional XAFS techniques using powdered polycrystalline samples.

Distinct differences in the local structure of the sorbed chromium species were found for the different surfaces as well as for the two different oxidation states of chromium (III and VI) (compare Figures 3 and 4). The reduction of chromium(VI) to chromium(III) by partially reduced hematite surfaces leads to surface species similar to those found after chromium(III) sorption on hematite surfaces (Figure 3). The structural information obtained using GI-XAFS, coupled with the Pauling bond valence principle, was used to rationalize interfacial chromium species and their mode of bonding to the surface (Grolimund et al. 1999).

Certain results of the present spectroscopic investigation are inconsistent with assumptions commonly used in surface complexation modeling, where different coordination environments of *isolated* surface species are postulated without direct molecular-level knowledge of the types of surface complexes present (Dzombak and Morel 1990). We found, for example, strong evidence for *multinuclear* chromium surface complexes on the hematite (0001) surface in contact with aqueous solution (Figure 3). Such multinuclear chromium species were observed even at extremely low surface coverages and

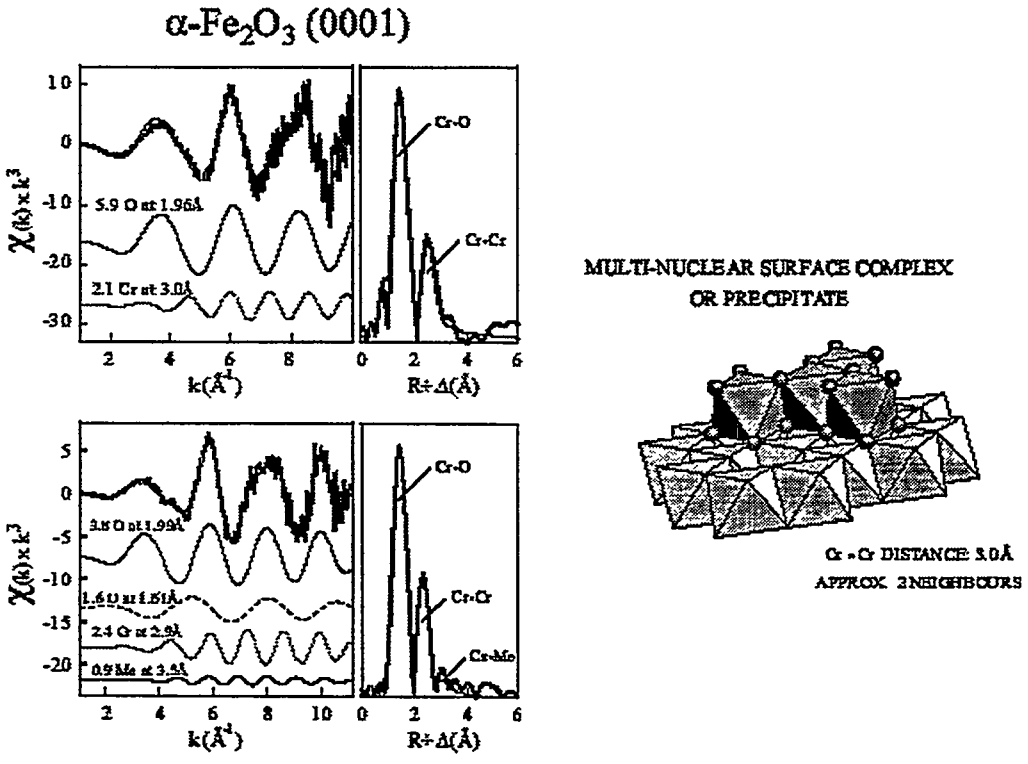

Figure 3. Chromium- K-Edge GI-XAFS Data for Chromium Sorbed on an α-Fe_2O_3(0001) Single Crystal Surface (left) and Corresponding Visualization of the Proposed Interfacial Complex (right). The spectrum shown on the top-left corresponds to unreduced hematite reacted with chromium(III), while the spectrum shown on the bottom-left represents partially reduced hematite exposed to chromium(VI). Least-squares fits of the EXAFS including shell-by-shell deconvolution and Fourier transforms uncorrected for phase shift are shown.

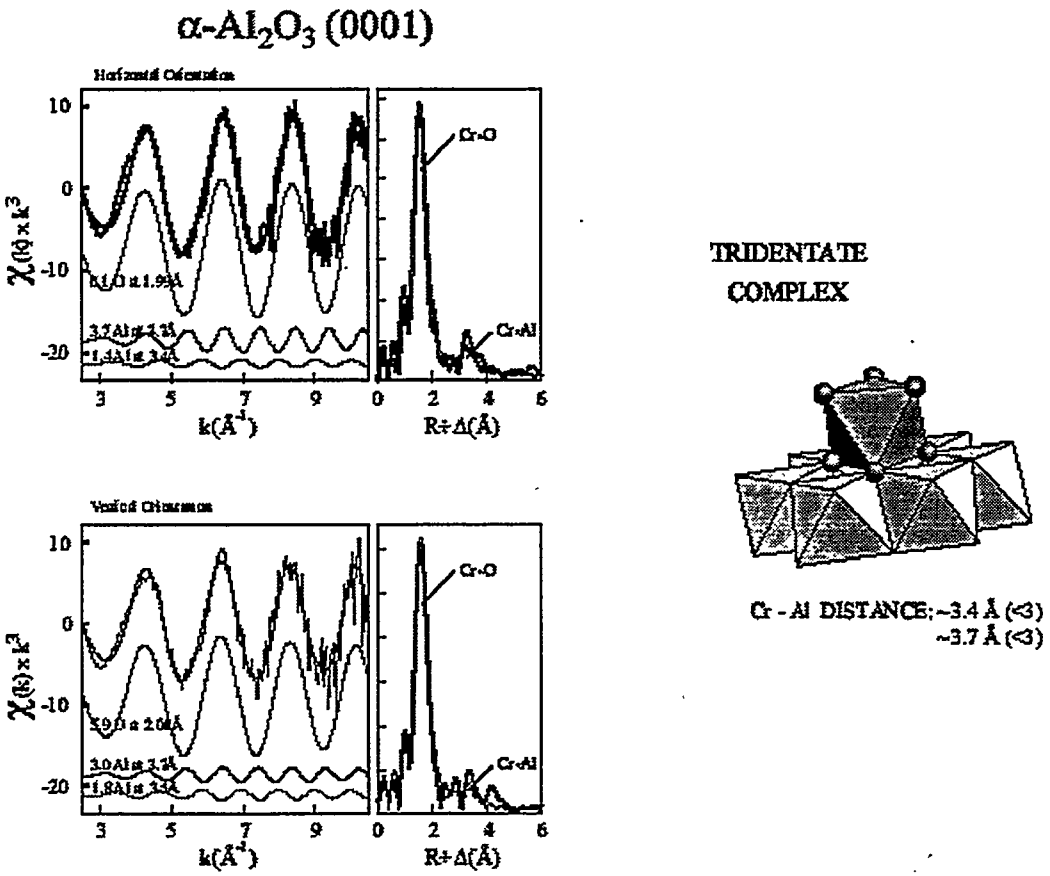

Figure 4. Chromium- K-Edge GI-XAFS Data of Chromium Sorbed on an α-Al_2O_3(0001) Single Crystal Surface (left) and Corresponding Visualization of the Proposed Interfacial Complex (right). The spectrum at the top left was taken with the electric field vector of the x-ray beam parallel to the surface plane. The spectrum at the bottom left was taken with the electric field vector of the x-ray beam perpendicular to the surface plane. Least-square fits of the EXAFS including shell-by-shell deconvolution and Fourier transforms uncorrected for phase shift are shown.

solution conditions undersaturated with respect to precipitates. These hydroxo-bridged chromium-polymers were either limited in size and predominately "two-dimensional" or correspond to more extended clusters with a considerable degree of structural disorder. The existence of chromium at the oxide-water interface in the form of multinuclear complexes even at a surface coverage of <0.1 mono-layer was not anticipated based on the findings of earlier EXAFS studies of metal ion surface complex-ation as a function of metal loading. For example, earlier EXAFS studies (Chisholm-Brause et al. 1996; O'Day et al. 1996; Towle et al. 1999) report evidence for mononuclear complexes of cobalt(II) at the lowest surface coverages examined (~0.05 $\mu M/m^2$), with multinuclear complexes or precipitates forming at higher surface coverages. Nevertheless, our finding of multinuclear chromium surface complexes is consistent with observations presented in a previous study investigating chromium(III) sorption on iron oxides using STM (Eggleston and Stumm 1993). Such multinuclear complexes can be expected to have a distinctively different reactivity than isolated monomeric species, including a higher threshold for desorption.

In contrast to the multinuclear species present in the chromium/hematite sorption samples, mononuclear chromium(III) complexes were found at the aqueous solution-corundum interface. The observed two shells of aluminum backscatterers at 3.5 and 3.7 Å (Figure 4) is consistent with the presence of isolated, uniform tridentate chromium(III) complexes on the α-Al_2O_3 single crystal surface as the dominant surface species. Significant levels of other potential interfacial species can be ruled out based on crystallographic arguments or the incompatibility of various sorption complex geometries with the observed polarization dependence (Figure 4).

The observed differences in surface complex type for the (0001) surfaces of α-Al_2O_3 and α-Fe_2O_3 suggest fundamental differences in the structures and reactivities of these two surfaces in contact with aqueous solutions. The finding of multinuclear surface complexes emphasizes the need for an improved, molecular-level conceptualization of reactions occurring at the solid-aqueous solution interface.

Redox Chemistry of Chromate on Magnetite

Having gained some understanding of the interaction of water with magnetite surfaces, we now turn to the interaction of aqueous chromate with Fe_3O_4(001) and (111). The speciation of chromate was investigated using core-level x-ray photoemission (XPS) and chromium L-edge, iron L-edge, and oxygen K-edge x-ray absorption spectroscopy using synchrotron radiation at the SSRL (Kendelewicz et al. 1999b). The adsorbed layer, which is deposited by dipping the magnetite surface in chromate solution and drying in a N_2-filled glovebox, consists mostly of chromate with negligible iron oxide. The chromate layer thickness increases to a maximum value of ~15Å with increasing chromate concentration in solution and exposure time. Oxygen 1s XPS reveals the presence of OH^- ligands surrounding chromium and the small amount of iron present. Chromium(VI) is reduced to chromium(III) upon adsorption on the magnetite surface. For Fe_3O_4(111) reacted with 5 mM chromate solutions for 10 minutes or longer, a significant amount of chromium(VI) remained in the outermost portion of the adlayer, indicating incomplete chromium(VI) reduction. Complete chromium(VI) reduction was found on surfaces exposed to 50 µM chromate solution for 1 minute or longer, indicating rapid reaction kinetics. These results are summarized in Figure 5. As seen in the figure, all chromium(VI) is converted to chromium(III) for µM concentrations.

However, mM concentrations result in incomplete reduction, presumably due to the complete consumption of iron(II) on the surface. Longer exposures at mM concentrations result in the accumulation of even more chromium(VI). In contrast, chromate adsorbed on well-defined surfaces of hematite (Fe_2O_3) remain unreduced, *unless* small amounts of iron(II) left over from surface preparation processes remain. In this case, limited reduction by an amount commensurate with the amount of iron(II) present initially is seen to occur.

An important implication of the above findings for reductive sorption of chromate on iron bearing minerals and "zero-valent" iron in the subsurface is that the process is very much self limiting as iron(II) is consumed on the surface. Zero valent iron is actually coated with a thin oxide skin consisting mostly of magnetite. The redox process converts magnetite and zero-valent iron, which are conductive and facilitate electron-transfer processes, to an insulating oxyhydroxide containing only iron(III). Chromium(III) oxyhydroxide builds up on of this layer. The insulating nature of these layers prevents electron transfer from deeper layers, thus bringing the redox process to a halt. *Therefore, high-surface area iron(II) bearing remediation agents and/or natural minerals are required for high reductive capacity of chromate.*

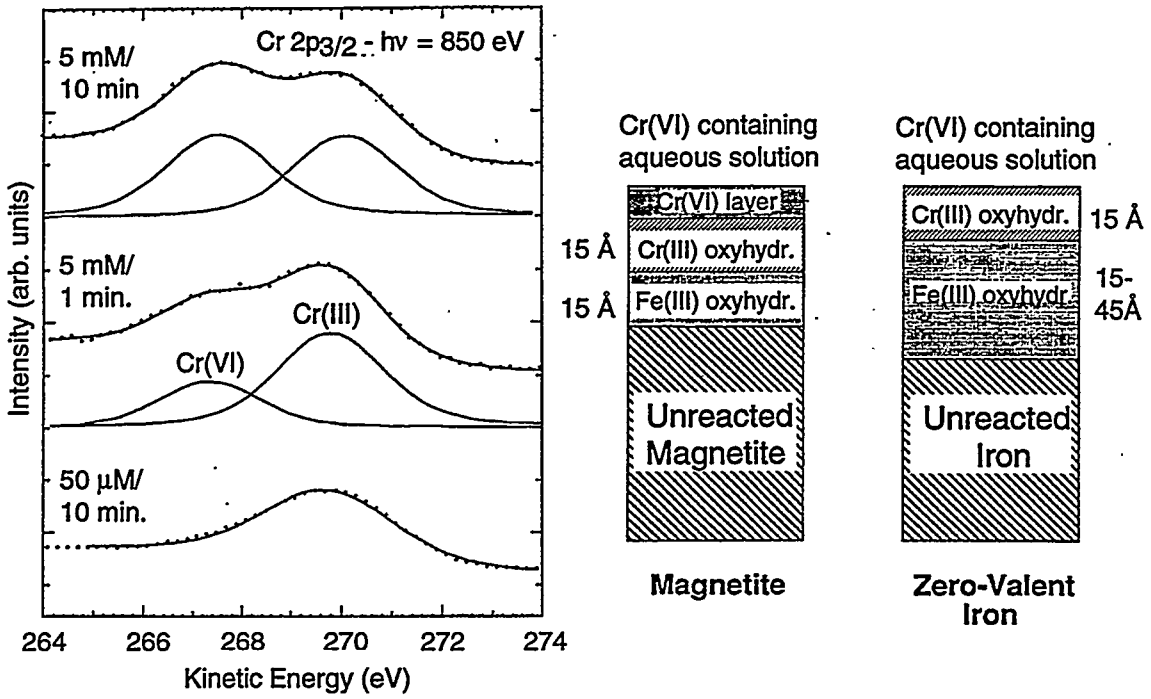

Figure 5. Chrominum $2p_{3/2}$ Photoemission Spectra of Chromate on $Fe_3O_4(111)$ for Various Chromate Concentrations and Exposure Times (left) and Structural Diagrams of the Aqueous Chromate/Magnetite and Chromate/Zero-Valent Iron Interfaces after the Redox Reaction Has Come to a Self-Limiting Halt

Chromate Sorption on Hematite Surfaces

Powdered hematites present several crystalline faces for surface reactions and thus represent a system that is intermediate in complexity between the single-crystal surfaces described above and the heterogeneous mixture of surfaces found in soils and sediments. We conducted several experiments with hematite powder to understand the thermodynamics and kinetics of chromium(VI) sorption, with particular emphasis placed on competitive sorption by chromate, phosphate, and sulfate oxyanions. Although our focus here is on the thermodynamic results, we note that improvements were made to our kinetic flow cell that decreased the experimental volume to 3 mL and shortened the mixing time to about 10 seconds, while retaining the ability to nondestructively analyze changes in trace-level chromate concentrations by laser photoacoustic spectroscopy (LPAS).

Batch sorption experiments with 20 mg of hematite powder (specific surface of 9.7 $m^2\ g^{-1}$ by BET-N_2) in a 15 mL solution were conducted at room temperature,with initial chromate, phosphate, or sulfate concentrations ranging from 2.7 to 54 µM (i.e., 140 ppb to 2.8 ppm). Preliminary experiments established that equilibration times of one hour were sufficient, and the concentrations of the anions remaining in solution after this time were determined by ion chromatography. The solutions were not buffered for pH to eliminate interferences from the anions associated with buffering agents, and as a consequence, final sorption pHs ranged from 6.0 to 6.8. Despite the range in final pH, the results of these sorption experiments (Figure 6a) could be described well by the linearized Langmuir isotherm equation:

$$C_{final}/C_{sorbed} = (1/C_{max})C_{final} + b$$

where C_{final} and C_{sorbed} are the equilibrium concentrations in solution and on the hematite surface, respectively, C_{max} is the maximum sorption capacity of the mineral under the conditions of the experiment, and b is a constant. Maximum sorption capacities of the hematite for sulfate, chromium(VI), and phosphate, were 3.5, 8.3, and 9.3 μM g^{-1}, respectively, indicating that chromium(VI) and phosphate were sorbed more strongly than sulfate. In fact, C_{max}, which is an estimate of the relative sorption affinity of each of the three anions, is strongly correlated with pK_2, the negative log of the second acid dissociation constant for each anion (Figure 6b). Such a relationship would be expected because the protons are the charge-determining ions on the hematite surface and larger pK_2 values indicate greater proton affinities on the part of the anions.

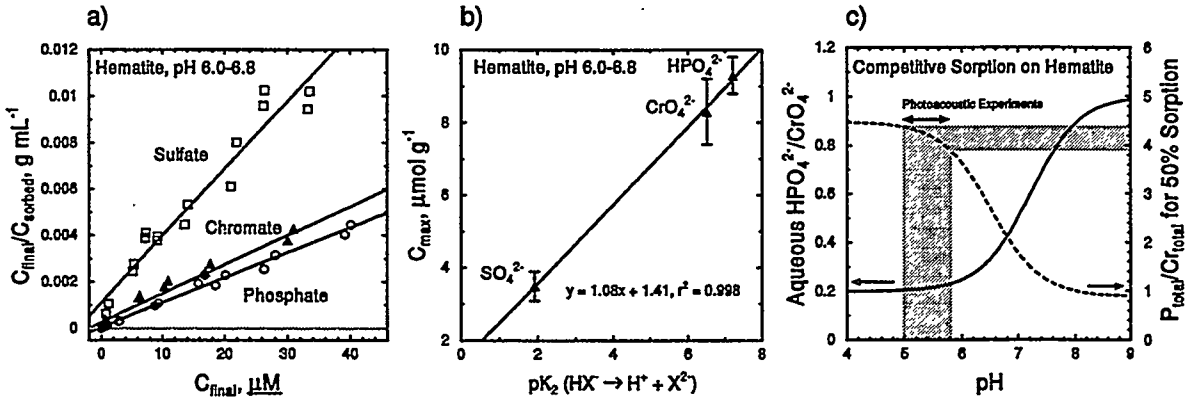

Figure 6. Results of Hematite Sorption Studies with Sulfate, Chromate, and Phosphate: a) linearized Langmuir isotherm plots of sorption of mono-anionic solutions; b) correlation between observed C_{max} values for mono-anionic solutions and the acidities of the anions; c) influence of pH on aqueous speciation of phosphate and chromate (solid line-left axis) and the Ratio of Total Phosphate to Chromium(VI) Needed to Achieve Equal Sorption (dashed line-right axis).

The correlation of C_{max} with pK_2 values suggests that only the divalent anion species (i.e., SO_4^{2-}, CrO_4^{2-}, and HPO_4^{2-}) contribute significantly to sorption. This premise can be tested by competitive sorption experiments because the amounts of divalent anion available for sorption will vary differently for each anion when pHs close to the pK_2 values are selected. Although experiments at pHs near the pK_2 of sulfate are impractical, such experiments with chromium(VI) and phosphate are both practical and directly relevant to groundwater chemistry because the pK_2 values for these anions are near 7. The expectation is that the relative sorption of chromium(VI) and phosphate would be directly proportional to the aqueous concentrations of CrO_4^{2-} and HPO_4^{2-}. Speciation calculations show the ratio of these two species in solution (i.e., HPO_4^{2-}/CrO_4^{2-}) varies from about 0.2 to 1 in going from pH 4 to 9 (Figure 6c, solid curve) and suggest that sorption of chromium(VI) would be favored over phosphate over much of this range. We can estimate the relative amount of total phosphate needed to achieve 50% sorption [i.e., equivalent sorption with chromium(VI)] by

$$[P_{total}/Cr(VI)_{total}]_{50\%} = [C_{max(Cr(VI)}/C_{max(P)}][CrO_4^{2-}/HPO_4^{2-}]$$

and this result is also plotted in Figure 6c (dotted curve, right axis). On this basis, we would predict that about 4.5 times as much phosphate as chromium(VI) would be needed at pH 5 for equal sorption by the two anions on hematite, whereas equal sorption would occur at pH 8 with equal concentrations of

chromium(VI) and phosphate. In fact, the prediction at pH 5 is in excellent agreement with the results of competitive sorption experiments carried out using LPAS and reported in last year's report (shown by the shaded portion of the graph).

Based on these results, we can draw the following conclusions. Sorption of chromium(VI) and phosphate species to hematite is dominated by divalent anions even at low pHs where monovalent anions predominate in solution. As a consequence, aqueous speciation (i.e., the fraction of the total species in solution available in the form of a divalent anion) is a more important determinant of the relative amount of chromium(VI) or phosphate sorbed than the intrinsic selectivity of the anions for the surface. In mixed-anion systems typical of groundwater, significantly different sorption affinities may be observed than predicted solely on the basis of relative single-anion sorption constants.

An important outcome of this work is the development of a powerful new tool with which competitive adsorption of anions on minerals in suspension can be investigated in real time. We have demonstrated that nontoxic anions present in the subsurface environment, such as phosphate, may compete with toxic anions, such as chromium(VI), for sorption sites on redox-active minerals to an extent that is highly pH dependent. Significantly, LPAS can be used for studies of pure mineral phases, such as hematite in the present experiments, as well as for multi-component soil mixtures. Thus, controlled and "real-world" experiments can be carried out to determine the extent to which competing nontoxic anions can prevent adsorption and reduction of toxic anions by minerals or redox-active remediation agents, such as zero-valent iron.

Summary

This project involves the coordinated efforts of a multidisciplinary team of scientists using state-of-the-art experimental and computational methods to attack complex and important problems in heterogeneous contaminant/mineral chemistry. Our approach is reductionist by design. Activities range from determining and understanding the structure of well-defined, clean, redox-active mineral surfaces, such as $Fe_3O_4(001)$, to investigating the interaction of such surfaces with water (the universal solvent), to determining the rates and extents of redox chemistry of important aqueous contaminants, such as chromate, with these surfaces. While we have made significant progress toward our stated goal of understanding the interaction of chromate with iron oxide surfaces, we have only scratched the surface of what could be learned, given the opportunity. It is with considerable regret that this outstanding team will be disbanded in September without renewal of the 1996 EMSP projects.

Planned Activities

Between now and the end of the project, our activities will include the following tasks:

1. Complete the surface structure determination by XPD of $Fe_3O_4(001)$.

2. Resolve some uncertainties related to determining the conditions under which the A and B terminations of $Fe_3O_4(001)$ are formed.

3. Determine the nature of the (1x3) reconstruction of $Fe_3O_4(001)$ that forms after extensive annealing in ultrahigh vacuum.

4. Complete theoretical analysis of the solvated Fe_3O_4(001)surface.

5. Compute structures of chromate surface complexes on Fe_3O_4(001).

6. Conduct water and aqueous chromium sorption experiments on a variety of natural and MBE grown manganese-oxide surfaces.

7. Conduct competitive sorption experiments on hematite powder for chromium(VI) with carbonate and with sulfate.

8. Conduct competitive sorption experiments for chromium(VI) with phosphate on single-crystal MBE-synthesized hematite.

References

Baes CF Jr. and RE Mesmer. 1976. *The Hydrolysis of Cations*. Krieger, Malabar.

Chambers SA and SA Joyce. 1999. *Surf. Sci.* 420:111 (and B Stanka and U Diebold, unpublished).

Chisholm-Brause CJ, PA O'Day, GE Brown Jr., and GA Parks. 1990. *Nature* 348:528-531.

Dzombak DA and FMM Morel. 1990. *Surface Complexation Modeling: Hydrous Ferric Oxide*, Wiley-Interscience, New York.

Eggleston CM and W Stumm. 1993. *Geochim. Cosmochim. Acta* 57:4843-4850.

George GN and IJ Pickering. 1995. "EXAFS-PAK: A Suite of Computer Programs for the Analysis of X-ray Absorption Spectra." Technical Report, Stanford Synchrotron Radiation Laboratory, Stanford, California.

Gibson AS and JP LaFemina. 1996. "Structure of Mineral Surfaces." In *CRC Series in the Physics and Chemistry of Surface and Interfaces*, CRC Press.

Giordano L, J Goniakowski, and J Suzanne. 1998. *Phys. Rev. Lett.* 81:1271.

Grolimund D, T Kendelewicz, TP Trainor, P Liu, JP Fitts, SA Chambers, and GE Brown Jr. 1999. "Identification of Cr species at the solution-hematite interface after Cr(VI)-Cr(III) reduction using GI-XAFS and Cr L-edge NEXAFS." *J. Synchrotron Rad.* (in press).

Henderson MA, SA Joyce, and JR Rustad. 1998. *Surf. Sci.* 417:68.

Kendelewicz T, P Liu, GE Brown Jr., EJ Nelson, and SA Chambers. 1999a. *Surf. Sci.* (in preparation).

Kendelewicz T, P Liu, CS Doyle, GE Brown Jr., EJ Nelson, and SA Chambers. 1999b. *Surf. Sci.* 424:219.

Liu P, T Kendelewicz, GE Brown Jr., EJ Nelson, and SA Chambers. 1998. *Surf. Sci.* 417:53.

O'Day PA, CJ Chisholm-Brause, SN Towle, GA Parks, and GE Brown Jr. 1996. *Geochim. Cosmochim. Acta* 60:2515-2532.

Rehr JJ, J Mustre de Leon, SI Zabinski, and RC Albers. 1991. *J. Am. Chem. Soc.* 113:5135-5140.

Rustad JR, E Wasserman, and AR Felmy. 1999. *Surf. Sci.* (to appear).

Smith RM and AE Martell. 1976. *Critical Stability Constants*. New York: Plenum Press.

Tarrach G, D Burgler, T Schaub, R Wiesendanger, and HJ Guntherodt. 1993. *Surf. Sci.* 285:1.

Towle SN, JR Bargar, GE Brown Jr., and GA Parks. 1999. "Sorption of Co(II) on metal oxide surfaces: Part II. Identification of Co(II)(aq) adsorption sites on (1-102) and (0001) surfaces of α-Al_2O_3 by grazing-incidence XAFS spectroscopy." *J. Coll. Interf. Sci.* (in press).

Voogt FC. 1998. "NO_2-Assisted Molecular Beam Epitaxy of Iron Oxide Films." Ph.D. thesis, Departments of Chem. Phys. and Nuc. Sol. St. Phys. University of Groningen, The Netherlands.

Publications and Presentations

Publications

Chambers SA, Y Gao, and YJ Kim. 1998. "Fe 2p core-level spectra for pure, epitaxial α-Fe_2O_3(0001), γ-Fe_2O_3(001), and Fe_3O_4(001)." *Surf. Sci. Spect.* 5:219.

Liu P, T Kendelewicz, GE Brown Jr., EJ Nelson, and SA Chambers. 1998. "Reaction of water vapor with α-Al_2O_3(0001) and α-Fe_2O_3(0001) surfaces: Synchrotron x-ray photoemission studies and thermodynamic calculations." *Surf. Sci.* 417:53.

Chambers SA and SA Joyce. 1999. "Surface termination, composition, and reconstruction of Fe_3O_4(001) and γ-Fe_2O_3(001)." *Surf. Sci.* 420:111.

Chambers SA and Y Liang. 1999. "Growth of β-MnO_2 films on TiO_2(110) by oxygen-plasma-assisted molecular beam epitaxy." *Surf. Sci.* 420:123.

Kendelewicz T, P Liu, CS Doyle, GE Brown Jr., EJ Nelson, and SA Chambers. 1999. "X-ray absorption and photoemission study of the adsorption of aqueous Cr(VI) on single crystal hematite and magnetite surfaces." *Surf. Sci.* 424:219.

Thevuthasan S, YJ Kim, SA Chambers, J Morais, R Denecke, CS Fadley, P Liu, T Kendelewicz, and GE Brown Jr. 1999. "Surface structure of MBE-grown α-Fe_2O_3(0001) by intermediate-energy x-ray photoelectron diffraction." *Surf. Sci.* 425:276-286.

Yi SI, Y Liang, and SA Chambers. 1999. "Effect of growth rate on the nucleation of α-Fe_2O_3 on α-Al_2O_3(0001) by oxygen-plasma-assisted molecular beam epitaxy." *J. Vac. Sci. Technol. A.*

Rustad JR, E Wasserman, and AR Felmy. 1999. "A molecular dynamics investigation of surface reconstruction on magnetite (001)." *Surf. Sci.* (in press).

Rustad JR, DA Dixon, JD Kubicki, and AR Felmy. 1999. "Gas-phase acidities of tetrahedral oxyacids from ab initio electronic structure calculations." *J. Phys. Chem.* (n press).

Foster NS, ST Autrey, JE Amonette, JR Small, and EW Small. 1999. "Laser photoacoustic spectroscopy: A versatile absorption spectroscopic technique." *Am. Lab.* 31:96s-108s.

Foster NS, JE Amonette, and ST Autrey. 1999. "In-situ detection of chromate using photoacoustic spectroscopy." *Appl. Spectrosc.* (in press).

Liu P, T Kendelewicz, GE Brown Jr., EJ Nelson and SA Chambers. 1998. "Reaction of water vapor with α-Al_2O_3 and α-Fe_2O_3 (0001) surfaces: Synchrotron x-ray photoemission studies and thermodynamic calculations." *Surface Science* 417:63-65.

Brown GE Jr., VE Henrich, WH Casey, DL Clark, C Eggleston, A Felmy, DW Goodman, M Grätzel, G Maciel, MI McCarthy, K Nealson, DA Sverjensky, MF Toney, and JM Zachara. 1999. "Metal oxide surfaces and their interactions with aqueous solutions and microbial organisms." *Chem. Rev.* 99:77-174.

Grolimund D, T Kendelewicz, TP Trainor, P Liu, JP Fitts, SA Chambers, and GE Brown Jr. "Identification of Cr species at the aqueous solution hematite interface after Cr(VI)-Cr(III) reduction using GI-XAFS and Cr L-edge NEXAFS." *J. Synchrotron Radiation* (in press).

Kendelewicz T, P Liu, GE Brown Jr., EJ Nelson, and SA Chambers. 1999. "Reaction of water with the (100) and (111) surfaces of Fe_3O_4." *Surface Science.*

Kendelewicz T, P Liu, CS Doyle, and GE Brown Jr. "O K-edge and Fe L-edge spectra of iron oxides and hydroxides" (in preparation for submission to *Surface Science*).

Bargar JR, GE Brown Jr., and SA Chambers. "Grazing-incidence XAFS study of the sorption of Pb(II) on the (0001) and (1-102) surfaces of hematite" (in preparation for submission to *Journal of Colloid and Interface Science*).

Chambers SA and SI Yi. 1999. "Persistent Fe termination of α-Fe_2O_3(0001) under heavily oxidizing conditions" (submitted to *Phys. Rev. Lett).*

Chambers SA and S Thevuthasan. 1999. "Surface structure of MBE-grown Fe_3O_4(001)." *Phys. Rev. B, Rapid Communications* (in preparation).

Presentations at National and International Meetings

Thevuthasan S. November 1998. "Rutherford Backscattering and Channeling Studies of Al and Mg Diffusion in Iron Oxide Thin Films," Fifteenth International Conference on the Application of Accelerators, Denton, Texas (invited).

Thevuthasan S, YJ Kim, SA Chambers, P Liu, T Kendelewicz, DE Brown Jr., J Morais, R Denecke, and CS Fadley. June 1998. "The Surface Structure Determination of α-Fe_2O_3 by Intermediate-Energy X-Ray Photoelectron Diffraction." Surface Analysis/8th Annual Pacific Northwest Symposium.

McCready DE, S Thevuthasan, W Jiang, YJ Kim, Y Gao, SA Chambers, NR Shivaparan, and RJ Smith. June 1998. "Rutherford Backscattering and Channeling Studies of Epitaxially Grown Iron Oxide Films on Various Substrates." Surface Analysis/8th Annual Pacific Northwest Symposium.

Thevuthasan S, W Jiang, DE McCready, and SA Chambers. November 1998. "Rutherford Backscattering and Channeling Studies of Al and Mg Diffusion in Iron Oxide Thin Films." 45th National Symposium of the American Vacuum Society.

Thevuthasan S, YJ Kim, SA Chambers, J Morais, R Denecke, CS Fadley, P Liu, T Kendelewicz, and DE Brown Jr. November 1998. "The Surface Structure Determination of α-Fe_2O_3 (0001) by Low-Energy X-Ray Photoelectron Diffraction." 45th National Symposium of the American Vacuum Society.

Thevuthasan S, DE McCready, W Jiang, SI Yi, and SA Chambers. July 1999. "Ion Beam Analysis of Interface Reactions in Iron Oxide Thin Films." Fourteenth International Conference on Ion Beam Analysis (IBA-14), Dresden, Germany (invited).

Chambers SA, S Thevuthasan, YJ Kim, SA Joyce, and Y Liang. August 1998. "Surface Structure Determination of MBE Grown Iron and Manganese Oxides." National Meeting of The American Chemical Society, Boston (invited).

Chambers SA. October 1998. "Molecular Beam Epitaxial Growth and Surface Structure Determination of Fe and Mn Oxides." Center for Catalysis and Surface Structure, Northwestern University, Evanston, Illinois (invited).

Chambers SA, S Thevuthasan, and SA Joyce. January 1999. "Structure and Reactivity of MBE-Grown Fe Oxides." First International Conference on Oxide Surfaces, Elmau, Germany (invited).

Chambers SA and Y Liang. November 1998. "Growth of β-MnO_2 Films on TiO_2(110) by Oxygen-Plasma-Assisted Molecular Beam Epitaxy." 45th International Symposium of the American Vacuum Society, Baltimore.

Rustad JR, E Wasserman, and SA Joyce. March 1999. "Structure and Energetics of the Magnetite(001) Surface Insights From Molecular Dynamics Calculations." ACS Meeting, Anaheim, California.

Rustad JR. August 1999. "Molecular simulation of the iron oxide-water interface." ACS Meeting, New Orleans (invited).

Amonette JE, NS Foster, BK William, and AE Taylor. March 1999. "Trace-level Chromate Sorption Dynamics at Hematite Surfaces: A Spectroscopic Approach." 217th National Meeting of the American Chemical Society, Anaheim, California.

Amonette JE, NS Foster, BK William, and AE Taylor. June 1999. "Competitive Trace-Level Sorption of Chromate and Phosphate to Hematite Surfaces: A Spectroscopic Approach." 36th Annual Meeting of the Clay Minerals Society, Purdue University, West Lafayette, Indiana.

Joyce SA, S Thevuthasan, and SA Chambers. March 21-25, 1999. "Growth and Structure of Synthetic Iron Oxide Mineral Surfaces." 217th National Meeting of the American Chemical Society, Anaheim, California.

Kendelewicz T, P Liu, GE Brown Jr., EJ Nelson, and SA Chambers. August 1998. "Reaction of water with clean (0001) and (1-102) surfaces of α-Fe_2O_3." International Conference on Surface Science 10, Birmingham, United Kingdom.

Kendelewicz T, P Liu, GE Brown Jr., and EJ Nelson. August 1998. "Reaction of water with (100) and (111) Surfaces of Magnetite (Fe_3O_4)." International Conference on Surface Science 10, Birmingham, United Kingdom.

Kendelewicz T, P Liu, GE Brown Jr., EJ Nelson, and SA Chambers. August 1998. "Fe $L_{2,3}$ and O K near edge structure of iron oxides and hydroxides." International Conference on Surface Science 10, Birmingham, United Kingdom.

Kendelewicz T, P Liu, GE Brown Jr., EJ Nelson, and SA Chambers. August 1998. "Reduction of the (0001) surface of hematite (α-Fe_2O_3) prepared under UHV conditions." International Conference on Surface Science 10, Birmingham, United Kingdom.

Grolimund D, T Kendelewicz, TP Trainor, P Liu, JP Fitts, GE Brown Jr., and SA Chambers. July 1998. "Identification of Cr Species at the solution-hematite interface after Cr(VI)-Cr(III) reduction using GI-XAFS and Cr L-edge NEXAFS." 10th International XAFS Conference, Chicago.

Kendelewicz T, P Liu, GE Brown Jr., SA Chambers, and MI McCarthy. August 1998. "Hydroxylation of the surfaces of simple metal oxides: spectroscopic and thermodynamic analysis." Goldschmidt Conference, Toulouse, France.

Grolimund D, JP Fitts, TP Trainor, GE Brown Jr., and SA Chambers. March 1999. "Identification of Cr species at the aqueous solution-oxide interface using grazing-incidence XAFS." 217th American Chemical Society Meeting, Anaheim, California.

Brown GE Jr., JR Bargar, S-F Cheah, CS Doyle, D Grolimund, JP Fitts, AL Foster, T Kendelewicz, C Kim, P Liu, JD Ostergren, GA Parks, A Templeton, HA Thompson, SN Towle, TP Trainor, and SA Chambers. March 1999. "Characterization of adsorbed chemical species at mineral surfaces." 217th American Chemical Society Meeting, Anaheim, California.

Mineral Surface Processes Responsible for the Decreased Retardation (or Enhanced Mobilization) of ^{137}Cs from HLW Tank Discharges

(First Year of Funding: 1997)

Principal Investigator

Dr. John M. Zachara
Pacific Northwest National Laboratory
Environmental Dynamics & Simulation
P.O. Box 999, MSIN K8-96
Richland, WA 99352
(509) 376-3254 (phone)
(509) 376-3650 (fax)
john.zachara@pnl.gov

Co-Principal Investigators

Mr. R. Jeffrey Serne
Pacific Northwest National Laboratory
Applied Geology & Geochemistry
P.O. Box 999, MSIN K6-81
Richland, WA 99352
(509) 376-8429 (phone)
(509) 376-5368 (fax)
jeff.serne@pnl.gov

Dr. James P. McKinley
Pacific Northwest National Laboratory
Interfacial Geochemistry
P.O. Box 999, MSIN K3-61
Richland, WA 99352
(509) 375-6841 (phone)
(509) 375-6954 (fax)
james.mckinley@pnl.gov

Dr. Paul M. Bertsch
University of Georgia
Savannah River Ecology Laboratory
P.O. Drawer E/Bldg 737A
Aiken, SC 29801
(803) 725-2472 (phone)
(803) 725-3309 (fax)
bertsch@srel.edu

Research Objective

Experimental research will determine how the sorption chemistry of cesium on Hanford vadose zone sediments changes after contact with solutions characteristic of high-level tank wastes (HLW). Our central hypothesis is that the high ionic strength of tank wastes (i.e., >5 mol/L $NaNO_3$) will suppress all surface-exchange reactions of cesium, except those to the highly selective frayed-edge sites (FES) of the micaceous fraction. We further speculate that the concentrations, ion selectivity, and structural aspects of the FES will change after contact with the harsh chemical conditions of HLW and these changes will be manifest in the macroscopic sorption behavior of cesium. We believe that migration predictions of cesium can be improved substantially if such changes are understood and quantified.

The research will integrate studies of ion-exchange thermodynamics on the FES, with high-resolution surface microscopes and spectroscopy to probe the structure of FES in Hanford sediments and to describe how the chemical environment of sorbed cesium changes when HLW supernatants promote silica dissolution and aluminum precipitation. Newly available atomic-force and high-resolution electron-beam microscopes afford previously unavailable opportunities to visualize and characterize FES. Our overall goal is to provide knowledge that will improve transport calculations of cesium in the tank-farm environment. Specifically, the research will

- identify how the macroscopic sorption behavior of cesium on the micaceous fraction of the Hanford sediments changes after contact with simulants of HLW tank supernatants over a range of relevant chemical ([OH], [Na], [Al], [K, NH_4]) and temperature conditions (23° to 80°C)

- reconcile observed changes in sorption chemistry with microscopic and molecular changes in adsorption-site distribution, chemistry, mineralogy, and morphology/structure of the micaceous sorbent fraction

- integrate mass-action-solution-exchange measurements with changes in the structure/site distribution of the micaceous-sorbent fraction to yield a multi-component/site-exchange model relevant to high ionic strength and hydroxide concentrations for prediction of environmental cesium sorption.

Problem Statement

Environmental Management Concerns

- Single-shell tanks (SSTs) containing HLW have leaked supernatant liquid containing large amounts of radioactive ^{137}Cs (10^6 Ci) and other cocontaminants into the Hanford vadose zone.

- In select locations, ^{137}Cs has exhibited "expedited" migration (up to 50 m when predicted migration distances are <10 m) into the saturated zone. The reasons for "expedited" migration are unclear.

- Deep ^{137}Cs migration has been observed beneath the SX tank farm at Hanford with redox wastes as the carrier, causing significant regulatory and stakeholder concern.

Scientific Context

- Micaceous 2:1 layer silicates are the primary environmental sorbents of cesium. Cs^+ is strongly sorbed by specific structural sites on these solids that exhibit nanometer scale dimensions with unique steric and geometric attributes.

- Micaceous 2:1 layer silicates exist as a small mass fraction of Hanford vadose zone sediments. These are known to impart significant Cs^+ sorptivity to Hanford subsurface sediments.

Science Issues

- REDOX wastes were self-concentrating by boiling and contain molar plus concentrations of Na^+, NO_3^-, OH^-, and $Al(OH)_4^-$. The sorption behavior of Cs^+ from this complex waste matrix is unknown.

- The chemical composition and temperature of the redox wastes is "harsh" and will induce dissolution and precipitation reactions upon contact with Hanford vadose zone sediments, possibly changing mineral surface structure and the selectivity of the micaceous fraction for Cs^+. The extent, kinetics, and impacts of these reactions on contaminant fixation and migration are unknown.

- There is no literature information upon which to base scientifically credible estimates of Cs^+ adsorptive-retardation beneath SSTs that have leaked high pH-high ionic-strength waste waters.

Research Progress

Research since the last time of reporting (May 1998) has continued to investigate 1) the cesium retention characteristics of a mica-containing composite sediment from the Hanford formation and 2) the mineral association of ^{137}Cs in 35-year-old contaminated sediment from beneath a leaked SST at Hanford (SX-109). Highlights from this work will be presented in the text that follows. Studies to determine the influence of high base on highly selective sorption/exchange of cesium to the micaceous fraction of the Hanford sediments were initiated at the beginning of the fiscal year, as planned in the proposal. The results of these experiments are preliminary and are not reported here.

1. *Thermodynamics of Cesium Exchange.* Adsorption isotherms of cesium were measured over a wide sorbate range on homo-ionic Hanford sediments (Na^+, K^+, Ca^{2+}) in salt solutions of different concentrations. The objective of these measurements was to predict the magnitude of Cs^+ adsorption to Hanford sediment. Salt concentrations ranged between 10^{-2} to 10^{-69} mol/L to bracket those observed in natural and HLW impacted environments. The results were analyzed in terms of a conditional thermodynamic equilibrium constant (K_v) for the generalized exchange reaction:

$$uCs^+_{(aq)} + vAX_u = uCsX + vA^{u+}_{(aq)} \qquad (K_v)$$

where $K_v = [A^{u+}]^v[N_{CsX}]^u/[Cs^+]^u[N_{AXu}]^v$ and N is mole fraction of the exchanger phase components (AX_u, CsX). The mole fractions are defined as follows:

$$N_{CsX} = [CsX]/([CsX] + [AX_u]) \text{ and } N_{Axu} = [AX_u]/([CsX] + [AX_u])$$

The K_v is often termed a "selectivity coefficient" that is a measure of the binding affinity of the sorbate (Cs) relative to the index or saturating cation (e.g., $A^{u+}_{(aq)}$) that was either Na^+, K^+, or Ca^{2+} in this case.

The Cs^+ - Na^+, Cs^+ - K^+, and Cs^+ - Ca^{2+} exchange data each conformed to a single K_v relationship in the different salt solutions (Figure 1, where E(CsX) is the equivalent fraction of Cs on the exchanger [= adsorbed Cs concentration/cation exchange capacity]). Cs^+ was sorbed in great preference to the other cations, with K_v ranging from 10 to 10^{10}. Consistent with ionic radius and hydration enthalpy, K^+ was the most effective competitor for cesium. The dependence of K_v on E(CsX) indicates the presence of approximately three different types of exchange sites in the sediment with different adsorption/exchange energies. A high-affinity site is present at low concentration, e.g., log E = 10^{-4}. The high-affinity site exists in the sediment at a total concentration of 10^{-8} mol/g, which is 1% of the operational frayed-edge site pool defined by silver-thiourea exchange (data not shown). The high-affinity site is slightly lower in concentration than $^{137}Cs^+$ in HLW (e.g., 10^{-7} mol/g). The exchange coefficient functions in Figure 1 can be used to model Cs^+ adsorption by ion exchange in Hanford sediments.

2. *Desorption and Fixation of Cesium.* Cesium is known to diffuse within the interlammellar space in specimen illites, leading to its partial or complete fixation. Fixation is highly significant in the Hanford sediments. If fixation occurs, ^{137}Cs may be held in place by the geomedia for sufficient periods to allow full decay to daughter products. Fixation, therefore represents a natural attenuation process that may prevent cesium migration to groundwater and that should be quantified as a basis for the "leave-it-in-place" remediation scenario.

   Several experiments have been performed to evaluate Cs^+ fixation, and one is shown here. In that experiment, $^{137}Cs^+$ (at 10^{-4} mol/L representative of HLW supernatant) was adsorbed to Hanford sediment in two different salt solutions (0.005 and 5 mol/L), and these were allowed to age for periods ranging from 0.5 to 120 days. After the aging period, the salt solutions with residual unadsorbed Cs^+ were removed and replaced with K^+-containing electrolyte. The K^+ was present at a concentration (10^{-2} mol/L) that was 100 times the total Cs^+ concentration. Cesium

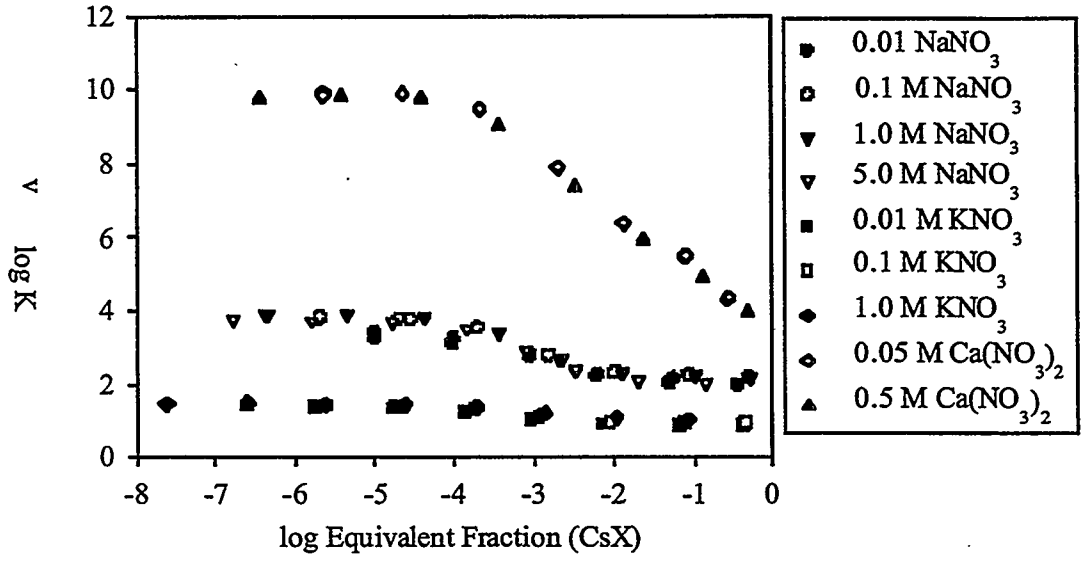

Figure 1. Dependence of the Conditional Thermodynamic Equilibrium Constant on Surface Saturation (CsX) and Electrolyte Concentration

concentrations in the aqueous phase were then followed for extensive time periods to assess the extent to which K^+ induced Cs^+ desorption from the sediment (Figure 2a,b). Cesium that is not desorbable by 100 times molar in excess of K^+ is effectively fixed. The Y-axis in Figure 2 defines the normalized concentration, C/C_0, where C is the concentration at any time (t), and C_0 is the initial soil-bound concentration after the adsorption/aging period. Most importantly, the initial adsorbed concentration in 5 mol/L salt (3.7×10^{-7} mol/g) was 38 times lower than that in 0.005 mol/L salt (1.4×10^{-5} mol/L) as a result of the mass action effect of Na^+.

The desorption behavior of Cs^+ was similar in the two different salt solutions. That is, a significant fraction of the adsorbed Cs was immediately released upon K^+ addition. After this initial desorption episode, which was presumed to be an ion-exchange displacement, little additional Cs^+ was released by the sediment. There was slight tendency for the shorter-aged samples to release more Cs^+, but a distinct correlation with aging time was not observed. In spite of the noted similarity, there was a major difference in the fractional extent of Cs^+ desorption in the two salt solutions (Figure 2a,b). In 5 mol/L Na^+, approximately 55% of the adsorbed Cs^+ was desorbable, while 85%, on average, was released in 0.005 mol/L Na. However, because significantly more Cs^+ was adsorbed in 0.005 mol/L Na^+, a larger Cs^+ concentration was actually fixed at low salt than at high salt, e.g., 2.10×10^{-6} mol/g compared with 1.66×10^{-7} mol/g. These results support two important conclusions: 1) Cs^+ fixation occurs on only a subset of the high-affinity exchange sites and 2) Na^+ competes with Cs^+ for access to fixation sites. This latter conclusion was unexpected given the significant differences in ionic radius and hydration energy of Na^+ and Cs^+. The fixation process is presumed to involve highly selective exchange followed by the dehydration and interlamellar migration of the Cs^+ ion.

3. *Cesium-Distribution in Hanford Micas.* The differential abilities of micaceous minerals in Hanford sediments to immobilize cesium and the variable binding of cesium to disparate reactive sites on mica plates are under investigation using wet-chemical experimentation and compositional imaging. Flakes of three micaceous minerals (biotite, muscovite, and vermiculite) were identified in Hanford sediments using a binocular microscope. They were carefully hand-picked and segregated for experimentation. Each mica reacted separately with cesium by suspension in solution concentrations of 10^{-2} to 10^{-4} M Cs for periods of one and three months. The reacted micas were washed and air dried, then mounted as whole flakes or sectioned to expose external and internal surfaces. Micas were hypothesized to preferentially sorb Cs at relatively high-energy frayed-edge sites and to strongly bind Cs by displacement of K at internal sites accessed by diffusion along crystallographic cleavage planes.

   The distribution of cesium was investigated using the electron (EMP) and x-ray (XMP) microprobes. In biotite, cesium was preferentially sorbed at the edges of broken platelets (Figure 3a). This result supported the hypothesis that cesium is more strongly bound at edge sites but did not address the (frayed or unfrayed) nature of those sites. Examination of sectioned biotite (Figure 3b) also supported the hypothesis that internal sites can sequester cesium from solution.

   Data from these studies are near the detection limit for the EMP method (note the granularity in the cesium image below). We are using the x-ray microprobe technique (at the Argonne National Laboratory [ANL] synchrotron light source; see Figure 3b) to produce data with a higher compositional resolution to more fully evaluate our hypotheses; preliminary data from this method are at relatively low optical resolution but show promise for detection of cesium with 100 times the sensitivity of EMP methods.

   Investigations of different micaceous minerals suggest that muscovite and vermiculite do not sorb cesium as strongly as biotite. Data to date are preliminary; these results have not been confirmed.

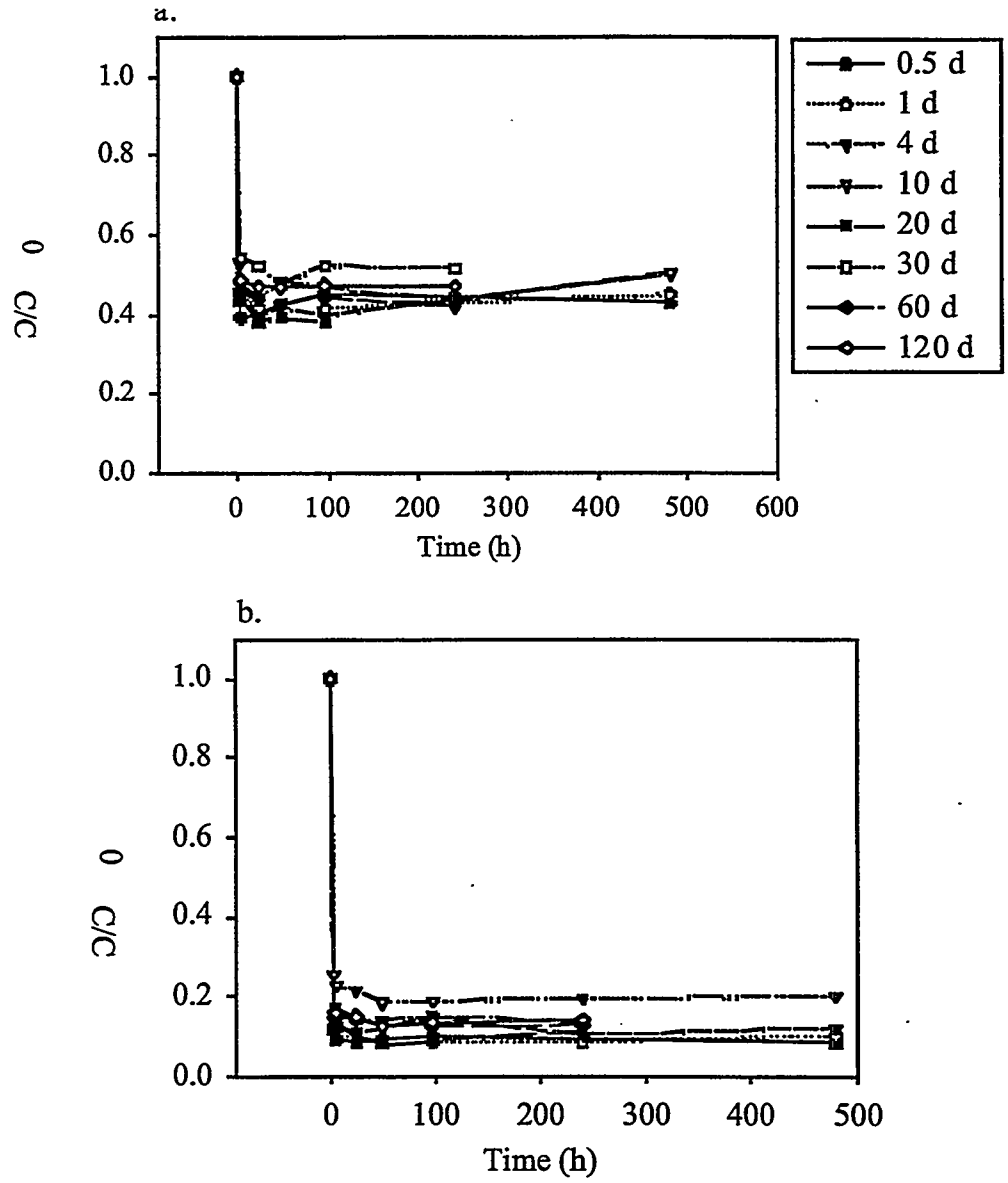

Figure 2. Desorption of Cs^+ from Hanford Sediment by 10^{-2} mol/L K^+ after Aging from 0.5 to 120 days a) Cs^+ contact and aging in 5.0 mol/L NaCl; and b) Cs^+ contact and aging in 0.005 mol/L NaCl. Initial Cs^+ contact solution was 10^{-4} mol/L Cs^+. C/C_0 is the normalized adsorbed concentration, e.g., the adsorbed concentration at time t (c) divided by the initial adsorbed concentration at the start of desorption.

4. *Identification of Cesium-Sequestering Minerals in Contaminated Hanford Sediments.* Contaminated sediments from Hanford core 41-09-39 collected beneath Hanford Site storage Tank SX-109 were examined to determine the relative abilities of different in situ minerals to bind and sequester cesium from leaked wastes. It is unlikely, given the physicochemical differences among these minerals, that cesium would be found to be evenly distributed across the different mineral species.

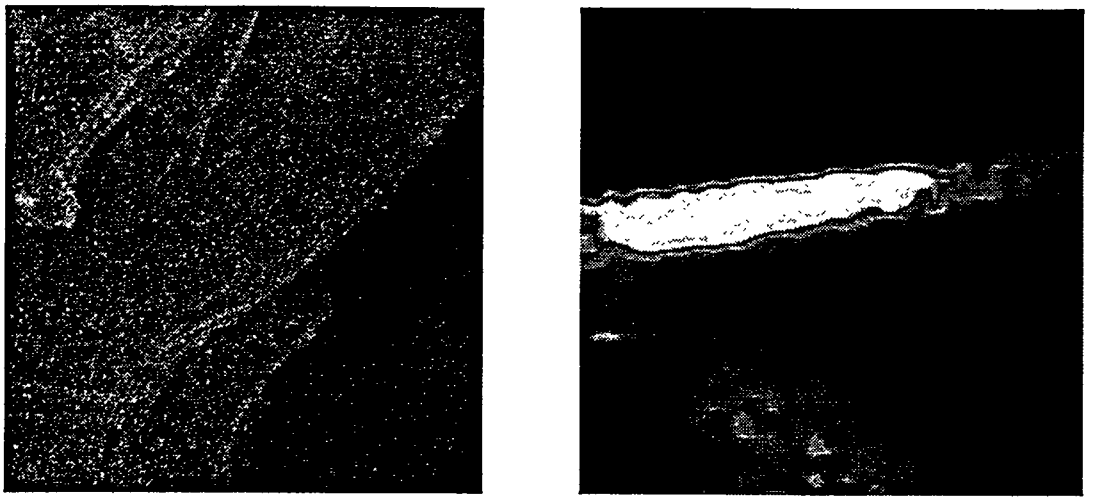

Figure 3. Adsorbed Cs^+ Distribution Maps for Hanford Site Biotite Exposed to a Solution of 10^{-2} M Cs for Three Months. The left image is by EMP analysis of a plan-view specimen (200 μm across) and the right is by x-ray microprobe of a thin section (100 μm across). White intensity is proportional to Cs^+ concentration. Cs^+ is preferentially bound at platelet edges in plan-view (left image) and within internal, structural channels (right image).

Sediment samples from several (closely spaced) depths beneath a leaked tank were assayed for cesium contamination using bulk chemical techniques. These sediments were then wet-sieved and size-segregated for further study.

We wanted to optically identify mineral components of each size fraction and instrumentally determine the chemical association of cesium with dissimilar grains. Mineral grains from each size fraction were dispersed in a binding agent on glass slides. Optical examination showed some mineralogic differences between size fractions, but in general the sediments consisted of primary silicate mineral grains, including abundant feldspars and micaceous minerals, along with secondary or detrital Fe oxides and clay minerals. After optical examination and preliminary mineral identification, mineral grain mounts were placed in a phosphorescence detector and incubated overnight. The detector stores gamma radiation chemically on a phosphor screen, allowing the detection and comparative quantitation of radiation from materials having relatively low activity. Exposure and digitization of phosphorescent images yielded radiation maps (autoradiographs) of dispersed particles, showing the relative abundance of cesium on mineral grains (Figure 4).

The comparison of mineral dispersions with radiation intensity maps allowed the identification of individual mineral grains having either "cesium positive" or "cesium negative" characteristics. New preparations were made from these mounts, in which 20 positive and 20 negative grains remounted in physically separate clusters. The positive and negative properties of the segregated grains were confirmed by repeating the radiation imaging step. This step allowed the direct determination of mineral phase identity for individual particles.

Mineral identities, primarily for positive grains but also for a minority of negative grains, were established using transmission electron microscopy (TEM) methods. Compositional information (collected using energy-dispersive x-ray spectroscopy) was collected in the microscope and combined with electron diffraction patterns captured on film. The combined data were used to search the JCPDS x-ray powder diffraction library for mineral identification (x-ray diffraction patterns are synthesized from electron diffraction data). Preliminary results indicated that

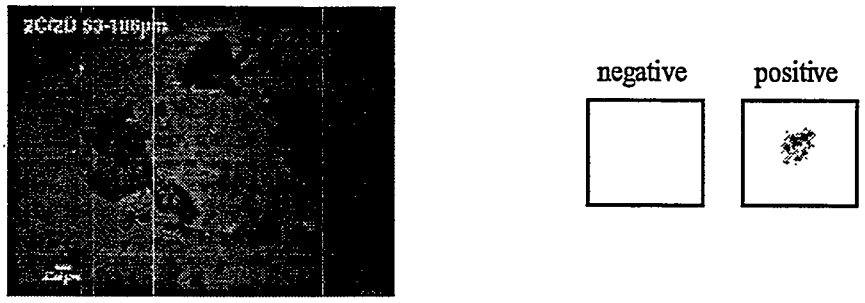

Figure 4. Optical Image of Segregated Mineral Grains (left), with Final Autoradiographic Image (right) of Segregated Positive and Negative Particles. The darkness of autoradiographic spots indicates the radiation intensity; the clear area in the autoradiograph corresponds to grains that were negative for radiation. Clear, negative silicate grains are apparent in the optical image, as are positive phyllosilicate aggregates.

cesium was not significantly bound to iron oxides and non-phyllosilicates in these sediments. Cesium was preferentially bound by smectites and micas. These results have not been confirmed and require additional experimentation to complete.

Implications to Site Restoration

Our proximity to Hanford has allowed us to share our results with site remediation contractors that are developing closure plans for the Hanford tank farms, where massive subsurface ^{137}Cs contamination exists. This information exchange has occurred through Hanford's Groundwater-Vadose Zone Integration Project. We have shown that cesium migration depth is strongly controlled by Na^+ concentration over its entire concentration range to saturation with $NaNO_3$. These observations and comparable ones with K^+ and Ca^{2+} electrolytes provide the basis for an improved mass-action model of cesium exchange-adsorption with Hanford sediments. Our desorption results from high sodium imply that a significant fraction of the sediment-bound cesium becomes rapidly fixed and is not available for further migration. Further analysis of the desorption results and the performance of selected other experiments should allow firm guidance on whether in-ground cesium beneath the tanks can be left in place without environmental controls.

Planned Activities

The remainder of FY 1999 activities will focus on the impacts of high-base, variable temperature-induced mineral dissolution on Cs^+ sorption in Hanford sediments and isolated mica fractions. We will identify whether the selectivity of the mica fraction for Cs^+ is changed by molar concentrations of hydroxide and whether changes result from competitive ion effects (e.g., K^+ release by dissolution) or structural destabilization of the FES. The latter issue will be resolved by application of scanning-probe microscopy and high-resolution TEM. In FY 2000, similar studies will be performed using high-base waste stimulants containing $Al(OH)_4^-$ at concentrations that mimic those in the SSTs. At issue is whether $Al(OH)_4^-$ precipitation that follows base neutralization will cause marked changes to Cs^+ sorption selectivity, kinetics, and reversibility. Important questions to be resolved include the nature of the precipitated Al-phase and whether it causes hydroxy pillaring and alteration of the structural environment of the FES. A combination of microscopy, solution-phase thermodynamic measurements, and chemical modeling will be employed to interpret results and resolve hypotheses.

Publications

McKinley JP, RJ Serne, and JM Zachara. 1999. "Mineral phase association of Cs^+ in subsurface sediments contaminated with high-level nuclear waste." *Environmental Science and Technology* (submitted).

McKinley JP, JM Zachara, and PL Gassman. 1999. "Cs^+ distribution in natural micas: an electron and synchrotron x-ray microprobe study." *Clays and Clay Minerals* (in preparation).

Zachara JM, SC Smith, RJ Serne, and PL Gassman. 1999. "Highly selective Cs^+ adsorption by subsurface sediments from the Hanford Site, U.S.A." *Clays and Clay Minerals* (submitted).

Presentations

Zachara JM. August 1999. "New advances in the understanding of ^{137}Cs interactions with micas and implications to Cs geochemistry in the Hanford vadose zone." Keynote address given to the EMSP National Program Workshop, Chicago.

Rapid Migration of Radionuclides Leaked from High-Level Waste Tanks: A Study of Salinity Gradients, Wetted Path Geometry and Water Vapor Transport

(First Year of Funding: FY 1998)

Principal Investigators

Dr. Anderson L. Ward (Lead)
Pacific Northwest National Laboratory
P.O. 999, MSIN K9-33
Richland, WA 99352
(360) 574-5874 (phone)
(360) 571-5874 (fax)
andy.ward@pnl.gov

Dr. Glendon Gee
Pacific Northwest National Laboratory
P.O. 999, MSIN K9-33
Richland, WA 99352
(360) 574-5874 (phone)
(360) 571-5874 (fax)
glendon.gee@pnl.gov

Dr. John Selker
Department of Bioresource Engineering
Oregon State University
Corvallis, OR 97331-3906
(541) 737-6304 (phone)
(541) 737-2082 (fax)
selkerj@engr.orst.edu

Dr. Scott Tyler
Desert Research Institute
755 E. Flamingo Rd.
Las Vegas, NV 89119-7363
(775) 673-7391 (phone)
(775) 673-7363 (fax)
scott@dri.edu

Research Objective

The primary objective of this project is to develop a basic understanding of the fate and transport of caustic radioactive brines through the vadose zone. Research is focused primarily on migration of high-level waste leaked from single-shell tanks under environmental conditions, and over temporal and spatial scales relevant to the Hanford Site. Understanding the fate and transport of these wastes through the vadose zone is critical to the development of a framework for evaluating different waste retrieval/ remediation strategies and the associated health risks. The hypothesis underlying this project is that elevated surface tension of the leaked tank wastes will strongly inhibit lateral contaminant spreading, giving rise to narrow fingers of infiltration through the vadose zone. The extent and persistence of these fingers will be enhanced by the water migrating into the saline zone in response to the osmotic potential gradient. To validate this hypothesis, this project combines a series of laboratory, field, and numerical experiments with the following specific objectives:

1. investigate the effect of elevated surface tension of highly saline fluids on wetting front instability, finger formation, and contaminant mobility

2. investigate the conditions under which osmotically driven vapor flux is operative and quantify its impact on plume transport

3. develop and incorporate a theory describing these processes into an existing DOE-developed, numerical simulator to allow prediction of contaminant migration at realistic spatial and temporal scales.

Problem Statement

Previous attempts to predict field-scale contaminant transport through the vadose zone have often neglected driving forces and mechanisms that can lead to non-uniform flow. Nonuniform flow has been shown capable of producing erratic transport patterns and can cause contaminants to bypass much of the unsaturated soil matrix. These processes not only lead to fast transport of contaminants to underlying groundwater, but the resulting lack of interchange between the main soil matrix and the fast pathways reduces the potential for natural attenuation.

Two mechanisms that could strongly influence flow non-uniformity and speed the movement of tank wastes in the vadose zone are 1) wetting front instability, due to the high interfacial energy of the saline waste and 2) osmotically driven vapor fluxes, due to the high ionic strength of the waste. Although wetting front instability has been studied extensively in the laboratory, little is known about the formation and persistence of gravity-driven fingers under hydro-geological conditions characteristic of tank farms. The contribution of gravity-driven unstable flow to vadose zone transport could also be enhanced by the migration of water vapor from the surrounding soil into the saline plume. Studies of osmotically driven vapor flux, which have been mostly limited to agricultural fertilizers, suggest that this mechanism can significantly increase the resident water content of the saline soil zone. This mechanism, when coupled with formation of gravity-driven fingers, has the potential to significantly increase contaminant migration rates through the vadose zone. Our strategy is to combine innovative laboratory, field, and numerical experiments to identify the conditions under which these mechanisms are active and to quantify the impact of vadose zone transport processes. The product will be a tool that DOE can use to perform more realistic analyses to predict fate and transport of vadose zone contaminants, evaluate different tank waste retrieval strategies and their impact on the vadose zone, and assess the associated health risks.

Research Progress

This project combines a theoretical, experimental, and numerical approach to developing an understanding of the driving forces and complex mechanisms affecting the migration of caustic, radioactive brines through the vadose zone. The project is divided into three main components: 1) controlled laboratory experiments, 2) controlled field experiments in the 200 Area of the Hanford Site, and 3) numerical modeling studies. Controlled laboratory experiments are being conducted at the Desert Research Institute, Pacific Northwest National Laboratory (PNNL), and Oregon State University (OSU). The numerical component is being performed at PNNL, and the controlled field experiments are being conducted at the Hanford Site. Although the project has been in operation for only six months, progress has been made in each of these areas and is summarized in the following sections.

Controlled Laboratory Experiments

Traditional approaches to interpreting and predicting contaminant transport distributions generally assume ideal properties for water and the water-solid-air interfaces. However, the solute concentrations found in Hanford tank wastes may invalidate this simplification. Density- and osmotically driven flows studied in this project must be coupled with measured fluid and porous media properties. To accommodate this data need, a detailed laboratory analysis of fluid-soil interactions is being conducted to determine the effect of concentration of salt in the imbibing solution, surface tension of imbibing and resident fluids, osmotic potential of imbibing fluid, soil texture, and antecedent moisture content.

Laboratory Analysis of Fluid Transport Properties

To date, work has focused on the design of fluids to mimic the ionic strengths and surface tensions of the Hanford tank fluids. These fluids are to be used in the field experiment phase of the research and will be used in the laboratory on a smaller scale. A review of the literature on these physical properties and the properties of the Hanford tank fluids has been completed to choose appropriate field and laboratory fluids for testing. Increases in surface tension above that of pure water are easily obtained using common salts such as NaCl, $NaNO_3$, and $MgCl_2$. In each of these cases, surface tension may be extended to 10–30% over pure water. In addition, at concentrations required for surface tension augmentation, the fluid ionic strengths and water activity are sufficient to induce steep osmotic gradients between the fluid and vapor phases present in soil water.

To achieve much higher surface tensions than those above, it was determined that adding NaOH would be most appropriate. While such compounds are present in many of the Hanford tank fluids, their chemical and safety attributes are less than desirable. This is especially true for the field setting. The strong base developed with an NaOH solution may be highly reactive in the soils found at Hanford; in particular, reaction of basalt-derived sediments and the fluid phase will result in the release of large volumes of silica. As fluids infiltrate deeper into the profile, the solution pH will decline due to these reactions and silica is likely to then precipitate into the pore spaces, perhaps as amorphous silica. The resulting changes in soil porosity and permeability due to silica translocation could be extreme. Such reactions would significantly confound the objectives of both the field and laboratory analysis of the processes called out in our objectives.

We have concluded that for the field experimental portion, a concentrated $NaNO_3$ solution will be used as the permeant ($\sigma = 87.05$ at 47% by weight). The field experiments will mimic the infiltration of high surface tension, low water activity solutions into typical Hanford sediments with relatively pure

water forming the antecedent moisture. Significant degradation reactions are unlikely to occur in the subsurface at the concentrations to be used. In addition, microbial uptake of the NO_3 is unlikely, again due to the high ionic strength of the solution.

In the laboratory, we have developed two procedures. We will conduct water retention and imbibition experiments using Hanford sediments and $NaNO_3$ solutions to confirm behavior in the field. These experiments will look at the effects of surface tension and high ionic strength on water retention and conductivity. To assess the effects of surface tension only on wetting front instability, we have developed an alternative to the concepts of significantly raising the surface tension of the imbibing fluid. We will produce the same net effect, i.e., imbibition of high surface tension fluid into low surface tension fluid, by first wetting the soil samples with a solution of water and 1-butanol, which can dramatically lower the surface tension at very low concentrations (Smith and Gillham 1999). Pure water will then be used as the imbibing fluid. In this manner, we can study the effects of high surface-tension imbibition (pure water) into low surface-tension antecedent moisture (1-butanol). The processes will be identical to those found with Hanford fluids but will be free of geochemical and osmotic effects. Soil core samplers have been prepared for the field to obtain intact core samples at the field site for laboratory analysis. Construction of a surface tension measurement system (Sugden 1922, Maximum Bubble Pressure Method) is under way.

Flow and Transport in Miller Similar Sands

Work at OSU's Flow Visualization Laboratory involves the use of light transmission chambers and digital camera systems to study the migration of dense fluids through well-characterized Miller similar porous sands. This technique provides a powerful system for exploring the effects of the large number of variables that can influence transport behavior.

The project required a post-doctoral fellow to conduct the laboratory and field experiments. Following immediately upon receipt of the grant, advertisements were written for a post-doc with a closing date of December 31, 1998. A short list was developed on January 31, 1999, and full applications and references were received in February. Dr. Noam Weisbrod was selected in March and will begin work on the project on June 1, 1999.

In the interim, tests were conducted with Hanford sediments on light transmission systems. The Hanford sands, being basaltic in nature, are black and have proven not to be amenable to the conventional light transmission method. Over the past months, a variety of techniques have been tried for enhancing the visualization system. It is now apparent that the nature of the Hanford sediments may prove to be a limitation in the use of this technology. This problem will be overcome using blended quartz sands as surrogates to the site sands. These sands have already been painstakingly characterized for hydraulic and chemical properties at OSU. The comparison of flow behavior in the various textural blends will allow discrimination of the controlling flow processes through hydrodynamic scaling and will allow for ready interpretation of results.

Flow and Transport in Hanford Sediments

This main purpose of this component of the project is to obtain a data set from real Hanford soils to complement those obtained from the Miller similar sands. It is unclear to what extent wetted path geometry is influenced by minor soil morphological heterogeneity and how the combined effects of osmotically driven vapor flux will affect transport in real systems. Thus, this task will also seek to measure and compare the effects of the salt concentration, osmotic potential, and surface tension of the infiltrating fluid.

Early tests at the OSU Flow Visualization Laboratory show that the opacity of the Hanford sediments disqualifies the use of light-based flow visualization techniques. Furthermore, this technique is not applicable to the coarser gravel-dominated series of the Hanford Formation (discussed below). Over the past few months, a series of experiments has been conducted with the goal of adapting existing techniques for monitoring controlled flow and transport in these soils at scales relevant to the understanding of finger formation and persistence.

One technique that shows promise is x-ray computed tomography (XRCT), on which testing was initiated in early 1999 at PNNL. In the tests, four columns (15 cm long x 3.8 cm) were packed with soil. One-half of the columns were packed at air-dry moisture content while the other half was packed 10% by volume of water. Each column received a 5-mL application of saturated NaI solution (1.4 g L^{-1}), to simulate a dense saline fluid, and was monitored over time by XRCT to evaluate its efficacy for monitoring flow in opaque soils and identifying the conditions under which gravity-driven flow instability occurred.

Figure 1 shows an example of a transverse 2-dimensional image from the opaque basaltic sand. The volume displayed is representative of the attenuation values in gray scale. These attenuation values, corresponding to the density within the volume, display rocks or dense material as white and air as black. Not only is the pore space, consisting of various channels and voids, clearly seen in these images, but the plume of NaI is also quite clear. Finger formation is clearly seen in Figure 1a, while the solute front is somewhat more diffused in the wet soil (Figure 1b). Finger formation and persistence in the wetter soil may have been overcome by the heterogeneities caused by packing.

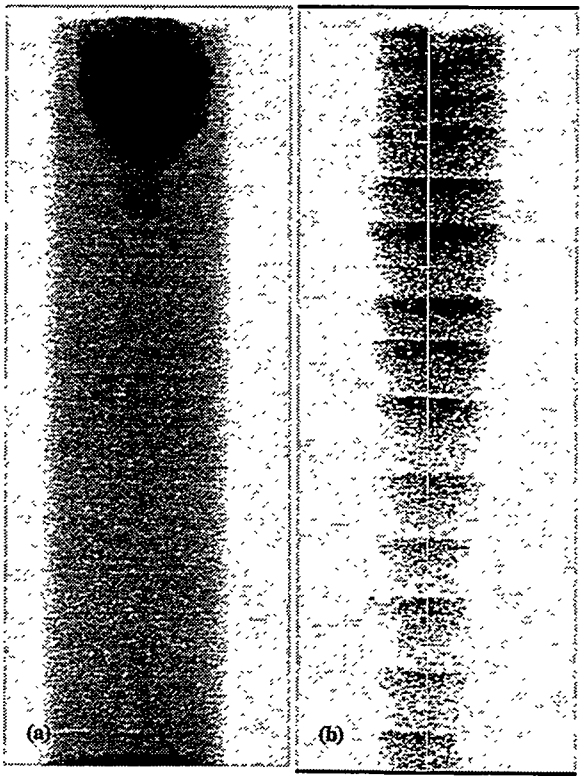

Figure 1. Sagittal CT Image Displaying Pore Space and Distribution of a Dense NaI Plume After 24 Hours of Redistribution (a) initially air-dry soil, (b) soil wet to a water content of 0.10 m^3 m^{-3}

Figure 2 shows cross-sectional views of the same two columns at about 4 cm from the surface. In Figure 2a, a compact, well-defined outline of the NaI plume is clearly seen as a denser (white) zone. In the wetter soil, the solute front spread laterally along the stratification, essentially wetting most of the pore space, hence the more widely distributed, high-density zones (Figure 2b).

These images clearly show that the XRCT technique has potential for monitoring finger formation and persistence in opaque soils. These micro-lysimeter studies are being used to provide information on the initiation and persistence of fingers over a range of conditions. A major advantage of the XRCT system is that the transverse images can be assembled and rendered as 3-dimensional images from which the multidimensional features of fingers can be studied. Thus far, studies of fingers have been limited to thin, 2-dimensional columns that can be monitored using light-based transmission techniques. The results of these experiments will be used as a basis to design an intermediate scale (2 m x 1 m flow cell) laboratory experiment in which fingering phenomena will be monitored, including a fully automated dual-energy gamma radiation system and time-domain reflectometry (TDR) systems.

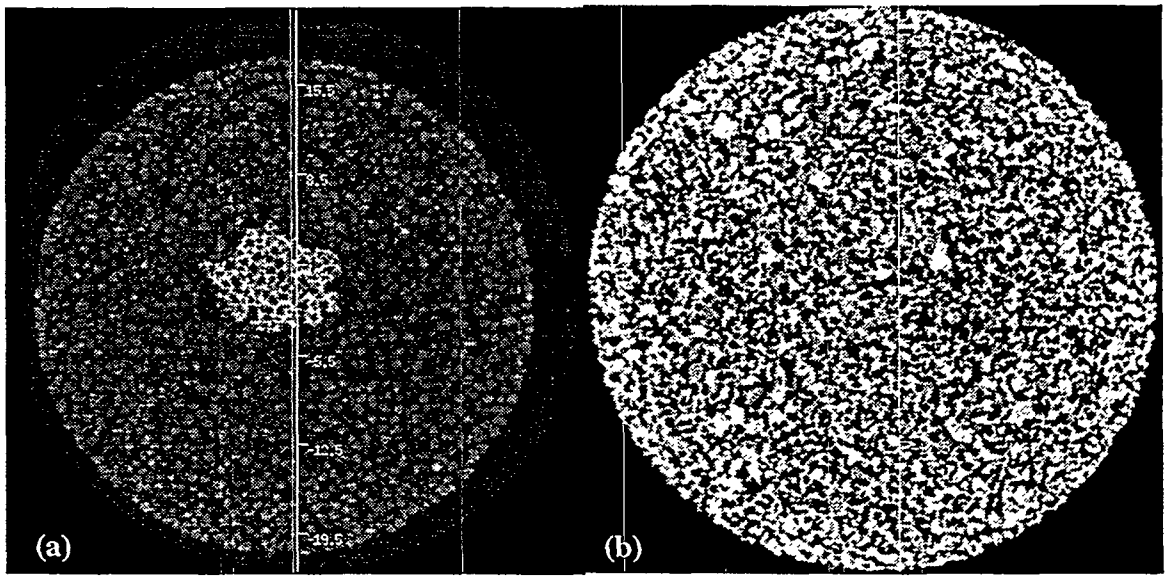

Figure 2. Transverse XRCT Image Displaying Pore Space and Distribution of a Dense NaI Plume After 24 Hours of Redistribution (a) the compact finger is maintained in the initially air-dry soil, (b) finger is dispersed due to layering in soil initially wet to a water content of 0.10 m^3 m^{-3}

Field Experiments

The field experiments are intended to explore saline plume transport at two time scales, a reflection of the different time scales at which initial imbibition and vapor migration processes proceed. The objectives of the field component of this project are to

1. identify the degree to which field conditions mimic the flow processes observed in the laboratory

2. provide a validation data set to establish the degree to which our conceptual models, embodied in a numerical simulator, explain the observed field behavior.

We toured the Hanford Site in the fall of 1998 to investigate possible field sites. Based on the findings of the tour and subsequent discussions, planning and preparation for field activities were started. Two sites were selected to represent the extreme in porous media properties representative of the Hanford tank farms and the paperwork started to obtain the necessary permits. The permits were obtained in May 1999, and instrumentation has commenced.

Most of the tanks at Hanford were placed in the upper Hanford formation, and much of the site outside of the tank farms is covered with a 1–2-m layer of Holocene eolian deposits. Therefore, before the field experiments are conducted, the top 1–2-m of deposits had to be removed to expose the Hanford formation. The first site is located near the 200 West Area of the Hanford Site and is representative of the gravel-dominated Hanford formation (Figure 3a), the unit in which most of the waste resides.

The second site is located in the 200 East Area and is representative of the sand-dominated Hanford formation (Figure 3b). Both sites have been excavated in preparation for instrumentation and the conduct the characterization and long-term plume migration studies.

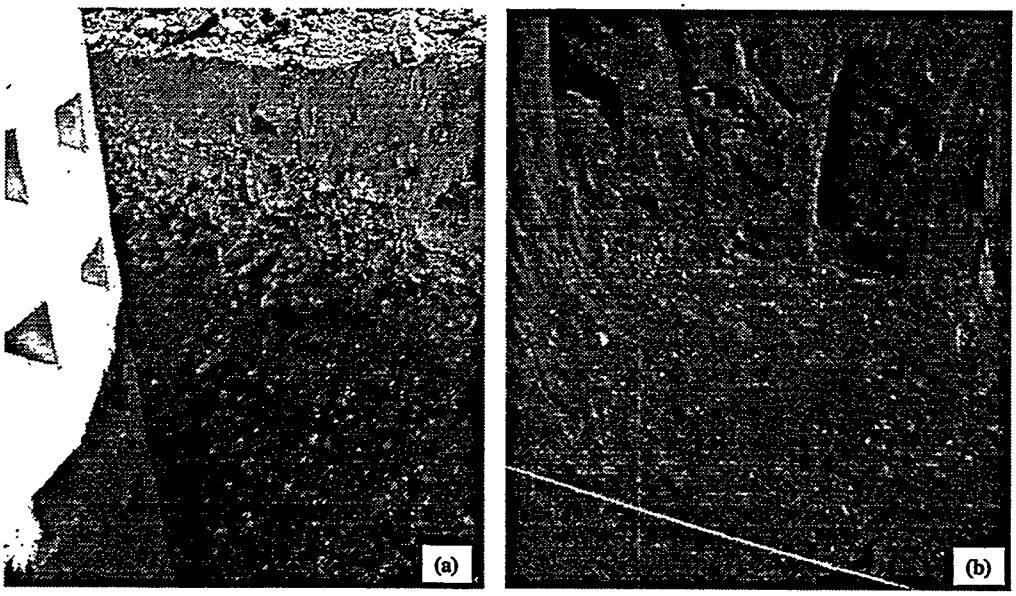

Figure 3. Photograph of (a) Typical Soil Profile in the Upper Hanford Formation at the 200 West Area Site and (b) the Sand-Dominated Site in the 200 East Area

The field experiment requires a 48 probe, multiplexed five-level TDR system. The entire system is designed to be fully automated with remote download capacity via cellular phone. The system will document the movement of water and salt along the flow paths of six separate plumes on a twice-daily basis. All system components have been acquired and the system is largely assembled (Figure 4a). The system is to be installed in the field in early June 1999. Each probe has been calibrated before installation (Figure 4b shows the method outside of calibration fixture).

Numerical Studies

Numerical modeling of gravity-driven flow instabilities using a continuum approach has only recently been successful through adjustment of the upstream weighting coefficient of permeability in a finite element model (Nieber 1996). It has also been suggested that the mechanism for the initial formation of

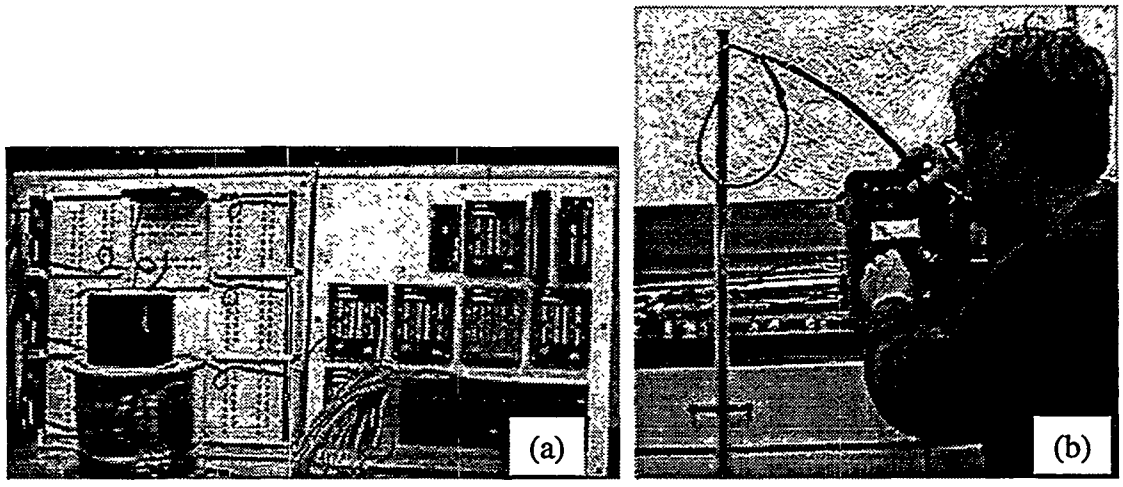

Figure 4. Photograph of Moisture Monitoring System for the Field Experiment. Each probe has been calibrated before installation (a) assembly of system, (b) system outside of calibration fixture

flow instabilities and their persistence is best described in terms of the water retention $\psi(\theta)$ and hydraulic conductivity $K(\theta)$ relations for the given soil. Although the nature of the problem means that the solutions to the flow and transport equations may possess highly localized properties in both space and time, application of these techniques has been limited to relatively small domains ($\leq$2 m x 2 m) with uniform 2-dimensional grids.

It has become increasingly clear that multigrid methods represent the most efficient approach for iteratively solving the large system of algebraic equations that arise from large-scale numerical simulations modeled by partial differential equations (Bramble et al. 1996). To scale the highly localized behavior of fine-scale fingering generated by heterogeneous porous media or flow instabilities up to computational and field scales, work has started on techniques for obtaining effective parameters for coarse-grid models that are consistent with fine-grid simulations. Over the past months, work has been ongoing to modify the multidimensional Subsurface Transport Over Multiple Phases (STOMP) computer software program to incorporate an adaptive mesh refinement. The approach is to use adaptive mesh refinement to cluster grid points in regions where they are most needed, e.g., around a developing flow instability or other regions where the solution has steep gradients. This strategy is being developed for both temporal and spatial refinements on Cartesian grids and will ultimately take advantage of the vectorization of the STOMP simulator.

The time-stepping scheme is an integral part of the adaptive gridding solution technique; the first step was to implement a second-order, two-step implicit backward differentiation formula (BDF) method for solving the differential-algebraic equations into STOMP. A series of tests to compare the default Euler scheme in STOMP with the new BDF scheme has been successful. In a test involving a one-dimensional infiltration problem, the Euler scheme executed the problem in 65 time steps with one convergence failure, while the BDF scheme executed the same problem in 49 time steps with no convergence failures and produced essentially the same results. Schemes to allow description of a variable upstream weighting parameter and definition of the hysteretic water retention and hydraulic conductivity models, critical to modeling flow instability, have also been implemented.

Planned Activities

During the next year, work will continue at the Desert Research Institute to obtain water retention and unsaturated hydraulic conductivity measurements on samples recovered from the field beginning in the summer of 1999. Pure water, $NaNO_3$, and 1-butanol solutions will be used. Following completion of this characterization, imbibition experiments will be conducted using both pure water imbibing into pure water (as a control) and 1-butanol imbibing into pure water. It is anticipated that these experiments will begin at the end of summer 1999 and will be completed by winter 1999-2000.

Work at the OSU Flow Visualization Laboratory will continue to study the effects of heterogeneity of finger formation and persistence using simple horizontally layered systems of pairs of Miller similar sands. These experiments will attempt to determine the ability of the surface tension effects to overcome the attenuating effect on fingered flow observed in naturally occurring layered systems. These tests are expected to start in July 1999.

In the PNNL-controlled laboratory studies, work will proceed on calibration of the XRCT system to permit conversation of attenuation values into soil water content/solute concentration. We will further investigate the conditions that lead to finger formation and the characteristics that influence persistence during wetting and drying cycles. The medium-scale flow experiment will begin in late summer 1999.

Starting in June 1999, and before the field-scale experiments at the two sites begin, detailed hydraulic and stratigraphic analysis will be performed. Based on these analyses, experimental design parameters (e.g., water application rates, sensor location, sampling frequency) will be developed using predictive models. Site instrumentation should be completed by the end of July 1999, after which the long-term plume migration studies should begin. Following the long-term plume migration experiments, the plots will be excavated to further investigate the tracer transport as well as to characterize the hydraulic properties directly beneath the field site.

Theoretical analysis and model simulations of pure water entering initially dry soils show that finger formation results from hysteresis in the water retention function and that the characteristics of the finger depends on the shape of the main imbibition and drainage branches. During the next year, work will continue to incorporate the effects of surface tension inferred from the laboratory water retention and unsaturated hydraulic conductivity measurements using tank waste simulants. Work will also continue toward the implementation of the adaptive mesh refinement strategy. Numerical experiments will continue with the goal of elucidating the regime that leads to the onset of fingering and to determine how finger characteristics are influenced by vapor flux in response to osmotic potential gradients.

References

Bramble JH, RE Ewing, JE Pasciak, and J Shen. 1996. "The analysis of multigrid algorithms for cell centered finite difference methods." *Advances in Computational Mathematics* 5(1):15-19.

Nieber JL. 1996. "Modeling finger development and persistence in initially dry porous media." *Geoderma* 70:207-229.

Smith J, and RW Gillham. 1999. "Effects of solute concentration-dependent surface tension on unsaturated flow: Laboratory sand column experiments." *Water Resources Research* 35(4):973-982.

Sugden J. 1922. *Journal of the American Chemical Society* 121:858.

Presentations

Selker JS. December 5-10, 1998. "Fingered flow from high salinity sources." Presented at the AGU Fall Meetings, San Francisco.

Ward AL and GW Gee. October 31-November 4 1999. "A Numerical Analysis of Wetting Front Instability Induced by Infiltration of Highly Saline Fluids." Symposium on Preferential Flow, Soil Science Society of America Annual Meeting, Salt Lake City.

Health Effects

Mechanisms Involved in Trichloroethylene-Induced Liver Cancer: Importance to Environmental Cleanup

(First Year of Funding: 1996)

Principal Investigator

Richard J. Bull, Ph.D.
Pacific Northwest National Laboratory
P.O. Box 999, MSIN P7-56
Richland, WA 99352
(509) 373-6218 (phone)
Dick.bull@pnl.gov

Co-Principal Investigator

Brian D. Thrall
Pacific Northwest National Laboratory
P.O. Box 999, MSIN P7-56
Richland, WA 99352
(509) 376-3809 (phone)
Brian.thrall@pnl.gov

Contributors

Lyle B. Sasser (Lyle.sasser@pnl.gov)
John H. Miller (John.h.miller@pnl.gov)
Irvin R. Schultz (Irvin.schultz@pnl.gov)

Research Objectives

The objective of this project is to develop critical data for improving risk-based cleanup standards for trichloroethylene (TCE).

Importance to DOE. Cleanup costs for chlorinated solvents found on DOE sites are most frequently driven by TCE because it is the most widespread contaminant and is generally present at the highest concentrations. Data that would permit increases in risk-based standards for TCE would reduce complex-wide cleanup costs by hundreds of millions of dollars.

Current Regulatory Actions that Research will Impact. EPA is currently reviewing its risk assessment for TCE. Richard J. Bull has worked with EPA on this review by writing the mode of action section of their determination. A presentation by James Cogliano of EPA at the 1999 Annual Society of Toxicology Meeting indicates that they have accepted the concept of nonlinear extrapolation for liver tumor induction by TCE. This project will end in FY 1999 with its major technical and policy objectives satisfied.

Problem Statement

One impetus for this research was data that indicated that TCE induced a shift in the mutation spectra observed in the H-ras codon 61 in mouse liver tumors. Such effects have been generally interpreted as indicating that the chemical is acting as a mutagen. As the project progressed, additional data were published that indicated that one metabolite of TCE, dichloroacetate (DCA), has mutagenic activity in vivo (Leavitt et al. 1997). Adaptations were made in the experimental design to address the importance of these effects to the induction of liver tumors by DCA. The results of this project argue strongly that selection (or promotion) is more likely responsible for these observations than are DCA-induced mutagenic effects.

The project is organized around two interrelated tasks:

Task 1 addresses the tumorigenic and dosimetry issues for the metabolites of TCE that produce liver cancer in mice, DCA, and trichloroacetate (TCA). Early work had suggested that TCA was primarily responsible for TCE-induced liver tumors, but several more mechanistic observations suggest that DCA may play a prominent role. This task is aimed at determining the basis for the selection hypothesis and seeks to prove that this mode of action is responsible for TCE-induced tumors. This project will supply the basic dose-response data from which low-dose extrapolations would be made.

Task 2 seeks specific evidence that TCA and DCA are capable of promoting the growth of spontaneously initiated cells from mouse liver in vitro. The data provide the clearest evidence that both metabolites act by a mechanism of selection rather than mutation. These data are necessary to select between linear (i.e., no threshold) and nonlinear low-dose extrapolation models.

Research Progress

Task 1 - Tumorigenesis Studies. Biologically based models for assessing health risk from TCE exposure requires that the metabolites responsible be known and the likely mode of action by which they act identified. Classically, TCA was considered the active metabolite in inducing liver cancer with TCE. However, a less abundant metabolite, DCA, received considerable focus in the past five years because the incidence and spectra of H-ras mutations are similar in tumors induced by DCA and TCE (Anna et al. 1994). Data on TCA were too sparse at the time to make a judgment.

We have now sequenced codon 61 of the H-ras protooncogene in a total of 30 TCA-induced and 64 DCA-induced liver tumors. In the past year, we sacrificed 47 mice that had been treated with 1 g/kg TCE in an aqueous emulsion (Alkamuls®) by gavage for 79 weeks. The aqueous vehicle was considered important because all the mechanistic work with the metabolites had been done using water vehicles. Corn oil has effects that might modify responses to a peroxisome proliferator like TCA. Forty-four tumors were recovered from these mice. This response rate was greater than that observed in lifetime studies done by the National Toxicology Program that used corn oil as the vehicle. The mutation frequency and spectra from tumors produced by TCE are compared with those produced by the two putative metabolites in Figure 1. Note that the period of exposure used in each experiment is identified at the top of the bar because data were presented last year that made it apparent that the mutation rate observed in DCA-induced tumors increased as the treatment period was extended. The TCA-induced tumors were examined at a single time point and dose (2 g/L for 52 weeks), whereas DCA-induced tumors were obtained at 0.5 and 2 g/L and at 52 and 87 weeks, respectively. Literature data (Maronpot et al. 1995) for the corn-oil-treated controls and TCE in corn oil groups were derived from mice treated for a full two years. Data generated in the present study show that there are substantial differences in the mutation frequency in H-ras codon 61 in tumors induced by DCA and TCA.

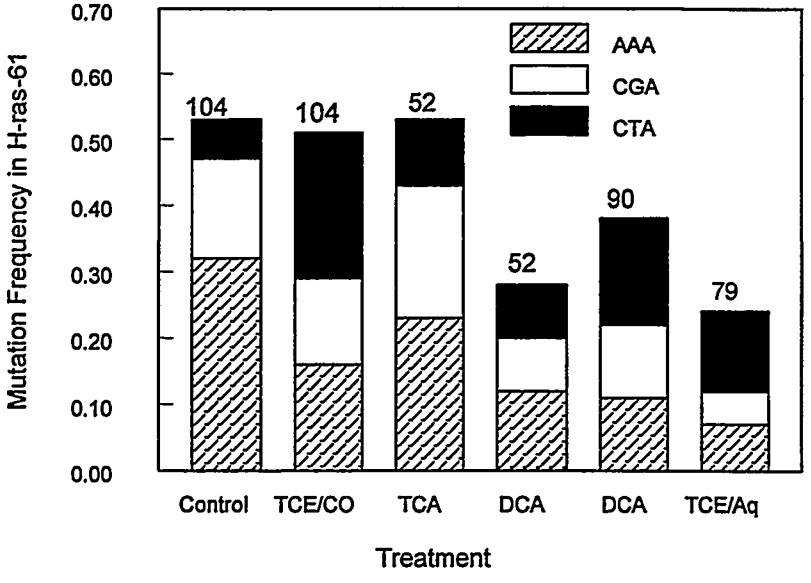

Figure 1. Mutation Frequency and Spectra of Codon 61 of the H-ras proto-oncogene in Liver Tumors of Mice Treated with TCE and its Metabolites. Historical control and TCE in corn oil (CO) groups are taken from Maronpot et al. (1995); remaining data from this study TCE/Aq indicate TCE was administered in an aqueous emulsion (Alkamuls).

The mutation frequency observed in control, TCE administered in corn oil, and TCA were all in excess of 50%. In contrast, the frequency in DCA-induced tumors and when TCE was administered in an aqueous vehicle are seen to approximate 25%. These data suggest that the high mutation spectrum previously reported for TCE (Anna et al. 1994) was influenced by the use of a corn oil vehicle.

The CTA mutation was observed in tumors induced by TCE in the aqueous vehicle at a higher fraction of total mutations observed than seen in historical control animals (Maronpot et al. 1995). This confirmed the nature of the spectra seen when TCE was administered with corn oil (Anna et al. 1994). DCA-induced tumors also appear to have a greater fraction of mutations at this site.

The lower mutation frequencies seen with DCA and TCE in the aqueous vehicle are much more consistent with previous observations made with other tumor promoters (Maronpot et al. 1995). Differences in the mutation spectra are not as convincing. If these data were expressed as the spectra of mutations within tumors carrying a H-ras mutation, as has conventionally been done, the results with DCA are more similar to that of TCE than that of TCA.

These data show that there are severe limitations in the use of mutation spectra as an indicator of the mode of action of a chemical carcinogen. Data presented below are much more consistent with the shifts in mutation spectra being produced by a selection process rather than compound-induced mutation. This is supported by the fact that, in tumors in which mutations were observed, the fraction of mutated DNA was always <50% of the DNA recovered from the lesion, strongly suggesting that H-ras mutations are late events in the development of mouse liver tumors. Clearly, relationships between mutation frequency and spectra are much more complicated than previously thought (Maronpot et al. 1995).

Because TCA has been shown to be a peroxisome proliferator, and that mechanism has already been discounted as having relevance for humans, much of our work has focused on DCA. We have been working with Kevin Minard and Robert Wind of the William R. Wiley Environmental Molecular Sciences Laboratory (EMSL) on imaging of tumors with magnetic imaging resonance (MRI) methods. An example of a high-resolution image of a mouse liver tumor is provided in Figure 2. We used this capability to demonstrate that the major effect of DCA on tumor induction was its effect on growth rates. This was done by treating mice until small tumors were detected in a set of 15 animals. The mice were randomly assigned to two groups: one was maintained on DCA treatment and the other placed on distilled water for the next two to three weeks. At the end of the period, the same liver tumors were re-imaged. As shown in Figure 3, tumors in those animals whose treatment was suspended stopped growing. This effect is most easily detected in smaller tumors because their fractional growth rate is much larger than that of larger tumors.

Using parameters obtained from the imaging of tumors, a model was developed to determine whether the effects of DCA on growth rates within tumors could explain the small lesion distribution. The model explicitly considered data previously developed on DCA's effects of replication rates in normal liver and tumors (Stauber and Bull 1997) and the observation of Snyder et al. (1997) that DCA suppressed apoptosis in normal hepatocytes. The combination of these two effects would provide a lesion distribution similar to that observed in mice that had been continuously treated with a genotoxic carcinogen. Not only do these data account for the lesion size distribution problem, they also explain the observation of Leavitt et al. (1997). These investigators found that increased numbers of *lac I* mutations were recovered in Big Blue transgenic mice treated with 3.5 g/L of DCA for 60 weeks but not at shorter time periods or at lower doses. These investigators were simply recovering cells from the mutations that

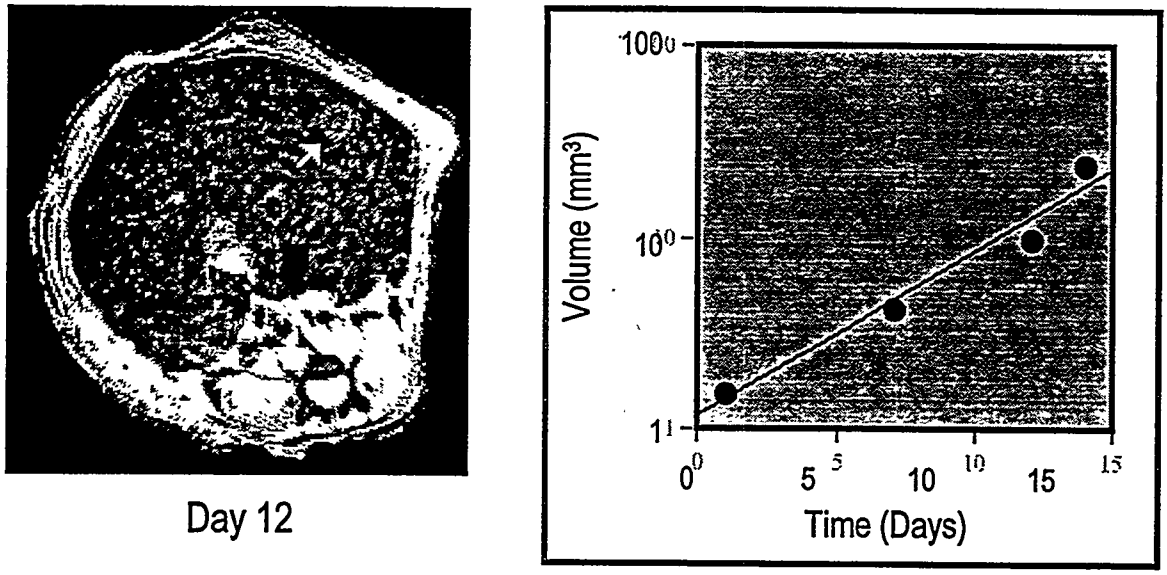

Figure 2. Measuring Rates of Tumor Growth with MRI. Tumor was produced by initiation with vinyl carbamate followed by administration of DCA at 2 g/L for approximately 24 weeks. The tumor was imaged on successive days indicated in the chart. Image provided was on day 12 of the experiment.

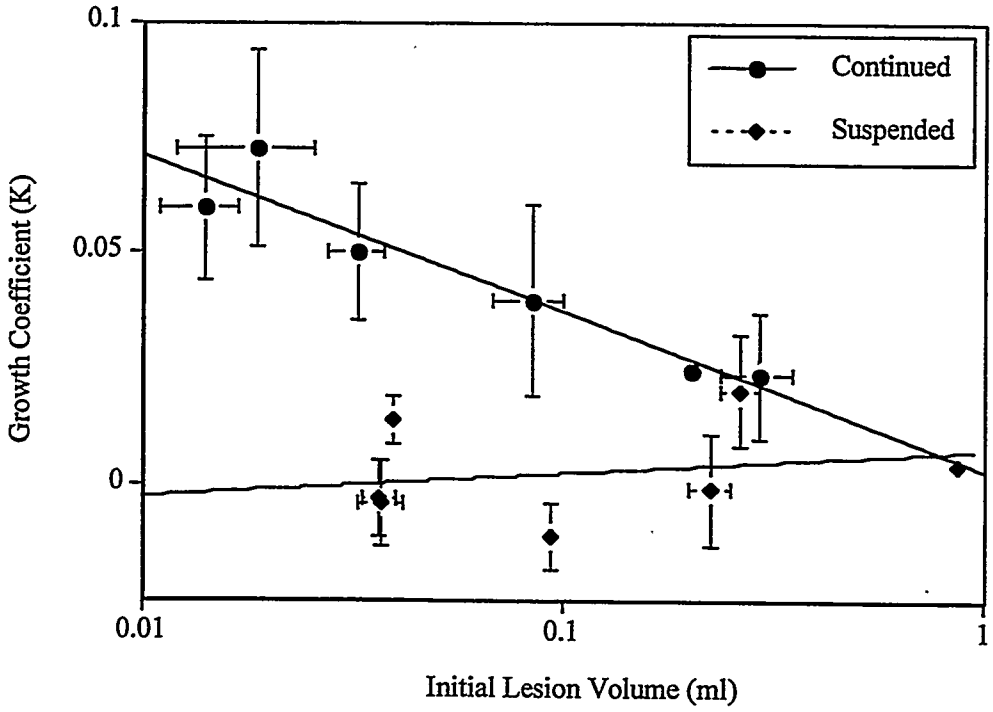

Figure 3. Effect of Suspending DCA Treatment (2 g/L) for Two Weeks on the Growth Rate of Hyperplastic Nodules in the Liver of B6C3F1 Mice. Each point represents the rate of growth of a single lesion between two successive MRI measurements 2-3 weeks apart. Horizontal represents the SD of lesion volume measurements, while the vertical bars represent the corresponding SD for the growth rate measurement.

were occurring in microscopic lesions, even though they had been careful to exclude tumor tissue from their samples. Therefore, these data add further support to the hypothesis that DCA is acting primarily, if not exclusively, as a tumor promoter.

Pharmacokinetic Results. Issues related to the dosimetry of the DCA that is produced from the metabolism of TCE have become much clearer in the past year. There are two issues: 1) the amount of DCA that is generated from a given dose of TCE and 2) the amount of DCA that must be in the liver to induce a carcinogenic response. As previously reported, DCA treatment results in substantial decreases in the metabolic clearance of the compound when mice are on chronic treatment at the high doses that have been used to induce cancer. Considerable confusion has been generated in the literature concerning the actual blood levels of DCA that result from the metabolism of TCE. Issues related to internal versus external doses of DCA were resolved in a paper published this last year (Kato-Weinstein et al. 1999). Blood concentrations resulting from treatment with 2 g DCA/L of drinking water are very high (approximately 500 μM) if measured during the period of water consumption (i.e., during the night in mice) and are less than 10 μM during the day. Lowering the concentration in drinking water by only 4-fold to 0.5 g/L resulted in peak concentrations of only 2-5 μM during the night, but which were immeasurable during the day (limit of quantitation = 1 μM). This is because the metabolism of DCA at these low doses is extremely rapid, in the range of 5-10 minutes. A concentration of 0.5 g/L of drinking water gives rise to an 80% tumor incidence in mice when administered for a lifetime; thus it indicates that low systemic concentrations of DCA are sufficient to induce cancer. Data from our initiation/ promotion studies indicates that 0.1 g DCA/L does not induce cancer. Concentrations of DCA seen in the blood from a dose of 1000 mg/kg TRI (the lowest carcinogenic dose tested by the National Toxicology Program) are maximally 1-2 μM. These data have brought the potential contribution of DCA to liver tumor induction by TCE to a much more reasonable level. A paper published last year (Merdink et al. 1998) demonstrated that the amounts of DCA produced in the metabolism of TCE, chloral hydrate, or TCA were very low. While there is evidence (i.e., the mutation frequency data) that DCA is contributing to the carcinogenic response, that contribution is shared with and fully accounted for by its effects in combination with TCA.

Task 2 - Establishing Selective Advantage as a Mode of Action for DCA and TCA. The most important aspect of this project was to show that the hepatocarcinogenic activity of TCE in mice is accounted for by a mode of action that does not involve direct interaction of the active metabolites with DNA.

The potency of a nongenotoxic tumor promoter depends on the ability of the compound to stimulate the survival and replication of initiated cells, and measuring this effect requires the actual isolation of initiated cells. A reliable characteristic of initiated cells is the ability to proliferate under anchorage-independent conditions, such as in culture over soft agar. Although growth over soft agar has been extensively studied using continuous cell lines (which are by definition already initiated), less is known about the response in primary cells.

The assay was used to measure the relative potency of DCA and TCA to promote the clonal growth of initiated hepatocytes (Stauber et al. 1998). As is shown in Figure 4, incubation of hepatocytes from untreated mice with TCA or DCA caused a dose-dependent increase in anchorage-independent colonies that form over soft agar. Both DCA and TCA were approximately equally effective in promoting colony formation in vitro. In vitro, the effective concentration of either haloacetate to promote an increase in colony formation was between 200-500 μM. Furthermore, analysis of gene expression markers on DCA or TCA-promoted colonies indicated that the phenotype of these colonies reflect the phenotype of tumors promoted by chronic exposure in vivo (Stauber et al. 1998). Given the limited evidence for mutagenicity

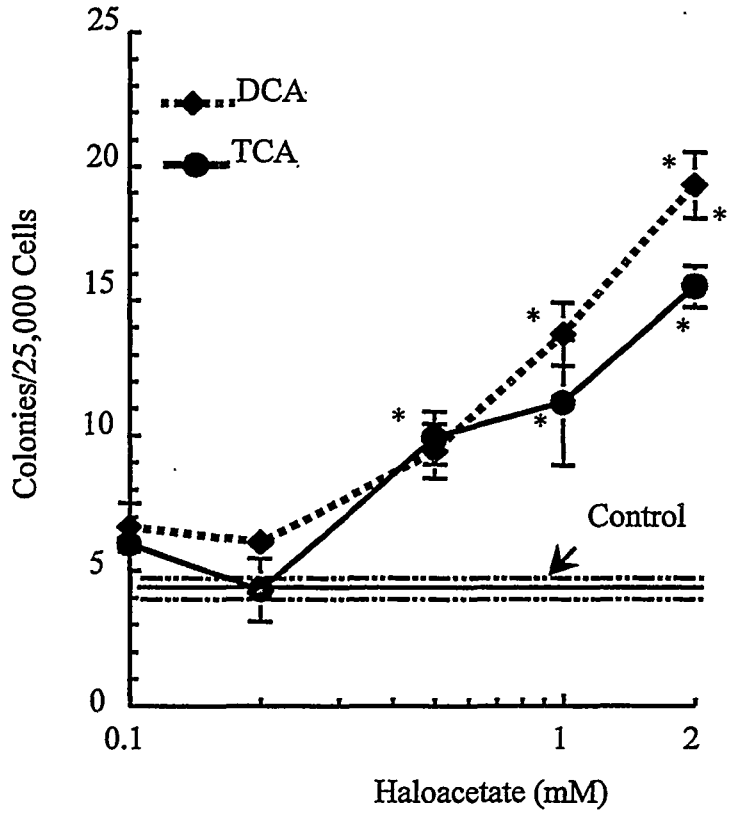

Figure 4. Effect of DCA and TCA on Anchorage-Independent Hepatocellular Colony Foundation in Vitro. Hepatocytes were isolated from untreated mice and cultured over agar in the presence of the DCA or TCA for 10 days. The number of anchorage-independent colonies was scored by microscopy.

*Differs from untreated control ($p<0.05$).

by these chemicals, these studies suggest that TCA and DCA promote the survival and growth of different populations of spontaneously initiated hepatocytes (Stauber et al. 1998), similar to previous reports for chronic in vivo exposure (Stauber and Bull 1997).

Although DCA and TCA exposures are equally potent in promoting anchorage-independent growth in vitro, comparison of these results with the kinetic analysis of potential DCA and TCA formation after TCE exposure raises questions about the role of DCA in tumors induced by TCE. At carcinogenic doses of TCE typically used in bioassays, sustained blood concentrations of ≥200 μM TCA are easily achieved. In contrast, the production of such concentrations of DCA in blood from metabolism of TCE is neither measurable nor predicted by kinetic models (Merdink et al. 1998).

Prior work has shown that DCA inhibits its own metabolism (Gonzalez-Leon et al. 1997). Therefore, the potency of DCA on stimulating colony formation was examined in hepatocytes taken from mice that were pretreated with a minimally carcinogenic concentration of DCA in drinking water (0.5 g/L). In hepatocytes isolated from DCA-pretreated mice an increase in colony formation above untreated controls was observed with concentrations of DCA as low as 20 μM in vitro (Figure 5). For comparison, concentrations ≥200 μM DCA were necessary to stimulate colony formation in hepatocytes from naïve mice, indicating that DCA pretreatment in vivo caused an increase in hepatocellular sensitivity by ≥10-fold. These data largely rectify the discrepancies in the in vivo and in vitro potency of DCA.

Recent reports have associated increased serum insulin concentrations with occupational exposures to trichloroethylene (Goh et al. 1998). Increased amounts of insulin could also account for the large accumulations of glycogen in the liver of mice treated with DCA. However, our studies found that serum insulin levels were significantly depressed by DCA treatment. Figure 6 provides data obtained

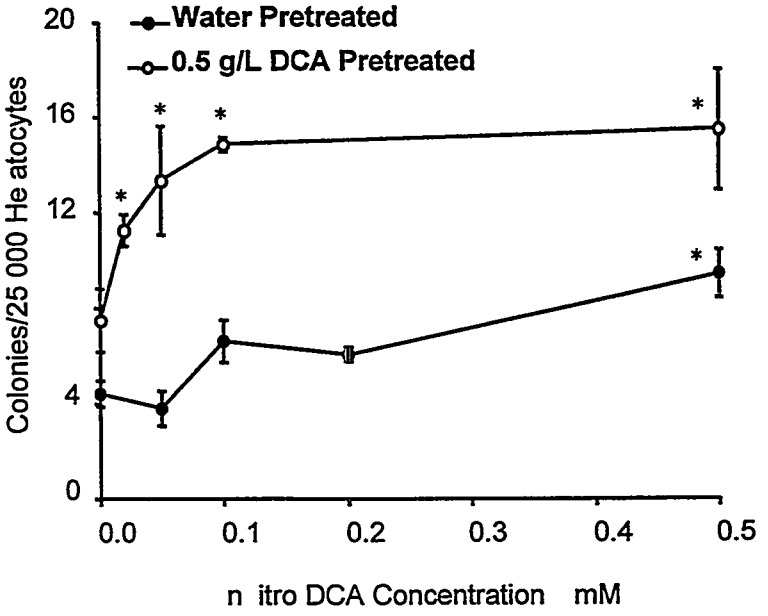

Figure 5. Effect of In Vivo DCA Pretreatment on the Sensitivity of Hepatocytes to Subsequent In Vitro DCA Exposure. Hepatocytes were isolated from mice pretreated with either water or 0.5 g/L DCA in water for two weeks. The cells were then cultured over agar in the presence of 0-0.5 mM DCA for 10 days and anchorage-independent colonies were scored.

*Differs from controls lacking DCA in vitro ($p<0.05$).

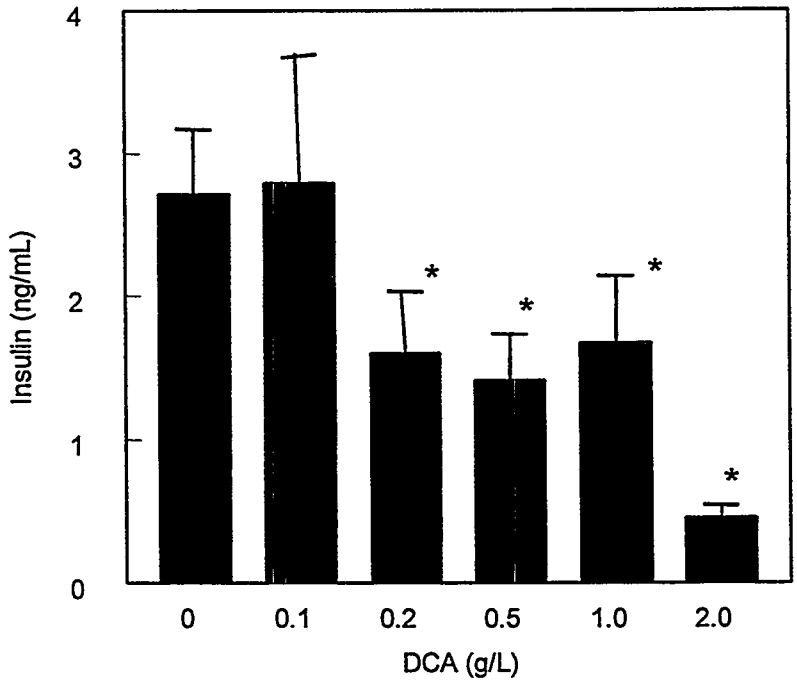

Figure 6. Serum Insulin Concentrations in B6C3F1 Mice that Have Been Treated with the Indicated Concentrations of DCA in Their Drinking Water for 10 Weeks, Measured at 3 AM; vertical bars indicate SEM of not less than six mice at each treatment level.

from animals on DCA treatment at 3 AM. This corresponds to the time when the mice are drinking water actively, when blood levels of DCA are at their highest, and during the active feeding period of mice. TCA did not have consistent effects on serum insulin concentrations (data not shown).

Parallel to the decreases in serum insulin is a decrease in the insulin receptor in the liver. Concentrations of DCA in drinking water that produce cancer cause substantial decreases in insulin-receptor expression after 10 weeks of treatment (Figure 7). Measurements of insulin receptor expression in normal liver and tumors in mice treated with DCA for 52 weeks displayed an interesting pattern (Figure 8). Insulin receptor in normal hepatocytes of treated mice again depressed (not as dramatically

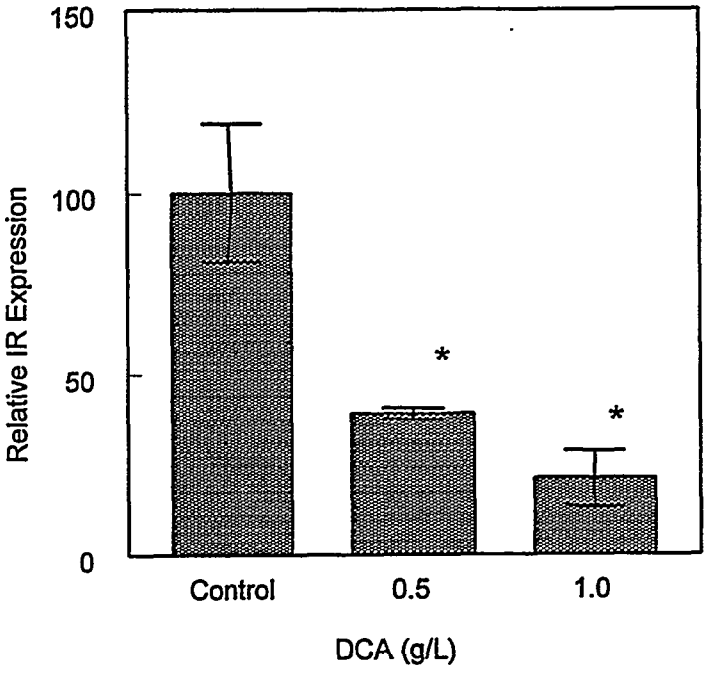

Figure 7. Insulin Receptor Expression in the Liver of Male B6C3F1 Mice Treated with the Indicated Concentrations of DCA in Drinking Water for 10 Weeks. Mice were sacrificed at 3 AM. Vertical bars indicate the ± SEM of not less than six mice at each treatment.

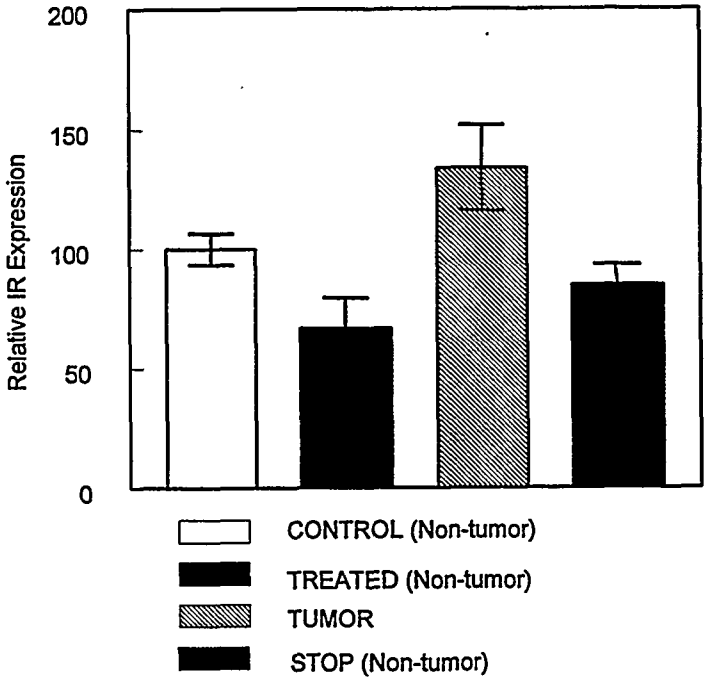

Figure 8. Insulin Receptor Expression in Hepatocellular Tumors of B6C3F1 Mice Treated with DCA (2 g/L) Relative to Surrounding Normal Tissue. Note that non-tumor tissue levels recovered to the point of control levels of IR expression when treatment was suspended for two weeks. Vertical bars indicate ± SEM for not less than six animals or tumors.

as that observed at 10 weeks, but mice were sacrificed during the day rather than at night). In contrast, the expression of insulin receptor in tumors was twice that of surrounding tissues in DCA-treated mice. An interesting additional finding was that suspension of treatment for two weeks allowed insulin receptor expression to recover to control levels in the normal portions of the liver.

The insulin signaling pathway can influence carcinogenic effects by altering the rates of cell division and apoptosis (Tanaka and Wands 1996). In Figure 9, the levels of an active form of a downstream effector protein in liver from control animals, and normal liver and tumors from DCA-treated mice, are displayed. The activity of this protein (as measured by phosphorylation) was substantially increased in tumors. However, it is not activated by DCA treatment in the normal parts of the liver. These results are very compatible with the differential effects that DCA treatment has on replication rates in normal tissue and tumors. The depressed replication rates in normal tissue could be accounted for by the decrease in serum insulin concentrations, while the increased replication rates may be associated with the activation of the MAPK pathway. Increased sensitivity to insulin by increased insulin receptor levels could be one contributor to the increased activity of the MAPK and may contribute to the increased replication rates in tumors in DCA-treated mice.

Although there are effects of DCA that can be measured at the molecular level with chronic DCA treatment, these effects appear to have a latent period and are not reflected by in vitro treatment with DCA. This suggests that the mechanism by which DCA induces hepatic tumors may be indirect. DCA has been known for its ability to affect intermediary metabolism at high doses, primarily by inhibiting the pyruvate dehydrogenase kinase, resulting in accelerated Kreb's cycle activity. However, the apparent K_I for such effects is approximately 200 μM (Pratt and Roche 1979), whereas data provided in this study indicate that it can induce tumors at systemic concentrations two orders of magnitude lower. The only biochemical effect of DCA that occurs at these low concentrations in the blood is accumulation of glycogen (Kato-Weinstein et al. 1998). The dose-response relationship for glycogen accumulation in the liver parallels the low range of the tumorigenic doses (Figure 10). It is known that glycogen accumulation in DCA treatment apparently inhibits glycogen synthesis by a feedback mechanism. It is possible that this feedback is broader than previously appreciated, including the down regulation of insulin receptor expression and depressing serum insulin concentrations observed in this study. A characteristic common to all DCA-induced hyperplastic nodules and tumors is that they lack glycogen (Bull et al.

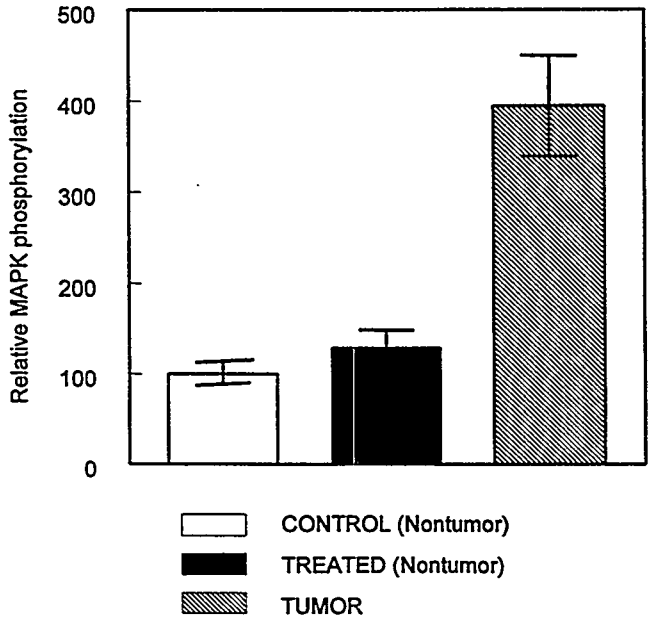

Figure 9. Mitogen-Activated Protein Kinase (MAPK) Phosphorylation Levels in Tumors and Non-Tumor Tissue in the Liver of B6C3F1 Mice Treated with DCA. Vertical bars indicate ± SEM of tissue samples obtained from not less than six mice.

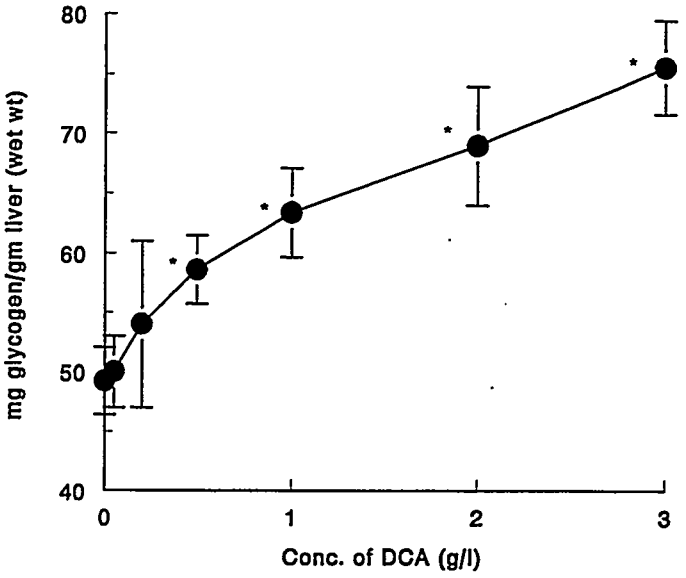

Figure 10. Liver Glycogen Concentrations in the Liver of B6C3F1 Mice Treated with Increasing Concentrations of DCA in Their Drinking Water for two Weeks. Each data point represents the mean of means obtained from not less than six mice + SEM.

1990). Others have demonstrated that this phenotype lacks glycogen synthase (Bannasch et al. 1984). This could also account for the fact that insulin receptor is not down-regulated, but appears up-regulated in DCA-induced tumors.

Implications for EM

This research has demonstrated that DCA and TCA can completely account for liver tumor induction in mice by TCE. The bulk of the experimental evidence suggests that neither TCE nor its two hepatocarcinogenic metabolites are mutagenic at concentrations that are relevant in vivo. Data in this project identify alternative modes of action for the two metabolites that are sufficient explanations for the carcinogenic response of TCE. These data have been accepted by the National Center for Environmental Assessment as a reasonable argument for a less than linear method of low-dose extrapolation.

The results from the colony formation assay clearly establish that these metabolites cause colony growth from initiated cells that spontaneously occur in the liver of B6C3F1 mice. In the case of DCA, a second mechanism, involving the release of insulin, occurs at a lower dose. However, this has not yet been shown to be responsible for liver tumor induction.

TCA carcinogenic activity is associated with its activity as a peroxisome proliferator. On principle, EPA has accepted that such compounds should be dealt with by the margin of exposure rather than the linear low-dose extrapolation. Peroxisome proliferation is of equivocal relevance as a tumorigenic mechanism in humans. In addition, TCA does not even induce liver tumors in rats.

The mechanism by which DCA produces liver cancer is still unclear, but it appears to be somewhat novel. It appears that one or more effects on intermediary metabolism creates alterations in insulin-signaling processes that may make a contribution to the carcinogenic responses. However, the key result of the present study has been to show that it clearly acts as a tumor promoter.

The following are critical data elements from this study:

- Both TCA and DCA stimulate the growth of anchorage-independent colonies from suspensions of hepatocytes derived from naïve mice that faithfully reflect the different phenotypes observed in vivo.
- DCA's effects on tumorigenesis was shown to directly affect the growth rate of tumors in vivo using MRI. This strongly supports the hypothesis that it is acting as a tumor promoter.
- Modeling of growth data obtained from MRI measurements indicates that previously reported effects of DCA on cell replication rates with hyperplastic nodules and suppressed rates of apoptosis can account for the lesion size distribution.
- These data also provide an explanation of the increased recovery of *lac I* mutant cells from mice chronically treated with DCA.
- The carcinogenicity of DCA in the liver appears to arise primarily as an indirect manifestation of its effects on intermediary metabolism.

A member of our research team (Richard J. Bull) is preparing the final draft on the mode of action paper being used by the EPA as a test case for their new Proposed Cancer Risk Assessment Guidelines. The arguments put forward above have been generally accepted by EPA and will form the basis for their decision. Because kidney tumors in rats are also produced with TCE, the impact of this work will be to change the potency estimate from that derived from liver tumor induction in the mouse to kidney tumor induction in mice. This should decrease the estimated risk per unit dose by approximately 10-fold. Informal discussion has been conducted with the Office of Water of the EPA. If the new guidelines are adopted in treating liver tumor induction by TCE, they intend to determine whether the drinking water MCL will need to be revised.

References

Anna CH, RR Maronpot, MA Pereira, JF Foley, DE Malarkey, and MW Anderson. 1994. *Carcinogenesis* 15:2255-2261.

Bannasch P, HJ Hacker, F Klimek, and D Mayer. 1984. "Hepatocellular glycogenosis and related pattern of enzymatic changes during hepatocarcinogenesis." *Adv. Enzyme Regul.* 22:97-121.

Bull RJ, IM Sanchez, MA Nelson, JL Larson, and AL Lansing. 1990. "Liver tumor induction in B6C3F1 mice by dichloroacetate and trichloroacetate." *Toxicology* 63:341-359.

Goh VH-H, S-E Chia, and CN Ong. 1998. "Effects of chronic exposure to low doses of trichloroethylene on steroid hormone and insulin levels in normal men." *Environ. Health Persp.* 106:41-44.

Gonzalez-Leon A, IR Schultz, and RJ Bull. 1997. "Pharmacokinetics and metabolism of dichloroacetate in the F344 rate after prolonged administration in drinking water." *Toxicol. Appl. Pharmacol.* 146:189-195.

Leavitt SA, AB DeAngelo, MH George, and JA Ross. 1997. "Assessment of the mutagenicity of dichloroacetic acid in *lacI* transgenic B6C3F1 mouse liver." *Carcinogenesis* 18:2101-2106.

Maronpot RR, T Fox, DE Malarkey, and TL Goldsworthy. 1995. "Mutations in the *ras* proto-oncogene: Clues to etiology and molecular pathogenesis of mouse liver tumors." *Toxicology* 101:125-156.

Pratt ML, and TE Roche. 1979. "Mechanism of pyruvate inhibition of kidney pyruvate dehydrogenasea kinase and synergistic inhibition by pyruvate and ADP." *J Biol Chem* 254:7191-7196.

Snyder RD, J Pullman, JH Carter, HW Carter, and AB DeAngelo. 1995. "In vivo administration of dichloroacetic acid suppress spontaneous apoptosis in murine hepatocytes." *Cancer Res.* 55:3702-3705.

Stauber AJ, and RJ Bull. 1997. "Differences in phenotype and cell replicative behavior of hepatic tumors inducted by dichloroacetate (DCA) and trichloroacetate (TCA)." *Toxicol. Appl. Pharmacol.* 144:235-246.

Tanaka S, and JR Wands. 1996. "Insulin receptor substrate 1 overexpression in human hepatocellular carcinoma prevents transforming growth factor β1-induced apoptosis." *Cancer Res.* 56:3391-3394.

Publications

Kato-Weinstein J, MK Lingohr, BD Thrall, and RJ Bull. 1998. "Effects of dichloroacetate on carbohydrate metabolism in B6C3F1 mice." *Toxicology* 130:141-154

Lingohr MK, BD Thrall, and RJ Bull. 1999. "Serum insulin levels and differential insulin receptor expression in livers and liver tumors of mice treated with dichloroacetate (DCA)." *Toxicol. Appl. Pharmacol.* (in press).

Merdink JL, A Gonzalez-Leon, RJ Bull, and IR Schultz. 1998. "The extent of dichloroacetate formation from trichloroethylene, chloral hydrate, trichloroacetate, and trichloroethanol in B6C3F1 mice." *Toxicological Sciences* 45:33-41.

Miller JH, K Minard, RA Wind, GA Orner, LB Sasser, and RJ Bull. 1999. "Is Initiation a Necessary Component for the Induction of Liver Tumors by DCA or Does DCA Only Affect Growth Rates?" *Toxicol. Appl. Pharmacol.* (submitted).

Mounho BJ, and BD Thrall. 1998. "Peroxisome proliferator-induced activation of extracellular signal-regulated kinase (Erk) pathway contributes to hepatocellular clonal expansion." *Toxicol. Appl. Pharmacol.* (submitted).

Orner GA, JA Malone, LC Stillwell, RS Cheng, AJ Stauber, L Sasser, BD Thrall, and RJ Bull. 1998. "H-ras codon 61 mutation frequency and spectra in trichloroethylene, dichloroacetate, and trichloroacetate –induced liver tumors in male B6C3F1 mice" (in preparation).

Schultz IR, JL Merdink, A Gonzalez-Leon, and RJ Bull. 1999. "Comparative toxicokinetics and metabolism of chlorinated and brominated haloacetates in F344 rats." *Toxicol. Appl. Pharmacol.* (in press).

Stauber AJ, RJ Bull, and BD Thrall. 1998. "Dichloroacetate and trichloroacetate promote clonal expansion of anchorage-independent hepatocytes, in vivo and in vitro." *Toxicol. Appl. Pharmacol.* 150:287-294.

Presentations

Bull RJ, K Minard, LB Sasser, MK Lingohr, and RA Wind. 1999. "Dichloroacetate-induced liver tumors cease growing on removal of treatment: Result of an insulin-sensitive phenotype?" AACR Proceedings 40:3321.

Gonzalez-Leon A, JL Merdink, IR Schultz, and RJ Bull. 1998. "Dichloroacetate auto-inhibits its degradation in the cytosol." Society of Toxicology, 37th Annual Meeting #426.

Kato-Weinstein J, BD Thrall, and RJ Bull. 1998. "The effect of haloacetates on carbohydrate metabolism in B6C3F1 mice." Society of Toxicology, 37th Annual Meeting #308.

Lingohr MK, BD Thrall, and RJ Bull. 1998. "Dichloroacetate (DCA) affects proteins involved in insulin signaling in mouse liver cells." Society of Toxicology, 37th Annual Meeting #61.

Merdink JL, IR Schultz, and RJ Bull 1998. "Formation of dichloroacetic acid in B6C3F1 mice from trichloroethylene or its metabolites." Society of Toxicology, 37th Annual Meeting #1621.

Mounho BJ and BD Thrall. 1998. "Tumor promotion by peroxisome proliferators may involve the activation of mitogenic activated protein kinases (ERK1/ERK2)." Society of Toxicology, 37th Annual Meeting #51.

Orner GA, LC Stillwell, RS Cheng, LB Sasser, RJ Bull, and BD Thrall. 1998. "Effects of trichloroacetate (TCA) and dichloroacetate (DCA) on H-ras in male B6C3F1 mice." Society of Toxicology, 37th Annual Meeting #60.

Stauber AJ, RJ Bull, and BD Thrall. 1998. "Dichloroacetate and trichloroacetate promote clonal expansion of anchorage-independent hepatocytes." Society of Toxicology, 37th Annual Meeting #62.

Schultz IR, A Gonzalez-Leon, JL Merdink, and RJ Bull. 1998. "Comparative toxicokinetics and metabolism of halo-acetic acids in F344 rats." Society of Toxicology, 37th Annual Meeting #1045.

Distribution

No. of
Copies

OFFSITE

John Ahearne
Sigma Xi
99 Alexander Drive
Research Triangle Park, NC 27709

Professor Mansoor Alam
Department of Materials
New Mexico Tech
Socorro, NM 87801

G. Ballew
Pacific Rim Enterprise Center
660 George Washington Way, Suite B
Richland, WA 99352

J. R. Beall
Office of Energy Research
U.S. Department of Energy
19901 Germantown Road (ER-72)
Germantown, MD 20874-1290

Richard Begley
101 Red Oak Lane
Aiken, SC 29803

Jimmy Bell
Bell Consultants, Inc.
137 Bowsprit Lane
Kingston, TN 37763

Professor John D. Berg
Department of Chemical
Engineering (BF-10)
University of Washington
Seattle, WA 98195

Edgar Berkey
Concurrent Technologies Corporation
320 William Pitt Way
Pittsburgh, PA 15238

No. of
Copies

Paul Bertsch
University of Georgia
Savannah River Ecology Laboratory
P.O. Drawer E/Bldg 737 A
Aiken, SC 29801

Robert C. Birtcher
Argonne National Laboratory
Building 212
9700 South Cass Avenue
Argonne, IL 60439

David R. Boone
Dept of Env. Sci. and Engineering
Oregon Graduate Institute of Science
and Technology
2000 Northwest Walker Road
Beaverton, OR 97006

G. G. Boyd
Office of Environmental Management
U.S. Department of Energy
19901 Germantown Road (5B-014)
Germantown, MD 20874-1290

Michelle Broido
U.S. Department of Energy
19901 Germantown Road, MSIN F-240
Germantown, MD 20874-1290

G. Brown
Stanford University
Department of Geological and
Environmental Sciences
Stanford, CA 94305-2115

Barry Burks
Oak Ridge National Laboratory
P.O. Box 2008, Bldg. 7601, MSIN-6304
Oak Ridge, TN 37831-6304

No. of
Copies

B. Calloway
Westinghouse Savannah River Company
Savannah River Technology Center
Building 773-A/Rm A-229
Mail Stop 28
Aiken, SC 29802

John Carberry
Dupont
Experimental Station
Building 249/119
P.O. Box 80249
Wilmington, DE 19880-0249

P. M. Castle
Lockheed Martin Idaho Technologies Company
P.O. Box 1625, MSIN 5205
Idaho Falls, ID 83415

Gregory Choppin
Florida State University
Department of Chemistry (B-164)
600 W. College Ave.
Tallahassee, FL 32606-3006

Sue B. Clark
Washington State University
Chemistry Department
Pullman, WA 99164

Paul Clayton
Vice President for Academic Affairs and Provost
Oregon Graduate Institute
P.O. Box 91000
Portland, OR 97291-1000

Jim Cochran
Washington State Univ. at Tri-Cities
100 Sprout Road
Richland, WA 99352-1643

No. of
Copies

Roger G. Collis
Environmental Technology Partnership
Washington Dept of Community, Trade, and Economic Development
2001 Sixth Avenue, Suite 2700
Seattle, WA 98121

L. Coleman
Washington State Department of Ecology
1315 W. 4th
Kennewick, WA 99336

Julie Conner
U.S. Department of Energy
Idaho Operations Office
785 DOE Place
Idaho Falls, ID 83402

Allen Croff
Martin Marietta Energy Systems, Inc.
Oak Ridge National Laboratory
P.O. Box 2008
Oak Ridge, TN 37831-6178

Rico Cruz
Nez Perce Indian Nation
P.O. Box 365
Lapwai, ID 83450

John H. Cushman
Depts of Math and Agronomy
Purdue University
West Lafayette, IN 47907

P. M. Davidson
Office of Energy Research
U.S. Department of Energy
19901 Germantown Road (ER-15)
Germantown, MD 20874-1290

Professor Morton M. Denn
Lawrence Berkeley National Laboratory
Chemical Engineering Department
University of California
Berkeley, CA 94720-1462

No. of
Copies

S. L. Domoter
Office of Environmental Management
U.S. Department of Energy
19901 Germantown Road (EH-412)
Germantown, MD 20874-1290

Gary Eller
Los Alamos National Laboratory
MSIN E5-10
Nuclear Material Technology Division
Los Alamos, NM 87544

Tom Engel
University of Washington
Department of Chemistry
Bagley Hall Room 109
Seattle, WA 98195-1700

Robert Erdmann
P.O. Box 922
Grass Valley, CA 95945

Dennis Faulk
U.S. Environmental Protection Agency
MAF Plaza
712 Swift, Suite 5 (B5-01)
Richland, WA 99352

M. M. Fletcher
Belle W. Baruch Institute for Marine
Biology and Coastal Research
University of South Carolina
Columbia, SC 29208

Tom French
Westinghouse Savannah River Company
Bldg 773-A, A209
P.O. Box 616
Aiken, SC 29802

David Geiser
U.S. Department of Energy EM-52.1
19901 Germantown Road
1183/Cloverleaf Bldg.
Germantown, MD 20874-1290

No. of
Copies

Joe Gentilucci
JAG Technical Services, Inc.
127 Savannah Drive
Aiken, SC 29803

Kurt D. Gerdes
Office of Science & Technology
U.S. Department of Energy (EM-541)
19901 Germantown Road
1186 Cloverleaf Bldg.
Germantown, MD 20874-1290

P. W. Gibbons
P.O. Box 1970, MSIN H5-61
Richland, WA 99352-1300

Mark Gilbertson
U.S. Department of Energy (EM-52)
19901 Germantown Road
5A-031/FORS
Germantown, MD 20874-1290

T. R. Ginn
172 Everson Hall
Department of Civil and Environmental
Engineering
University of California, Davis
Davis, CA 95616-5294

Dib Goswami
Washington State Department of Ecology
1315 W. 4th
Kennewick, WA 99336

D. J. Grimes
Office of Energy Research
U.S. Department of Energy
19901 Germantown Road
Germantown, MD 20874-1290

Barbra Harper
Yakama Indian Nation
1933 Jadwin, Suite 110
Richland, WA 99352

No. of
Copies

Stuart Harris
Confederated Tribes of the
Umatilla Indian Reservation
Old Mission Hwy 30
Pendleton, OR 97801

Paul Hart
Morgantown Energy Technology Center
3610 Collins Ferry Road
Morgantown, WV 26507-0880

Peter E. Haustein
Brookhaven National Laboratory
P.O. Box 5000
Upton, NY 11973

Thomas Hirons
Los Alamos National Laboratory
P.O. Box 1663, MSIN J591
Los Alamos, NM 87545

Roland Hirsch
U.S. Department of Energy
Medical Applications and
Biophysical Research Division
19001 Germantown Road (ER-73)
Germantown, MD 20874-1290

Earl Holtzscheiter
Westinghouse Savannah River Company
Building 773-A/Rm A-229
Mail Stop 28
Aiken, SC 29802

Ken Hubbard
Asst Asso. Provost for Research
and Economic Development
Dean of Graduate School
University of Montana
University Hall 118
Missoula, MT 59812-1329

Tom Isaacs
Lawrence Livermore National Laboratory
P.O. Box 808, MS/L-19
Livermore, CA 94551

No. of
Copies

Professor Art Janata
School of Chemistry and Biochemistry
Georgia Institute of Technology
Atlanta, GA 30332-0400

Moses Jaraysi
Washington State Department of Ecology
1315 W. 4th
Kennewick, WA 99336

Arvid Jensen
Lockheed Martin Idaho Technologies
Company
P.O. Box 1625
Idaho Falls, ID 83415-3204

Dawn Kaback
Colorado Center for Environmental
Management
999 18th St, Ste 2750
Denver, CO 80202

James R. Karr, Ph.D.
Dept. Fisheries and Zoology
104 Fisheries Center
University of Washington
Seattle, WA 98195

Dr. Ken Kemner
Argonne National Laboratory
ER203 C-129
9700 S. Cass Ave.
Argonne, IL 60439

Roy Koch
Vice Provost for Research
Dean of Graduate Studies
Portland State University
P.O. Box 751
Portland, OR 97207-0751

Bruce Kowalski
Chemistry Department (BG-10)
University of Washington
Seattle, WA 98195

No. of
Copies

Jerome J. Kukor
Biotechnology Center, Foran Hall
Cook College Campus, Rutgers University
The State University of New Jersey
59 Dudley Road
New Brunswick, NJ 08901-8520

Alvin Kwiram
Vice Provost for Research
University of Washington
312 Gerberding Hall
P.O. Box 351237
Seattle, WA 98195-1237

Brenda Lewis
Westinghouse Savannah River Company
P.O. Box 616
Aiken, SC 29802

Paul Lurk
U.S. Department of Energy (EM-542)
19901 Germantown Road
1168/Cloverleaf Bldg.
Germantown, MD 20874-1290

Theodore E. Madey
Rutgers University
P.O. Box 849
Piscataway, NJ 08855-0849

R. S. Marianelli
Office of Energy Research
U.S. Department of Energy
19901 Germantown Road (ER-14)
Germantown, MD 20874-1290

J. A. Martin
Sandia National Laboratories
P.O. Box 5800
Albuquerque, NM 87185-0709

M. R. Martin
Lockheed Martin Idaho Technologies
Company
P.O. Box 1625, MSIN 2424
Idaho Falls, ID 83415

No. of
Copies

Todd Martin
Hanford Advisory Board
West 1408 Broadway
Spokane, WA 99201

R. N. Massey
Office of Environmental Management
U.S. Department of Energy
19901 Germantown Road (EM-64)
Germantown, MD 20874-1290

C. Phil McGinnis
Martin Marietta Energy Systems, Inc.
Oak Ridge National Laboratory
P.O. Box 2008
Oak Ridge, TN 37821-6273

M. E. McIlwain
Lockheed Martin Idaho Technologies
Company
P.O. Box 1625, MSIN 2210
Idaho Falls, ID 83415

D. Meisel
Argonne National Laboratory
9700 South Cass Avenue
Argonne, IL 60439

W. D. St. Michel
Lockheed Martin Idaho Technologies
Company
P.O. Box 1625, MSIN 1061
Idaho Falls, ID 83415

D. L. Miller
Lockheed Martin Idaho Technologies
Company
P.O. Box 1625, MSIN 2208
Idaho Falls, ID 83415

W. S. Millman
Office of Energy Research
U.S. Department of Energy
19901 Germantown Road (ER-14)
Germantown, MD 20874-1290

No. of
Copies

Jerry Morin
Westinghouse Savannah River Company
Savannah River Technology Center
P.O. Box 616
Aiken, SC 29802

Professor Susan J. Muller
Chemical Engineering Department
University of California
Berkeley, CA 94720-1462

Alexandra Navrotsky
Department of Chemical Engineering
and Material Science
University of California-Davis
Davis, CA 95616

Tina Nenoff
Sandia National Laboratories
P.O. Box 5800
Albuquerque, NM 87185-0709

Professor Ronald Olsen
Department of Microbiology and
Immunology
5605 Medical Science Building II
University of Michigan Medical School
Ann Arbor, MI 48109-0620

J. M. Owendoff
Office of Environmental Management
U.S. Department of Energy
19901 Germantown Road (5A-014)
Germantown, MD 20874-1290

Ken Osborne
DOE Idaho Operations Office
785 DOE Drive
Idaho Falls, ID 83401

Robert T. Paine
Department of Chemistry
University of New Mexico
Albuquerque, NM 87131

No. of
Copies

Frank Parker
Vanderbilt University
400 24th Avenue South
New Engineering Building, Room 108C
Nashville, TN 37235

A. A. Patrinos
Office of Energy Research
U.S. Department of Energy
19901 Germantown Road (ER-70)
Germantown, MD 20874-1290

Michael R. Pfister
U.S. Department of Energy, EM-1
Environmental Management Advisory
Board
1000 Independence Ave., SW, Rm. 5B-171
Washington, DC 20585

Ken Picha
U.S. Department of Energy (EM-32)
Office of Eastern Operations
19901 Germantown Road 343/TREV
Germantown, MD 20874-1290

Bill Prindle
1556 Crestline Drive
Santa Barbara, CA 93105

10 Rod Quinn
801 University Blvd SE
Suite 102
Albuquerque, NM 87106

Linfeng Rao
Lawrence Berkeley National Laboratory
MS 70A-1150
1 Cyclotron Road
Berkeley, CA 94720

Professor Kenneth N. Raymond
Department of Chemistry
University of California at Berkeley
Berkeley, CA 94720

No. of
Copies

Doug Riggs
Legislative Director
Office of Congressman Doc Hastings,
4th District, Washington
1323 Longworth Building
Washington, DC 20515

Gary D. Roberson
DOE Albuquerque Operations Office
Pennsylvania and H St
Kirtland Air Force Base
Albuquerque, NM 87116

Dave Robertson
DOE Idaho Operations Office
785 DOE Drive
Idaho Falls, ID 83401

Professor William R. Rossen
Petroleum and Geosystems
Engineering Department
The University of Texas at Austin
Austin, TX 78712-1061

Professor D. Max Roundhill
Department of Chemistry
Texas Tech University
Lubbock, TX 79409-1061

Richard Scanlan
Dean of Research
Oregon State University
Administration Services Bldg A312
Corvallis, OR 97331

Wally Schulz
5314 Arbustos Court, NE
Albuquerque, NM 87111

William L. Scott
DOE Idaho Operations Office
785 DOE Drive
Idaho Falls, ID 83401

No. of
Copies

Dr. John S. Selker
Oregon State University
Corvallis, OR 97331

D. R. Sherwood
U.S. Environmental Protection Agency
MAF Plaza
712 Swift, Suite 5 (B5-01)
Richland, WA 99352

Jean'ne Shreeve
Vice President for Research and
Graduate Studies
Professor of Chemistry
University of Idaho
Moscow, ID 83843-4199

Leon T. Silver
Div. of Geological and Planetary Sciences
California Institute of Technology, 170-25
1200 East California Street
Pasadena, CA 91125

Robert Smith
Vice Provost for Research
Dean of Graduate School
Washington State University
Pullman, WA 99164-1030

R. N. Snelling
Lockheed Martin Idaho Tech Co
P.O. Box 1625, MSIN 2213
Idaho Falls, ID 83415

Stan Sobczyk
Nez Perce Indian Nation
P.O. Box 365
Lapwai, ID 83450

Joseph D. Spencer
SCUREF
Strom Thurmond Institute
Clemson, SC 29634-5701

No. of
Copies

Peter Spencer, Director
Center for Research on Occupational and
Environmental Toxicology L606
Oregon Health Sciences University
3181 SW Sam Jackson Park Road
Portland, OR 97202-3098

Ellen Stallings
Los Alamos National Laboratory
SM #30 Bikini Road
Los Alamos, NM 87545

Alex Stone
Washington State Department of Ecology
1315 W. 4th
Kennewick, WA 99336

Harold Sullivan
Los Alamos National Laboratory
P.O. Box 1663
Los Alamos, NM 87545

John Swanson
1318 Cottonwood
Richland, WA 99352

Robert Swenson
Vice President for Research
Montana State University
Montana Hall 207
Bozeman, MT 59717

Larry Tavlarides
Syracuse University
334 Hinds Hall
Syracuse, NY 13244

Tom Thomas
Lockheed Martin Idaho Technologies
Company
P.O. Box 1625, MSIN 3458
Idaho Falls, ID 83415-3423

No. of
Copies

Major Thompson
Steadman Upham
Vice Provost for Research and
Graduate Education
Dean of Graduate School
University of Oregon
112 Johnson Hall
Eugene, OR 97403-1226

Dr. Scott W. Tyler
Desert Research Institute
7010 Dandini Blvd.
Reno, NV 89512

Nancy Uziemblo
Washington State Department of Ecology
1315 W. 4th
Kennewick, WA 99336

George Vandegrift
Argonne National Laboratory
Building 205
9700 South Cass Avenue
Argonne, IL 60439

John Veldman
Westinghouse Savannah River Company
Bldg 773-A, A-210
P.O. Box 616
Aiken, SC 29802

Paul Wang
Concurrent Technologies Corp.
320 William Pitt Way
Pittsburgh, PA 15238

Westinghouse Savannah River Company
Building 773-A, C140
P.O. Box 616
Aiken, SC 29802

Jack Watson
Oak Ridge National Laboratory
P.O. Box 2008
Bldg 4500N, MS-6178
Oak Ridge, TN 37831-6178

No. of Copies

Tom Weber
6622 West Victoria
Kennewick, WA 99336

JR Wilkinson
Confederated Tribes of the
Umatilla Indian Reservation
Old Mission Hwy 30
Pendleton, OR 97801

Thomas Williams
DOE Idaho Operations Office
785 DOE Drive
Idaho Falls, ID 83401

Tom Winston
Ohio Environmental Protection Agency
401 East 5th Street
Dayton, OH 45402

Tom Woods
Yakama Indian Nation
1933 Jadwin, Suite 110
Richland, WA 99352

Jim Wright
U.S. Department of Energy
Savannah River Operations Office
P.O. Box A
Aiken, SC 29802

Lin Yarborough
U.S. Department of Energy
Albuquerque Operations Office
P.O. Box 5400
Albuquerque, NM 87185-5400

ONSITE

No. of Copies

13 **Hanford Contractors**

Tom L. Anderson	E6-28
John N. Appel	A3-03
John April	H0-17
W. Blaine Barton	R2-12
Roger E. Bauer	G1-54
Robert J. Cash	S7-73
Steven C. Foelber	H0-09
Ken A. Gasper	A3-03
Jim O. Honeyman	R2-58
Jerry D. Johnson	S7-73
Kim Koegler	H0-02
Stephen K. Pulsford	X9-10
Jerry D. White	H0-02

24 **U.S. Department of Energy Richland Operations Office**

Jay Austenborg	S7-41
Linda K. Bauer	H0-12
Dennis A. Brown	K8-50
Jeff Day	K8-50
Richard French	A6-54
Marcus J. Glasper	K8-50
James P. Hanson	K8-50
Richard Holten	H0-12
Maureen A. Hunemuller	S7-50
Peter M. Knollmeyer	A5-11
Catherine S. Louie	A0-21
Lance S. Mamiya	K8-50
Billie M. Mauss	K8-50
John P. Neath	K8-50
Ted Pietrok	K8-50
Lloyd L. Piper	A7-50
Craig Richins	K8-50
Robert M. Rosselli	K8-50
Shannon W. Saget	K8-50
Fred R. Serier	H0-12
K. Mike Thompson	H0-12
Deborah E. Trader	K8-50
Joseph J. Waring	T5-54
Don D. Wodrich	A0-21

200 **Pacific Northwest National Laboratory**

Joan Adams	K8-15
Richard C. Adams	K9-32
Cal Ainsworth	K3-61
Mike Alexander	K8-93
Robert W. Allen	K9-69
Greg Anderson	K8-93

No. of Copies		
Jack Bagley		K1-71
Sharon A. Bailey		K5-08
Eddie G. Baker		K2-12
Mari Lou Balmer		K8-93
William R. Barchet		K9-30
Dave Blanchard		P7-25
William F. Bonner		K9-14
Donald M. Boyd		K7-50
Fred Brockman		P7-50
Joseph W. Brothers		K9-20
Tom M. Brouns		K9-02
Sam Bryan		P7-25
Merwin L. Brown		K5-02
James L. Buelt		K9-09
Richard J. Bull		P7-56
Don M. Camaioni		K2-57
James A. Campbell		P8-08
Clark Carlson		P7-25
Scott A. Chambers		K8-93
Steven D. Colson		K8-88
Louis R. Corrales		K8-91
James P. Cowin		K8-88
John Darab		K3-59
Joseph L. Devary		K6-96
John L. Daschbach		K8-93
David A. Dixon		K1-83
Terrence J. Doherty		K8-21
Dennis D. Doneen		K8-21
Thomas H. Dunning		K9-44
Richard M. Ecker	Sequim	L5/312
Paul D. Ellis		K8-98
Gregory J. Exarhos		K2-44
Linda L. Fassbender		K8-07
Andrew R. Felmy		K8-96
Jim Fort		K7-15
Jim Fredrickson		P7-50
Mark D. Freshley		K9-36
Teresa A. Fryberger (5)		K8-84
Glen Fryxell		K2-44
James L. Fuller		K6-48
John Fulton		P8-19
Bobi A. Garrett		K8-09
Suzanne M.K. Garrett		K7-94
Phillip A. Gauglitz		K6-28
Glendon Gee		K9-33
Roy E. Gephart (5)		K9-76

No. of Copies	
Karen Goodman (10)	K9-02
Yuri Gorby	P7-50
Margaret Greenwood	K5-26
Bob L. Gruel	K8-60
Mark S. Hanson	K9-02
John S. Hartman	K5-25
Benjamin P. Hay	K1-83
Scott W. Heaberlin	K8-31
Howard Heinisch	P8-15
Michael A. Henderson	K8-93
Nancy Hess	P7-50
Wayne Hess	K8-88
Pavel Hrma	K6-24
Tim Hubler	K8-93
Landis D. Kannberg	K5-02
Paul K. Kearns	K2-20
James Kelley	P7-07
David W. Koppenaal	K8-98
W.L. (Bill) Kuhn	K7-15
John P. LaFemina	P7-27
Carlton D. Lee	K7-28
Mike Lilga	K2-12
Jun Liu	K2-54
Philip E. Long	K9-33
Greg J. Lumetta	P7-25
William J. Madia	K1-46
Judith A. Mahaffey	K8-38
Steven C. Marschman	P7-27
Wayne J. Martin	K3-54
Louis Martucci	K7-10
B. Peter McGrail	K6-81
Gary W. McNair	K7-94
Gary L. McVay	K2-50
Barry J. Merrill	K8-21
Ellyn M. Murphy	K3-61
Khris Olsen	K6-96
Jon L. Olson	BSRC/S128
Norman J. Olson	K9-46
Yasuo Onishi	K7-15
Mart Oostrom	K9-33
Thomas M. Orlando	K8-88
Thomas L. Page	K9-18
Charles H.F. Peden	K8-93
Larry R. Pederson	K2-44
William Pennell	K9-34
Loni M. Peurrung (30)	K6-24

No. of Copies		No. of Copies	
Linda R. Pond	K8-23	S. K. Sundaram	K6-24
Brent A. Pulsipher	K5-12	Guillermo Terrones	K7-15
Marilyn J. Quadrel	K9-18	S. Thevuthasan	K8-93
Dhanpat Rai	P7-50	Jim J. Thomas	K7-10
Brian M. Rapko	P7-25	Joel Tingey	P7-25
Scot Rassat	K6-28	Brian D. Thrall	P7-56
Bernard F. Saffell, Jr.	K5-02	Karla Thrall	P7-59
Jeffrey D. Saffer	K7-40	Jud W. Virden	K2-44
R. Jefferey Serne	K6-81	John Wacker	P7-07
Steve N. Schlahta	K9-69	Ron Walters	K1-79
Paul A. Scott	K9-46	Terry L. Walton	K9-46
L John Sealock	K9-04	Yong Wang	K8-93
Billy D. Shipp	K9-01	Andy Ward	K9-33
Steve C. Slate	K1-50	William J. Weber	K2-44
Gary Smith	K6-24	Walter C. Weimer	P7-27
Kelvin L. Soldat	K3-53	Mark White	K9-36
Dave Springer	P7-56	Raymond E. Wildung	P7-54
Steven L. Stein	BSRC/S171	R. E. Williford	K2-44
Terri L. Stewart	K9-18	Kwong K. Wong	P7-56
Gerry M. Stokes	K9-95	Clement Yonker	K2-57
Denis Strachan	K6-24	John M. Zachara	K8-96
B. Ray Stults	K9-76	Tom Zemanian	P7-07
Yali Su	K8-93	TFA Library (2)	K9-69
Johanes Sukamto	K8-93	Information Release (7)	K1-06